**Karlsruhe Institute of Technology**

# Analysis of Laser Shots of the Aeolus Satellite Observed with the Fluorescence Telescopes of the Pierre Auger Observatory

Masterarbeit
von

## Felix Knapp

am Institut für Astroteilchenphysik

| | |
|---|---|
| Reviewer: | Prof. Dr. Ralph Engel |
| Second Reviewer: | Prof. Dr. Guido Drexlin |
| Advisor: | Dr. Michael Unger |

Bearbeitungszeit: 25.05.2020  –  25.05.2021

# Erklärung zur Selbstständigkeit

Ich versichere, dass ich diese Arbeit selbstständig verfasst habe und keine anderen als die angegebenen Quellen und Hilfsmittel benutzt habe, die wörtlich oder inhaltlich übernommenen Stellen als solche kenntlich gemacht und die Satzung des KIT zur Sicherung guter wissenschaftlicher Praxis in der gültigen Fassung vom 17.05.2010 beachtet habe.

Karlsruhe, den 25.05.2021,  _____

Felix Knapp

Als Ansichtsexemplar genehmigt von

Karlsruhe, den 25.05.2021,  _____

Prof. Dr. Ralph Engel

# Contents

# 1. Zusammenfassung

Das Pierre-Auger-Observatorium ist mit einer Fläche von über $3000\,\mathrm{km}^2$ das weltweit größte Luftschauerexperiment. Es wurde mit dem Ziel entwickelt, die Herkunft und Zusammensetzung der kosmischen Strahlung mit höchsten Energien zu untersuchen. Dafür verwendet das Observatorium eine Kombination aus Oberflächendetektoren, welche Schauerteilchen am Erdboden nachweisen, und Teleskopen, die Fluoreszenzlicht messen, das durch die Anregung von Luftmolekülen durch Schauerteilchen erzeugt wird.

2019 wurde in den Daten der Fluoreszenzteleskope ein wiederkehrendes Signal entdeckt, welches Aeolus zugeordnet werden konnte, einem von der European Space Agency (ESA) betriebenen Satelliten mit der Aufgabe Windprofile in der Erdatmosphäre zu erstellen. Für diesen Zweck verwendet Aeolus einen zur Erde gerichteten UV-Lidar. Die Laserstrahlen passieren dabei einen Bereich nahe des Pierre-Auger-Observatoriums, wodurch in der Atmosphäre gestreutes Laserlicht von den Fluoreszenzteleskopen gemessen werden kann.

Das Thema dieser Arbeit ist, diesen neuartigen Datensatz systematisch zu analysieren und zu prüfen, ob er sich für eine Messung der Aerosole über dem Observatorium eignet. Dafür wurde zunächst eine Methode entwickelt, um Ort und Zeitpunkt des Laserdurchgangs aus öffentlich zugänglichen Satellitendaten vorherzusagen, mittels einer Projektion des Laserstrahls von der Satellitenposition auf die Erdoberfläche. Es wurde gezeigt, dass dadurch die Position der gemessenen Laserstrahlen und der Zeitpunkt des Laserdurchgangs korrekt vorhergesagt werden kann, sowie auch die Sichtbarkeit des Lasers über das Jahr hinweg.

Bereits vorhandene Methoden zur Rekonstruktion der in Auger für Atmosphärenmessung verwendeten Laser konnten weiterentwickelt werden, um verschiedene Eigenschaften der Aeolus-Laser zu bestimmen. Damit wurde insbesondere die Ankunftsrichtung der Laserstrahlen gemessen, welche gut mit der Erwartung seitens ESA übereinstimmt. Darüber hinaus wurde ein Likelihood-basierter Parameterscan entwickelt, welcher es ermöglicht sowohl die Laserenergie zu fitten, als auch Parameter, die das Aerosolprofil beschreiben. Es wurde demonstriert, dass der Parameterscan in der Lage ist, gleichzeitig Werte für Laserenergie und Aerosolparameter zu bestimmen. Dabei zeigte sich in Simulationsstudien, dass eine sehr gute statistische Genauigkeit erreicht wird. Diese ist allerdings von einer systematischen Verzerrung überlagert, dessen Ursprung bislang nicht geklärt werden konnte. Durch eine Anwendung des Scans auf gemessene Laserstrahlen wurden erste Werte für Laserenergie und Aerosole mithilfe von Aeolus-Laserstrahlen bestimmt.

Die Resultate zeigen, dass diese Methode als eine Vergleichsmessung der Aerosole zu bislang verwendeten Instrumenten vielversprechend ist. Für die Zukunft sind dabei weitere Studien notwendig, um die systematischen Effekte in Gänze zu verstehen, die diesen Likelihoodscan beeinflussen. Weitere interessante Anwendungsmöglichkeiten liegen in der Untersuchung von horizontaler Uniformität der Atmosphäre und ein Vergleich zu einer möglichen Aeolus-Messung durch das Luftschauerobservatorium Telescope Array in den USA.

# 2. Introduction

The Earth is constantly bombarded by particles from space. Since the discovery of these so-called cosmic rays by Viktor Hess in 1912, the question about their origin and acceleration mechanism has still not been fully answered. To solve this mystery, the properties of cosmic radiation were and still are investigated by a large variety of different experiments. Pierre Auger discovered in 1939 that cosmic rays generate huge showers of secondary particles, which extend through the atmosphere and down to Earth. This insight made it possible to use the atmosphere as an enormous calorimeter to detect the extremely small flux of these cosmic particles with the highest energies.

The Pierre Auger Observatory is the world's largest experiment that uses air showers to detect cosmic rays. It extends over three thousand square kilometers to reliably measure cosmic rays of the highest energies. For this purpose, a hybrid detection method is used. The area of the observatory is covered by a ground array of surface detectors that measure the shower particles reaching the ground. Additionally, telescopes measure the fluorescence light that is created during the shower development as charged particles excite the air molecules. The measurements of these fluorescence telescopes are crucial to set the energy scale of the surface detector and to determine the mass composition of cosmic rays. However, for a good reconstruction of air shower properties with fluorescence telescopes, a good knowledge of the atmosphere is vital. The fluorescence light of showers travels long distances until it reaches the telescopes. The atmospheric conditions, thereby, have a large impact on the light transmission. Light gets attenuated by scattering with air molecules and aerosol scattering. The contribution of aerosols to the light attenuation is especially important close to the ground, where the aerosol concentration can vary rapidly within time scales of less than one hour.

For this reason, the atmosphere is constantly monitored, utilizing a wide range of devices. Among others, the Central Laser Facility is used to measure aerosols. To this end, a laser beam is shot upwards from the center of the observatory. The beam photons scatter on air molecules and aerosols; the scattered light can be seen by the telescopes. From the amount of light at the telescopes, the aerosol attenuation can be determined. Due to the importance of aerosol knowledge for the interpretation of the fluorescence detector measurements, an independent instrument for cross-checks with the monitoring devices would be highly desirable. As will be shown in this thesis, the serendipitous discovery of laser tracks of the Aeolus satellite might provide a unique opportunity for such an independent cross-check.

Aeolus is a satellite with the purpose of measuring wind profiles on earth. These profiles are an important input for numerical weather predictions and help to understand the transport of dust, aerosols, pollution, and water through the air. For this purpose, Aeolus uses a lidar system. A laser beam is emitted towards Earth, the Doppler shift of the backscattered light contains information about the wind speed. By a fortunate coincidence, this laser beam repeatedly passes close to the Pierre Auger Observatory. Therefore it becomes visible in the fluorescence detector by similar means as the Central Laser Facility.

In the context of aerosol determination, it is of specific interest that, during one transition past the observatory, the laser beam is measured over a large range of distances to the telescopes. This provides access to a determination of the aerosol attenuation.

The presence of Aeolus laser shots in the data of the Pierre Auger Observatory was first noticed at the end of 2019. The topic of this thesis is the first thorough analysis of this new data to test its quality and applicability for systematic studies of the aerosols above the observatory. After analyzing the satellite orbit and laser visibility for cosmic ray observatories, the measured laser shots have been reconstructed and studied to derive key parameters such as the arrival direction and the energy per laser shot. Taking advantage of the observations of these laser shots from different distances as the satellite passes over the Pierre Auger Observatory, a systematic simulation study has been carried out to demonstrate the scientific potential of the Aeolus data. The simulation results have been complemented by the analysis of representative Aeolus data sets. Based on these studies, an alternative method for measuring the vertical aerosol optical depth is proposed.

The structure of the thesis is as follows: First, an introduction to cosmic rays is given, including an explanation of the development of air showers and considerations about the atmospheric light attenuation. This is followed by a description of the Pierre Auger Observatory with a brief overview of the devices used to monitor the atmosphere over the observatory. The next chapter will then introduce the Aeolus satellite and its laser instrument ALADIN.

After these more theoretical chapters, a description of the new data from the Aeolus laser beams is presented. The question is answered, where and when the Aeolus laser crosses the Pierre Auger Observatory and whether it can also be observed by Telescope Array, the biggest air shower array in the northern hemisphere. From this, predictions are made when the laser is visible by the fluorescence detectors. The following chapter is devoted to the algorithms used to reconstruct the laser properties. First, an explanation is given how the geometry of the laser beam is reconstructed, then the methods of calculating the laser energy are discussed, and eventually, they are used to determine the Aeolus laser geometry and energy. In the subsequent chapter, a method to extract aerosol information is introduced. This method is first tested with simulated laser shots and afterwards applied to the measured Aeolus laser events. In the final chapter, we conclude by discussing the applicability of this new type of data in the form of laser shots from space to systematically study aerosols, and give an outlook on future applications of this data.

# 3. Cosmic Rays and Air Showers

## 3.1. Ultra High Energy Cosmic Rays

The existence of cosmic rays could for the first time be demonstrated by Viktor Hess in 1912 [1]. He investigated how the abundance of ionizing radiation changes in relation to the altitude. Therefore he undertook multiple balloon flights up to an altitude of 5 km. During these flights he used electroscopes, developed by Theodor Wulf [2], to measure the amount of radiation at different altitudes. These electroscopes consisted of a closed volume of air, in which two parallel strings are positioned. By electrically charging the electroscope, the two strings repel each other. When ionizing radiation creates pairs of ions in the volume, the conductivity of the air is amplified, which increases the rate at which the electroscope discharges. Thus, by the observation of the separation between the two strings one can determine the rate of created ions in the volume and thus make a statement about the flux of ionizing radiation.

The combined result of all of his balloon flights is shown in figure 3.1. The ionization rate first drops with an increasing altitude, but then notably increases above an altitude of 1 km. Hess explained this behavior with a type of radiation coming from above. At lower altitudes the ionization is determined by the radioactivity in the Earth's crust. With increasing altitude this radiation is more and more absorbed by the air, causing the ionization rate to initially drop. At the same time, the radiation coming from above is less and less absorbed with increasing altitude. At some point, therefore, the ionization starts to rise again. Hess also did some of his measurements during nighttime and during a partial eclipse, to test for a correlation with the Sun. Since he found no reduction of ionization when the path to the Sun is obstructed by the Moon or the Earth, he concluded that the Sun is not the origin of this kind of radiation [1].

The results of Hess could in the following be confirmed by Werner Kolhörster, who also showed with a balloon flight up to an altitude of over 9 km, that the ionization continues to increase with the altitude [3]. Later Robert Millikan could prove, that the observed radiation is indeed of cosmic origin, by taking underwater measurements in lakes at different altitudes. By comparing the absorption in water and in air, he could rule out a terrestrial origin. The term "Cosmic Rays" also leads back to Millikan, who at the time assumed that the radiation consists of gamma rays. Arthur Compton could prove him wrong in this regard, by finding a dependence of the intensity of cosmic rays on the geographic latitude [4], which is caused by the geomagnetic field. This proves that cosmic rays contain charged particles, yet the name "rays" remained.

In 1939 Pierre Auger was the first to detect extensive air showers [5]. During coincidence studies with multiple Geiger counters, he noticed that he could still observe timely coincidences, when separating the detectors. This was an indication that he was detecting secondary particles, originating from a common primary particle, that are spatially divided. By placing Geiger counters up to a distance of 300 m apart while still measuring coinciding
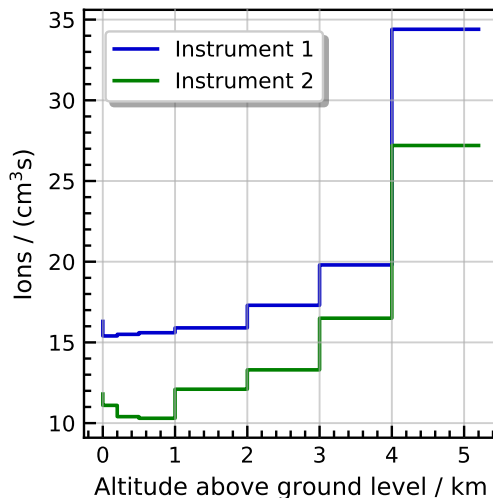
**Figure 3.1.:** Result of the balloon flights of Viktor Hess. Shown are the created ions in the electroscope per volume and time, as a function of the altitude. Each altitude bin contains the averaged data of the combined balloon flights, for two separate instruments that were used. The instruments differed in their detection volume and capacitance. After an initial drop, the ion flux increases for higher altitudes. The data is taken from [1].

events, he could prove that showers of these secondary particles can cover such a large area. He also estimated the primary particles to have energies beyond $10^{15}$ eV. This marked the beginning of air shower experimentation by arrays of ground detectors. In 1962 the Volcano Ranch experiment measured the first cosmic particle with an estimated energy of $10^{20}$ eV [6].

### 3.1.1. Origin and Acceleration

Cosmic rays are measured in a wide range of different energies, the lower energies being more frequent than higher ones. The bulk of all cosmic rays originates within our Galaxy. A particle source at the low energy end (up to 100 MeV) is the Sun, emitting primarily[1] protons and alpha particles. Other particle sources within our Galaxy (like supernova shock fronts as discussed below) can reach energies as large as $100\,\text{TeV} \cdot z$, accelerating also heavier nuclei up to iron [7]. Particles with energies of more than $10^{18}$ eV (ultra-high-energy cosmic rays or UHECRs) are assumed to reach us from outside of the Galaxy. These extragalactic cosmic rays can reach energies of over $10^{20}$ eV. The type of sources which are able to accelerate the particles to these energies is however still under debate.

The composition of the (charged) cosmic rays reaching Earth mostly follows composition of the elements found in the solar system, as can be seen in figure 3.2. Most of the particles are protons (86%), followed by Helium nuclei (11%). Heavier nuclei make up only 1%, electrons 2% [8]. Differences to the solar system composition are especially present in the amount of Lithium, Beryllium and Boron, which are rapidly destroyed in nuclear reactions in stars. The abundance of these elements in the cosmic-ray composition hints at their production through spallation of heavier nuclei during transition through interstellar matter.

Neutral cosmic ray particles consist of $\gamma$-rays and neutrinos. Since the trajectory of neutral particles is not affected by magnetic fields, they are especially of interest for the search for point sources of cosmic radiation. Neutrinos could for example point to the Sun or to a supernova, $\gamma$-rays to an AGN.

---

[1]in terms of charged particles
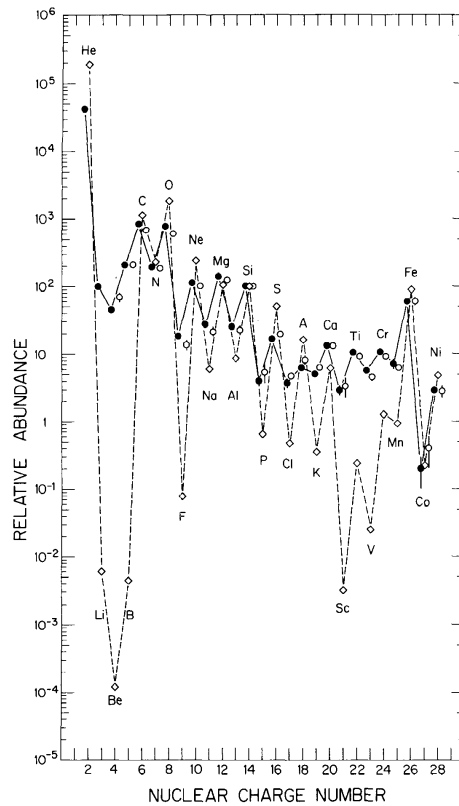
**Figure 3.2.:** The abundance of elements in cosmic rays as measured on Earth (circles, connected by a solid line) in comparison to the solar system (diamonds, connected by a dashed line). The abundances are given relative to silicon. From [9]

In 1949 Enrico Fermi proposed a mechanism that describes the acceleration of cosmic particles [10]. According to this model the particles are reflected at moving interstellar magnetic fields, formed by clouds of magnetized plasma. The particle can either win or lose energy in such a reflection, depending on if the magnetic field is hit head-on or from the back. The particle is on average accelerated, since a head-on collision is slightly more likely.

The acceleration is a stochastic process, happening over many collisions. The energy gain of one reflection scales with the energy ($\Delta E = \alpha E$), therefore after $n$ reflections the particle energy is

$$E = E_0(1 + \alpha)^n \ . \tag{3.1}$$

At the same time the probability of leaving the region of acceleration is $p$ for each reflection and thus the number of particles after $n$ reflections is

$$N = N_0(1 - p)^n \ . \tag{3.2}$$

With this, one obtains an energy spectrum of the type

$$\frac{\mathrm{d}N}{\mathrm{d}E} \propto \left(\frac{E_0}{E}\right)^\gamma \ , \tag{3.3}$$

thus following a power law, which is in accordance to the measured spectrum, as will be shown in section 3.1.2.

Problematic with Fermi's original assumption of clouds of magnetized plasma as magnetic mirrors is the acceleration efficiency. In this so called Fermi acceleration of second order, one has

$$\alpha \propto \beta^2 \ , \tag{3.4}$$

with the cloud velocity $\beta = \frac{v}{c}$. In this case the energy accumulation is too slow compared to the lifetime of the particle before it is lost to the acceleration process [8]. A more efficient acceleration can be achieved, if one assumes shock fronts as magnetic mirrors. In this case a particle collides with a shock front, as for example present in a supernova remnant. Here the stellar material gets pushed outwards by the supernova explosion with velocities larger than the acoustic velocity of the interstellar medium, creating a shock front at the edge. The incoming particle gets reflected at electromagnetic fields inside the shock front. It is ejected towards interstellar matter, where it can be reflected again by clouds of magnetized plasma, similar to the second order acceleration. By multiple reflections between interstellar matter and shock front, the particle energy grows more rapidly with

$$\alpha \propto \beta \; , \tag{3.5}$$

where $\beta$ is the shock front velocity. This Fermi acceleration of first order predicts a spectral index $\gamma$ (as in equation (3.3)) of about 2. This is lower than what is measured, as shown in section 3.1.2, but it could be explained by an energy dependence of $p$ and propagation effects between the acceleration and the measurement on Earth. However, this mechanism only feasibly explains energies up to $10^{14}\,\mathrm{eV} \cdot z$. The mechanism responsible for the highest measured energies of cosmic rays has yet to be understood [8].

To estimate which astrophysical objects could come into question for the acceleration of UHECRs, their size has to be considered. For an object to come into play as a possible accelerator, its size $L$ has to be at least (twice) the cyclotron radius

$$r = \frac{\gamma m v}{q B} \tag{3.6}$$

of the particle in a magnetic field. This leads to a maximal obtainable energy of

$$E_{\mathrm{max}} \propto \beta \cdot Z \cdot B \cdot L \tag{3.7}$$

with a shock front velocity $\beta$. Therefore an object either has to be very large or has to have a large magnetic field to be able to accelerate a particle to very high energies. Large shock front velocities $\beta$ and charge numbers $Z$ are favored. This also shows, that particles of the highest energies ($> 10^{18}\,\mathrm{eV}$) have to have an origin outside of our Galaxy, since its magnetic field would not be able to contain them.

The relation of $L$ and $B$ is pictured in figure 3.3. The diagonal lines correspond to a proton of $10^{20}\,\mathrm{eV}$. For an object to be able to contain such a proton, it has to be above this line, thus either have a large enough magnetic field or size. As can be seen, for a shock front velocity of $\beta \leq 1/300$ none of known objects drawn in the plot meet the requirement. Even for an extreme value of $\beta = 1$ only few objects come into question. Candidates are AGNs, gamma ray bursts and radio galaxy jets.

### 3.1.2. Energy Spectrum

The energy of cosmic rays covers many orders of magnitude, reaching values of over $10^{20}\,\mathrm{eV}$. As mentioned before, the measured energy spectrum follows a power law

$$\frac{\mathrm{d}N}{\mathrm{d}E} \propto E^{-\gamma} \tag{3.8}$$

with a spectral index $\gamma$. In the measured energy spectrum this index is not constant over the whole range, but several features have been observed at which the spectral index changes. A possible reason for the individual regimes is the transition between different methods of acceleration or transport through the universe. A plot of the energy spectrum
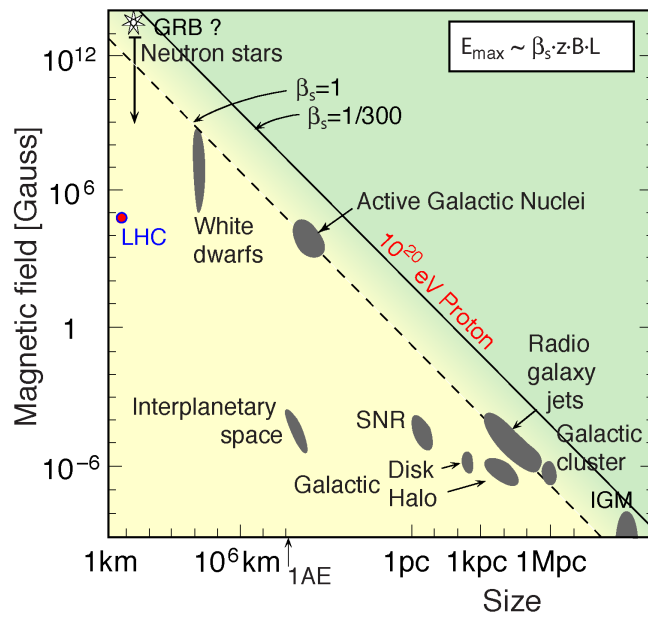
**Figure 3.3.:** Hillas plot, after [11]. Astrophysical objects are plotted by their size and magnetic field strength. The diagonal lines correspond to the requirement for accelerating a proton to $10^{20}$ eV, for a shock front velocity of $\beta = 1$ or $\beta = 1/300$ respectively. Accelerators have to be above these lines. From [12]
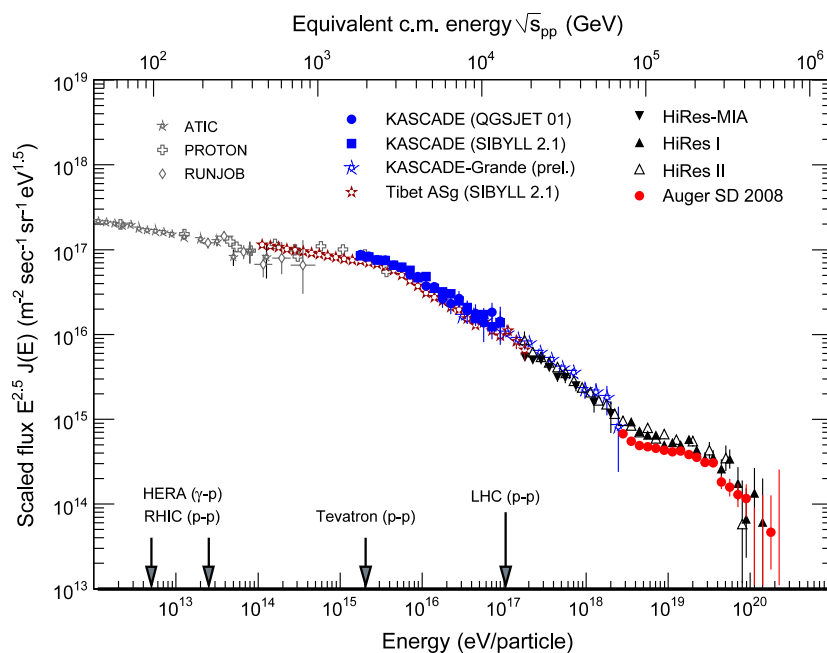


**Figure 3.4.:** Measured energy spectrum of cosmic rays. Shown is the combined data of multiple experiments. The spectrum was multiplied with a factor of $E^{2.5}$ to emphasize some features. Visible is the knee at $\approx 4 \cdot 10^{15}$ eV, the ankle at $3 \cdot 10^{18}$ eV and a cut off below $10^{20}$ eV. From [13]

above $10^{11}$ eV can be seen in figure 3.4. To highlight the features more clearly the flux was multiplied with a factor of $E^{2.5}$. The data includes measurements from different kinds of experiments [13].

The first feature is the so called "knee" at an energy of around $4 \cdot 10^{15}$ eV. Here the spectrum steepens, the spectral index changes from $\gamma \approx 2.7$ to $\gamma \approx 3.1$. One possible explanation for the knee is the energy limit of Galactic accelerators. As discussed above, the capability of acceleration in a shock front is limited by the size of the accelerator. If the maximum obtainable energy is reached, the spectrum steepens, because of the lack of these accelerators for higher energies.

At an energy of around $3 \cdot 10^{18}$ eV (the "ankle") the spectrum flattens again, the spectral index changes to a value of $\gamma \approx 2.6$. One explanation is the transition between accelerator sources. If the energy reached by sources within our Galaxy is limited to this value, then the spectrum above will consist mainly of extragalactic sources. The flux of these sources is lower, but might follow a harder energy spectrum, which would explain the ankle. A different possible explanation is given by the energy loss of extragalactic protons. According to the dip-model, high energy protons originating in extragalactic accelerators interact with the cosmic microwave background via pair production

$$p + \gamma_{\mathrm{CMB}} \rightarrow p + e^- + e^+ \ , \tag{3.9}$$

losing energy in the process. The shift to lower energies causes the spectral region beyond the ankle to flatten [14].

Finally, at the higher end of the energy spectrum a suppression is noticeable, where the flux abruptly drops. This (GZK) cut off was predicted by Kenneth Greisen, Georgiy Zatsepin and Vadim Kuzmin at an energy of approximately $6 \cdot 10^{19}$ eV. The principle behind it is again a reaction of the ultra high energy cosmic rays with the cosmic microwave background. A proton can for example lose energy in the inelastic scattering with a CMB photon

$$\begin{aligned} p + \gamma_{\mathrm{CMB}} &\rightarrow \Delta^+ \rightarrow p + \pi^0 \\ p + \gamma_{\mathrm{CMB}} &\rightarrow \Delta^+ \rightarrow n + \pi^+ \ . \end{aligned} \tag{3.10}$$

In the process a $\Delta^+$-resonance is created as a spin excitation of the proton. The $\Delta^+$-resonance then decays back into a proton or neutron and a pion. The larger the traveled distance, the higher the average energy loss through such reactions is, with an interaction length of $\sim 6$ Mpc. Therefore, protons traveling further than $\sim 100$ Mpc are likely to have lost some of their energy in scattering processes, which explains the suppression of high energies in the spectrum [15]. This is illustrated in figure 3.5, which shows how the energy changes on average during transition, for protons of different starting energies. For distances further than $100$ Mpc it is unlikely to measure energies above the GZK threshold.

Recent measurements of the Pierre Auger Observatory regarding the composition and spectrum of UHECRs however challenge the GZK- and dip-models. Alternative explanations for the ankle include for example interactions in the sources of UHECRs ([17]). The debate about the origin of these features in the flux of cosmic rays is still ongoing [18].

## 3.2. Air Showers

Air showers are created when a high energy cosmic particle hits the atmosphere. The particle penetrates the atmosphere up until it collides with an air nucleus. This first collision happens some $10$ km above the ground, the average penetration depth is dependent on the primary particle's mass. The heavier it is, the further above in the atmosphere the collision happens, a proton travels further through the air than an iron nucleus.
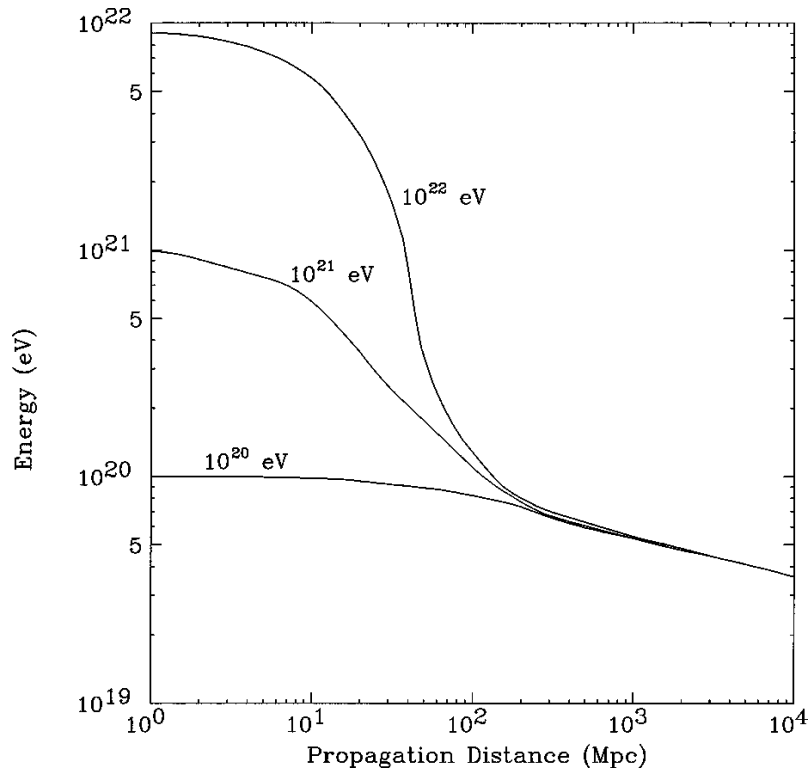
**Figure 3.5.:** Attenuation of the proton energy for different starting energies. Plotted is the energy trend as a function of the propagated distance, with the average energy loss due to the GZK-mechanism. Distances over 100 Mpc make it unlikely to detect protons with energies above the GZK threshold. From [16]
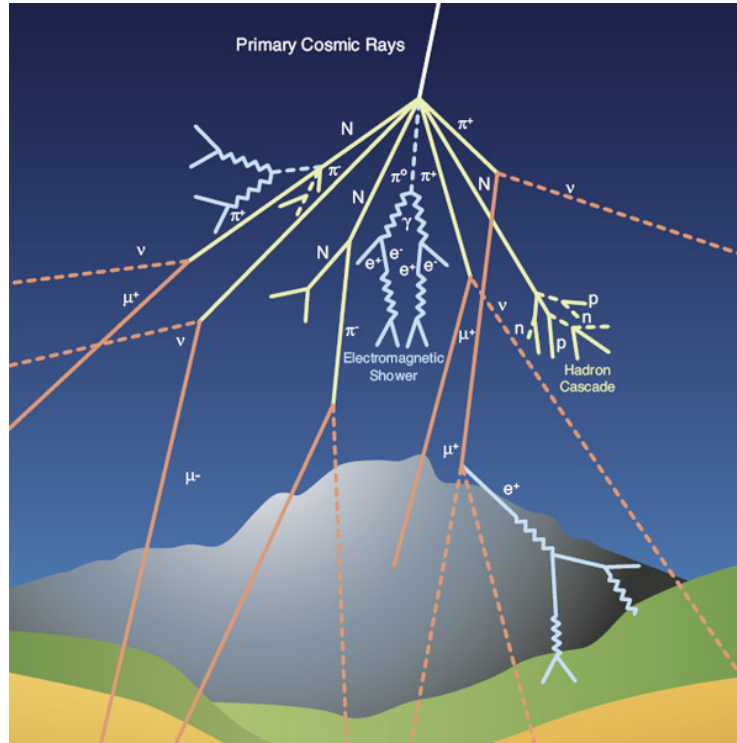
In the collision of the primary particle with an air nucleus several new particles are created. Each of the secondary particles can itself react with the atmosphere to create new particles, resulting in a cascade of rapidly growing numbers. One can differentiate between electromagnetic showers, if the primary particle is an electron or $\gamma$-ray, or hadronic showers in case of a primary nucleon or core. Hadronic showers however also include an electromagnetic and muonic component, as discussed below. An illustration of the air shower development can be seen in figure 3.6.

The number of secondary particles reaches values of $10^6$ (for a $10^{15}$ eV primary particle) to $10^{11}$ (for a $10^{20}$ eV primary particle) [20]. The energy of the particles decreases with each generation, until it reaches a threshold where no new particles are created. At this point the shower starts to attenuate, after reaching its maximum number of particles. The position of the shower maximum is dependent on the energy of the primary particle. For higher energies the shower reaches its maximum deeper in the atmosphere. If the primary energy is lower than around $10^{13}$ eV, the shower dies out before the majority of the electromagnetic particles can reach the ground.

The shower position within the atmosphere $X$ and the location of the shower maximum $X_{\mathrm{max}}$ is usually specified as atmospheric depth or slant depth. It is a measure for the amount of material penetrated by the shower and defined by the integral of the air density. For a vertical shower it is [21]

$$X = \int_h^\infty \rho\left(h'\right) \mathrm{d}h' \ . \tag{3.11}$$

The slant depth is thus a traveled distance, weighted with the density. The unit is therefore g/cm$^2$. The depth increases as the shower gets closer to the ground. At sea level, the vertical atmospheric depth is approximately 1000 g/cm$^2$.

**Figure 3.6.:** Illustration of an air shower. The primary cosmic ray produces secondary hadrons in an initial collision with an air molecule. These hadrons produce more particles in further collisions. Electromagnetic showers are initiated by the decay of pions or muons in $\gamma$ or electrons and positrons. The muonic component of muons and muon neutrinos origins in the decay of charged pions. From [19].

### 3.2.1. Electromagnetic Showers

Electromagnetic showers consist of electrons, positrons and photons. They accompany hadronic showers or can occur individually. An electromagnetic shower is created by a high energy electron or photon as primary particle. In case of a photon as primary particle, the shower is started by pair production of the photon, in presence of a recoil nucleus. In the process an electron and a positron are created, which each carry approximately half of the original photon energy. The electron and positron at some point get deflected in the electric field of a nucleus. In the process bremsstrahlung is emitted, thus creating a new $\gamma$ for each of the particles. The creation of one electron and positron from a gamma and the emission of $\gamma$ from each electron and positron generate a cascade of a growing number of particles.

A threshold for the production of new particles in the electromagnetic cascade is given by the energy of electrons and positrons. The average energy loss through bremsstrahlung

$$\left\langle \frac{\mathrm{d}E}{\mathrm{d}X} \right\rangle = -\frac{E}{X_0} \tag{3.12}$$

decreases with the energy. If a critical value $E_c \approx 600\,\mathrm{MeV}/Z$ ($\sim 80\,\mathrm{MeV}$ in air) is reached, the mean energy loss by ionization overtakes the one of bremsstrahlung [8]. At this point the number of shower particles starts to decrease. $X_0$ is the electromagnetic radiation length, after which the energy of a particle is on average fallen to $1/e$ of its original value, due to bremsstrahlung. The atmosphere corresponds to $\approx 25$ radiation lenghts, depending on atmospheric parameters (as pressure and temperature) and the shower inclination. For the pair production the comparable conversion length $\lambda_{\mathrm{pair}}$ can be stated, which is the
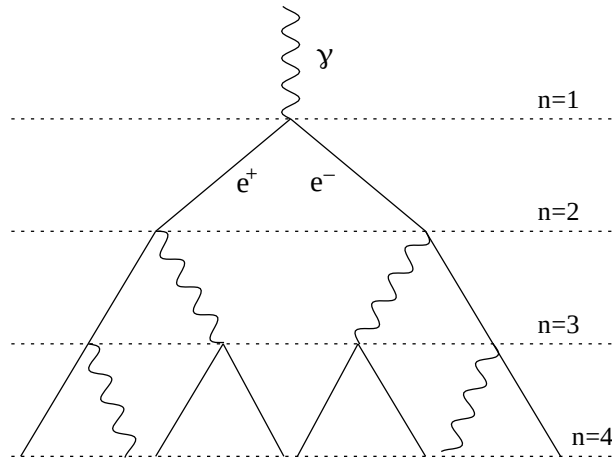
**Figure 3.7.:** Illustration of the Heitler model. With each generation the number of particles is doubled, each particle carries the energy of $E_0/2^n$. From [23].

average traveled distance of a photon before pair production. Its magnitude is with

$$\lambda_{\text{pair}} \approx \frac{9}{7} X_0 \tag{3.13}$$

comparable to the radiation length. This allows for a simplified model to describe the electromagnetic shower development, as proposed by Walter Heitler [22]. Starting for example with one photon, after approximately one radiation length a pair of electron and positron is created, each carrying half the original energy $E = E_0/2$. Both of the secondary particles emit a new photon after another radiation length, losing half of their energy in the process. This is repeated for every particle with each iteration. Therefore, after $n$ generations there exist $2^n$ particles with an energy of

$$E(n) = \frac{E_0}{2^n} \tag{3.14}$$

each. The such created cascade is visualized in figure 3.7. This continues until the secondary particles reach the energy $E_c$. This leads to

$$E(n_{\text{max}}) = E_c \quad \Leftrightarrow \quad n_{\text{max}} = \frac{\ln\left(\frac{E_0}{E_c}\right)}{\ln 2} \tag{3.15}$$

and to the number of particles at the shower maximum

$$N_{\text{max}} = \frac{E_0}{E_c} \; . \tag{3.16}$$

The slant depth of the shower maximum is then given by

$$X_{\text{max}} = n_{\text{max}} \cdot X_0 \propto \ln\left(E_0\right) \; , \tag{3.17}$$

and therefore increases logarithmic with the primary energy.

### 3.2.2. Hadronic Showers

A hadronic shower is composed mainly of protons, neutrons, pions and kaons. These particles are produced in nuclear interactions of first the primary particle and subsequently

the secondary particles with the atmosphere. During every reaction many secondary particles are produced, most of them pions.

The hadronic interaction length $\lambda_{\mathrm{had}}$ is the mean free path of an inelastic scattering. The atmosphere corresponds to roughly 11 interaction lengths $\lambda_{\mathrm{had}}$. The hadronic interaction length is therefore larger as the electromagnetic equivalent.

A hadronic shower is accompanied by an muonic and an electromagnetic component. Origin are the decay products of pions. The decay of charged pions

$$
\begin{aligned}
\pi^+ &\to \mu^+ + \overline{\nu}_\mu \\
\pi^- &\to \mu^- + \nu_\mu
\end{aligned}
\tag{3.18}
$$

creates muons and the corresponding neutrinos. The decay of neutral pions

$$
\pi^0 \to \gamma + \gamma
\tag{3.19}
$$

creates photons, which can start an electromagnetic shower.

### 3.2.3. Muonic Component

Similar to the electromagnetic component, a hadronic shower is accompanied by a muonic component, originating in the decay of hadrons. The muonic shower component consists of $\mu^+$, $\mu^-$ and the neutrinos of corresponding flavor. They are produced in the decay of pions, as shown in (3.18), or the decay of kaons[2]

$$
\begin{aligned}
K^+ &\to \mu^+ + \nu_\mu \\
K^- &\to \mu^- + \overline{\nu}_\mu \ .
\end{aligned}
\tag{3.20}
$$

The muons are long-lived minimum ionizing particles and thus easily penetrate through the atmosphere. Muons created in large altitudes are therefore still measurable on the surface of Earth. Electrons however are stopped more easily and are primarily measured coming from lower altitudes. Therefore the ratio $N_e/N_\mu$ between the measured number of electrons and muons on the ground can be used as a measure for the height of the first interaction, and thus for the mass of the primary particle. A larger value of $N_e/N_\mu$ corresponds to a larger penetration depth, indicating a lighter primary particle. Additionally, the total number of electrons and muons is also a measure for the energy of the primary particle.

### 3.3. The Atmosphere as a Detection Medium

As shown above, the particle flux of cosmic rays decreases drastically with higher energies. The direct measurement of UHECRs with single small detectors therefore becomes very inefficient. The CREAM experiment for example used a series of long duration balloon flights, with a detector as payload. It was able to measure the cosmic ray spectrum up to energies of $10^{15}$ eV [24]. For higher energies the particle flux within the detector becomes too small. Above an energy of $10^{19}$ eV, the flux is reduced to $0.5$ events/(km² · yr · sr), making it almost impossible to measure events with a small scale detector.

To increase the rate of high energy particles therefore the detection volume needs to be increased. This is achieved by using the atmosphere as a calorimeter. The UHECR creates extended air showers, while depositing its energy in the atmosphere. These showers can be detected by using large arrays of detectors on the surface of Earth.

---

[2]or indirectly by the decay of kaons into pions and then further into muons.

A measurement of the secondary particles reaching the surface can be achieved by using scintillators or water-Cherenkov detectors, spaced over a large area. The combined measurement of many such detectors in a array yields the lateral distribution of particle densities. As stated above, the number of electrons and muons can be used to deduce the mass and energy of the primary particle.

Additionally to the secondary particles, a shower also produces fluorescence light by excitation of the air molecules. This creates $\sim 5$ photons per traveled meter, with a wavelength between $300\,\mathrm{nm}$ and $450\,\mathrm{nm}$ [8]. On top of that, the charged particles at velocities close to the speed of light emit Cherenkov radiation. The emission cone is narrow around the shower axis (with an opening angle of $\sim 1°$ around a particles trajectory), diffuses however to a certain degree by the multiple scattering of electrons and positrons in the shower. This makes it possible to detect an air shower also by measurement of its emitted light, with telescopes recording the shower light by looking at it from the side. Therefore a longitudinal shower profile can be observed, that includes among others also information about the position of the shower maximum, which is linked to the mass of the primary particle. The integrated light flux along a shower profile can be used to reconstruct the primary particle's energy.

The created fluorescence (and Cherenkov) light has to be transported through the atmosphere up to the telescopes. Thereby it is exposed to scattering processes that influence the light yield at the telescope. Most notably are hereby Rayleigh scattering with air molecules and Mie scattering with aerosols.

The intensity of a light source is attenuated exponentially through the atmosphere, according to the Lambert Beer law

$$T = \mathrm{e}^{-\tau} \ . \tag{3.21}$$

Thereby represents $\tau$ the optical depth and is dependent on the light's wavelength and the traversed path. Under the assumption, that the atmosphere is uniform along the horizontal directions (therefore consisting of layers of same conditions each), the travel path dependence of $\tau$ can be reduced to an altitude dependence

$$T(h, \lambda, \theta) = \exp\left(-\frac{\tau(h, \lambda)}{\cos\theta}\right) \ , \tag{3.22}$$

with the altitude $h$, the wavelength $\lambda$ and a zenith angle $\theta$, indicating the inclination. The vertical optical depth $\tau$ now only depends on the altitude (and the wavelength).

The main contribution to the light attenuation in the atmosphere is given by elastic Rayleigh scattering on air molecules and Mie scattering on aerosols. A small contribution is also the inelastic Raman scattering, where rotations and oscillations are excited in $\mathrm{N_2}$ or $\mathrm{O_2}$ molecules. The scattering cross section therefore is however small in comparison [25]. The optical depth $\tau$ can thus be divided into a molecular and a aerosol part

$$\tau = \tau_\mathrm{m} + \tau_\mathrm{a} \ . \tag{3.23}$$

### 3.3.1. Rayleigh Scattering

Rayleigh scattering is an elastic scattering of photons with air molecules. The classical molecular differential scattering cross section, normalized with the total Rayleigh cross section $\sigma$, is [26]

$$\left(\frac{1}{\sigma}\frac{\mathrm{d}\sigma}{\mathrm{d}\Omega}\right)_\mathrm{m} = \frac{3}{16\pi}\left(1 + \cos^2\theta\right) \ . \tag{3.24}$$

This is also called the phase function, it describes the probability per unit of solid angle of a scattering under the angle $\theta$. This phase function can be refined, by considering molecular
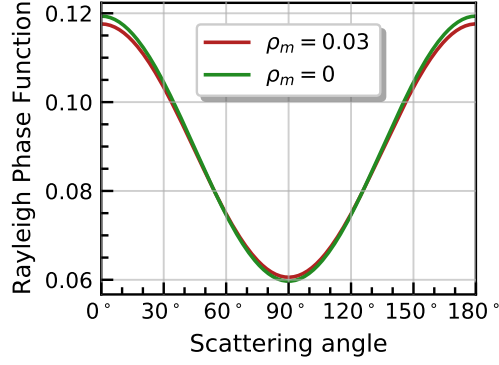
**Figure 3.8.:** The phase function of molecular Rayleigh scattering. Shown is the classical case for a depolarization of $\rho_m = 0$ and a small correction due to molecular anisotropy with $\rho_m = 0.03$.

anisotropy [26]. For isotropic scattering the scattered light at $\theta = \pi/2$ is completely polarized, thus the relative amplitude along the electric field component is 0 and orthogonal to it 1. For anisotropic scattering this is no longer the case, the ratio between the amplitudes parallel and orthogonal to the electric field component is called the depolarization factor $\rho_m$.

The depolarization factor can be expressed as [27]

$$\rho_m = \frac{2\gamma}{1 + \gamma} \; , \tag{3.25}$$

and with it the phase function can be modified to

$$\left(\frac{1}{\sigma}\frac{\mathrm{d}\sigma}{\mathrm{d}\Omega}\right)_{\mathrm{m}} = \frac{3}{16\pi(1 + 2\gamma)} \cdot \left((1 + 3\gamma) + (1 - \gamma)\cos^2\theta\right) \; . \tag{3.26}$$

For $\rho_m = 0 = \gamma$ this transitions into the classical case. Values of $\rho_m > 0$ increase the Rayleigh scattering cross section. For the Pierre Auger Observatory a value of $\rho = 0.03$ is used [28]. The corrections are only small, as can be seen in figure 3.8. There the cases $\rho_m = 0$ and $\rho_m = 0.03$ are compared. Notable is the angle dependence of the phase function following $\cos^2\theta$, thus being symmetrically in forward and backward scattering.

The optical depth for the Rayleigh scattering at an altitude $h$ is obtained as the integral from the ground level $h_{\mathrm{gnd}}$ to $h$ [29]

$$\tau_{\mathrm{m}}(h, \lambda) = \int_{h_{\mathrm{gnd}}}^{h} \beta_{\mathrm{m}}(h', \lambda) \, \mathrm{d}h' \; , \tag{3.27}$$

$\beta_{\mathrm{m}}$ being the probability per path length unit of a scattering event. It is given as

$$\beta_{\mathrm{m}}(h, \lambda) = N(h)\,\sigma(\lambda) \; , \tag{3.28}$$

where $N$ is the particle density and $\sigma$ the scattering cross section. The particle density is dependent on pressure and temperature, which has to be considered for the Rayleigh scattering. The data for the Pierre Auger Observatory therefore is obtained by the Global Data Assimilation System GDAS [30] (see also section 4.3).

### 3.3.2. Mie Scattering

Aerosols are small particles in the atmosphere like dust or water droplets. Their size is with $\sim \mu$m significantly larger than an air molecule. The scattering process of photons on

**(a)** Seasonal VAODs

**(b)** Distribution of VAODs
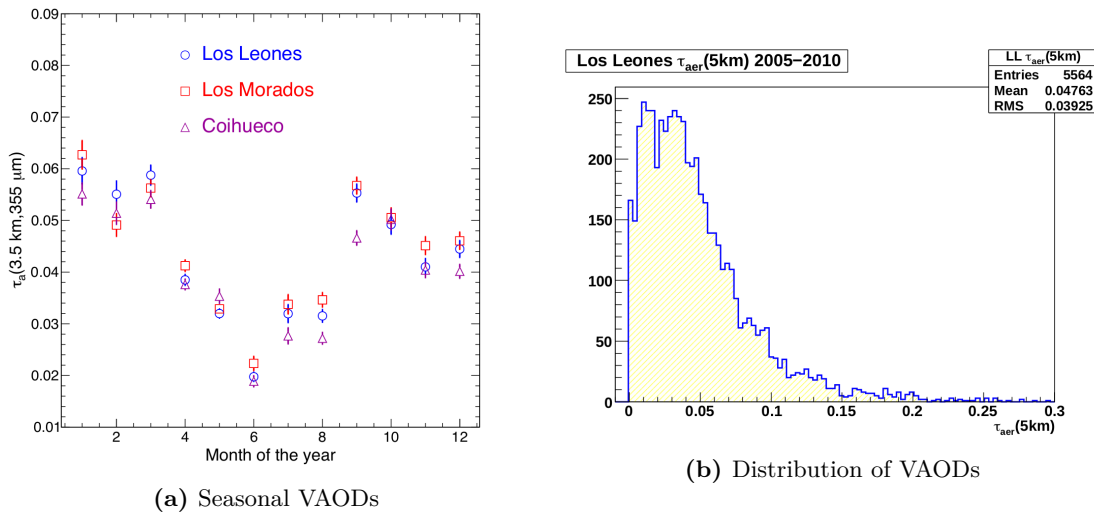
**Figure 3.9.:** Figure (a) shows the vertical aerosol optical depth as measured throughout the year at three sites at the Pierre Auger Observatory. A lower optical depth corresponds to fewer aerosols in the atmosphere. The amount of aerosols is lower during the southern hemisphere winter. From [31]. Figure (b) shows the distribution of VAODs, measured at Los Leones between 2005 and 2010. From [32]

aerosols is therefore different and more complicated, due to the different possible shapes that an aerosol particle can have. This kind of scattering can be described by the Mie scattering theory. Compared to molecular scattering the aerosol concentration is also more fluctuating with the time, within a scale of hours, and highly impacted by weather conditions. Therefore no analytic calculation of the optical depth can be done. Instead, frequent measurements of the amount of aerosols have to be performed (see section 4.3).

Sources of aerosols include dust stirred up from the ground, NaCl crystals formed over the ocean or salt flats, pollution coming from urban areas, biomass burnings and wildfires [31]. Most of the aerosols are found within the planetary boundary layer, up to an altitude of around 1 km. Above that the aerosol concentration decreases rapidly with the altitude. Regarding the amount of aerosols over the Pierre Auger Observatory, a relation to the season can also be observed, as can be seen in figure 3.9a. During the winter in the southern hemisphere winter the aerosol concentration is lower. Reasons therefore are snow layers covering the soil, rain washing out some of the aerosol particles and clearer air masses coming from the pacific ocean [31].

The measurement of the vertical aerosol optical depth (VAOD) $\tau_a$ is done for a reference wavelength of $\lambda_0 = 355$ nm. The wavelength dependency of $\tau_a$ can be parametrized as

$$\tau_a (h, \lambda) = \tau_a (h, \lambda_0) \left(\frac{\lambda_0}{\lambda}\right)^\gamma , \tag{3.29}$$

where $\gamma$ is the Ångström coefficient, which is a measure of the size of the aerosol particles.

The phase function of Mie scattering can be approximated by the Henyey-Greenstein-function

$$\left(\frac{1}{\sigma}\frac{d\sigma}{d\Omega}\right)_a = \frac{1-g^2}{4\pi} \left(\frac{1}{\left(1+g^2-2g\cos\theta\right)^{\frac{3}{2}}} + f\frac{3\cos^2\theta - 1}{2\left(1+g^2\right)^{\frac{3}{2}}}\right) . \tag{3.30}$$

$f$ is thereby the relative amplitude of the backward peak, compared to the forward peak. A value $f = 0$ would mean the absence of a backwards peak. $g$ represents the deviation from an isotropic scattering in forward-backward-direction, with $g = 1$ being a pure forward scattering, $g = -1$ being a pure backward scattering and $g = 0$ meaning isotropy. The

Pierre Auger Observatory measures the parameters $f$ and $g$ with aerosol phase function monitors (see section 4.3).

### 3.3.3. The Parametric Aerosol Model

A simplified model of the light attenuation through aerosols can be achieved by describing the vertical aerosol profile with a small set of parameters. The base assumption of this model is, that the atmosphere is horizontally uniform. The aerosols can then be described separately in two layers. Directly connected to the surface is the mixing layer (also planetary boundary layer). Here the transport of aerosols is determined by turbulence of the air. The ground is heated by the Sun, causing the air masses above it to swirl. This layer is therefore described in the model as a domain of a constant aerosol density. Above this mixing layer the aerosol density is then assumed to decrease exponentially.

The mixing layer can be described by two parameters. One being the height of the mixing layer $H_{\mathrm{mix}}$ and the other one being the attenuation length $L$, which is the mean free path for Mie scattering within the mixing layer. To describe the phase above the mixing layer a third parameter is needed: The scale height $H$ describes how the attenuation decreases with the height, it is the scaling parameter of the exponential decrease in aerosols.

In accordance to (3.22), the aerosol transmission is given as

$$T_{\mathrm{a}} = \exp\left(-\frac{\tau_{\mathrm{a}}}{\cos\theta}\right) \ , \tag{3.31}$$

with the vertical aerosol optical depth $\tau_{\mathrm{a}}$ (VAOD). The VAOD in turn is calculated (analogue to equation (3.27)) as the integral

$$\tau_{\mathrm{a}} = \int_{h_{\mathrm{gnd}}}^{h} \beta_{\mathrm{a}}\left(h'\right) \mathrm{d}h' \ , \tag{3.32}$$

where $\beta_{\mathrm{a}}(h)$ (the extinction coefficient) is the probability of an aerosol scattering incident, per traveled distance.

To calculate the aerosol attenuation, the contributions of the two layers are examined individually. For the mixing layer the aerosol density is constant. In this case the scattering probability per path length is simply given by the inverse of the attenuation length

$$\beta_{\mathrm{a}}\left(h < H_{\mathrm{mix}}\right) = \frac{1}{L} \ . \tag{3.33}$$

The VAOD in this layer is then given by the integration over the height

$$\tau_{\mathrm{a}}\left(h < H_{\mathrm{mix}}\right) = \frac{h}{L} \ . \tag{3.34}$$

Above the mixing layer the aerosol density, and therefore also the scattering probability, decreases exponentially with the scale parameter $H$. Therefore $\beta$ is described by an exponential function as $\beta \propto \exp\left(-h/H\right)$. However, the exponential decrease only starts at the mixing layer height $H_{\mathrm{mix}}$, thus this function has to be shifted by this value. Also the boundary condition, that $\beta$ has to transition into the mixing layer solution for $h = H_{\mathrm{mix}}$, and thus $\beta_{\mathrm{a}}(h = H_{\mathrm{mix}}) = 1/L$, yields the proportionality factor. Combined one obtains

$$\beta_{\mathrm{a}}\left(h \geq H_{\mathrm{mix}}\right) = \frac{1}{L}\exp\left(-\frac{h - H_{\mathrm{mix}}}{H}\right) \tag{3.35}$$
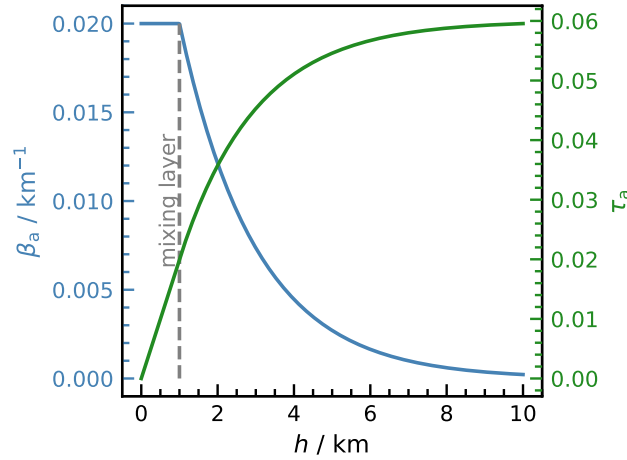
**Figure 3.10.:** The extinction coefficient $\beta_\mathrm{a}$ and the VAOD $\tau_\mathrm{a}$ as a function of the height. The chosen aerosol parameters were $H = 2\,\mathrm{km}$, $H_\mathrm{mix} = 1\,\mathrm{km}$ and $L = 50\,\mathrm{km}$.

To obtain the VAOD, this has to be integrated over $h$. The total VAOD from the ground up to a height $h > H_\mathrm{mix}$ is then given as

$$
\begin{aligned}
\tau_\mathrm{a}(h) &= \int_0^h \beta(h')\mathrm{d}h' \\
&= \int_0^{H_\mathrm{mix}} \beta_\mathrm{a}\left(h' < H_\mathrm{mix}\right)\mathrm{d}h' + \int_{H_\mathrm{mix}}^h \beta_\mathrm{a}\left(h' \geq H_\mathrm{mix}\right)\mathrm{d}h' \\
&= \frac{H_\mathrm{mix}}{L} + \frac{H}{L}\left[1 - \exp\left(-\frac{h - H_\mathrm{mix}}{H}\right)\right]
\end{aligned}
\tag{3.36}
$$

The behavior of $\beta_\mathrm{a}$ and $\tau_\mathrm{a}$ as a function of the height is plotted in figure 3.10. For this example the parameter values $H = 2\,\mathrm{km}$, $H_\mathrm{mix} = 1\,\mathrm{km}$ and $L = 50\,\mathrm{km}$ were chosen.

If one only wants to calculate the attenuation between two heights $h_1$ and $h_2$ above the mixing layer, one gets accordingly

$$
\begin{aligned}
\tau_\mathrm{a}(h_1, h_2) &= \int_{h_1}^{h_2} \beta_\mathrm{a}\left(h'\right)\mathrm{d}h' \\
&= \frac{H}{L}\left[\exp\left(-\frac{h_1 - H_\mathrm{mix}}{H}\right) - \exp\left(-\frac{h_2 - H_\mathrm{mix}}{H}\right)\right]
\end{aligned}
\tag{3.37}
$$

(if $h_1 > H_\mathrm{mix}$ and $h_2 > H_\mathrm{mix}$). With the VAOD determined, the aerosol transmission factor can be calculated as in equation 3.31.

In this manner the aerosol profile and with it the transmission factor can be calculated from the three parameters $H$, $H_\mathrm{mix}$ and $L$. This is used in both simulation and reconstruction of FD events, as will be apparent in chapter 8.

# 4. The Pierre Auger Observatory

The initial concept of the Pierre Auger Observatory was devised by Jim Cronin and Alan Watson during the International Cosmic Ray Conference of 1992, as an experiment to answer the question about the origin of the highest energy cosmic rays [33]. For such an experiment a huge detection volume is necessary, to achieve a reasonable exposure, as described above. Therefore the atmosphere is utilized to serve as a detection medium, detectors on the surface of Earth measure the evidences of a CR induced air shower. To honor Pierre Auger, the discoverer of air showers, the observatory was named after him.

The Pierre Auger Observatory is located in the Argentinian Pampa Amarilla, in the province of Mendoza[1]. This site fulfills some important characteristics that are crucial for an observatory of this kind. There is enough space available for a large scale detector array, a relatively clear atmosphere, little light pollution, a flat surface and an elevation level of $\sim 1400\,\mathrm{m}$, which puts it close to the depth where the number of particles in air showers reaches its maximum [34]. The construction of the Pierre Auger Observatory took from 2002 to 2008, however measurements were already taken from 2004 onward.

One main goal of the Pierre Auger Observatory is to identify and understand the sources of UHECRs. Therefore the energy and arrival direction of cosmic rays are measured, as well as their composition. To achieve this goal, a hybrid detection method is used. On the one hand the observatory employs a large array of surface detectors (SD), that cover an area of $3000\,\mathrm{km}^2$. These detect the secondary shower particles that reach the ground, which allows for a measurement of the lateral distribution of the particle density. With the spacial and temporal resolution of the detector signals, the arrival direction of the primary particle can be reconstructed.

On the other hand, 27 telescopes act as a fluorescence detector (FD). These measure the fluorescence light emitted by the excitation of air molecules by shower particles. The amount of created light is proportional to the energy deposited in the atmosphere by the shower. Integrating the fluorescence light of a complete shower therefore is a form of calorimetric measurement of the primary energy. The longitudinal shape of the shower development additionally gives information about the shower maximum (and therefore the mass of the primary particle), a reconstruction of the shower axis yields the arrival direction.

A map of the observatory with the positions of the surface detector stations marked by red circles and of the four FD locations can be seen in figure 4.1. The goal of the hybrid detection mode is the measurement of the same shower properties with two separate and complementary systems, which allows for cross-checks and calibrations. The FD has a better angle resolution and is able to make a calorimetric measurement of the primary particle's energy. However, the FD can only operate during dark nights, which limits the duty cycle to about 15% [33]. Using hybrid events (events that are both detected by the FD

---

[1]The coordinates are at $35.0°$ to $35.3°$ South and $69.0°$ to $69.4°$ West [33]

**Figure 4.1.:** Map of the Pierre Auger Observatory. The red dots mark the positions of the surface detectors. The field of view of the four FD stations is indicated by the green lines. Also included are the positions of the laser facilities CLF and XLF, that are introduced in section 4.3. From [33]

and the SD), the signal of the surface detectors can be calibrated. This makes it possible, to determine the energy only from the SD signal, when no FD data can be taken, which is advantageous due to the 100 % duty cycle of the SD.

Additionally, the hybrid detection of events provide measurements of a very good quality. The inclusion of the SD information into the shower geometry reconstruction for example significantly improves the obtained result[2].

## 4.1. The Surface Detector

The surface detector array consists of 1660 individual detectors, placed in a triangular pattern with a distance of 1.5 km between them [33]. One detector station consists of a tank of 3.6 m diameter, filled with 12,000 liters of ultrapure water. An image of one such tank can be seen in figure 4.2. The water has to have a high purity, to prevent the growth of bacteria, which would reduce the water's clarity. The inner walls of the tank are lined with a reflective surface. Each tank contains three photomultiplier tubes, looking into the tanks from above.

If relativistic charged shower particles pass through the water, they emit Cherenkov radiation. The created light is diffusely reflected by the inner coating of the tanks, so that it can be detected by the photomultiplier tubes. High energy photons can also be detected, if they convert into an electron-positron-pair within the water tank.

Each surface detector is powered by a solar panel, in combination with two batteries. The communication and data transmission happens wirelessly by antennas.

The threshold of the detectable primary energy is determined by the spacing between the surface detectors. The distance of 1.5 km limits the observable energy range to energies above approximately $3 \cdot 10^{18}$ eV. To extend the sensitivity to lower energies, a smaller detector spacing would be necessary [35]. For this purpose the additional Auger Muons and Infill for the Ground Array (AMIGA) was installed. It consists of an array of detector systems, that combine buried scintillators with Cherenkov water tanks. The distances

---

[2]The methods of the geometry reconstruction are discussed in section 7.1.1, albeit for laser shots instead of showers.

**Figure 4.2.:** Image of a surface detector. Visible is the battery box on the left, antennas on top and the solar panel on the right side of the tank. In the background the Argentinian Andes can be seen. From [33]

between the individual detectors is with $750\,\text{m}$ only half of what is used for the rest of the array. This allows for the detection of cosmic rays with energies down to $3 \cdot 10^{17}\,\text{eV}$. The AMIGA detectors act as an infill incorporated in the larger spaced array. This infill is located near Coihueco (around $6\,\text{km}$ from the FD building) and covers an area of $23.5\,\text{km}^2$ [33]. The area is thus only a small fraction of the entire observatory, but this is compensated by the much larger flux of lower energy cosmic rays.

## 4.2. The Fluorescence Detector (FD)

The fluorescence telescopes measure the fluorescence light that is created as a shower develops in the atmosphere. Charged shower particles excite the nitrogen molecules in the air, which subsequently emit isotropic light in a region of $300\,\text{nm}$ to $430\,\text{nm}$ [36]. The number of created photons is proportional to the energy deposited in the atmosphere by the charged shower particles. Therefore the measured light flux as a function of the atmospheric depth $X$ can be used to establish the longitudinal shower development profile $\frac{\mathrm{d}E}{\mathrm{d}X}(X)$. With this profile on the one hand the position of the shower maximum $X_{\text{max}}$ can be determined. On the other hand an integration over $X$ yields the total energy of the primary particle that was converted in electromagnetic processes[3].

### 4.2.1. Fluorescence Detector Stations

The fluorescence detector consists of four stations ("eyes"), located at the sites of Los Leones, Los Morados, Loma Amarilla and Coihueco, which are shown in the map in figure 4.1. The stations are build on small ridges or hills at the edge of the detector array, so they are elevated by several tens of meters compared to the SD. Coihueco is an exception, sitting at an altitude of $\sim 1700\,\text{m}$ and therefore significantly higher than the $\sim 1400\,\text{m}$ altitude of the pampa [37].

---

[3]This amounts to $\approx 90\%$ of the original particle energy. To reconstruct the energy of the primary particle also the invisible contributions of neutrinos and muons have to be considered [36].

**Figure 4.3.:** Image of the FD building at Los Leones. From [33]

Every FD station contains six telescopes, combining to a total of 24 telescopes (not including HEAT, see further below). The telescopes are placed inside one of four buildings that were constructed at each of the sites, to shelter them from weather and dust. An image of the FD building at Los Leones can be seen in figure 4.3. The telescopes look outwards through windows, that are covered by shutters during daytime or in case of strong wind and rain [33].

**Telescope**

Each telescope has a field of view of $30° \times 30°$, with a minimum elevation angle of $1.5°$. The six telescopes of one FD station therefore cover the full angle of $180°$ in horizontal direction. The telescopes point towards the array, which is also indicated in figure 4.1.

The structure of one telescope can be seen in figure 4.4. The telescope receives light through a circular aperture, marking the entrance of the telescope. Here a wavelength filter acts as a window, which on the one hand protects the telescope from the weather, and on the other hand filters out visible light. Only UV light up to a wavelength of 410 nm passes the filter, which includes most of the fluorescence light created by air showers. This helps to reduce the background caused by visible light, which would otherwise dominate the light flux.

The light that passes the filter is collected by a spherical mirror, with an area of $13 \, \text{m}^2$. These mirrors exist two different configurations. The ones of the telescopes in Los Leones and Los Morados consist of 36 rectangular segments, made from coated aluminium. The mirrors of Loma Amarilla and Coihueco are made up of 60 hexagonal segments, made from borosilicate glass that was coated with aluminium [36]. The mirrors focus the incoming light and direct it towards a camera placed in the focal plane.

**Camera**

In the camera the amount of light is then measured. The camera consists of 440 pixels, arranged in a hexagonal pattern of 22 rows and 20 columns, as shown in figure 4.5a. The angular distance between two pixels corresponds to a resolution of $1.5°$.

The body of the camera is milled out of an aluminium block. It contains holes with 40 mm diameter, corresponding to the positions of the pixels. In these holes photomultiplier tubes
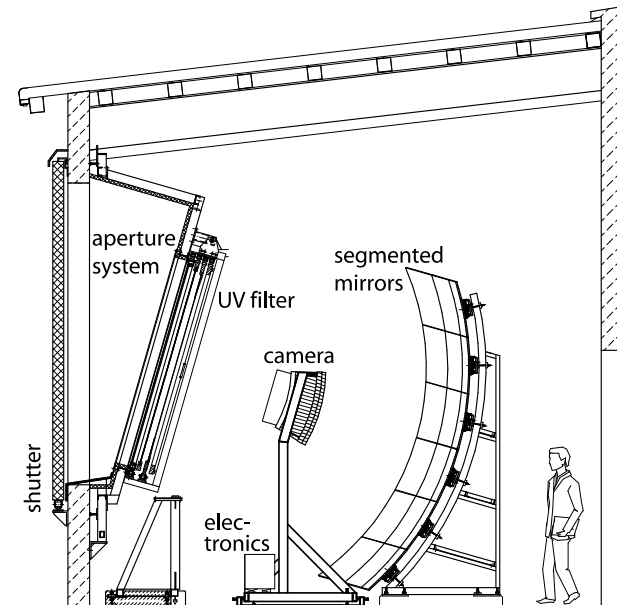
**Figure 4.4.:** Sketch of the structure of one telescope. From [33]
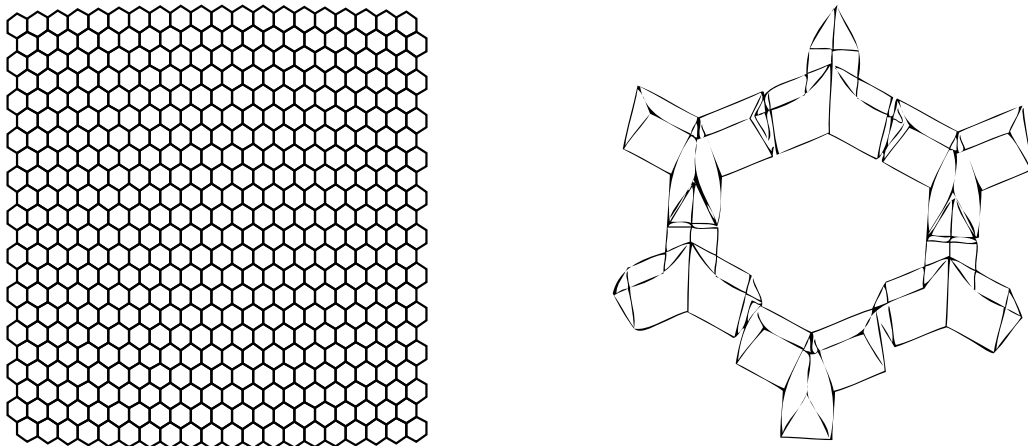


**(a)** pixel arrangement                          **(b)** Mercedes stars

**Figure 4.5.:** Figure (a) shows the arrangement of the 440 camera pixels in 22 rows and 20 columns. Figure (b) shows six Mercedes stars surrounding one pixel. From [36]

are inserted, which have a hexagonal light collection area. The photomultiplier tubes generate an electronic signal, when they collect photons. As an air shower develops in the atmosphere, its fluorescence light is imaged onto the camera, where it creates a line of activated pixels.

To avoid a loss of signal if the light falls onto the area between two pixels, additional light collectors are attached to the photomultiplier tubes. These are shaped as "Mercedes stars", with three arms spread under an angle of 120°. One of these stars is placed at every vertex of the hexagonal pattern, therefore each pixel is surrounded by six stars. An illustration is shown in Figure 4.5b. The Merdedes stars are made from plastic, coated with a reflective foil. The arms have a triangular profile, which guides incoming light towards the photomultiplier tube. Monte Carlo simulations with ray tracing show, that the stars increase the collection efficiency from 70% to 94% [36].

### 4.2.2. High Elevation Auger Telescopes (HEAT)

HEAT is an upgrade to the fluorescence detector, consisting of three additional telescopes near Coihueco. The structure of these telescopes is similar to the remaining 24, with the difference that the three HEAT telescopes can be tilted upwards. As a result their field of view ranges from an elevation of 30° to 58° and is therefore above the visual range of the other telescopes [33].

Purpose of HEAT is to lower the detection threshold of cosmic rays. In combination with the aforementioned array infill AMIGA, showers with energies above $10^{17}$ eV can be measured.

### 4.2.3. Calibration

For the reconstruction of showers from fluorescence light it is important to know precisely which signal amplitude at the photomultiplier tubes corresponds to which number of photons at the aperture. Therefore a calibration has to be performed for every pixel in every telescope. This is done with the help of a large cylindrical light source, called drum. A pulsed UV LED (of 265 nm) illuminates the inside of the drum, the light gets diffused within the drum and is emitted with an even intensity to the outside.

The drum can be attached to the aperture of a telescope, uniformly illuminating all pixels of the camera. The intensity of the drum is known through measurements with NIST-calibrated photo diodes. Therefore one can use the known intensity to determine the calibration constant for each pixel. This calibration is done periodically for each single telescope. The wavelength dependent efficiency can also be determined, with the help of a monochromator in combination with a xenon flash lamp. With it the efficiency can be screened in 5 nm steps [33].

Additionally to this absolute calibration, that matches the collected light flux to the measured signal, a relative calibration is done at least twice per measurement night, once before and once after every measurement shift [36]. The main device to assure the relative calibration is a pulsed LED. Its light gets transported by optical fibers to a diffuser in the center of the telescope mirror. The light is aimed at the camera, therefore one can track the camera response over time. The result is not an absolute calibration as achieved with the drum, but a detection of a relative drift in the performance of the photomultiplier tubes.

### 4.3. Atmospheric Monitoring Devices

The measurement of the fluorescence detector is strongly influenced by the atmospheric conditions. As discussed above, the atmospheric state variables influence the amount of
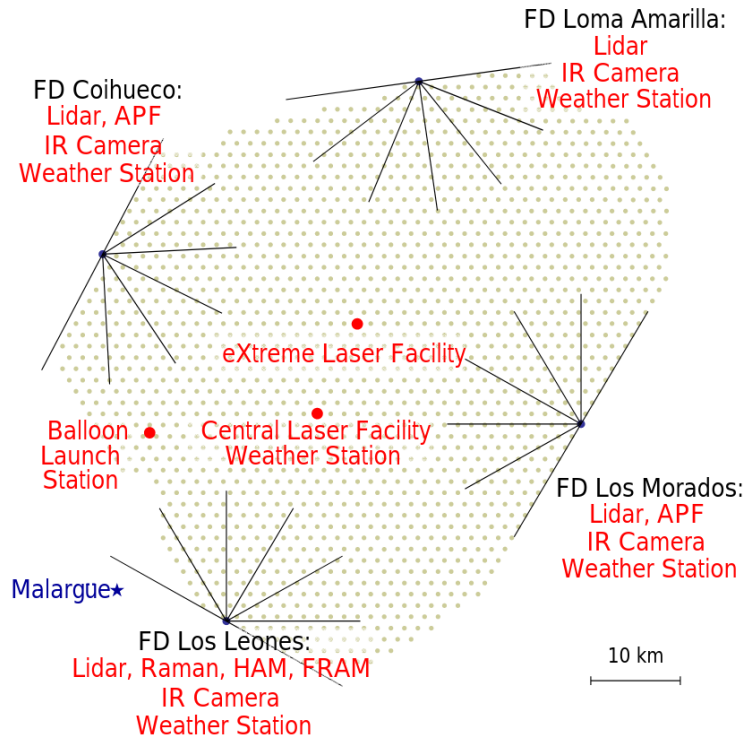
**Figure 4.6.:** The location of some of the atmospheric monitoring devices at the Pierre Auger Observatory. For comparison the FD stations and the positions of the SD tanks are drawn. From [38]

Rayleigh scattering, the highly variable aerosol concentration determines the Mie scattering. Therefore the atmosphere has to be constantly observed, to understand the impact on the light transportation to the telescopes. For that purpose the Pierre Auger Observatory employs a number of monitoring devices.

An overview of some of these devices and their location within the observatory can be seen in figure 4.6. As reference the four stations of fluorescence detectors and the positions of the surface detectors are included in this map.

**The Laser Facilities CLF and XLF**

The Central Laser Facility (CLF) and Extreme Laser Facility (XLF) are two laser systems located roughly in the center of the array. The distance to the individual telescopes is between 26 km and 39 km. These laser facilities shoot laser pulses from the ground upwards, that can be used to test the viewing conditions of the fluorescence detectors. The laser beams scatter in the atmosphere (by Mie and Rayleigh scattering, as discussed in the previous chapter). The fraction of the scattered light that is emitted in the right direction, is then detected by the telescopes (see also figure 4.7).

For this purpose a pulsed laser of 355 nm is used, with an energy of around 7 mJ and 7 ns long pulses [28]. In this manner 50 shots are fired every 15 minutes.

While the possibility of inclined laser shots exists, vertical shots are used to determine the vertical aerosol optical depth $\tau_a$, as introduced in section 3.3.2. For this purpose the number of photons at the telescope is considered, which is given as

$$N_\gamma = N_{\gamma,0} \cdot T_{m,1} T_{a,1} \cdot (S_m + S_a) \cdot T_{m,2} T_{a,2} \ . \tag{4.1}$$

$N_{\gamma,0}$ is the number of photons emitted by the laser. This number is attenuated on the way upwards through scattering, and is therefore multiplied by the transmission factors
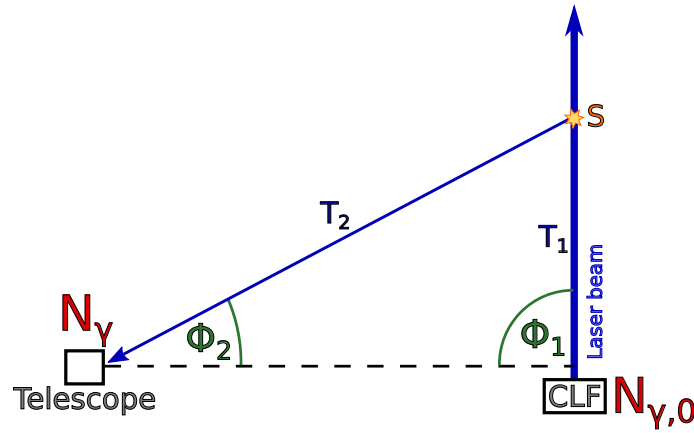
**Figure 4.7.:** Sketch of the light path from the CLF laser to the telescope.

$T_{m,1}$ and $T_{a,1}$ for molecular and aerosol scattering. The remaining laser beam then has a probability to scatter towards the Telescope, which is given by the molecular and aerosol scattering factors $(S_m + S_a)$. Finally the scattered light has a transmission probability of $T_{m,2} T_{a,2}$ to reach the telescope, again including molecular and aerosol scattering.

If a perfectly clear night without aerosols is considered (only molecular scattering), the equation above simplifies to

$$N_{\gamma,m} = N_{\gamma,0} \cdot T_{m,1} \cdot S_m \cdot T_{m,2} \tag{4.2}$$

and the ratio between the two cases is

$$\frac{N_\gamma}{N_{\gamma,m}} = T_{a,1} T_{a,2} \left( 1 + \frac{S_a}{S_m} \right) \; . \tag{4.3}$$

According to equation (3.22) the aerosol transmission is (under assumption of horizontal uniformity) given as[4]

$$T_a = \exp\left( -\frac{\tau_a}{\sin \phi} \right) \; , \tag{4.4}$$

where $\phi$ is the elevation angle, as labeled in figure 4.7. Since $\tau_a$ is only dependent on the altitude, which is the same for the two transmissions $T_{m,1}$ and $T_{m,2}$, only the angle $\phi$ is different (see figure 4.7). Plugging it into equation (4.3) one yields

$$\tau_a = -\frac{\sin \phi_1 \sin \phi_2}{\sin \phi_1 + \sin \phi_2} \ln \left[ \frac{N_\gamma}{N_{\gamma,m}} - \left( 1 + \frac{S_a}{S_m} \right) \right] \; . \tag{4.5}$$

Problematic is here, that the scattering factor $S_a$ is itself dependent on the number of aerosols, which is the goal of the calculation. One can however neglect[5] the contribution of $S_a$ in this case, since the aerosol scattering is predominantly a forward scattering [32]. Thus one can assume $S_a/S_m \ll 1$. Also, in the case of a vertical CLF laser shot $\sin \phi_1$ becomes 1, yielding

$$\tau_a \approx -\frac{\sin \phi_2}{1 + \sin \phi_2} \ln \left( \frac{N_\gamma}{N_{\gamma,m}} \right) \tag{4.6}$$

Thus the vertical aerosol optical depth can be determined by the ratio of the signal under an angle $\phi_2$, compared to the signal of a pure molecular scattering. This Data Normalized Analysis therefore has to utilize measured profiles of clear reference nights. An alternative approach uses a Laser Simulation Analysis, which compares the measured flux to a simulation based on a parametric aerosol model (see section 3.3.3).

---

[4]here the cosine of the zenith angle $\theta$ was exchanged with the sine of the elevation angle $\phi$

[5]It is however possible, to include corrections that account for the aerosol side scattering, see also [25]
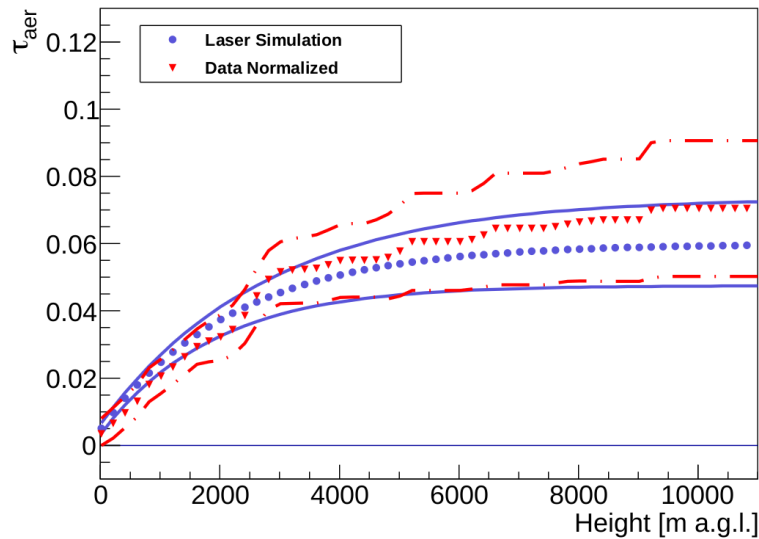
**Figure 4.8.:** Measured VAOD as a function of the height. The data corresponds to a measurement taken at Los Leones on 4th April 2008. Shown are the values obtained via the Data Normalized and a Laser Simulation method, including systematic uncertainties. From [32]

Figure 4.8 shows an example of the VAOD as a function of the height above ground level, as measured by the CLF for both the Data Normalized Analysis and a Laser Simulation Analysis. The VAOD of this measurement (taken on the 4th April 2008 at Los Leones) corresponds to an average amount of aerosols. Shown are also the systematic uncertainties of the two approaches. At a height of $5\,\mathrm{km}$ one can roughly estimate a VAOD of $\tau_\mathrm{a} \approx 0.06 \pm 0.015$ ($\approx 25\,\%$ uncertainty) for the Data Normalized method.

**Aerosol Phase Function Monitors**

The Aerosol Phase Function Monitors (APF) are used to determine the parameters $f$ and $g$ of the aerosol phase function, as introduced in section 3.3.2. Two instances of the APF were installed, in a distance of about $1\,\mathrm{km}$ from Los Morados and Coihueco respectively [28]. The setup consists of a Xenon flash lamp, that sends out flashes of light horizontally through the field of view of the Telescope. The telescope therefore sees the scattered light under a large range of scattering angles between $30°$ and $150°$. This makes it possible to extract the two parameters $f$ and $g$.

**Horizontal Attenuation Monitor and Photometric Robotic Atmospheric Monitor**

[28] The Horizontal Attenuation Monitor HAM was used to determine the Ångström coefficient $\gamma$, which describes the wavelength dependence of the VAOD (see section 3.3.2). Meanwhile, it is no longer in use. The HAM consisted of a high intensity discharge lamp positioned at Coihueco, sending out light flashes over the array. At Los Leones at a distance of $45\,\mathrm{km}$ the light was measured by a CCD camera. With that the horizontal attenuation of the light over the array could be measured. A series of different wavelength filters could be placed in front of the camera, to measure the attenuation as a function of the wavelength. This makes the Ångström coefficient accessible to a fit.

The Photometric Robotic Atmospheric Monitor (FRAM) has a similar purpose. It consists of a telescope located at Los Leones, also equipped with a series of wavelength filters. In contrast to the HAM now a selection of bright stars is used as a light source. By comparing
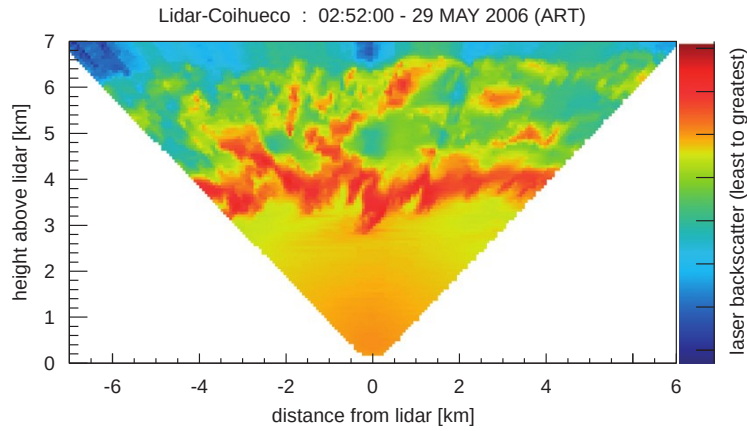
**Figure 4.9.:** The intensity of backscattered light as measured by the lidar located at Coihueco. A band of clouds is visible through a localized increase in the backscatter intensity. From [39]

the measured light flux to the expected star light known from literature, one can determine the vertical optical depth, again as a function of the wavelength. This can also be used to determine the Ångström coefficient.

**Lidar Stations**

At each of the four FD-buildings a lidar station is installed. It uses an UV-laser with 351 nm and three parabolic mirrors of 80 cm diameter to collect the backscattered light [39]. The intensity of the scattered light is measured as a function of the time of flight by photomultiplier tubes. The whole construction can be rotated around two axes (an alt-azimuth mount) with up to 2° per second. This way the whole sky can be scanned.

The lidars can be used to determine the VAOD, and are thus complementary to the CLF and XLF. Another use is the detection of clouds. The backscattered light contains information about height and position of clouds over the observatory, as well as the optical depth. Clouds are recognized as strong localized scattering regions. The time difference between emission and detection of the light is used to determine their distance. An example is shown in figure 4.9, where a band of clouds is visible at a height of 3.5 km, through an increased intensity in the backscattered light.

An additional Raman lidar is located at the CLF, using a 354.7 nm laser. It is able to separate the received backscattered light based on the wavelength. The elastic Rayleigh and Mie scattering is measured at the same wavelength as the emitted laser, the inelastic Raman scattering on $N_2$ is measured at 386.7 nm and the Raman scattering with $H_2O$ at 407.5 nm. This allows for a determination of the VAOD as well as the aerosol backscatter coefficient and the amount of water vapor [40].

**Cloud Cameras**

On top of all of the four FD-buildings cameras are installed, that observe the sky over the observatory. The cameras are sensitive to light in the infrared region ($\sim 10\,\mu m$). The pointing direction of the cameras coincides with the FDs, allowing for a match of camera-pixel and FD-pixel data [41]. The height of the clouds can however not be resolved, for this purpose the lidar system is necessary.

**Weather Stations**

Weather stations are placed at each of the FD-buildings and at the location of the CLF. Here the atmospheric state variables are regularly measured. Every 5 minutes new values of

temperature, pressure, humidity and wind speed are obtained. These variables are crucial for the molecular transmission, as mentioned in section 3.3.1, as well as for the creation of fluorescence light by air showers. To a certain degree these measurements can also be used to check the assumed horizontal uniformity [28].

**Weather Balloons and GDAS Data**

Between 2002 and 2008 balloons with meteorological measurement devices were launched on a regular basis up to an altitude of 25 km, to obtain altitude dependent measurements of pressure, temperature and humidity. Using this data a monthly model could be created to describe the atmosphere conditions for different times of the year. Meanwhile the Pierre Auger Observatory also uses the Global Data Assimilation System (GDAS), which provides predictions for these atmospheric state variables in intervals of three hours. Therefore GDAS includes meteorological data from measurements all over the world into numerical weather predictions. The GDAS data is available for different height levels (sea level up to $\sim 26$ km) and in a latitude-longitude-grid of $1° \times 1°$ [30].

# 5. The Aeolus Satellite

Aeolus is the name of a mission conducted by the ESA that contains measurements taken with a satellite orbiting Earth, as well as the name of the satellite itself. The name is a reference to Greek mythology where Aeolus appears as the ruler of the winds. An artist's impression of Aeolus can be seen in Figure 5.1, with some of its components labeled. Centerpiece of the satellite is the Doppler lider instrument ALADIN, which will be discussed in more detail in section 5.3.

## 5.1. Mission

Aeolus has the main objective of demonstrating the capability of using a Doppler-lidar-system for measurements of wind profiles taken from space. It is the worldwide first use of wind lidar measurements taken by a satellite. These wind profile measurements taken on a global scale are used to increase the accuracy of numerical weather predictions but are also useful for the study of climate models and atmospheric dynamics. Thus a secondary goal of the Aeolus mission is to provide data that helps characterizing the transport and circulation of water, aerosols, dust, air pollution and other substances that are carried in the atmosphere [42]. Additionally the Aeolus measurements allow for studies of the optical properties of aerosol and cloud layers [43].

The Aeolus satellite was launched on 22 August 2018. The nominal lifetime of the mission is three years, but the possibility for an extension up to the end of 2022 is currently discussed. European weather services are already assimilating Aeolus data into their models, after tests showed, that this data can improve the weather forecasts [44].

## 5.2. Satellite Orbit

The orbit that was chosen for Aeolus is a compromise between the different necessities demanded by the mission and technical feasibility.

Aeolus is placed in a Sun-synchronous orbit. This means that its orbital plane is rotating with the same rotational velocity and direction as the Earth's rotation around the Sun, thus the orbital plane rotates exactly 360° in one year and therefore always has the same alignment to the Sun [45]. As a consequence a specific place on Earth crosses the orbital plane always at the same local time[1]. The implications for the time at which the laser is seen in the Pierre Auger Observatory is discussed in section 6.1.3.

A Sun-synchronous orbit is especially interesting for satellites because of the possibility of placing the orbit over the day-night-border (*dawn-dusk orbit*). This has the advantage that the satellite is ideally never in Earth's shadow, which increases the thermal stability and the power generation with solar panels [47]. However, in the case of Aeolus the mission

---

[1]Another definition would be that the satellite crosses the equator always at the same local time. For Aeolus this time is 6.00 h during a descending and 18.00 h during an ascending path [46].
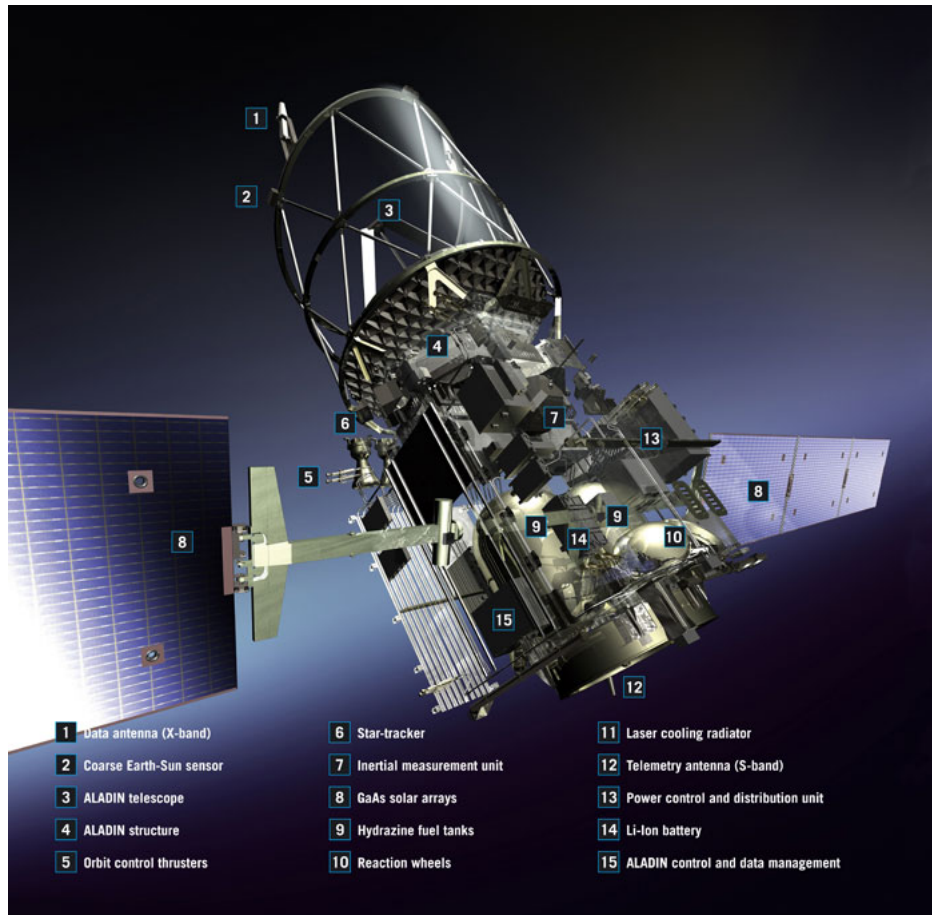
**Figure 5.1.:** An artist's rendering of Aeolus with some of its components. Most notable is the telescope in the top part of the image, which emits the laser pulses created by ALADIN (see section 5.3). Credit: ESA/ATG medialab

requirements call for additional constraints on the orbit inclination. Since a world-wide scan of wind profiles has to be performed, a near polar orbit is necessary to achieve global coverage. As a compromise an inclination of 97° was chosen. This is close enough to a polar orbit and limits the flight duration through Earth's shadow to about 20 min per Orbit (which takes about 91 min in total) [46].

The average altitude of Aeolus is 320 km and ranges between 305 km and 335 km[2]. A lower orbit is preferred due to a higher lidar signal, increases however the fuel consumption for orbital corrections [46],[48].

An additional motivation for a low altitude polar orbit is the sampling rate of a complete Earth scan. The timescale that is relevant for the atmospheric observations of Aeolus is around one day, meaning that within 12 hours[3] a large number of completed orbits is preferred. An orbital period of 91 min allows for about eight orbits and therefore sixteen lines of evenly spaced measurements. Figure 5.2 shows a visualization of one complete Earth scan consisting of eight orbits. Aeolus is in a repeat cycle of seven days or 111 orbits respectively [46], meaning that this is the period between two overflights of the same location on Earth. As a consequence, the ground track of the satellite is shifted to the west

---

[2]This variation originates from Earth's ellipsoidal shape and the eccentricity of the satellite's orbit. The maximum altitude is over the arctic regions, the minimum over the equator.

[3]The Earth makes half a rotation within 12 hours. With the combination of the descending and ascending half of a satellite orbit, one complete Earth scan is achieved within this half Earth rotation. The larger the number of orbits within this time scale, the finer the scan.
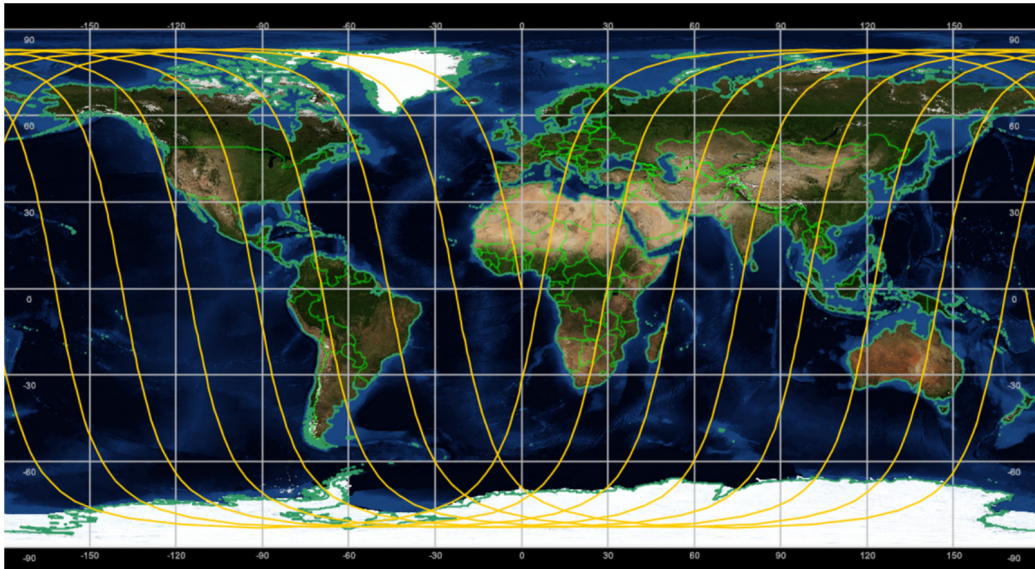
**Figure 5.2.:** Visualization of the Aeolus laser tracks withing 12 hours. This time period corresponds to about eight orbits that are spaced evenly over the surface of Earth. From [42]

**Table 5.1.:** Some relevant parameters of the orbit of the Aeolus satellite. Values are taken from [46].

| Parameter | Value |
| --- | --- |
| Average altitude | 320 km |
| Inclination | 96.7° |
| Orbital period | 90.8 min |
| Repeat cycle | 7 days (111 orbits) |

each day until it matches up again after one week. This has relevance for the visibility in the Pierre Auger Observatory that will be evaluated in section 6.1.2.

To ensure a timely integration of the measured data into numerical weather predictions, a maximal delay of three hours between measurement and transmission of the data is required. This is achieved by receiver stations in Svalbard and at the Troll research station in Antarctica. Due to their polar location and the near polar Aeolus orbit, a communication between satellite and ground station can be established during every orbit [47],[49].

The orbital parameters that were discussed above are summarized in table 5.1. The listed parameters do not fully determine the orbit but are the most relevant for this discussion.

## 5.3. The Atmospheric LAser Doppler INstrument (ALADIN)

ALADIN is the centerpiece of the Aeolus satellite and its only payload. It is a lidar system that uses the Doppler effect to measure the wind speeds used by Aeolus to create global wind profiles.

### 5.3.1. Principle of Lidar Wind Speed Measurements

The idea behind the measurement of wind speeds with a lidar system is as follows: A laser pulse is shot from the satellite towards Earth. Some of the light scatters via Rayleigh scattering on air molecules or via Mie scattering on aerosols and cloud particles. Rayleigh and Mie scattering are complementary, because of the small amount of aerosols present at
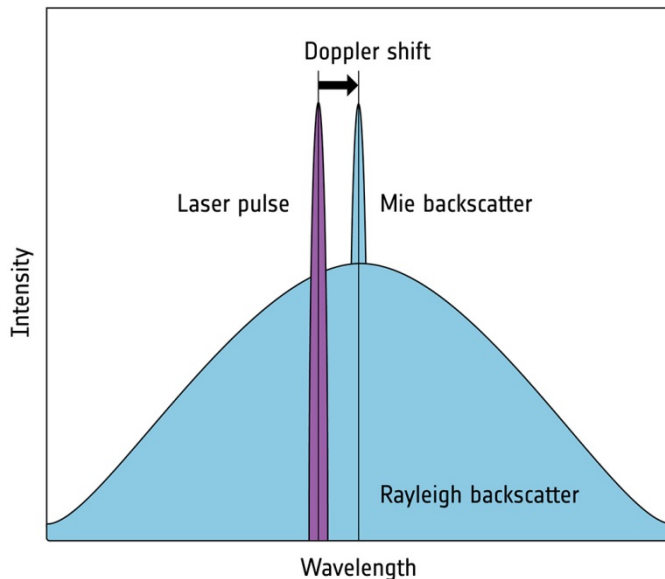
**Figure 5.3.:** Illustration of the frequency shifted back-scattered signal. The Rayleigh-scattered portion is broadened due to Brownian motion of the air molecules. From [42]

higher altitudes, here the measurement has to rely on Rayleigh scattering [50]. Light that is back-scattered returns to the satellite and can be detected. The relative velocity of the scattering medium causes the back-scattered light to be red or blue shifted to a different wavelength.

An illustration of the back-scattered signal can be seen in figure 5.3. The Doppler shift of Rayleigh-scattered light is affected by the Brownian motion of the air molecules. The obtained spectrum is therefore not only shifted by the wind speed but also broadened. The Rayleigh spectrum is overlaid with the Mie-signal, which generates a narrow frequency band, due to the higher mass and lower Brownian movement of the aerosol particles compared to air molecules.

The measurement of the frequency shift happens separately for the Mie and the Rayleigh signal in two different detectors. The two signals can be separated by applying a threshold above which only Mie scattered light remains, which allows for a decoupling of the Mie and Rayleigh signal [50].

For the Doppler shift measurement of the Mie signal a fringe imaging technique is used. The narrow-banded Mie portion of the back-scattered light is used to create an interference pattern, which is projected onto a detector array. The location of the interference maxima is dependent on the wavelength, thus by measuring the lateral displacement of the maximum and comparing it to the original non-shifted laser wavelength, one can determine the Doppler shift. A sketch of the principle of this technique can be seen in figure 5.4.

For the Rayleigh signal a double-edge technique is used. Two Fabry-Pérot etalons are used as wavelength filters that only allow light with a certain wavelength to pass. The two filter-wavelengths are chosen to be symmetrically above and below the reference wavelength of the emitted laser. The Doppler shift can then be derived by comparing the signal strength of the light that passes the two filters. The difference of the two signals

$$\frac{S_1 - S_2}{S_1 + S_2} \tag{5.1}$$

is then an estimator for the wavelength shift. An illustration of the double-edge technique
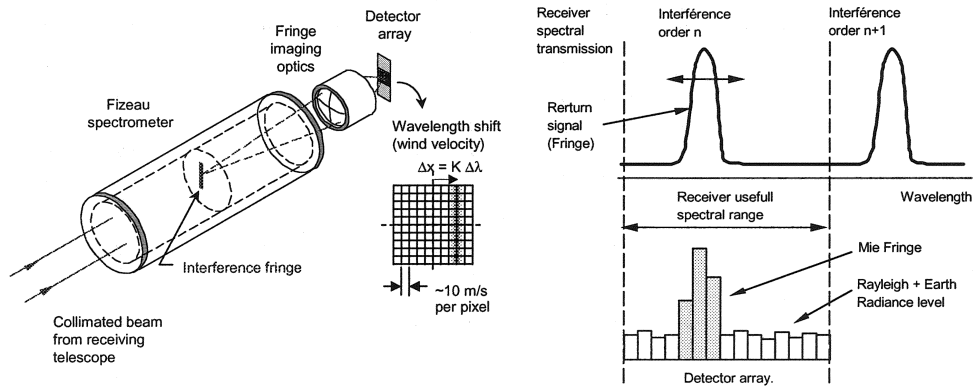
**Figure 5.4.:** Illustration of the fringe imaging technique used in the Mie spectrometer. The position of an interference pattern can be used to determine the wavelength. From [50]
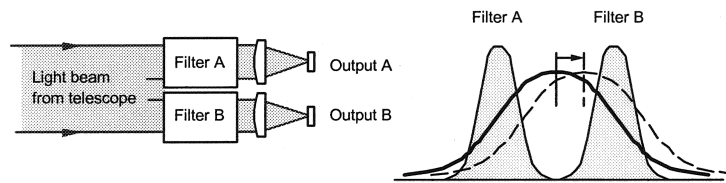


**Figure 5.5.:** Illustration of the double-edge technique used in the Rayleigh spectrometer. The Doppler shift is determined by comparing the output of two wavelength filters placed symmetrically around the reference wavelength. From [50]

can be found in figure 5.5.

With the Doppler shift determined, the velocity of the scattering medium and therefore the wind speed can be approximately calculated as [50]

$$v_{\text{LOS}} = \frac{\lambda}{2}\Delta f \ , \tag{5.2}$$

where $\Delta f$ is the shift in frequency and $\lambda$ the original laser wavelength. The thereby determined velocity corresponds the the wind projected along the line of sight of the lidar. For the usage in numerical weather predictions especially the profile of horizontal wind speeds is of interest. To be sensitive to horizontal winds, the line of sight has to be slanted. The velocity along the line of sight can then be projected onto the horizontal plane. To achieve this, the satellited is oriented in a way such that the laser points 35° to nadir. Due to the aforementioned dawn-dusk-orbit of Aeolus, the laser can constantly be pointed towards the night side of Earth, which is important to reduce background caused by ambient light. An illustration of the orientation of satellite and laser can be seen in figure 5.6.

The pointing direction orthogonal to the flight direction is also important to prevent an additional Doppler shift of the back-scattered light due to the satellite's velocity (the orbital velocity of Aeolus is 7.7 km/s, the ground track velocity amounts to 7.2 km/s) [46]. As a consequence of the satellite orientation, the laser points mostly towards west during descending and towards east during ascending. Therefore the horizontal component of the wind speeds that is accessible to Aeolus are mainly east-west-winds.

ALADIN does not only measure the Doppler shift of the back-scattered light, but also resolves the time of flight. This makes it possible to assign the measured signal to a distance along the line of sight and therefore to have information about the vertical position of wind speed measurements. Wind profiles can be taken from ground level up to an altitude of 30 km, the vertical resolution is between 250 m and 2 km, depending on the altitude [52].
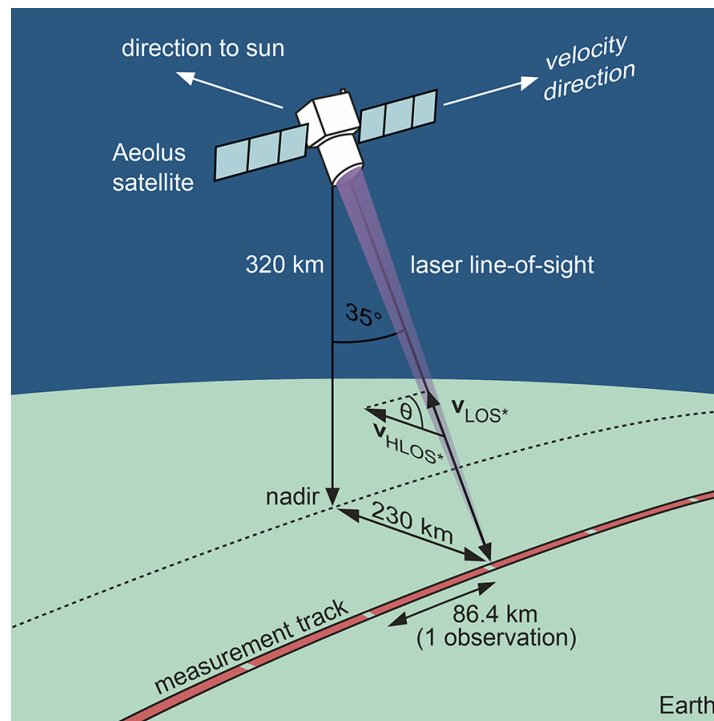
**Figure 5.6.:** Illustration of the satellite orientation. The laser points orthogonal to its flying direction towards the night side of Earth, under an angle of 35°. From [51]

One so-called observation consists of 600 Laser pulses fired with a frequency of 50.5 Hz. This corresponds to a track length of around 90 km on the ground or a flight time of around 12 s. To achieve a better signal to noise ratio in the light measurement, the signals of multiple laser pulses are accumulated in the detector, typically 20 pulses are integrated. This limits the horizontal resolution to around 3 km. The random error of the (horizontal) wind speed itself is specified to be between 1 m/s and 2.5 m/s, depending on the altitude [52].

### 5.3.2. The Optical Set Up of ALADIN

To guide the created laser pulses through the telescope and the back-scattered light onto the detectors, ALADIN uses an elaborate optical set up. An overview of the most important parts can be seen as a sketch in figure 5.7.

The laser pulses are created in a diode-pumped Nd:YAG laser, pulsed with a frequency of 50.5 Hz and an energy of around 65 mJ. The laser light is in the UV-region with a wavelength of 354.89 nm [53]. ALADIN is equipped with two laser transmitters (PLH in the sketch for *Power Laser Head*) for redundancy[4].

The laser beam is sent through a half-wave plate (HWP) and quater-wave plate (QWP) to set its circular polarization and a small part is deflected in a beam splitter for reference measurements. Afterwards it passes a beam expander and reaches the telescope. The telescope is used as both transmitter and receiver, the optical paths of outgoing and incoming light overlap. It consists of mirrors in a Cassegrain configuration, the outgoing laser pulse is first reflected and widened in a smaller convex secondary mirror and afterwards reflected outwards with a concave main mirror. The larger main mirror (with a diameter of 1.5 m) thereby creates a beam with a small divergence, the beam is widened to a diameter of only 7 m to 9 m at ground level [47], [54].

---

[4]The redundant laser was actually activated in June 2019, after the nominal laser was continuously losing energy [53].
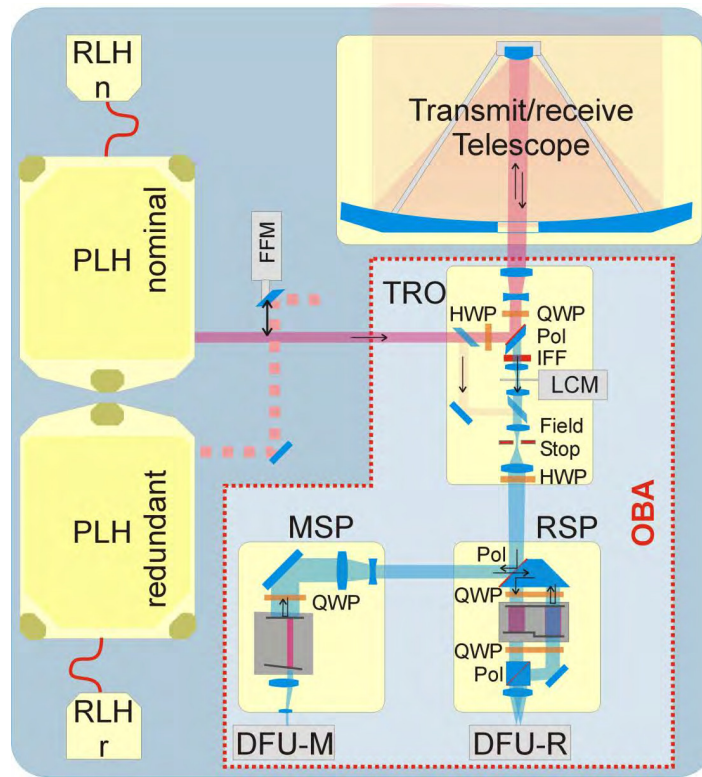
**Figure 5.7.:** Schematic of the optical set up of ALADIN. From [47]

The back-scattered light is focused in the telescope and again traverses the quarter-wave plate, thus getting linearly polarized. It then passes a polarizing beam splitter (Pol), and multiple elements that reduce the background light: The Laser Chopper Mechanism (LCM) blocks stray light while the laser is firing, the interference filter (IFF) filters background light with certain wavelengths and the Field Stop and an aperture limit the beam's diameter and the field of view of the telescope. Another half-wave plate is used to obtain a defined direction of polarization before entering the entrance to the spectrometers [46].

The light first gets reflected at a polarizing beam splitter at the input of the Rayleigh spectrometer (RSP) and is guided to the Mie spectrometer (MSP). The Mie spectrometer only transmits a small band width around the laser wavelength to the fringe imaging detector described above, the rest of the signal is reflected back towards the Rayleigh spectrometer, where this time it passes the polarizing beam splitter.

Inside the Rayleigh spectrometer the light first reaches filter A (a Fabry-Pérot etalon as described above). A fraction of the light with the fitting wavelength is transmitted, the rest gets reflected towards filter B. The output of both filters is then imaged onto a detector.

**Narcissus Reflection and Secondary Beam**

The laser pulses sent out by ALADIN can be detected by the Pierre Auger Observatory, as will be discussed in the following sections. These laser beams are however not the only Aeolus emissions detected in the Observatory. To avoid an internal reflection of the laser beam inside the satellite directly back onto the detectors (a so called narcissus reflection), a part of the laser beam is deliberately reflected out of the satellite. Without this reflection, the central part of the outgoing laser beam would not be guided towards Earth by the main mirror, but would instead travel directly towards the detectors. This is avoided by placing an additional small mirror in the telescope, which reflects the problematic part of the beam outwards. This reflection will subsequently be called *Secondary Beam*

to distinguish it from the so far discussed *Main Beam*. The properties of the secondary beam are unfortunately not well documented, as it has no significance for the Aeolus mission, other than an estimated offset of 20° to the main beam (and thus a nadir angle of approximately 55°) with an uncertainty of approximately 2°. The energy is in the order of magnitude of 1% of the main beam energy. [54]. It plays however an important role for the investigations done within the scope of this thesis.

# 6. The Aeolus Laser at the Pierre Auger Observatory

As Aeolus performs global scans, some of its measurement tracks come close to the Pierre Auger Observatory. Both the main beam and the secondary beam thereby come within reach of a detection with the Fluorescence Detectors. The presence of Aeolus laser shots in the FD data was first noticed and described in [55]. The methods of reconstructing the laser shots with data from the FDs will be discussed in chapter 7. This chapter will show how the position of the laser ground tracks can be obtained from Two Line Elements and how this can be used to predict the visibility of the Aeolus laser in the Pierre Auger Observatory and Telescope Array Project.

## 6.1. Visibility in the Pierre Auger Observatory

The position of the laser ground tracks is determined in two steps. First the satellite's position is extracted from Two Line Elements, then the laser is projected onto the surface of Earth.

### 6.1.1. Extrapolation of the Satellite Position

A convenient and publicly accessible way of obtaining orbital data of satellites are Two Line Elements, which store this information for different points in time. To interpolate between two points, one can use a certain family of algorithms based on a model called *Simplified General Perturbations* (SGP).

**Two Line Elements (TLEs)**

Two Line Elements are a format to store the orbital information of bodies that orbit around the Earth [56]. The data is stored in two lines of 69 ASCII-characters each[1], hence the name. In figure 6.1 one instance of a TLE is shown, that includes the orbital information of Aeolus for one point in time in 2020, along with a detailed description of the entries. Sets of two line elements can for example be obtained from `www.space-track.org`, as was done for the TLE data used in this thesis.

One Two Line Element contains a complete set of parameters to define the orbit and the satellite's position in it for the given epoch. TLEs do not exist for all arbitrary timestamps. To interpolate the position of a satellite between two epochs a so called SGP-algorithm is used.

---

[1]Originally the data was stored in punch cards. The format remained after the transition to ASCII-code.

```
1 43600U 18066A 20182.09722306 .00018334 00000-0 71880-4 0 9993
2 43600 96.7182 188.3046 0006029 67.3679 292.8231 15.86981312107372
```

**First line:**

| | |
|---|---|
| 1 | The line number. |
| 43600U | The satellite catalog number, a unique 5-digit code to identify the satellite. The letter "U" marks the security classification as "unclassified" (as for all publicly available satellites). |
| 18066A | International identifier. It consists of the launch year (2018), the launch number in this year (66) and the launch object (A). |
| 20182.09722306 | The *epoch* or timestamp for which the TLE is valid. It consists of the year (2020) and the day of the year, including a fractional part of a day (182.09722306 days, 30th June), to a precision of $\sim 1\,\mathrm{ms}$ |
| .00018334 | A drag coefficient used in calculations with the SGP-algorithms, given in revolutions/(day)$^2$. It corresponds to the time derivative of the average angular velocity. |
| 00000-0 | A drag coefficient of higher order. It corresponds to the second time derivative and is usually set to zero in the SGP-model. |
| 71880-4 | Another drag coefficient used in the SGP-model. It is given in units of the reciprocal Earth radius. The $-4$ is interpreted as an exponent and a preceded decimal point is implicit. The number written in this example is thus $0.71880 \cdot 10^{-4} R_\oplus^{-1}$ |
| 0 | Information about the type of model used. This affects the type of algorithm that has to be used for reconstruction (zero standing for the SGP4 Model). |
| 9993 | The first three digits count the number of TLEs created for the satellite (although unreliably [56]), the last digit is a checksum modulo 10 (sum of all digits in the line, "-" corresponds to 1, other non-digit characters are ignored) |

**Second line:**

| | |
|---|---|
| 2 | The line number |
| 43600 | The satellite catalog number, repeated from line 1 |
| 96.7182 | The inclination of the orbit in degrees. |
| 188.3046 | Right ascension of the ascending note in degrees. This corresponds to the angle between equinox and the point where the orbit crosses the equatorial plane from south to north. |
| 0006029 | The eccentricity. A preceded decimal point is implicit, the eccentricity in this case is thus 0.0006029 |
| 67.3679 | Position of perigee in degrees, determined as the angle between the ascending node and the lowest point in the satellite's orbit. |
| 292.8231 | The mean anomaly in degrees. This value is the angle between perigee and the position of the satellite within its orbit at time of the epoch. |
| 15.86981312107372 | This entry consists of three parts. The first part (15.86981312) describes the number of orbits completed per day, the second part (10737) counts the number of revolutions since launch and the last digit (2) is again the checksum for this line, modulo 10. |

**Figure 6.1.:** Example of a TLE with a description of the individual entries

**Simplified General Perturbation Algorithms**

Given the full set of orbital parameters for an epoch, one can calculate the position of the satellite at this time. However, to obtain the satellite's position for a point in time between two epochs, one has to calculate how the orbit propagates through time. This is done by the SGP algorithms, which therefore also use the drag coefficients listed in a TLE. This allows in particular for a determination of the satellite position, not only for a given TLE but for an arbitrary point in time. The precision is however limited. At epoch the position of a satellite is only accurate to about 1 km, rapidly diverging with the interpolated time [57].

The algorithm originates from a family of five models: SGP, SGP4, SDP4, SGP8 and SDP8 (SGP standing for Simplified General Perturbation, SDP for Simplified Deep Space Perturbations). The SGP model is used for lower orbits (orbital period below 225 min), the SDP model for higher orbits (above 225 min).

The algorithm used for the evaluation of orbits from TLEs is SGP4. This algorithm is implemented in programming libraries, for example in the python package `skyfield` [58], with the source code publicly available. Using it, the position of the Aeolus satellite can be interpolated for any given time, using a TLE as input. Each TLE corresponds to a certain time (epoch), thus the TLE used as input for the interpolation should be as close as possible to the time, for which the position is calculated. The reason is the decreasing accuracy of the interpolation with the amount of time spanned over. A new TLE is available approximately every 12 h, which means the interpolation time for one calculated satellite position is usually several hours. In case of Aeolus, interpolating from one epoch to the next, deviations of up to $\sim 50$ km are reached[2].

## 6.1.2. Projection of the Laser Ground Track

With the usage of Two Line Elements and the interpolation via SGP-algorithms, the position of the Aeolus-satellite can be obtained for an arbitrary point in time. To calculate the position on Earth where the laser beam impacts, one can project a vector from the position of the satellite onto the surface of Earth. Therefore, besides the position of the satellite also the pointing direction of the laser has to be known. As mentioned in previous chapters, the main beam is pointed under an angle of 35° to nadir, orthogonal to the flight direction of the satellite. With this information a pointing vector in the satellite's local coordinate system can be formulated, which has to be transformed into Earth centered coordinates for a projection onto the surface.

### 6.1.2.1. Transformation from Local Satellite to Earth Centered Coordinates

To obtain the pointing vector of the laser in Earth centered coordinates, first the pointing vector in local coordinate system has to be established. Afterwards a rotation matrix can be multiplied to rotate the vector into Earth centered coordinates.

**Local Satellite Coordinate System**

The local coordinate system of the satellite is given by the movement direction of the satellite ($x$- or roll-axis), the axis tangential to the Earth's surface ($y$- or pitch-axis) and the axis pointing from the satellite to the center of Earth ($z$- or yaw-axis), such that a right handed coordinate system is obtained. An illustration can be seen in figure 6.2. In

---

[2]although in practice one does not need to interpolate all the way from one epoch to the next, since backwards interpolations in the time are possible. Therefore only half the time range between to epochs has to be interpolated over.
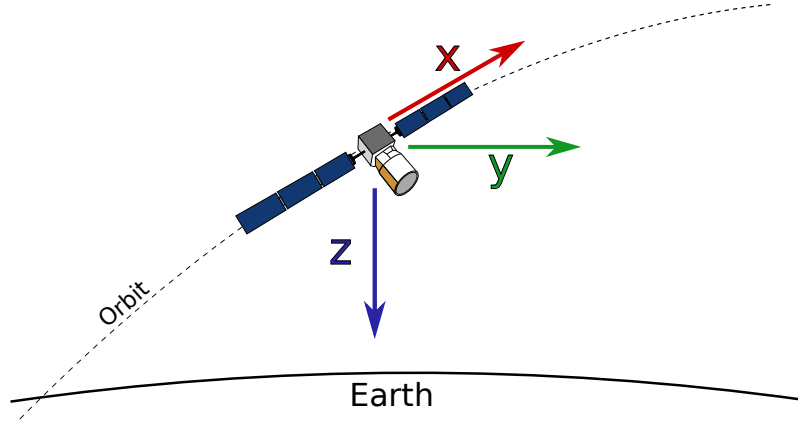
**Figure 6.2.:** Illustration of the local coordinate system. The $x$- or roll-axis is given by the direction of movement, the $z$- or yaw-axis points towards Earth and the $y$- or pitch axis is tangential to the surface of Earth, such that a right handed coordinate system is obtained.

this local coordinate system the pointing vector of the laser can be obtained by rotating the unit vector $\vec{z}$ (pointing to nadir) along the roll-axis. It can therefore be written as

$$\vec{a}_{\text{loc}} = R_{\text{loc}} \cdot \vec{z} = R_{\text{loc}} \cdot \begin{pmatrix} 0 \\ 0 \\ 1 \end{pmatrix} . \tag{6.1}$$

$R_{\text{loc}}$ is the rotation matrix describing the rotation around the roll-axis. For a general case, the rotation matrix is given by

$$R_{\text{loc}} = \begin{pmatrix} \cos\alpha\cos\beta & \cos\alpha\sin\beta\sin\gamma - \sin\alpha\cos\gamma & \cos\alpha\sin\beta\cos\gamma + \sin\alpha\sin\gamma \\ \sin\alpha\cos\beta & \sin\alpha\sin\beta\sin\gamma + \cos\alpha\cos\gamma & \sin\alpha\sin\beta\cos\gamma - \cos\alpha\sin\gamma \\ -\sin\beta & \cos\beta\sin\gamma & \cos\beta\cos\gamma \end{pmatrix} \tag{6.2}$$

with the yaw-angle $\alpha$, the pitch-angle $\beta$ and the roll-angle $\gamma$. Since in this case only a rotation around the roll-axis takes place (for the main beam with an angle of $\gamma = 35°$), the matrix simplifies to

$$R_{\text{loc}} = \begin{pmatrix} 1 & 0 & 0 \\ 0 & \cos\gamma & -\sin\gamma \\ 0 & \sin\gamma & \cos\gamma \end{pmatrix} . \tag{6.3}$$

**Co-Moving Earth Centered (Global) Coordinates**

The Earth centered coordinates are defined by the axis through the equator and the zero meridian ($x$), the axis through the north pole ($z$) and the one orthogonal to the former two ($y$), such that a right-handed coordinate system is obtained, that is co-moving with the Earth's rotation.

Assuming that the rotation matrix that transforms a vector from the Earth centered (global) into the satellite's local coordinates is given as $R_{\text{gl}}$, three identities can be derived:

1. The satellites flight direction defines the local $x$-axis and therefore:

$$R_{\text{gl}} \cdot \vec{n} = \vec{x} = \begin{pmatrix} 1 \\ 0 \\ 0 \end{pmatrix} , \tag{6.4}$$

where $\vec{n} = \frac{\vec{v}}{|\vec{v}|}$ is the normalized velocity vector of the satellite in Earth centered coordinates.

2. The vector pointing from the satellite towards the center of Earth defines the local $z$-axis and therefore:

$$R_{\mathrm{gl}} \cdot \vec{m} = \vec{z} = \begin{pmatrix} 0 \\ 0 \\ 1 \end{pmatrix} , \qquad (6.5)$$

where $\vec{m} = \frac{-\vec{r}}{|\vec{r}|}$ is the normalized vector that points from satellite to Earth in Earth centered coordinates.

3. The vector orthogonal to the former two (tangential to the Earth's surface) defines the local $y$-axis and therefore:

$$R_{\mathrm{gl}} \cdot \vec{l} = \vec{y} = \begin{pmatrix} 0 \\ 1 \\ 0 \end{pmatrix} , \qquad (6.6)$$

where $\vec{l} = \vec{m} \times \vec{n}$.

Each of these conditions yields three equations. In total they can be written as a system of linear equations:

$$\begin{pmatrix} n_1 & n_2 & n_3 & 0 & 0 & 0 & 0 & 0 & 0 \\ 0 & 0 & 0 & n_1 & n_2 & n_3 & 0 & 0 & 0 \\ 0 & 0 & 0 & 0 & 0 & 0 & n_1 & n_2 & n_3 \\ l_1 & l_2 & l_3 & 0 & 0 & 0 & 0 & 0 & 0 \\ 0 & 0 & 0 & l_1 & l_2 & l_3 & 0 & 0 & 0 \\ 0 & 0 & 0 & 0 & 0 & 0 & l_1 & l_2 & l_3 \\ m_1 & m_2 & m_3 & 0 & 0 & 0 & 0 & 0 & 0 \\ 0 & 0 & 0 & m_1 & m_2 & m_3 & 0 & 0 & 0 \\ 0 & 0 & 0 & 0 & 0 & 0 & m_1 & m_2 & m_3 \end{pmatrix} \cdot \begin{pmatrix} R_{\mathrm{gl}}^{11} \\ R_{\mathrm{gl}}^{12} \\ R_{\mathrm{gl}}^{13} \\ R_{\mathrm{gl}}^{21} \\ R_{\mathrm{gl}}^{22} \\ R_{\mathrm{gl}}^{23} \\ R_{\mathrm{gl}}^{31} \\ R_{\mathrm{gl}}^{32} \\ R_{\mathrm{gl}}^{33} \end{pmatrix} = \begin{pmatrix} 1 \\ 0 \\ 0 \\ 0 \\ 1 \\ 0 \\ 0 \\ 0 \\ 1 \end{pmatrix} . \qquad (6.7)$$

The vector $\vec{r}$ can be obtained from TLEs. The unit vector of the velocity $\vec{n} = \vec{v}/|v|$ is is obtained by calculating the difference between two positions in short succession (and normalization)

$$\vec{n}(t) = \frac{\vec{r}(t + \Delta t) - \vec{r}(t)}{|\vec{r}(t + \Delta t) - \vec{r}(t)|} . \qquad (6.8)$$

Thus, the vectors $\vec{n}$, $\vec{m}$ and $\vec{l}$ can be derived and thereby one can solve the system of linear equations to obtain $R_{\mathrm{gl}}$.

Since $R_{\mathrm{gl}}$ was defined as the matrix that transforms a vector from global into local coordinates, the inverse matrix $R_{\mathrm{gl}}^{-1}$ is used for a transformation from local satellite coordinates to global Earth centered coordinates. The pointing vector of the laser beam in Earth centered coordinates is therefore

$$\vec{a}_{\mathrm{gl}} = R_{\mathrm{gl}}^{-1} \cdot \vec{a}_{\mathrm{loc}} = R_{\mathrm{gl}}^{-1} R_{\mathrm{loc}} \cdot \begin{pmatrix} 0 \\ 0 \\ 1 \end{pmatrix} . \qquad (6.9)$$

The previous calculations are the same for main and secondary beam. The only difference is the used roll-angle $\gamma$. For the main beam this is $35°$, for the secondary beam a value of $54.1°$ was used. The motivation for the latter will become clear in section 7.3.2.1.

**6.1.2.2. Propagating the Laser Vector**

With the satellite position $\vec{r}$ and the laser direction $\vec{a}$ known, the impact point of the laser on the surface of Earth can be estimated. Therefore a simple iteration along the laser vector can be made:

1. Start with setting the lower limit of the distance that the laser travels $l_{\text{low}}$ to 0 and the upper limit $l_{\text{up}}$ to a sufficiently high value (e.g. $|\vec{r}|$)

2. Set the value for the distance traveled by the laser to the midpoint between the upper and lower limit $d = \frac{l_{\text{low}}+l_{\text{up}}}{2}$

3. Move from the satellite a distance $d$ along the laser vector: $\vec{p} = \vec{r} + d \cdot \vec{a}$

4. Check if the resulting point $\vec{p}$ is above or below the surface of Earth. If it is above the surface, set $l_{\text{low}} = d$. If it is below the surface set $l_{\text{up}} = d$.

5. Repeat steps 2 to 4 until the difference between upper and lower limit is sufficiently small (e.g. $1\,\text{m}$)[3]

This iteration yields the point where the laser hits the surface of Earth in Earth centered coordinates. For the conversion into longitude and latitude, the functionality of the python module `astropy` can be used.

**6.1.2.3. Results for the Ground Track Projection near the Pierre Auger Observatory**

The methods described earlier in this chapter can be used to check where the ground track of the Aeolus lasers are expected, in the proximity of the Pierre Auger Observatory. Due to the periodicity of the satellite's orbit described in section 5.2, a calculation of all ground tracks within one week should ideally suffice to get a complete image of the scanned positions on Earth. However, to account for small deviations from this perfect periodicity and to even out errors caused by the interpolation between TLE-epochs, a larger data set was used.

Therefore the complete set of TLEs from the year 2019 was utilized (around 750 elements). Since the satellite position is not guarantied to be over the observatory if only the position at epoch of each TLE is considered, the SGP-algorithms were used to calculate the position by extrapolating from the closest epoch. Thus a calculation of the satellite position for each minute of 2019 could be done. Using the aforementioned projection with a roll-angle of 35°, the laser ground track of the main beam could be estimated for all of 2019.

The result can be seen in figure 6.3a. Here the laser ground tracks belonging tho the main beam are plotted in the proximity of the Pierre Auger Observatory. Due to the repeat cycle of one week, the ground tracks are repeating after this time interval. Therefore one obtains blocks of around 50 lines each, since the tracks of one year are superimposed. These blocks of lines are broadened, due to variations in the satellite position between different orbits. On top of that one has to consider several uncertainties. One aspect is the interpolation between TLEs as mentioned before, as well as uncertainty within the TLE itself. Also the laser projection method has a limited precision, especially due to neglecting the surface terrain: The impact point is determined based alone on the latitude-dependent Earth radius as sea level. Finally also the orientation of the satellite was approximated, while assuming the pitch and yaw angles to be zero. In reality especially the yaw angle varies within several degree within one orbit due to the yaw-steering that was mentioned

---

[3]The achieved resolution is however not within $1\,\text{m}$, since effects like the surface terrain are not taken into account. However the iteration was in practice fast enough, so that a strict exit condition of $1\,\text{m}$ does not cause performance issues.
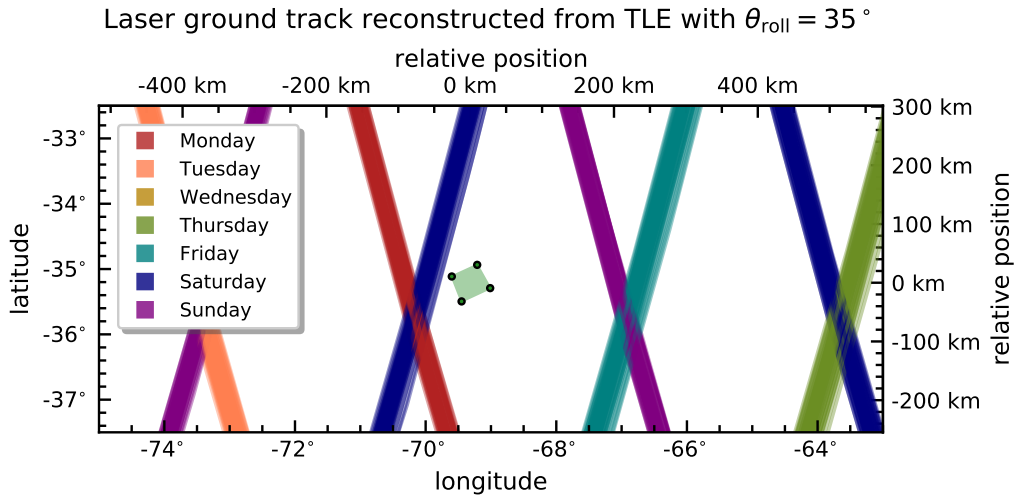
**(a)** main beam
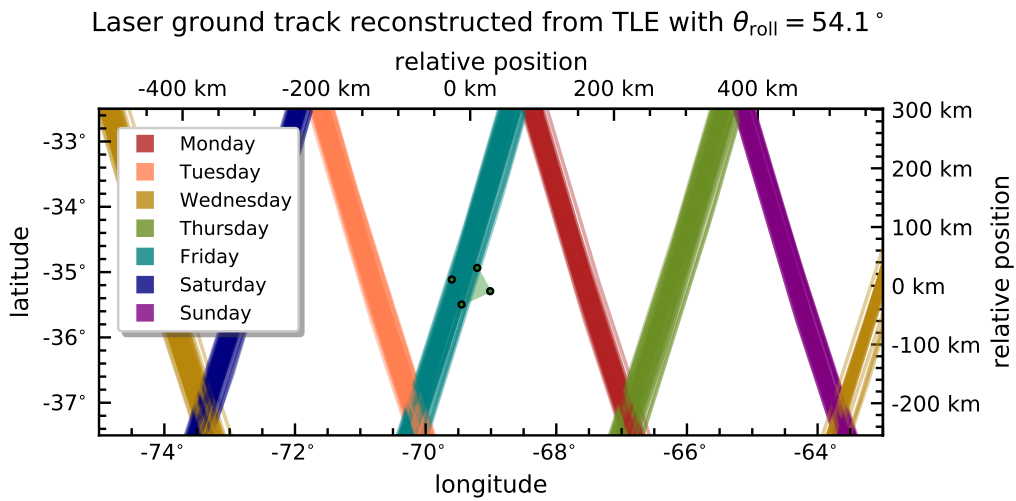


**(b)** secondary beam

**Figure 6.3.:** Ground tracks of the Aeolus beams near the Pierre Auger Observatory, based on TLE-positions. Plotted is the superposition of all tracks of 2019. Tracks from north-east to south-west correspond to the descending half of the orbit, tracks from south-east to north-west to the ascending half. The seven day repeat cycle causes the lines of each weekday to overlap. Plot (a) shows the main beam, calculated with a roll angle of 35°. Of interest is here the track belonging to a descending orbit on Saturday, when the laser beam crosses some kilometers west of the Pierre Auger Observatory (marked by the green quadrangle). Plot (b) shows the secondary beam, calculated with a roll-angle of 54.1°. Here, the laser beam traverses the observatory on Fridays.

in section 5.3.1. With all this the laser ground track obtained from TLEs can not provide a precise positioning within a few kilometers, but is useful to get a general image of the laser track position. On top of that information about the passage time can be obtained, as will be shown in the next chapter.

The plot in figure 6.3a also demonstrates some features of the specific Aeolus orbit. There are two families of tracks visible, one moving from north-east to south-west, the other moving from south east to north-west. The former belong to the descending half of an orbit, when the satellite moves in a north-south direction. After passing the south polar region, the satellite moves back from south to north, creating the other family of lines, moving from south-east to north-west[4]. Also visible is the progression of the tracks towards west with each day (marked by different colors in the plot). After one week the cycle begins anew.

The area enclosed by the Fluorescence Detectors is marked in the plot as a green quadrangle. It is notable that none of the main beam lines crosses this area. As will be seen in the next chapter, the main beam is however still visible on Saturdays, which correspond to the dark blue lines in figure 6.3a. On this weekday the laser beams are still close enough to create a measurable signal in the FDs[5].

The projection of the laser ground track can be done in the same way for the secondary beam. As already mentioned, the roll-angle used for the calculations is in this case $\gamma = 54.1°$. The result can be seen in figure 6.3b. The plot shows the same characteristics as the main beam tracks, with broadened lines corresponding to descending or ascending orbits. Again, the coloring indicates the weekday, with the visible daily progression from east to west. In this case the set of lines corresponding to Fridays cross the area of the observatory. As will be validated in section 7.3.2.2, the ground tracks of the secondary beam indeed traverse the observatory on Fridays.

### 6.1.3. Time of Transition

The previous calculations show, that both the main beam and the secondary beam have one weekday at which the laser is in principle visible, the main beam on Saturdays, the secondary beam on Fridays. The ground track projection from TLE positions can however be used to get a more precise prediction for the time at which each beam can be seen.

Base of this calculation is the same data set that was used before. As mentioned earlier, the ground position of the laser was calculated once every minute for the year 2019. The idea behind obtaining an estimation for the time at which the satellite is visible, is to look at the latitude of each calculated position and check when the latitude matches the one of the Pierre Auger Observatory. Since this latitude is crossed by the beam many times per day for various longitudes, only the points are selected, that are in proximity to the observatory. As a criteria the limits of $-75°$ to $-63°$ for the longitude and $-37.5°$ to $-32.5°$ for the latitude was chosen. These are also the limits for the plots in figure 6.3a and 6.3b, thus a laser position is selected if it falls within the window shown in these plots. Note that within one minute the ground position of the laser moves by approximately $432\,\mathrm{km}$ (the ground velocity is $7.2\,\mathrm{km/s}$), while the latitude range corresponds to over $500\,\mathrm{km}$. Therefore with these limits, for a fitting longitude at least one projected laser position per orbit falls within this window[6].

---

[4]The lines are not completely vertical, due to a combination of the not exactly polar orbit of Aeolus and the rotation of Earth underneath the satellite.

[5]The laser beams arrive from east, meaning that the ground tracks do not mark the closest distance to the telescopes.

[6]as mentioned earlier, the laser positions are calculated once every minute

For each of the selected positions it can be checked if they belong to a point in time before or after the passage of the observatory. As a criterion therefore the latitude of each point is compared with the average latitude of the four FD-stations[7]. This comparison is not ideal, since a matching latitude does not exactly equal the closest approach. It is however a reasonable approximation for the relevant tracks, that are very close to or traversing the observatory.

To get a more precise value for the passage time, one can interpolate between two points before and after the reference latitude is reached. The passage time is then

$$t_\text{pass} = t_{p1} + f \cdot (t_{p2} - t_{p1}) \ , \tag{6.10}$$

where $t_{p1}$ and $t_{p2}$ are the points in time corresponding to the positions before and after the passage of the observatory. The factor $f$ is obtained from the condition

$$y_\text{obs} = y_{p1} + f \cdot (y_{p2} - y_{p1}) \ , \tag{6.11}$$

where $y_{p1}$ and $y_{p2}$ are the latitudes of the two points and $y_\text{obs}$ is the reference latitude of the observatory. In total the passage time is interpolated via

$$t_\text{pass} = t_{p1} + \frac{y_\text{obs} - y_{p1}}{y_{p2} - y_{p1}} (t_{p2} - t_{p1}) \ . \tag{6.12}$$

Figure 6.4a shows the result for the main beam, figure 6.4b for the secondary beam. These plots correspond to the plots 6.3a and 6.3b, meaning that for all lines visible in the track-plots, the passage time was interpolated and plotted as a histogram. Note that for the passage time calculation only the descending ground tracks were considered, since these are the only ones close enough to the observatory[8]. Plotted are the time histograms for the same weekdays that are also relevant for the track-plots. The passage time is shifted by about 13 min between consecutive weekdays, since the tracks also move towards west with each following day.

As mentioned before, the important days for observation are the Saturdays for the main beam and the Fridays for the secondary beam. Based on the calculations done so far one can estimate a passage time of 10:10 UTC for the main beam and 9:57 UTC for the secondary beam.

### 6.1.4. Visibility Throughout the Year

So far it was established, that the Aeolus main beam passes the observatory on Saturdays at 10:10 UTC, the secondary beam on Fridays at 9:57 UTC. The Fluorescence Detectors underlie however an additional restriction regarding the measurability. Measurements with the FDs can only be taken during the night. The dusk-dawn-orbit of Aeolus however also causes the laser transitions to be close to dawn, running into the risk of happening too late for a FD-measurement.

To check weather the passage time calculated before falls into night time, the time of sunrise over the Pierre Auger Observatory can be calculated throughout the year. Therefore for a chosen position on Earth (again the average coordinates of the FD-stations) the time can be calculated for each day of a year at which the Sun is above or below the horizon. In more detail one can also include the different stages of twilight by their definition. Astronomical

---

[7]The average over the four FD-station coordinates is 69.3°W, 35.2°S.

[8]An analogue evaluation can however be done for the ascending tracks. This results in a passage time between around 22:30 UTC and 23:00 UTC, depending on the weekday. Since the ascending tracks can not be seen in the observatory, this case is not investigated further.
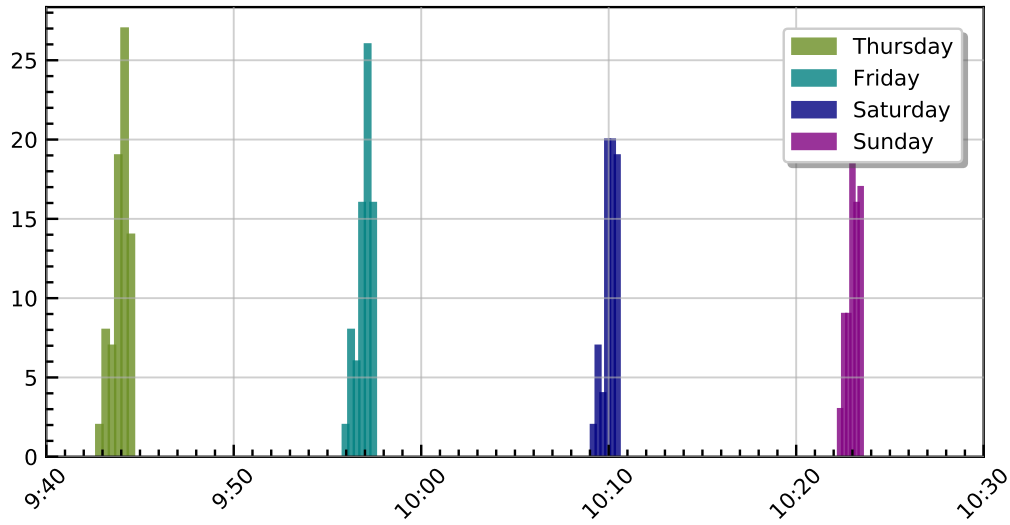
**(a)** main beam
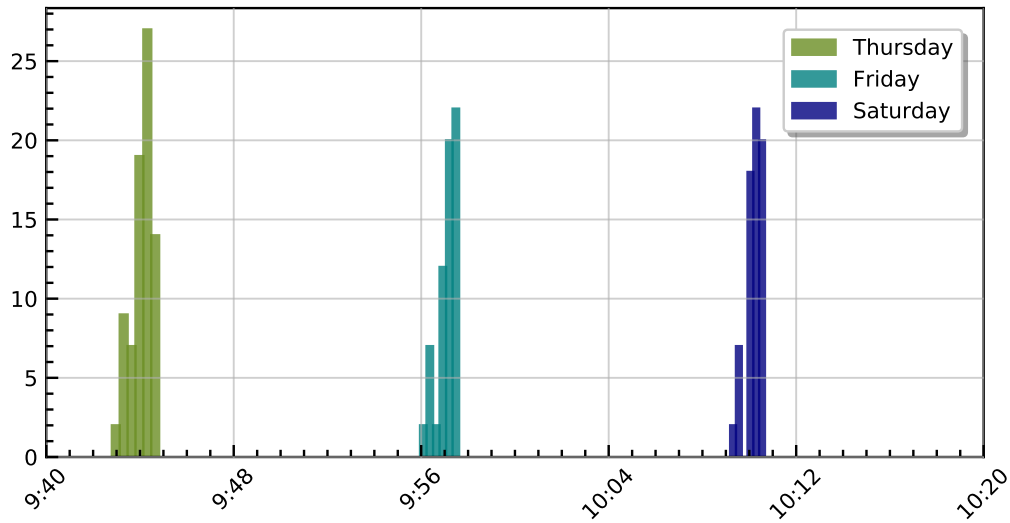


**(b)** secondary beam

**Figure 6.4.:** Histograms of the times at which the Aeolus beam crosses the latitude of $-35.21°$. This reference latitude originates from the average value of the four FD-station's latitudes. The data corresponds to the descending lines in figure 6.3. The track-shift of consecutive days towards west corresponds to the time shift towards later passage times. Plot (a) shows the case for the main beam. The relevant day for an observation is Saturday, which has a passage time of around 10:10 UTC. Plot (b) shows the case for the secondary beam, which is seen on Fridays, with a passage time of around 9:57 UTC.
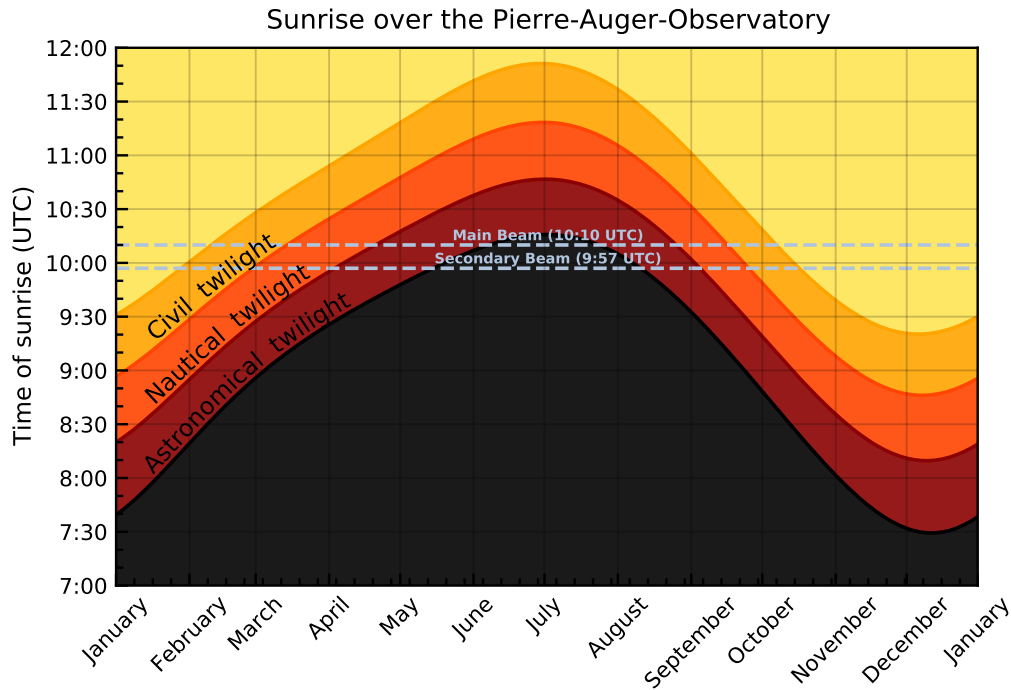
**Figure 6.5.:** Time of sunrise over the Pierre Auger Observatory. Plotted are the different stages of twilight based on the Sun's elevation angle. The horizontal dashed lines represent the passage time of main beam or secondary beam respectively. The visibility of the laser beams is limited to the intersection of these lines with the black area, which represents the time before astronomical twilight.

twilight starts with the Sun 18° below the horizon, nautical twilight at 12° and civil twilight at 6°. A convenient functionality for this issue is given by the python module `astropy`.

The sunrise and twilight time throughout one year obtained this way can be seen in figure 6.5. Because of the location of the Pierre Auger Observatory on the southern hemisphere, the Sun rises later during June and July and earlier during December. Also added in the plot are horizontal lines that indicate the passage time of main and secondary beam. Since the FD-measurements can only be taken during night time, the Aeolus lasers will only be visible for the time interval in which the passage time is below the start of dawn. This interval can be determined from the plot as the intersection of the horizontal lines with the black area, depicting the night time.

Therefore the secondary beam can only be measured between mid May and mid August. The main beam, passing a few minutes later, can only seen within June and July. This prediction also roughly matches the dates at which the Aeolus laser was measured so far, as will be seen in chapter 7.

## 6.2. Visibility in the Telescope Array Project

The Telescope Array Project is an air shower detector array in Utah, USA. It employs Fluorescence Detectors that work with a similar principle as the ones used by the Pierre Auger Observatory. If the laser beams of Aeolus were visible in both observatories, a direct comparison between the Fluorescence Detector systems could be made, which would be very useful for a comparison of the energy measurements of both observatories. Therefore it is worth doing the previous calculations also for Telescope Array, to check if the laser is potentially also visible there.

First the projection of the laser ground tracks can be done the same way as before, this time near the coordinates of Telescope Array. The resulting plots can be seen in figure 6.6. A similar image is obtained as for the Pierre Auger Observatory. As can be seen, the main beam passes a few kilometers to the west of Telescope Array (marked by the green triangle) on Wednesdays, the secondary beam traverses Telescope Array on Tuesdays. Also in both cases the tracks belong to the descending part of the orbit, putting Telescope Array in a very similar situation as the Pierre Auger Observatory.

The next step is to determine the passage time. This is done in the same way as before, the reference latitude is now chosen to be the average coordinates of Telescope Array's Fluorescence Detector stations (112.9° S, 39.3° N). The results for main and secondary beam are shown in figure 6.7. The relevant time for the main beam is approximately 13:44-13:45 UTC, for the secondary beam it is around 13:31 UTC.

The final step is then to check if these times fall into night time, for at least some time of the year. Just like for the Pierre Auger Observatory the twilight and sunrise times throughout the year are plotted in figure 6.8, this time for the location of Telescope Array. Since the location is this time on the northern hemisphere, the behavior is now inverse, the earliest sunrise is in June, the latest in January. The passage time of the laser is again marked by horizontal lines.

Unfortunately the passage time does not line up very well with the sunrise. Both the main and secondary beam pass at all times at best during twilight. A measurement of the Aeolus laser would thus only be possible if a measurement could take place during astronomical twilight, making it very challenging. Even then the laser could only be seen during a small window in December and January. The main beam, passing later than the secondary beam, would be even more difficult to detect.

A search for the Aeolus laser with Telescope Array could for this reasons not be done so far, as of winter 2020/2021 [59]. Since the Aeolus mission is planned to be extended until the end of 2022, the chance of an Aeolus measurement with Telescope Array still exists, if a special data taking can be achieved with reduced high voltage on the PMT cameras, for a measurement during twilight.

**(a)** main beam



**(b)** secondary beam
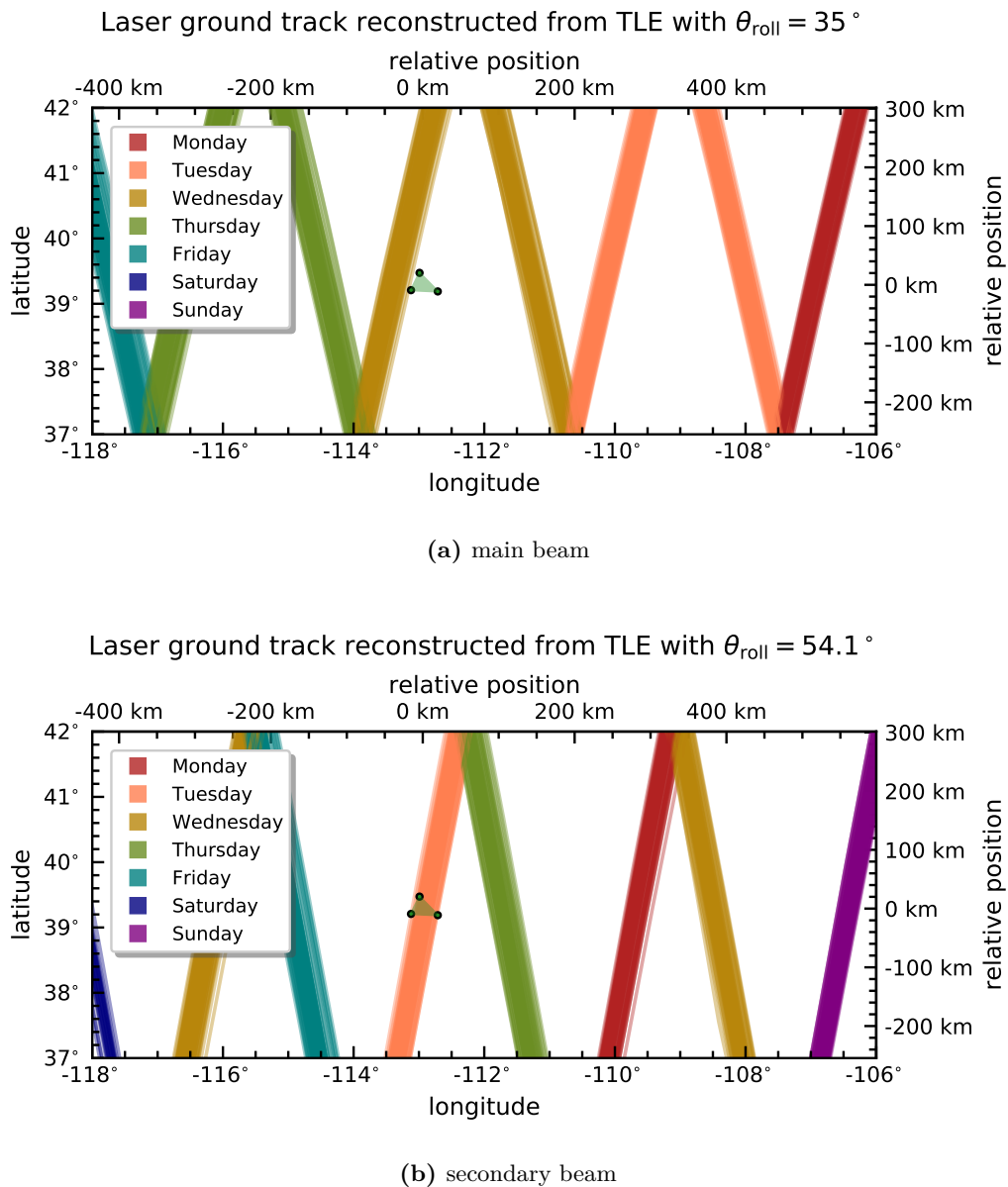
**Figure 6.6.:** Ground tracks of the Aeolus beams near the Telescope Array Project, throughout all of 2019. The positions of the three FD-stations of Telescope Array are marked by the green triangle. The main beam (a) passes close to the observatory on Wednesdays, during a descending orbit, the seconary beam (b) traverses the array on Tuesdays.

Time (UTC) at which the Aeolus Main Beam crosses the latitude of 39.29 °
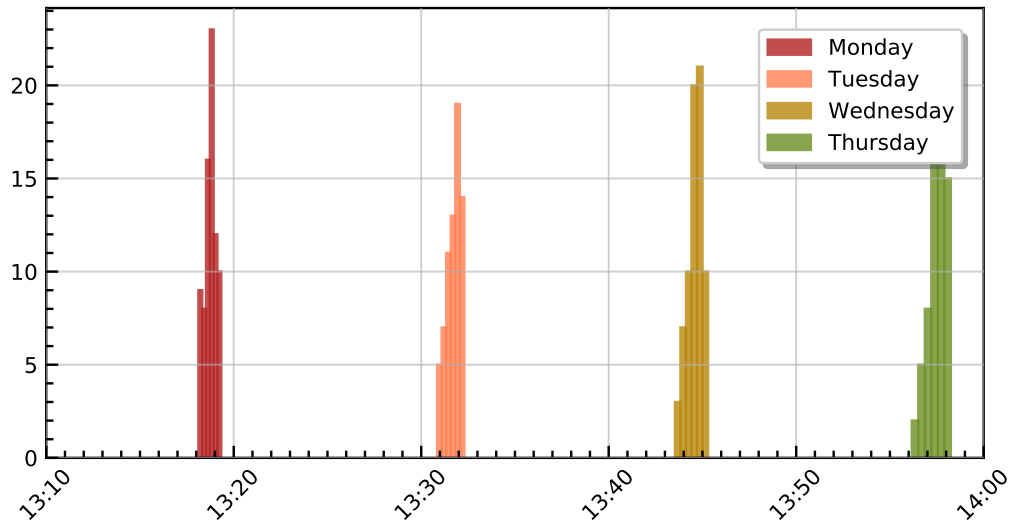


**(a)** main beam

Time (UTC) at which the Aeolus Secondary Beam crosses the latitude of 39.29 °
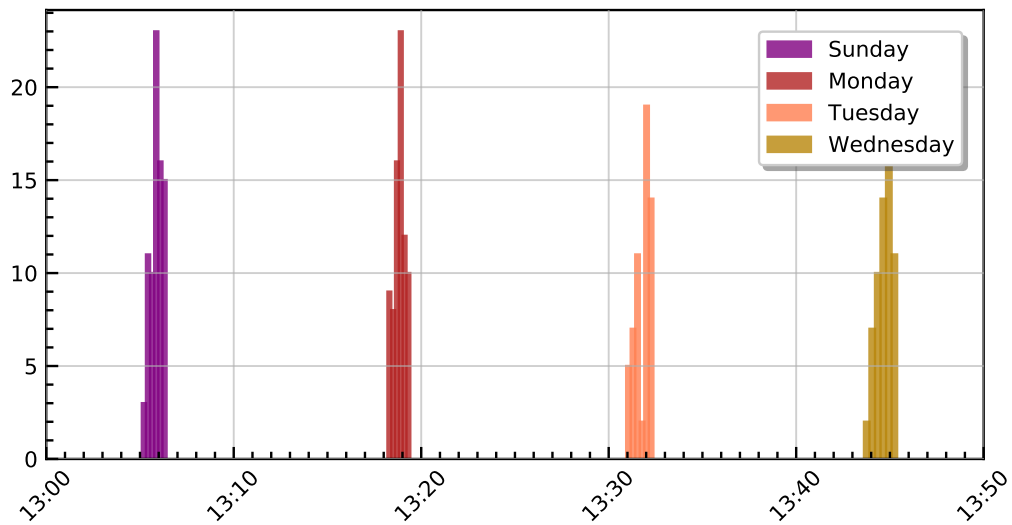


**(b)** secondary beam

**Figure 6.7.:** Histograms of the times at which the Aeolus beam crosses the latitude of 39.29°, which is the average latitude of the three FD-stations of Telescope Array. The data corresponds to the descending lines in figure 6.6. The relevant day for the main beam (a) near Telescope Array is Wednesday, which has a passage time of around 13:44 UTC. For the secondary beam (b) Tuesdays is of interest, which corresponds to a passage time of around 13:31 UTC.
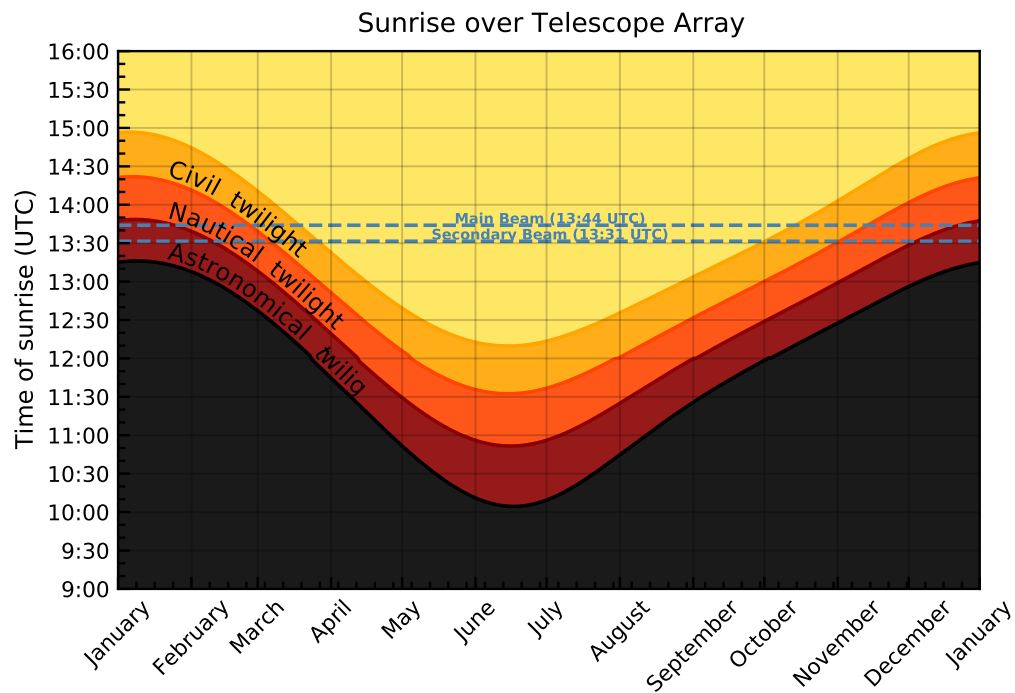
**Figure 6.8.:** Time of sunrise over Telescope Array. Plotted are the different stages of twilight as well as the passage time of main and secondary beam. The passage time is at all times at earliest during astronomical twilight, making it challenging to detect the laser in Telescope Array. The best chance would be a detection of the secondary beam during January, if a measurement during astronomical twilight can be accomplished.

# 7. Simulation and Reconstruction of the Aeolus Laser

After predicting when and where the Aeolus lasers can be measured by the Fluorescence Detectors, now the possibilities of reconstructing these events from the measured data will be discussed. This reconstruction includes on the one hand the laser geometry, meaning the position and direction of a laser beam. On the other hand also the laser energy can be obtained from the data. An evaluation of the reconstruction techniques can be done by simulating laser shots with known properties and reconstructing them afterwards. The reconstruction and simulation of the measured laser shots is done with the software framework $\overline{\text{Off}}\underline{\text{line}}$.

## 7.1. Reconstruction of the Laser Geometry

The first part of the reconstruction is the evaluation of the laser geometry. This includes the arrival direction of the laser beam as well as the ground position of each shot, forming the tracks that were predicted in the previous chapter.

### 7.1.1. Principle of the Geometry Reconstruction

The Aeolus laser beam becomes visible to the FDs through scattering in the atmosphere. As the laser traverses the air near the observatory it scatters on air molecules and aerosols. Some of the scattered light finds its way to the telescopes, leaving a trail of activated pixels in the camera, as shown in figure 7.1. This line of pixels is the basis for the geometry reconstruction.

**Monocular Reconstruction**

If one event is only seen by a single telescope, a monocular reconstruction of the geometry has to be done. This applies to most of the Aeolus events, as will be discussed in section 7.3.2.1. The geometry reconstruction for mono-events happens in two steps, as described in [33]. First the shower detector plane (SDP) is determined. This is the plane which is spanned by the laser axis and the position of the telescope. A visualization can be seen in figure 7.2. The plane has two free parameters which can be determined by a two parameter fit. Basis for the fit is the signal in the camera. Each pixel corresponds to a pointing direction, the intersection of the shower detector plane with the camera is given by a line of activated pixels. The fit can be performed using the pointing direction and amplitude of the signal for each measurement point, minimizing the scalar product of the plane normal and pixel directions, weighted by the detected signal.

The second step in the geometry reconstruction is to determine the position and direction of the laser beam within the shower detector plane. For this, the arrival times $t_i$ of the

**(a)** Coihueco
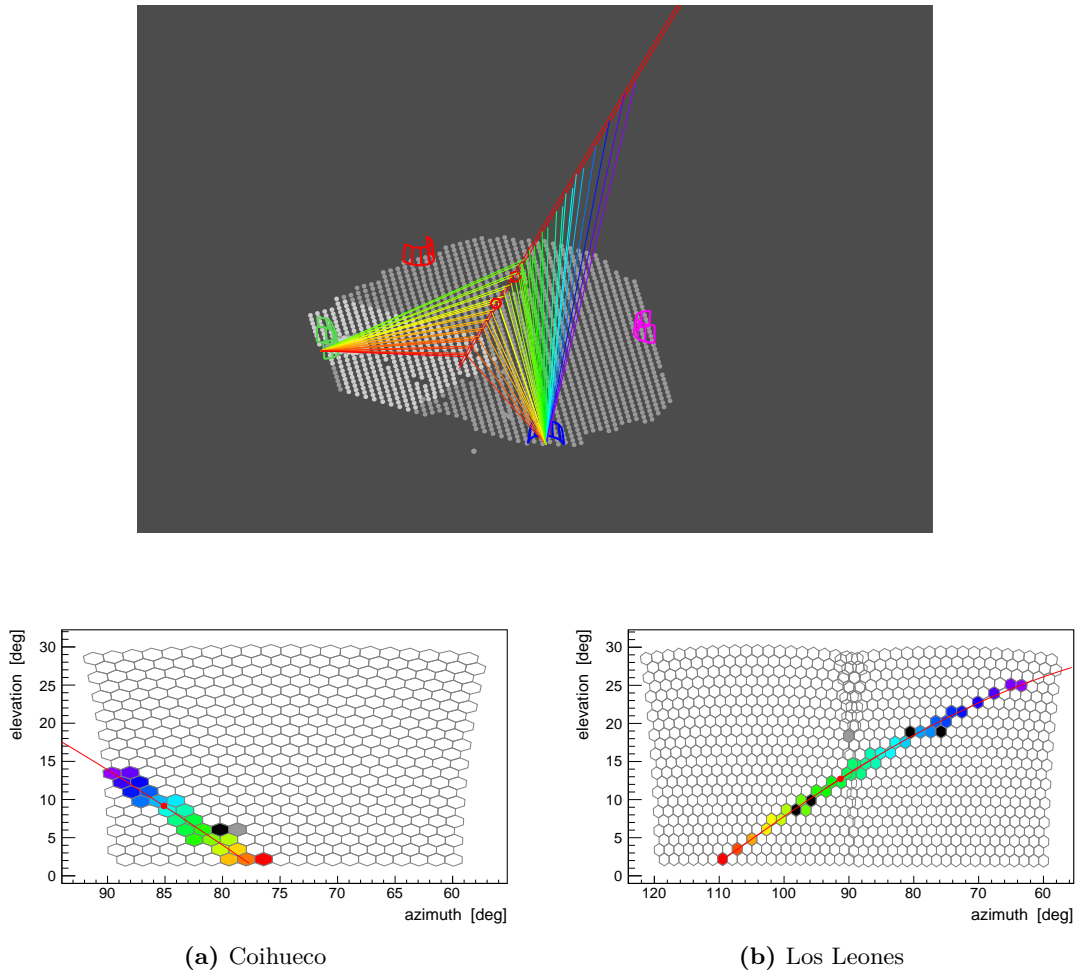


**(b)** Los Leones

**Figure 7.1.:** Example of one measured secondary beam stereo event. The top plot shows a three-dimensional visualization of the reconstructed laser axis. The beam was detected by Coihueco and Los Leones. The bottom plots show the corresponding camera images. Pixels with signal are colored with the color indicating the signal time. The red line marks the fitted shower detector plane. (Auger Event Id 192207903687)
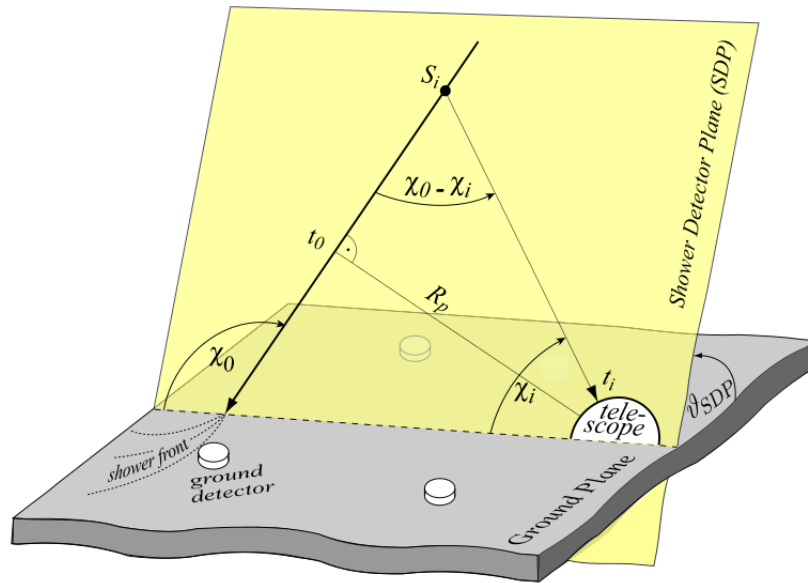
**Figure 7.2.:** Sketch describing the monocular reconstruction. First step is the determination of the shower detector plane (yellow). The angle within the SDP $\chi_0$ is determined in a 3-parameter-fit, together with the impact parameter $R_p$ and the according time $t_0$. Each pixel has a pointing direction given by $\chi_i$ and a signal time $t_i$, allowing for a fit to determine these three geometric parameters. From [60]

signals at the pixels are used. The arrival time of light reaching the detector for each pixel with signal is

$$t_i = t_0 + \frac{R_p}{c} \tan\left(\frac{\chi_0 - \chi_i}{2}\right) \ , \tag{7.1}$$

where $R_p$ is the closest distance to the laser beam (the impact parameter), $t_0$ is the time at the detector corresponding to the closest distance, $\chi_0$ is the angle of the laser to the horizontal within the shower detector plane, and $\chi_i$ is the elevation angle corresponding to the $i$-th pixel. Using the timing information of each pixel, a three parameter fit for $t_0$, $R_p$ and $\chi_0$ can be performed.

While for the reconstruction of the shower detector plane a fairly good resolution is achieved (0.2° [34]), the result of the three parameter fit within the SDP depends on the range of elevation angles that is fitted over. If all the elevation angles are within a small range, then the fit will not be able to yield a very precise resolution. For air showers the monocular reconstruction can be improved by including data from the surface detectors (hybrid events). The additional constraint of time and position of the SD-station improves the fit of the missing geometry parameters. This can however not be utilized for the Aeolus laser, as the surface detectors are not triggered by the laser beam.

The laser beam geometry is completely determined with the parameters described above. For the further investigations, however, we will look at an alternative set of parameters. Because of a more intuitive understanding and comparability to the Aeolus geometry, the zenith angle $\theta$ and the azimuth angle $\phi$ are used as non-local parameters, to describe the laser direction, and the ground position relative to the center of the array is used to describe the laser impact points.
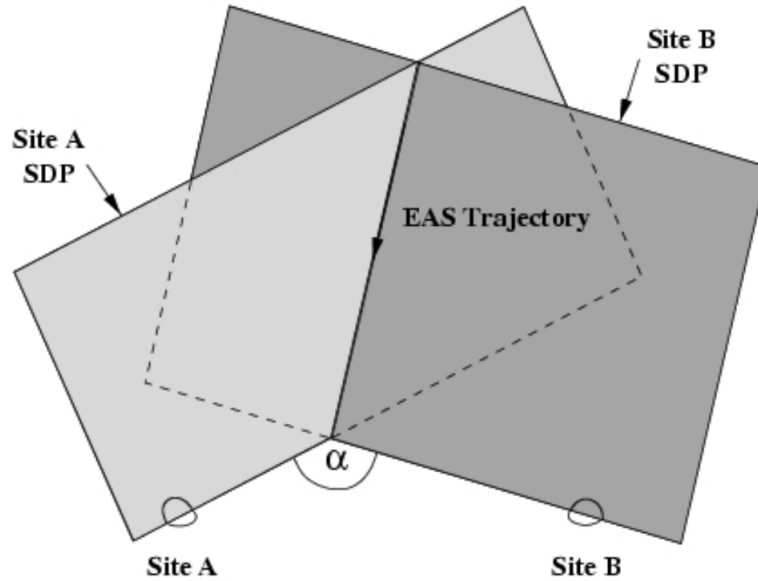
**Figure 7.3.:** Sketch of the stereo reconstruction. The laser axis is given by the intersection of one or more shower detector planes. Therefore the event must be seen by multiple eyes at once. From [61]

### Stereo Reconstruction

If one event is seen by multiple detectors, the reconstruction of the geometry is simplified. In this case the laser axis is directly given by the intersection of the two (or more) shower detector planes.(see figure 7.3). This also increases the precision of the laser direction measurement, since the SDP can be more precisely reconstructed than the obtained angles of a pure monocular reconstruction.

However, in practice only a small fraction of the measured Aeolus events are actually stereo-events, making the stereo reconstruction only partially usable. The reason is the dead-time of the fluorescence detector. Due to the high frequency of Aeolus events, not all laser shots can be processed by all telescopes. As a result, many events are only registered by one telescope, even though they are in visible range of other FD stations as well.

### 7.1.2. Monocular Reconstruction with Fixed Angles

Due to the small fraction of stereo events, a reconstruction of the laser ground track can only be achieved if the monocular events are used. The quality of the monocular reconstruction can however be improved, if the arrival direction of the laser beam is already known.

The first step therefore is to determine the laser geometry. This can be done applying the methods described above, utilizing especially the stereo events where possible. The result will be shown in section 7.3.2.1. If the geometry is known, the laser direction can be used as an input for the geometry reconstruction. By constraining the angles to the predetermined values, only the ground position remains to be determined, resulting in a more precise reconstruction of the laser ground tracks. For this purpose we set a fixed value for the zenith and azimuth angle in the reconstruction module `HybridGeometryFinderWG` [62]. Despite its name, this module can also reconstruct events without hybrid information. However, instead of the usual local parameters introduced above (SDP-angles, $R_p$, $t_0$, $\chi_0$), this module fits the global parameters (ground position, $\theta$, $phi$), making it ideal for this
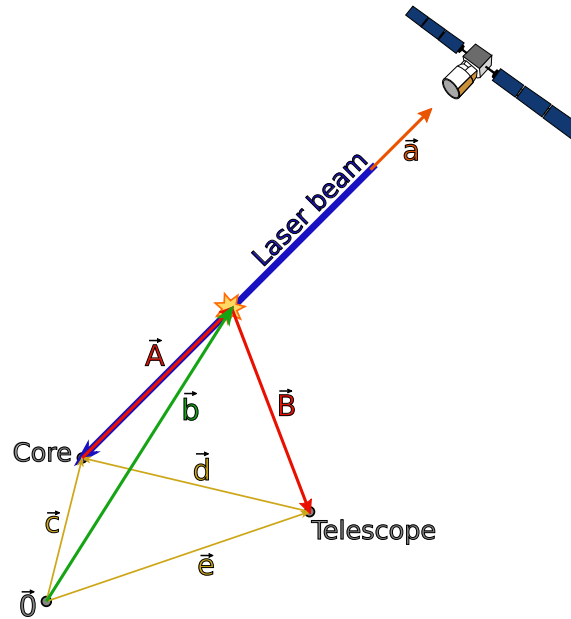
**Figure 7.4.:** Sketch of the geometric considerations for the calculation of the beam positions along the trace. The laser arrives from above, the axis $\vec{a}$ points to the laser origin. Goal is the calculation of the vector $\vec{b}$ which points to the scattering position within the laser beam. $\vec{0}$ is the origin of the coordinate system.

application. The result of using fixed angles in the monocular reconstruction will be shown in section 7.3.

## 7.2. Reconstruction of the Laser Energy

As the laser traverses the atmosphere, it scatters many times along the beam. The measurement of one laser shot as shown above consists thus of many individual measurement points along the laser beam, for each of which the photon flux at the detector is measured, as well as the signal time. The original laser beam energy can be calculated from each of these measurement points. The combination of all points of one laser beam or even one complete laser transition through the observatory can be used to investigate the energy of the Aeolus laser beams. The principle of the energy reconstruction is based on the work described in [63] for a CLF-energy measurement and are extended for a usage with the Aeolus-lasers.

### 7.2.1. The Beam Positions Along the Trace

Requirement for the reconstruction of the laser energy is, that the scattering positions along the laser beam are known. These positions can be derived from the timing information of each measurement point.

The subsequent calculations of the beam positions follow the evaluation of the aforementioned work in [63], where the CLF-case of a from the ground up-moving laser beam was considered. Although the calculation is independent from the direction of the laser, in practice it turned out, that the existing implementation did not work for a down-moving case. Therefore we carefully reformulated the geometrical calculation, as shown in the following, and re-implemented the algorithm to be applicable to both up- and down-moving lasers. The naming conventions of the original calculation were adopted.

Figure 7.4 shows the geometry of the following considerations. The laser beam arrives slanted from above, $C$ marks the ground position. The laser axis is given by the unit vector

$\vec{a}$. By convention this vector points to the origin of the laser, thus from the ground upwards. Ground position and laser direction are obtained by the geometry reconstruction described before.

The vector $\vec{b}$ points to the wanted point along the beam, where the scattering occurs. This point is obtained by moving from the ground position $\vec{c}$ a certain distance $k$ along the beam axis $\vec{a}$, thus

$$\vec{b} = \vec{c} + k \cdot \vec{a} \ . \tag{7.2}$$

To obtain the distance $k$, the time difference $\Delta t$ is considered, which describes the duration between the scattered light reaching the telescope and the laser beam reaching the ground position. This difference can be expressed through the length of the paths from the scattering point to the telescope ($\vec{B}$) and from the scattering point to the ground position $(-\vec{A})$[1]

$$\Delta t = \frac{|\vec{B}|}{c} - \frac{|\vec{A}|}{c} \tag{7.3}$$

with the speed of light $c$. $\vec{B}$ can be expressed by the vector pointing to the telescope $\vec{e}$ and the scattering point $\vec{b}$

$$\vec{B} = \vec{e} - \vec{b} = \vec{e} - \vec{c} - k \cdot \vec{a} \tag{7.4}$$

and the length of $\vec{A}$ is simply the distance $k$. Using also that $\vec{e} = \vec{c} - \vec{d}$, one obtains

$$\begin{aligned} c\Delta t = |\vec{B}| - |\vec{A}| = |\vec{e} - \vec{c} - k\vec{a}| - k \\ = \left| -\vec{d} - k\vec{a} \right| - k \\ = \left| \vec{d} + k\vec{a} \right| - k \end{aligned} \tag{7.5}$$

Rearranging and squaring then leads to

$$\begin{aligned} (c\Delta t + k)^2 &= \left( \vec{d} + k\vec{a} \right)^2 \\ \Leftrightarrow \quad c^2\Delta t^2 + k^2 + 2kc\Delta t &= d^2 + k^2 + 2k\vec{d}\vec{a} \\ \Leftrightarrow \quad k \left( 2\vec{d}\vec{a} - 2c\Delta t \right) &= c^2\Delta t^2 - d^2 \\ \Leftrightarrow \quad k &= \frac{c^2\Delta t^2 - d^2}{2 \left( \vec{d}\vec{a} - c\Delta t \right)} \ . \end{aligned} \tag{7.6}$$

With the distance $k$ determined, the beam position is then

$$\begin{aligned} \vec{b} &= \vec{c} + \frac{c^2\Delta t^2 - d^2}{2 \left( \vec{d}\vec{a} - c\Delta t \right)} \cdot \vec{a} \\ &= \vec{c} - \frac{d^2 - c^2\Delta t^2}{2 \left( \vec{d}\vec{a} - c\Delta t \right)} \cdot \vec{a} \ . \end{aligned} \tag{7.7}$$

The reason for the minus-shift in the second line is to match the formula to the up-moving case. For an up-moving laser beam two considerations are different. On the one hand the laser axis points in the opposite direction, thus the sign of $\vec{a}$ in equation (7.2) is reversed. On the other hand the time difference $\Delta t$ is the sum of the travel times along $\vec{A}$ and $\vec{B}$, rather than the difference as written in equation (7.3). Those two sign changes however cancel each other out, meaning the result obtained in equation (7.7) is valid for both an up- and down-moving laser beam.

---

[1]The direction that the light travels does not follow the vector $\vec{A}$ but instead $-\vec{A}$. The direction of this vector was kept for reasons of consistency.
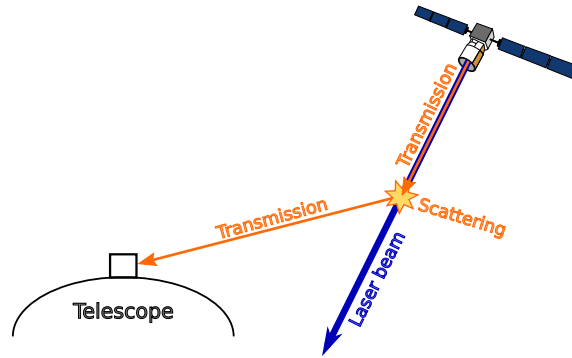
**Figure 7.5.:** Sketch of the light path from the satellite to the telescope.

### 7.2.2. Atmospheric Transmission and Scattering

Starting point for the calculation of the laser energy is the light flux at the telescope. This light flux is what remains of the laser light after transmission and scattering in the atmosphere. First the laser light has to traverse the atmosphere up to the point where it scatters on air molecules or aerosols. During this transmission the amount of light is attenuated, since some of it gets scattered away and will not be detected[2]. Then some of the light gets scattered in the right direction, so that it will be detected by a telescope. The scattering amplitude is thereby dependent on the angle relative to the laser beam direction. And finally, not all of the scattered light survives the transmission to the telescope, some will also be scattered away. This light path is also illustrated in figure 7.5.

To reconstruct the original laser energy, one therefore needs to calculate the attenuation of the light by Transmission $\times$ Scattering $\times$ Transmission, and apply it backwards to the amount of light at the telescope. As also described in [63], the number of detected photons for each measurement point along the beam is

$$N_{\gamma,i} = c_{\text{atm},i} \cdot N_{\gamma,0} \tag{7.8}$$

where $N_{\gamma,0}$ is the original number of photons, emitted by the Aeolus laser, and $c_{\text{atm},i}$ is the factor of each measurement point, that describes the attenuation in the atmosphere. The attenuation factor is calculated as

$$c_{\text{atm}} = T_{1,\text{R}} \cdot T_{1,\text{M}} \cdot T_{2,\text{R}} \cdot T_{2,\text{M}} \cdot (S_{\text{R}} + S_{\text{M}}) \cdot \varepsilon \ . \tag{7.9}$$

Here $T_{1,\text{R}}$ and $T_{1,\text{M}}$ are the transmission factors for Rayleigh- and Mie-scattering for the first segment of the travel path, from the satellite to the point of scattering. $T_{2,\text{R}}$ and $T_{2,\text{M}}$ are the according factors for the second segment from the point of scattering to the telescope. The factor $(S_{\text{R}} + S_{\text{M}})$ are the added scattering probabilities for Rayleigh- and Mie-Scattering and $\varepsilon$ is the wavelength dependent efficiency of the telescope.

The atmospheric coefficient and therefore the transmission- and scattering factors have to be calculated for every measurement point along the laser beam. The calculation of the scattering position is needed to evaluate the attenuation for the two travel segments up to this point and from this point to the telescope. For the calculation of the scattering factor additionally also the scattering angle has to be known. This angle is given by the vector pointing from the telescope to the scattering point ($-\vec{B}$ in the sketch) and the laser axis $\vec{a}$. The angle between these two vectors is also the scattering angle.

With the atmospheric coefficient determined, the laser energy and the signal at the telescope can be put into relation. To reconstruct the energy of one laser shot, two approaches were investigated. The first approach is to calculate the weighted mean energy of all measurement points, the second approach is to use a likelihood fit of the laser energy.

---

[2]Multiple scattering is hereby neglected.
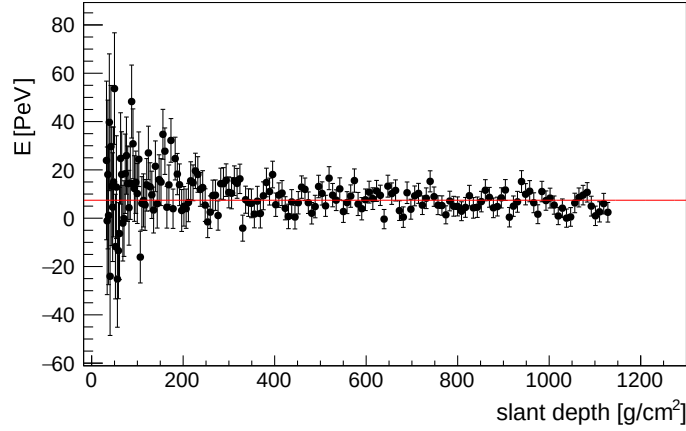
**Figure 7.6.:** The individual measurements of the laser energy $E_0$ of one event. For each measurement point along the laser beam, $E_0$ can be calculated. The red line marks the weighted mean energy of 7.46 PeV. (Coihueco, Auger Event Id 192207903203)

### 7.2.3. The Weighted Mean Beam Energy

According to (7.8), the laser energy can be calculated from the measured number of photons for each measurement point $N_{\gamma,i}$ as

$$E_0 = \frac{hc}{\lambda} \cdot \frac{N_{\gamma,i}}{c_{\mathrm{atm},i}} \ , \tag{7.10}$$

with the laser wavelength $\lambda$ and the energy per photon $\frac{hc}{\lambda}$. This calculation can be done for every measurement point along the beam, each with a different $N_\gamma$ and $c_{\mathrm{atm}}$. All of these calculated energies can be combined by building the weighted mean. Therefore also the uncertainty of each energy measurement is used. The weighted mean energy is then

$$\overline{E} = \frac{\sum_i w_i \cdot E_i}{\sum_i w_i} \tag{7.11}$$

with the energy $E_i$ of each measurement and the weight $w_i$, which is obtained from the uncertainty of the energy $\sigma_i$.

$$w_i = \frac{1}{\sigma_i^2} \tag{7.12}$$

$\sigma_i$ itself is calculated similarly as the energy from the uncertainty of the number of photons

$$\sigma_{E,i} = \frac{hc}{\lambda} \cdot \frac{\sigma_{N_\gamma,i}}{c_{\mathrm{atm},i}} \ . \tag{7.13}$$

Figure 7.6 shows an example of the many measurements of $E_0$ along one laser beam, with the calculated weighted mean.

The disadvantage of this approach is, that for far-away laser tracks, the signal per time bin is very small and difficult to discern from the background noise of the night sky. As a consequence, the energies calculated from a low photon count are scattered over a wide range. Even negative values are possible, due to the subtraction of the background photons from the signal. This can cause problems, when calculating the uncertainty of an energy value, and with it the weighting factor. If the Poissonian nature of the background and signal is not properly taken into account, the negative energy values are weighted too heavily. The result is a bias towards lower energies, which is especially present for larger telescope-laser-distances. An example of this bias can be seen further below in figure 7.8, where the energy reconstruction is tested with simulations.

### 7.2.4. Likelihood Fit of the Laser Energy

The bias of the weighted mean can be avoided by calculating the energy using a likelihood fit. Therefore the scattering position along the beam are calculated as before, and with them the atmospheric attenuation $c_{\mathrm{atm},i}$ for each measurement point. However, instead of reconstructing the energy from the number of photons at the telescope, now inversely the expected number of photons is calculated for a test value of the energy. By scanning over a range of energies, for each tested energy the expected number of photons at the aperture is given by rearranging equation (7.10) to

$$N_{\gamma,i} = E \cdot c_{\mathrm{atm},i} \cdot \frac{\lambda}{hc} \ , \tag{7.14}$$

which can be evaluated for every measurement $i$ along the laser beam. To compare the signal expectation for the tested energy to the measured signal, the number of photons is converted into the number of photo electrons created in the photo multiplier tubes. The photons at the aperture and the number of photo-electrons are related by the optical efficiency of the telescopes, which includes the filter transmissivity, mirror reflectivity and the quantum efficiency of the photomultiplier tubes. Overall this amounts to a factor of $\sim 0.1$. The number of photo electrons is thus obtained by multiplying the photon number with this proportionality factor and adding a number of background electrons.

The likelihood function is based on a Poisson distribution around the expected number of photo electrons at the photocathode $N_{\mathrm{exp}}$

$$f_{\mathrm{P}}\left(k, N_{\mathrm{exp}}\right) = \frac{N_{\mathrm{exp}}^{k}}{k!} \cdot \mathrm{e}^{-N_{\mathrm{exp}}} \ , \tag{7.15}$$

which gives the probability of measuring $k$ photo electrons, on the condition that $N_{\mathrm{exp}}$ describes the number of created photo electrons. This number of electrons is subsequently increased by the photomultiplier tube. Here the initial photo electrons, released by the incoming photons, are accelerated in a cascade of dynodes. In each step the accelerated electrons release several new electrons on impact, which then also are accelerated to the next dynode. The overall gain of electrons in the photomultiplier tube is itself a statistical process, which has to be considered in the likelihood calculation. The spread of the number of created electrons at the anode of the photomultiplier tube can be described by an additional Gaussian distribution

$$f_{\mathrm{G}}\left(k, N_{\mathrm{obs}}\right) = \frac{1}{\sqrt{2\pi\sigma_{G}^{2}}} \cdot \exp\left(-\frac{(k - N_{\mathrm{obs}})^{2}}{\sigma_{G}^{2}}\right) \ , \tag{7.16}$$

around the number of observed photo electrons $N_{\mathrm{obs}}$, with a gain variance of $\sigma_{G}^{2}$. The combined probability is obtained by multiplying the Poisson and Gauss distribution:

$$f(k, N_{\mathrm{exp}}, N_{\mathrm{obs}}) = f_{\mathrm{P}}\left(k, N_{\mathrm{exp}}\right) \cdot f_{\mathrm{G}}\left(k, N_{\mathrm{obs}}\right) \tag{7.17}$$

The likelihood value for one measurement point is finally given by summing over the possible values of $k$

$$\begin{aligned} L_i &= \sum_{k} f(k, N_{\mathrm{exp},i}, N_{\mathrm{obs},i}) \\ &= \frac{1}{\sqrt{2\pi\sigma_{G}^{2}}} \sum_{k} \frac{N_{\mathrm{exp},i}^{k}}{k!} \cdot \exp\left(-N_{\mathrm{exp},i}\right) \cdot \exp\left(-\frac{(k - N_{\mathrm{obs},i})^{2}}{\sigma_{G}^{2}}\right) \ . \end{aligned} \tag{7.18}$$

This can be calculated for every measurement point $i$ along a beam, the total likelihood is then obtained by multiplication[3] of the individual terms

$$L = \prod_i L_i \ . \tag{7.19}$$

The parameter that went into the likelihood calculation was the number of expected photo electrons $N_{\mathrm{exp}}$ for each point, which itself was calculated from an energy value $E$. Thus by scanning over an energy range and calculating the likelihood for each energy, the best fit energy is obtained by searching for the maximum likelihood value.

This likelihood scan over all measurements of one laser shot while using one value for the energy is possible, since the true laser energy is constant throughout the beam. The energy can be reconstructed for all measurement points along a beam, as shown above, but in an ideal scenario all of these measurements should yield the same result. An even stricter constraint on the energy is possible when looking at all laser shots of one transition simultaneously. Since the laser energy also does not change while the laser beam is traversing the observatory, a similar likelihood fit can be done including the measurements of all Aeolus events of one transition. The possibility of using this for aerosol studies is discussed in chapter 8.

### 7.2.5. Simulation Study of the Reconstruction Methods

Using simulated laser shots, a qualitative test of the different energy reconstruction methods can be done. The simulation of laser events is also done in $\overline{\mathrm{Off}\underline{\mathrm{line}}}$, which provides a framework to calculate the detector response of a laser beam with specified properties. To evaluate the approach of the weighted mean energy of each laser shot, a simulation of 400 laser shots was done. These shots were simulated going straight downwards and are evenly spaced throughout the observatory, placed in a $20 \times 20$ grid, covering[4] $54 \times 62\,\mathrm{km}^2$. The simulation was done using three different beam energies of $4\,\mathrm{mJ}$, $8\,\mathrm{mJ}$ and $16\,\mathrm{mJ}$.

For each laser shot the energy is calculated many times along the beam, according to the earlier description of the energy reconstruction. All these individual energies are plotted in figure 7.7, as a function of the distance between laser and telescope[5]. The earlier predicted spread of the energy values thereby becomes visible. For larger distances between laser and telescope the range of measured energies increases, including also negative values. This spread around the simulated value gets also larger with higher energies.

The consequence for the energy reconstruction based on the weighted mean becomes apparent when plotting the reconstructed energy of each beam against the distance, as done in figure 7.8a. The larger the distances, the more the reconstructed energies tend to be shifted towards lower energies. Reason is as discussed above the favoring of lower energies due to a higher weighting. This can be validated by simply calculating the arithmetic mean of the energy points and neglecting the weighting completely. For comparison the arithmetic mean can also be seen in figure 7.8b. Here the reconstructed energies stay closer to the simulated value for larger distances.

To test the performance of the likelihood approach, the same simulated data is now reconstructed using the likelihood fit described above. The result is shown in figure 7.9 (this time only for an energy of $8\,\mathrm{mJ}$ or $50\,\mathrm{PeV}$). The likelihood fit seems to work out better

---

[3]for numerical reasons in practice rather the natural logarithm of the likelihood is summed.

[4]as borders of the grid the positions of the four FD-stations were taken.

[5]As a measure of the distance here the value $R_p$ was used, which is the closest distance between laser beam and telescope (see also figure 7.2). This is not the exact distance between each measurement point and the telescope, but rather the lower limit of the distance within each beam, since the simulated beams are vertical in this scenario. It suffices however as an approximation for this demonstration.
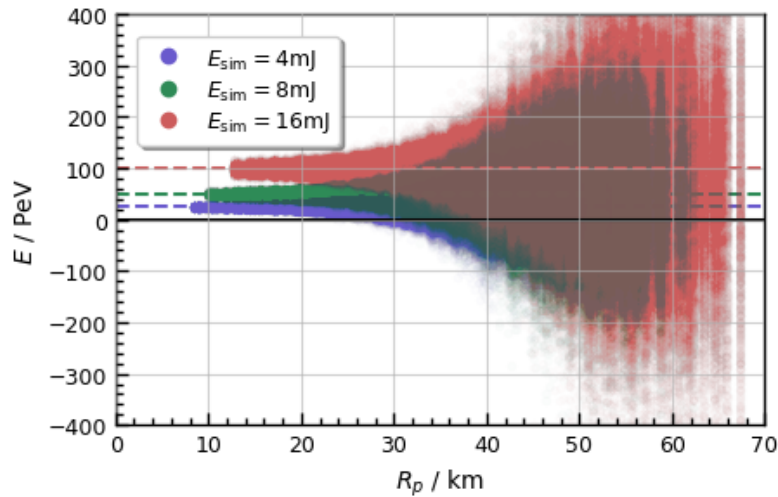
**Figure 7.7.:** Scatter plot of all individual energy reconstructions along each laser beam, using the simulation of 400 vertical laser shots of three different energies. The simulated energies are indicated by the dashed lines in the corresponding color. For larger distances the measure energies tend to spread over a large range, including negative values.



**(a)** Weighted mean energy

**(b)** Arithmetic mean energy
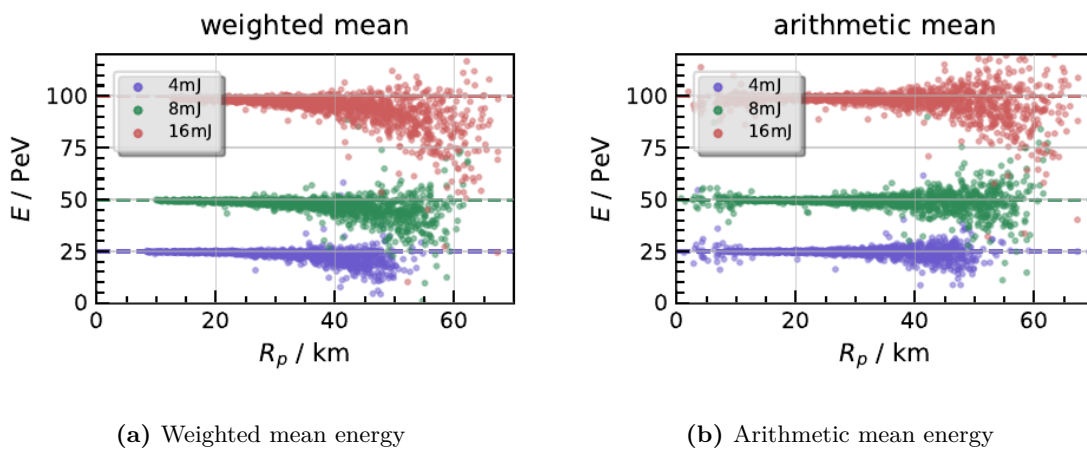
**Figure 7.8.:** Comparison of the energy reconstruction using the weighted mean and a simple arithmetic mean, based on the simulation of 400 vertical laser shots of three different energies. The simulated energies are indicated by the dashed lines. The weighted mean approach results in a drop of the energy for larger distances. The bias caused by the weighting can be confirmed by comparing the situation to a simple arithmetic mean of the energies.
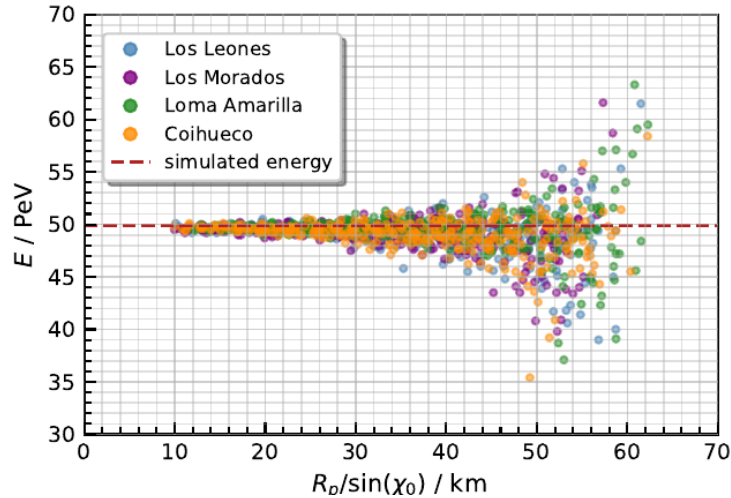
**Figure 7.9.:** Reconstructed energies using a likelihood fit for the simulation of 400 vertical laser shots. The simulated energy of 8 mJ is marked by the dashed line.

than the weighted mean, the energies do not have an increasing shift to lower values for larger laser-telescope-distances. However, a small overall bias towards lower energies is also present in this method. This becomes more apparent, when examining slanted laser shots, which are closer to the actual case.

Therefore the exact same simulation was also done with laser shots arriving from east under a zenith angle of 60°, similar to the measured secondary beam zenith angle as discussed later. The results are shown in figure[6] 7.10. To get even closer to the actual case, also the beam energy and position can be adjusted. For the energy a value of 6.52 PeV or approximately 1 mJ was chosen, based on an estimation of the secondary beam energy. Also the beam positions were changed, now instead of an evenly spaced grid the laser shots were simulated at the locations, where shots were measured during the transition on 9th August 2019 (see also the following chapter). This simulates the case of a secondary beam transition reasonably close. The result of this simulation can be seen in figure 7.11.

In both of these two simulations, the slanted grid simulation and the realistic case, the reconstructed energy has a bias of approximately 5% towards lower energies. This is also an indication for the limits of an energy reconstruction using this method. The consequences are also visible in the atmospheric studies as shown in chapter 8. At this point, the origin of this bias is unclear. It could be a bias of the estimator itself in the limit of low Poisson statistics. Or it is an effect of an inconsistency between the atmospheric and detector-efficiency used in the simulation and reconstruction. As long as the origin of the bias is unknown, it needs to be taken into account when quoting the systematic uncertainties of the laser reconstruction.

## 7.3. Reconstructed Properties of the Aeolus Laser Beams

After discussing the methods of reconstructing different properties of the laser beam, these methods will now be applied to the data.

### 7.3.1. Transition Time

The first step of reconstructing the laser properties from the FD data is to identify nights where an Aeolus transition is visible, and to isolate the Aeolus events from the rest of the

---

[6]The measure of the distance is now also normalized by $\sin(\chi_0)$, which is the angle of the laser axis within the shower detector plane, due to the slanted laser beams.
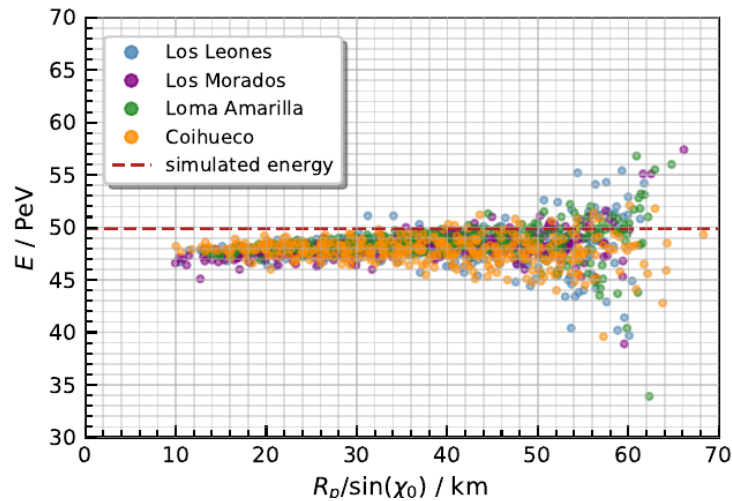
**Figure 7.10.:** Reconstructed energy using the likelihood fit. Base is the simulation of 400 slanted laser shots with a zenith angle of $60°$, distributed on a regular grid of $54 \times 62\,\text{km}^2$, centered on the observatory. The simulated laser energy of $8\,\text{mJ}$ is marked by the dashed line.
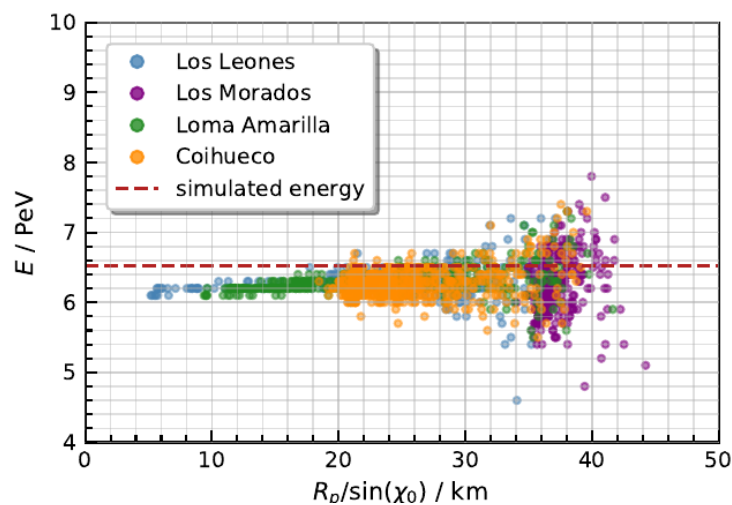


**Figure 7.11.:** Reconstructed energies of a simulated transition of the secondary beam through the observatory, using a likelihood fit. The events were simulated using an energy of $6.52\,\text{PeV}$ and at the positions of measured laser shots during one transition. The different eyes (distinguished by color) have different ranges of distances to the laser beam (see also section 7.3.2.2).

**Table 7.1.:** Date and time of the measured Aeolus transitions. The time interval between $t_{\text{start}}$ and $t_{\text{end}}$ marks the chosen limits for a selection of Aeolus events. $t_{\text{exp}}$ is the expected crossing time derived from TLEs. All times are UTC. The upper half of the table corresponds to secondary beam transitions on Fridays, the lower half to main beam transitions on Saturdays.

| Date | $t_{\text{start}}$ | $t_{\text{end}}$ | $t_{\text{exp}}$ |
|---|---|---|---|
| 31.05.2019 | 9:57:00 | 9:58:00 | 09:57:24 |
| 07.06.2019 | 9:57:15 | 9:57:35 | 09:57:32 |
| 28.06.2019 | 9:57:00 | 9:57:30 | 09:57:26 |
| 05.07.2019 | 9:55:25 | 9:57:25 | 09:57:31 |
| 02.08.2019 | 9:56:55 | 9:57:13 | 09:57:18 |
| 09.08.2019 | 9:57:03 | 9:57:18 | 09:57:22 |
| 01.05.2020 | 9:56:40 | 9:57:00 | 09:56:58 |
| 22.05.2020 | 9:56:10 | 9:56:40 | 09:56:29 |
| 29.05.2020 | 9:56:10 | 9:57:20 | 09:57:00 |
| 26.06.2020 | 9:56:35 | 9:56:53 | 09:56:57 |
| 17.07.2020 | 9:55:30 | 9:56:02 | 09:55:55 |
| 24.07.2020 | 9:56:30 | 9:57:12 | 09:56:49 |
| 29.06.2019 | 10:10:10 | 10:10:28 | 10:10:21 |
| 06.07.2019 | 10:10:00 | 10:10:30 | 10:10:25 |
| 03.08.2019 | 10:10:06 | 10:10:30 | 10:10:12 |
| 20.06.2020 | 10:08:07 | 10:09:39 | 10:09:19 |
| 27.06.2020 | 10:09:40 | 10:10:00 | 10:09:45 |
| 18.07.2020 | 10:08:36 | 10:09:15 | 10:08:59 |

data sets of these nights. This is achieved by looking at the timestamp of the events. The transition time determined in section 6.1.3 from TLEs can be used as a starting point for the selection. One laser transition only lasts for several seconds[7]. However, to cover all Aeolus transitions, a conservative time window of 3 min around the nominal times of 10:10 UTC for the main beam and 9:57 UTC for the secondary beam was chosen.

Using these time windows, a targeted search for nights with an Aeolus transition can be done. To this end, for all nights since launch of Aeolus, FD-events within this time window are investigated. An Aeolus transition can be identified by an increased number of FD-events, compared to the rest of the night, and the reconstructed laser positions form a characteristic straight line, as shown in the following chapter. Using this method, so far 18 nights with an Aeolus transition could be identified (between the launch in August 2018 and September 2020). Out of these, 12 correspond to the secondary beam on a Friday and 6 to the main beam on a Saturday. The dates of these nights are listed in table 7.1. All secondary beam nights occurred between May and August, all main beam nights between June and August. This is in good agreement with the expectation based on the results of section 6.1.4. Some of the dates (Fr, 1st May 2020 and Sa, 3rd August 2019) extend into the astronomical twilight, where a FD-measurement is to a limited extend still possible. The Aeolus lasers are however not visible every week within this time interval, since FD-measurements are limited to nights which are not too strongly illuminated by the Moon, which about halves the possible observation nights.

The aforementioned 3 min window still contains many events unrelated to Aeolus. For the reconstruction of the laser properties it is therefore desirable to further refine the time

---

[7]The ground track velocity is 7.2 km/s, the length of the ground-level projection is at most of the order of 100 km, as shown in section 7.3.2.2.
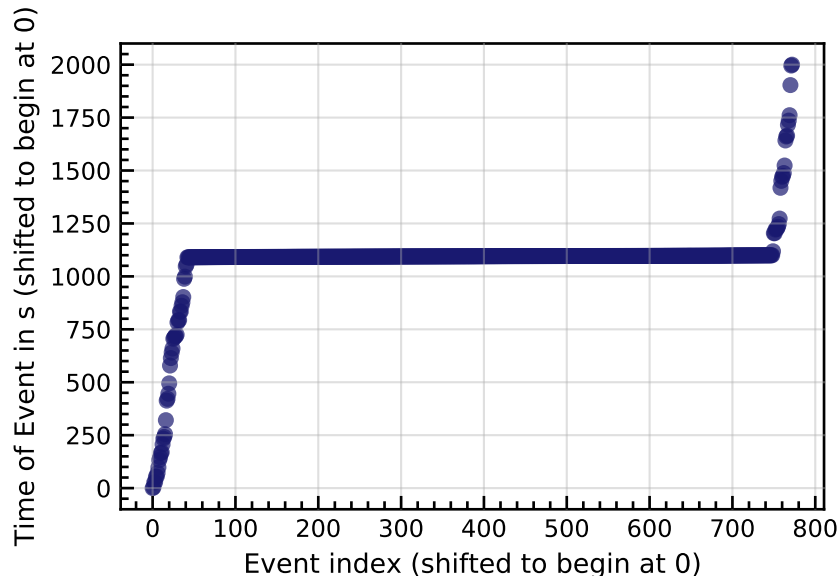
**Figure 7.12.:** Relative time of FD-events. Shown is only a section of one night that includes the Aeolus transition. The timestamps were shifted to start at 0 and are plotted against the event index (also shifted to 0). The Aeolus transition is visible as an almost horizontal line. Comparing to the rest of the night in this interval a lot of events are detected within a short amount of time. This can be used to manually select the time borders of each night, that separate the Aeolus events.

limits. This can be done for each individual day by looking at the timestamps of the events within this window. The transition of Aeolus is visible as an accumulation of many events in short succession, the time difference of $0.02\,\mathrm{s}$ thereby matches the laser pulse frequency of $50\,\mathrm{Hz}$. An example of one night can be seen in figure 7.12. A plot like this one is used for each transition to select only the Aeolus events from the rest of the data set, which results in a slightly different time limit for each individual day. The time limits used for the selection of Aeolus events are also shown in table 7.1, these limits were chosen to be as large as possible, without including non-Aeolus events. Therefore the actual time of transition is not as long as the limits listed there. The such obtained time intervals also confirm the prediction for the transition times, made with TLEs. This predicted time, based on the interpolated laser crossing of a reference latitude (the average latitude of the FD-stations, as explained in the previous chapter), is also listed for comparison in the table. For most of the transitions the TLE-predictions matches nicely with the data time interval. Only few entries deviate by a couple of seconds, which can be explained by the uncertainty of the TLE-positions.

## 7.3.2. Laser Beam Geometry

With the events selected that belong to an Aeolus transition, now the actual reconstruction of the laser properties can be done. Starting point is the reconstruction of the arrival direction.

### 7.3.2.1. Zenith and Azimuth Angle

**Main Beam**

As described in previous chapters, the geometry reconstruction would ideally performed with stereo events, due to the higher precision of the estimated arrival directions. However, this requires a sufficient amount of stereo events. In the case of the main beam, the number
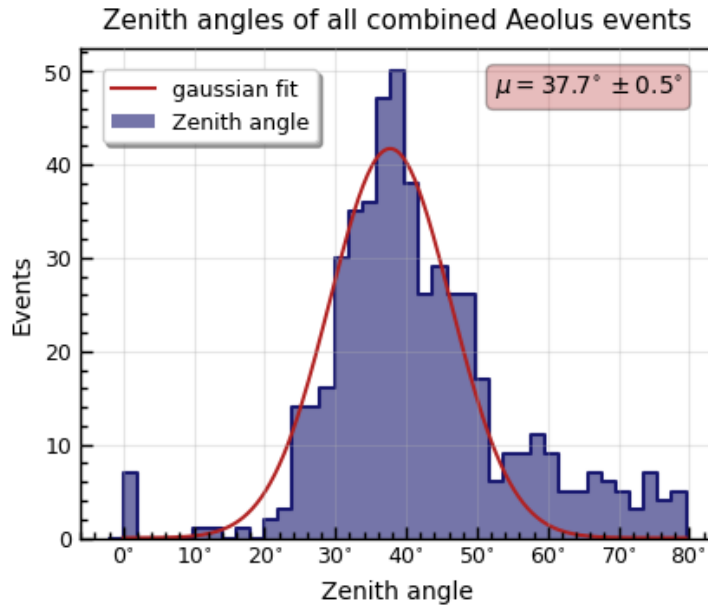
**Figure 7.13.:** Histogram of the zenith angles of the combined main beam events of all six Saturdays. The values are obtained by a monocular reconstruction.

of measured events is relatively low to begin with, let alone the number of stereo events. Reason is the large distance between laser and telescope and the small fraction of the track within the field of view of the telescopes. After the aforementioned time cut, the total number of measured main beam events of all six Saturdays is 510, out of which only 8 are stereo events. To determine the laser geometry of the main beam therefore the monocular reconstruction has to be used. Figure 7.13 shows a histogram of the zenith angle of all main beam events. Due to the monocular reconstruction, the angles are distributed over a wide range. The distribution is also asymmetric with higher angles being favored. To obtain an estimate for the mode of the zenith angle, a normal distribution has been fitted to the histogram. The resulting fitted curve is centered around a zenith angle of 37.7°, with a standard error on the fit parameter of 0.5°.

Figure 7.14 shows the analogue histogram for the azimuth angle, which is spread over an even larger range. Again, a fit of a normal distribution yields a value for the azimuth angle of 348.8° with a standard error of 0.5°. As will be discussed below, these values are in good agreement with the nominal emission angles of the laser beams, as expected by Aeolus.

**Secondary Beam**

The secondary beam has the advantage of passing through the observatory, reaching closer distances to multiple eyes at the same time. The chances of measuring stereo events are therefore higher. Additionally the secondary beam is seen on twice the number of nights as the main beam and the number of events per night is on average also higher. In total the number of secondary beam events of all 12 Fridays is 4648, out of which 262 are stereo events. This allows for an investigation of only the stereo events, if the data of all 12 nights is combined. The resulting histogram of the combined zenith angles is shown in figure 7.15. The angles are withing a relatively small range, compared to a monocular reconstruction. The zenith angle is in this case obtained by averaging the values, resulting in a zenith angle of 58.33° with a standard error of 0.06°.

A similar plot for the reconstruction of the azimuth angle is shown in figure 7.16. The average in this case is 355.4° ± 0.1°.
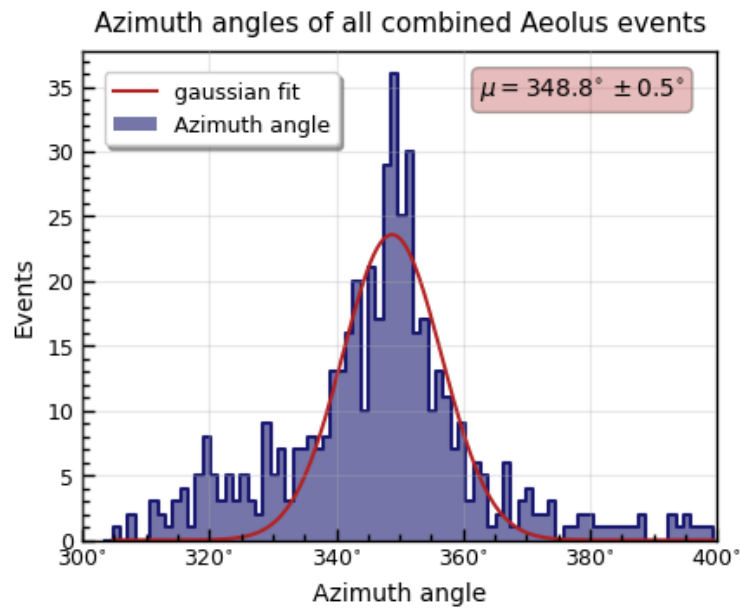
**Figure 7.14.:** Histogram of the azimuth angles of the combined main beam events of all six Saturdays. The values are obtained by a monocular reconstruction.
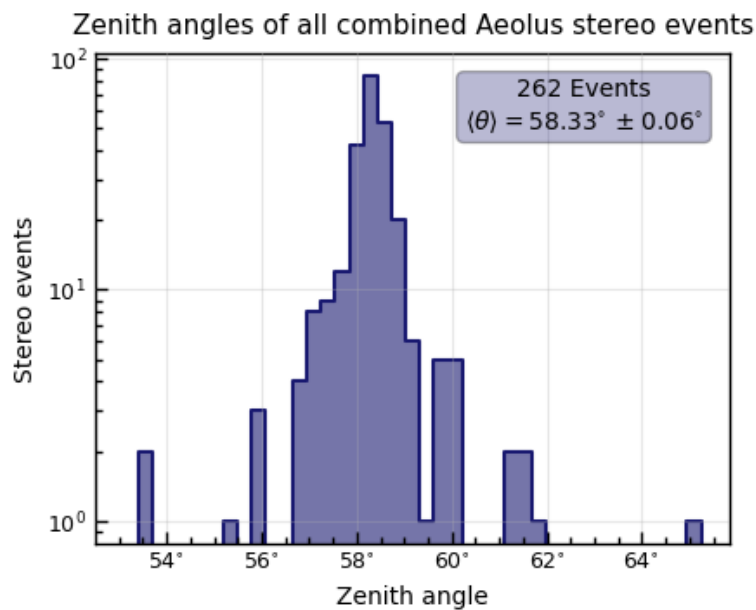


**Figure 7.15.:** Histogram of the zenith angle of all combined secondary beam events. Included are only the stereo events. Note the smaller range in angle on the $x$-axis, compared to figure 7.13.
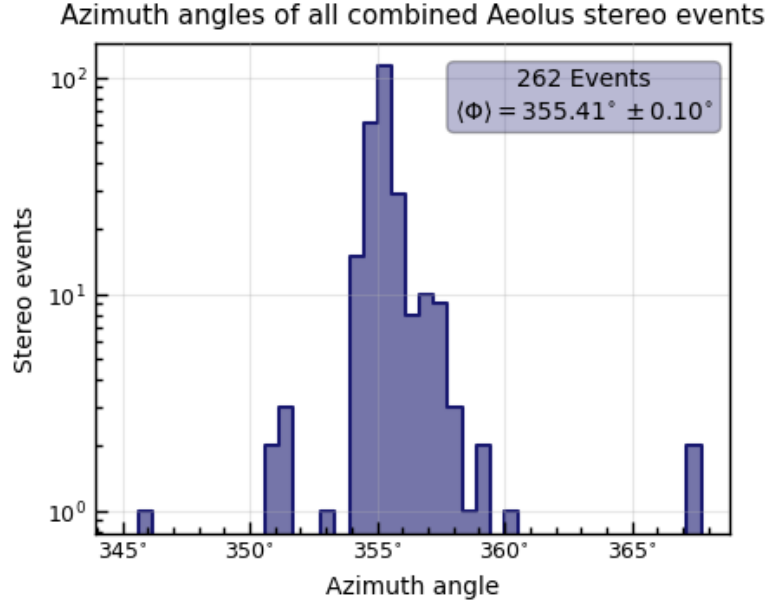
**Figure 7.16.:** Histogram of the azimuth angle of all combined secondary beam events. Included are only the stereo events.

### Relation Between the Laser Emission Angle and the Measured Zenith Angle

With the methods above the zenith angles were determined, under which the Aeolus lasers are measured in the Pierre Auger Observatory. Due to the curvature of Earth this angle does not exactly translate to the emission angle to nadir at the satellite, but is a bit larger. It is therefore interesting to calculate the satellite emission angle based on the measured zenith angles.

Assuming the angle to nadir under which the satellites laser is emitted is $\beta$ and the zenith angle under which the laser beam is measured on Earth is $\theta$ (see the sketch in figure 7.17), then the following relation holds for the zenith angle:

$$\theta = \pi - \gamma = \pi - (\pi - \beta - \alpha) = \alpha + \beta \tag{7.20}$$

In the sketch the side $b$ of the triangle is the Earth radius at the latitude of the Pierre Auger Observatory ($\approx 6371\,\text{km}$) and $c$ is the distance of the satellite from the center of Earth ($\approx 6694\,\text{km}$[8]). The law of cosines gives for this triangle

$$b^2 = a^2 + c^2 - 2ac \cdot \cos(\beta) \quad . \tag{7.21}$$

Solving for $a$ yields the following relation:

$$a = c \cdot \left( \cos(\beta) \pm \sqrt{\cos^2(\beta) - 1 + \frac{b^2}{c^2}} \right) \tag{7.22}$$

Hereby the smaller solution ("-" instead of "+") is of interest, the other solution would be the second intersection of the laser with the surface of Earth. The law of sines additionally gives

$$\frac{\sin(\alpha)}{a} = \frac{\sin(\beta)}{b} \quad , \tag{7.23}$$

---

[8]this value is taken from one sample satellite position. In reality this distance changes not only slightly within one orbit but also over the span of many orbits due to atmospheric drag and gravitational effects. This also forces the satellite to regularly use thrusters to maintain altitude. However, typical changes of this distance between the observed transition are within $7\,\text{km}$, and lead to a change in the observed zenith angle of less than $0.09°$.
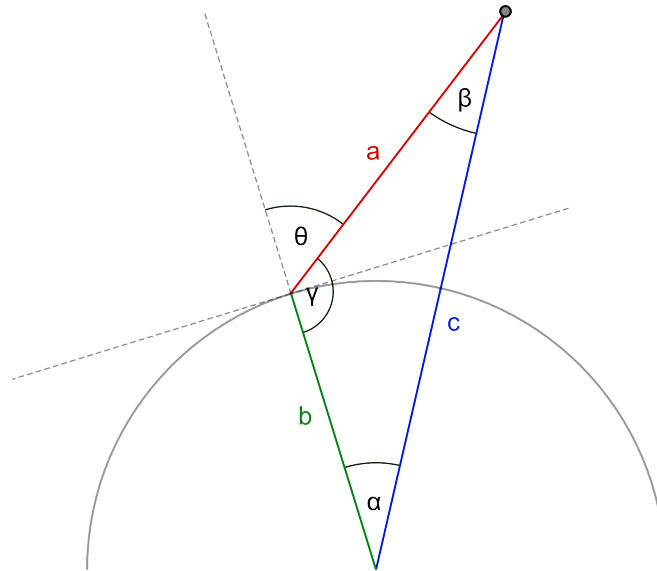
**Figure 7.17.:** Sketch of the laser beam geometry. The laser is emitted under a nadir (roll) angle $\beta$ and measured under an zenith angle $\theta$. $b$ is the Earth radius at the latitude of the Pierre Auger Observatory and $c$ the distance of the satellite from Earth's core.

with which

$$\alpha = \arcsin\left(\frac{a}{b} \cdot \sin(\beta)\right) \ . \tag{7.24}$$

Substituting this expression for $\alpha$ in equation (7.20), leads to the final expression for the observed zenith angle

$$\theta = \beta + \arcsin\left(\frac{c}{b}\sin(\beta) \cdot \left(\cos(\beta) - \sqrt{\cos^2(\beta) - 1 + \frac{b^2}{c^2}}\right)\right) \ . \tag{7.25}$$

This function is plotted in figure 7.18. In this plot also the two points of interest are drawn. The nadir angle of the main beam of $35°$ corresponds to a zenith angle of $37.1°$. This is in good agreement with the measured value of $37.7° \pm 0.5°$. For the secondary beam a zenith angle of $59° \pm 2°$ is expected, which also matches the measured angle of $58.33° \pm 0.06°$.

The measured main beam zenith angle of $37.7°$ corresponds to a nadir angle of $35.6°$, which is slightly over the expected $35°$ but within the uncertainty of the measurement. Inversely, according to this formula a nadir angle of $35°$ should result in a measured zenith angle of $37.1°$. The secondary beam zenith angle of approximately $58.3°$ corresponds to a nadir angle of $54.1°$, which also matches the estimated value of $55°$ of section 5.3.2.

#### 7.3.2.2. Ground Level Tracks

The reconstructed geometry of the laser beams also includes the ground position of each laser shot. This position can be expressed as points relative to the site coordinate system. To visualize the ground track of the laser beams, the positions of all mono events are calculated instead of the ones from the stereo reconstruction, because the latter are much rarer than the former. Figure 7.19a shows the reconstructed ground position for one exemplary Saturday with the Aeolus main beam. The day chosen was the 3rd of August 2019, which is also the Saturday with the most events. The colors in the plot correspond to the different FD-stations, different parts of the track are seen by mainly different eyes. The approximate position matches the expectation based on the TLE projections. However, especially the events seen by Los Leones and Coihueco seem to be stretched along a the
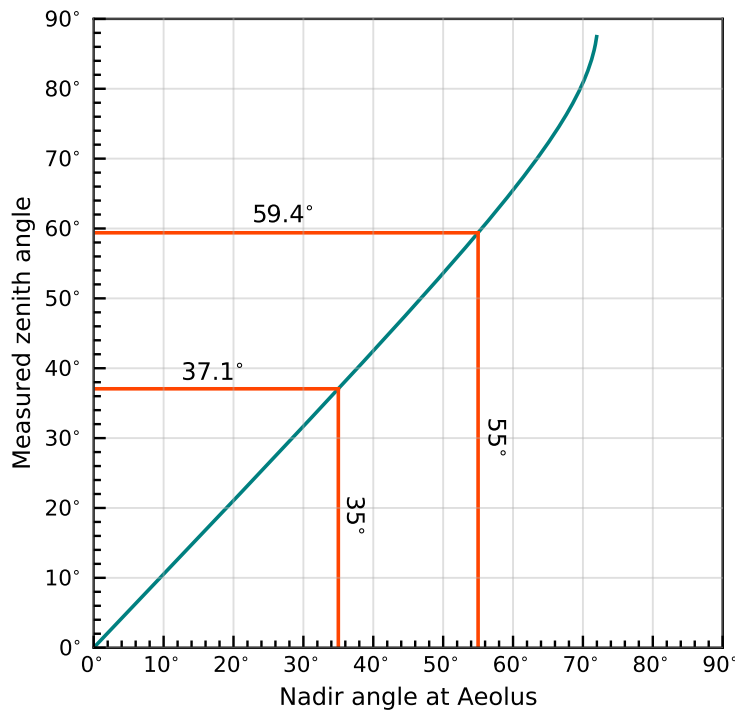
**Figure 7.18.:** Connection between the measured zenith angle and the laser emission angle at the satellite. Due to the curvature of Earth the measured zenith angle is larger than the emission angle.

line of sight of the telescopes. Reason therefore is the poor resolution of the $\chi_0$ angle (see figure 7.2) within the shower detector plane of the monocular reconstruction.

Figure 7.20a shows the according plot for one exemplary Friday (9th August 2019) with a secondary beam transition. The laser track is visible more clearly in general on Fridays. Again different parts of the tracks are seen by different eyes, based on the proximity of laser and telescopes.

**Tracks with Fixed Geometry**

As described earlier the monocular reconstruction can be improved by fixing the beam direction. Using fixed zenith and azimuth angles yields the corresponding plots in figures 7.19b and 7.20b. Compared to the pure monocular reconstruction the tracks are now visible more clearly with a smaller dispersion. Especially the main beam events now all seem to be arranged along a straight line. The tracks of all Aeolus laser transitions can be found in the appendix A. There an overview of the most interesting properties of each transition is listed, including the track plots.

While the measured tracks are qualitatively in good overall agreement with the approximate projection from TLEs, there are systematic differences between the measured and expected position, upon closer inspection. Figure 7.21 shows the measured ground track position of the events of one Saturday with main beam transition. As a comparison also the predicted ground track for the same time interval done by ESA is plotted [54]. Since the ground position represents the intercept of the laser track with a plane at a certain height and different heights also correspond to different horizontal positions (due to the slanted laser beam), both the positions and the predicted ESA ground track have been shifted to a
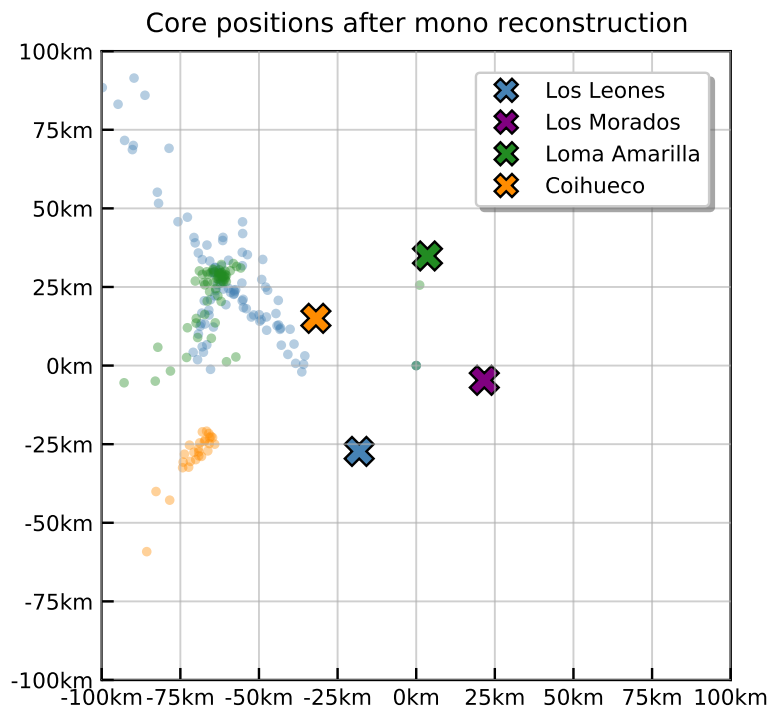
**(a)** Monocular reconstruction
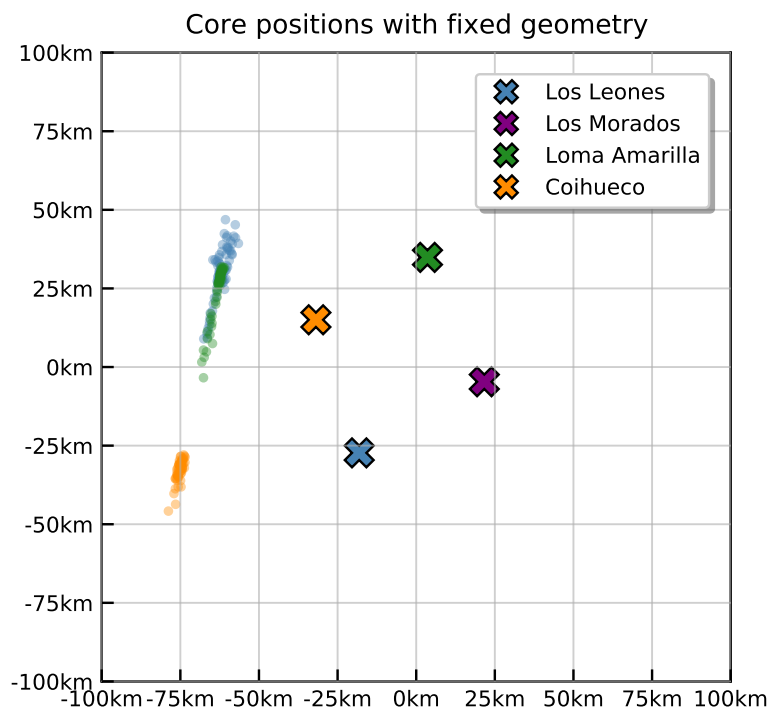


**(b)** Monocular reconstruction with fixed angles

**Figure 7.19.:** Laser ground positions of the main beam on Saturday 3rd August 2019. The positions in (a) are obtained from a pure monocular reconstruction, in (b) the zenith and azimuth angles were fixed in the monocular reconstruction.
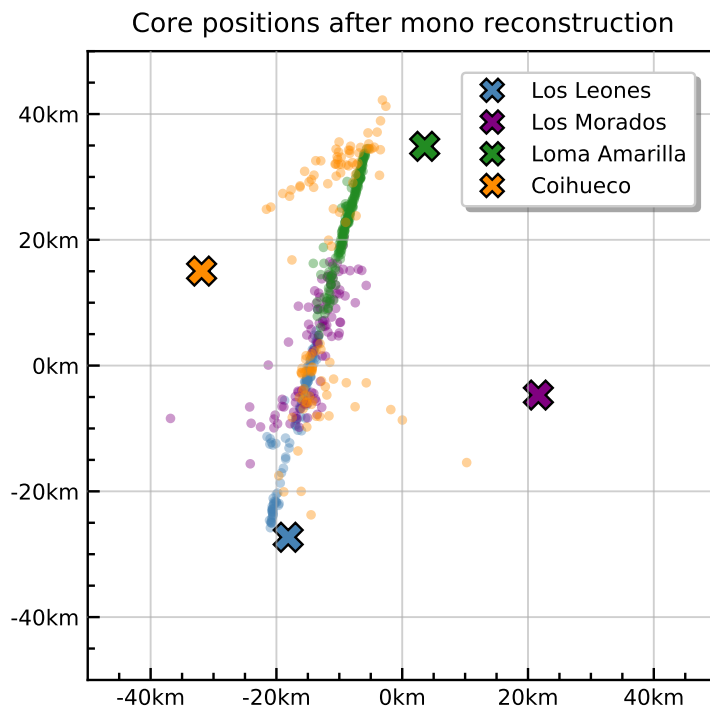
**(a)** Monocular reconstruction
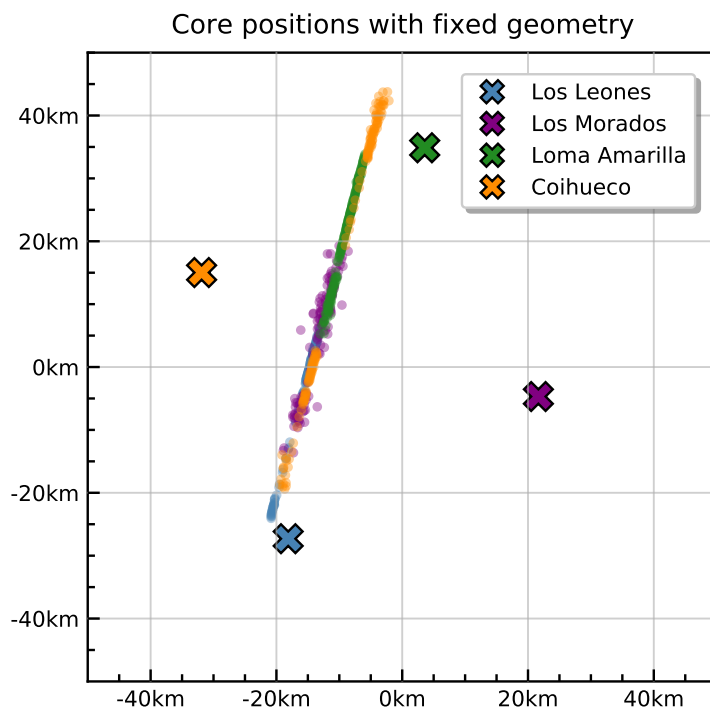


**(b)** Monocular reconstruction with fixed angles

**Figure 7.20.:** Laser ground positions of the secondary beam on Friday 9th August 2019. The positions in (a) are obtained from a pure monocular reconstruction, in (b) the zenith and azimuth angles were fixed in the monocular reconstruction.
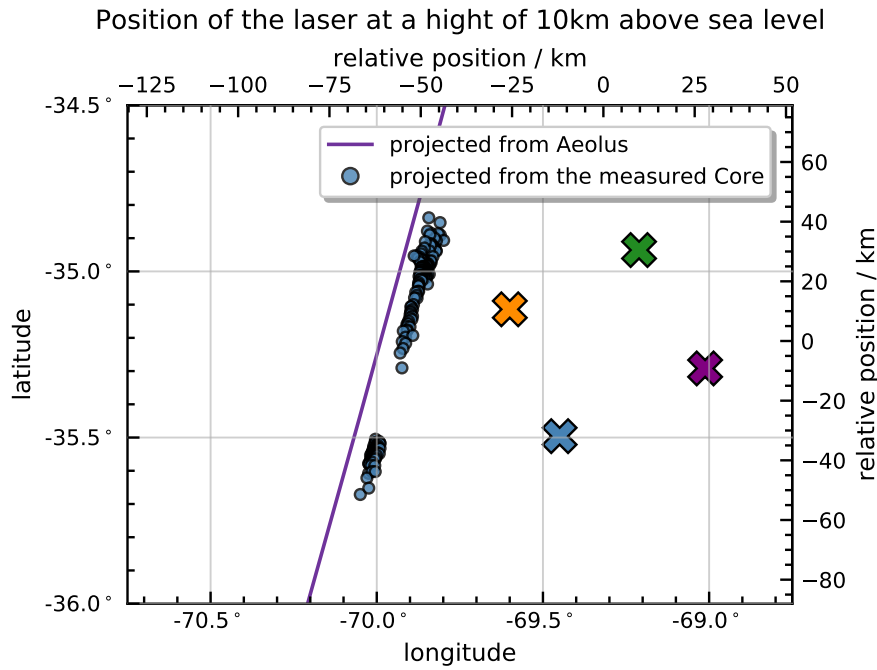
**Figure 7.21.:** Discrepancy between the measured ground track and the prediction by ESA. For comparison all positions are adjusted to a height of 10 km over sea level.

common reference height, to ensure comparability. Here we choose 10 km above sea level. As shown in the plot, there is an offset of $\approx 6$ km separating the measurement from the prediction.

**Impact of a Fix Zenith Angle on the Ground Track Position**

A possible reason for the ground level discrepancy could be a bias due to the fixed angles of arrival, that we use to improve the accuracy of the monocular reconstruction. It is therefore worthwhile to investigate how much the uncertainty in the arrival direction impacts the reconstruction of the ground position. Therefore the laser ground positions were reconstructed for one day, while slightly varying the fixed zenith angle used for the fixed angle reconstruction. Four values between 37.0° and 37.8° were tested. The result can be seen in figure 7.22a. The reconstructed positions only differ by a small amount. To be able to better distinguish the four reconstructions, a zoom of a small cutout is shown in figure 7.22b. The four positions corresponding to the same event differ by a few hundred meters, within the chosen range of tested zenith angles. An error of the zenith angle that is much larger than the range tested here, is unlikely, since it would not only disagree with the measured data but also with the orientation of the satellite.

### 7.3.3. Laser Beam Width

The laser beams emitted by Aeolus widen, while they travel from the satellite down to Earth. As mentioned in section 5.3.2, the main beam was designed to have a small divergence and at ground level the diameter is expected to be within 7 m to 9 m. For the secondary beam no such estimation exists. The width of the beam can however be calculated by considering the image projected onto the cameras of the telescopes.

The activated pixels of one laser event depict an image of the laser beam. With the information about the width of the image at the camera and the distance between laser beam and camera, the beam width can be reconstructed.

**(a)** Full scale

**(b)** Zoom
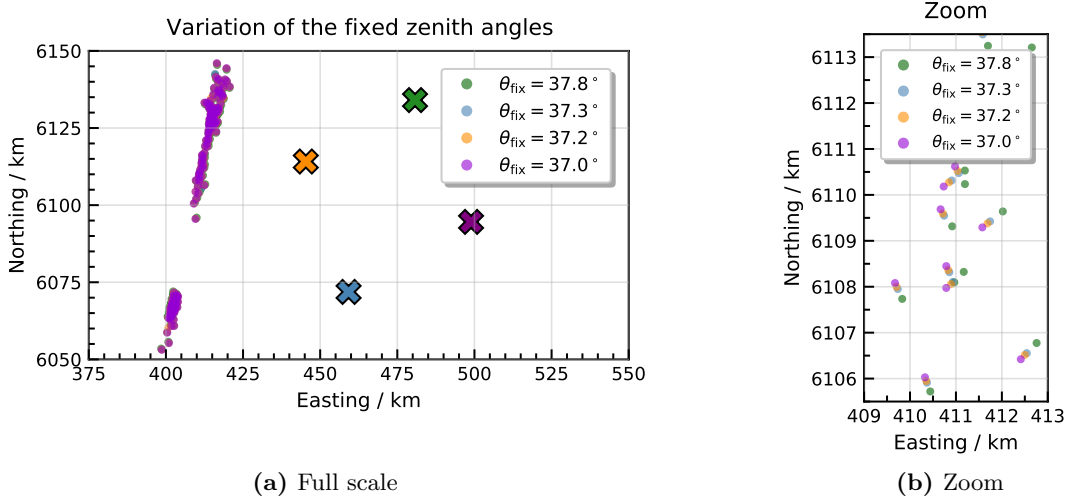
**Figure 7.22.:** Ground track positions of reconstructions with varied fixed zenith angles.

Therefore the $\zeta$-angle can be utilized. The $\zeta$ angle is used in the event reconstruction [64]0. It is calculated as the angle around the reconstructed axis within which the signal of each pixel is collected. To calculate this angle, the single time bins of one event are considered individually. For each time bin, the corresponding signal is given by all pixels that are within the $\zeta$ environment, relative to the focal point of the camera. Different values for $\zeta$ are tested for each time bin of the event. Then the one value for $\zeta$ is chosen, which maximizes the signal to noise ratio. Thus one obtains one value for $\zeta$ that describes the signal collection for one event.

The closer the laser beam is to the camera, the larger the angle $\zeta$ is. To estimate the laser beam width one can assume the relation

$$\tan\left(\zeta\right) = \frac{r_{\mathrm{beam}}}{d}\ ,\tag{7.26}$$

where $r_{\mathrm{beam}}$ is the radius of the laser beam and $d$ the distance to the camera. This does however not perfectly describe the situation. On the one hand, the distance between camera and laser beam is different for the individual points along the beam. The $\zeta$ angle is however only calculated once for the entire beam. To put one pair of $\zeta$ and $d$ into relation, the average value of all the distances along the beam can be used. On the other hand, the $\zeta$-angle should approach zero for large distances. In reality this angle approaches a nonzero value[9], since the camera pixels have a finite size and thus the angle of light collection can not get arbitrarily small. Therefore $\zeta$ is more precisely described as

$$\zeta = \max\left(\arctan\left(\frac{r_{\mathrm{beam}}}{d}\right), \zeta_{\mathrm{min}}\right)\ ,\tag{7.27}$$

where $\zeta_{\mathrm{min}}$ is a constant value for the lower limit. Using this relation, the beam width can be obtained by doing a two parameter fit of $\zeta(d)$. Figure 7.23 shows this fit for the secondary beam corresponding to the 9th August 2019. The parameters obtained by this fit are a beam radius of $r_{\mathrm{sb}} = (548 \pm 3)\,\mathrm{m}$ and an angle threshold of $\zeta_{\mathrm{min}} = 1.18° \pm 0.01°$. Visible in this plot is also, that the events of Coihueco are shifted to higher $\zeta$ angles (or higher distances, depending on the point of view). The reason is as mentioned above, that the distance between telescope and laser changes along the beam. Coihueco is looking roughly in the direction of the laser origin, meaning that the zeta angles of the events

---

[9]Usually a small safety margin is also added onto the value of $\zeta$. This was disabled for the calculations done here, the $\zeta$ limit at large distances is however still nonzero.
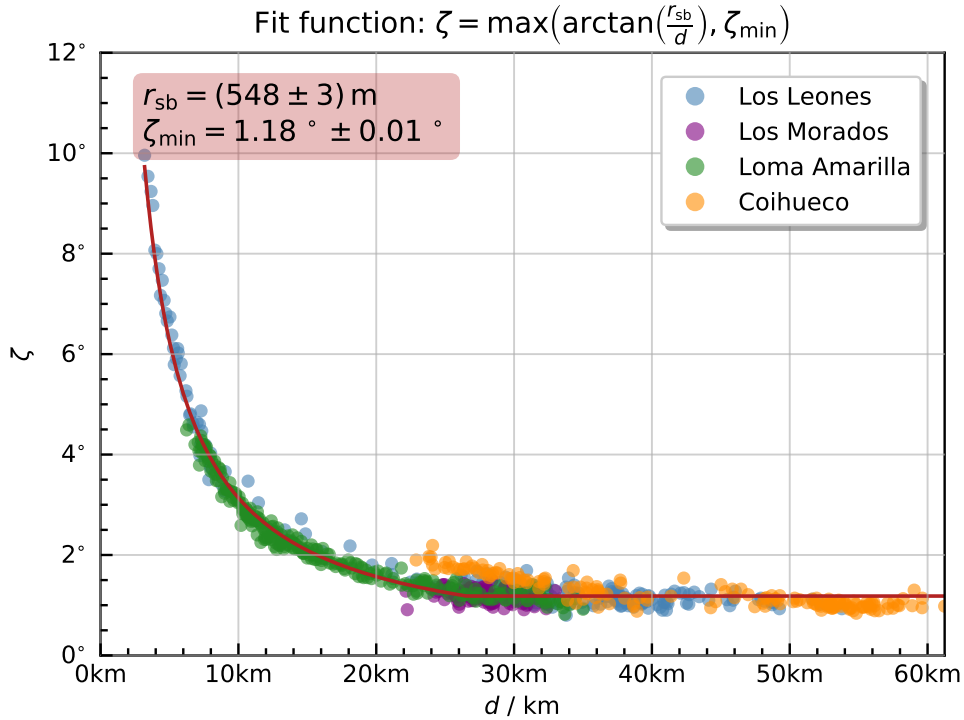
**Figure 7.23.:** Zeta angle as a function of the distance between laser beam and telescope. The zeta angle is calculated for each event of the transition, the distance is the average over all measurement points along each beam.

are determined by points close to the telescope, while the average distance is significantly larger. This may result in a mismatch of $d$ and $\zeta$.

For this method it is crucial that the beam passes close to a telescope. The fit performs better if a large range of $\zeta$ angles are used, the angle decreases however rapidly with the distance. Therefore this method can unfortunately not be used to check the beam radius of the main beam. The distance between main beam and telescope is at all times between $50\,\mathrm{km}$ and $80\,\mathrm{km}$ and the width of the beam is much narrower than the secondary beam. Therefore the $\zeta$ angle is basically constant for all events, at its lowest value $\zeta_{\mathrm{min}}$.

### 7.3.4. Energy

#### 7.3.4.1. Impact of Clouds on the Energy Reconstruction

One factor that greatly affects the laser reconstruction are clouds over the observatory, if they are within the light path of the laser beam or the scattered light. Clouds can affect the reconstructed energy in two ways, as illustrated in figure 7.24. One possibility is that the laser beam hits a cloud on the way through the atmosphere. Due to additional scattering with the cloud particles, more scattered light is emitted from the laser beam within the scope of the cloud. Thus also a larger amount of light is scattered towards the telescope, causing an increase of the measured energy in the direction of the cloud.

The other possibility is that a cloud obstructs the path between laser beam and telescope. In this case the light gets scattered away within the cloud and is lost to the telescope. Thus a drop in the energy is detected.

One way of detecting the impact of clouds is to resolve the height dependence of the energy measurements. As stated before the energy of the laser beam can be reconstructed for

**(a)** Increased light collection

**(b)** Decreased light collection
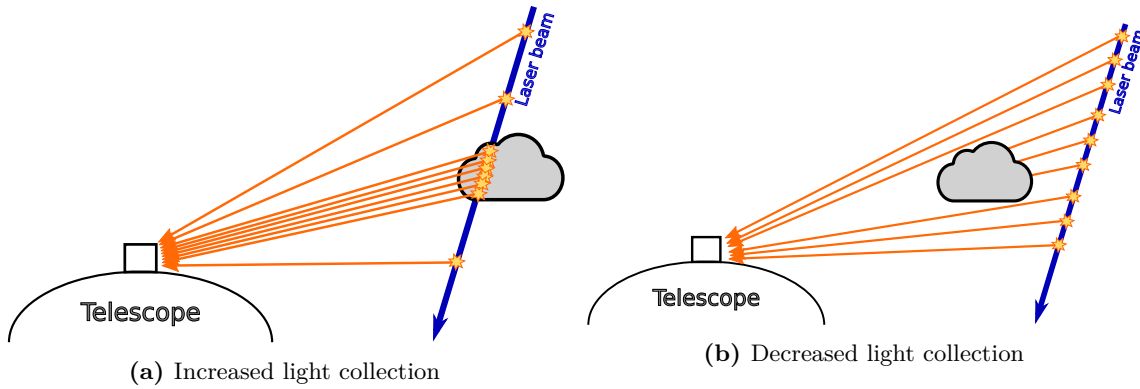
**Figure 7.24.:** Sketch of the two possible ways of clouds impacting the laser energy reconstruction. The laser beam can hit the cloud, causing additional scattering light at the telescope. Alternatively a cloud can obstruct the path of the scattered light, causing a light deficit at the telescope.

many points along the laser beam. If one does not take all these measurement points to reconstruct a single energy but directly evaluates them as a function of the atmospheric depth (or height over sea level respectively), one gets a vertical scan of the reconstructed energy. The obtained energy profiles can be averaged over one transition to make the effect more clearly visible. Examples for the two possible cases are shown in figure 7.25. For the first case there is a distinct peak visible where a cloud is hit by the laser beam. This also shifts the total reconstructed energy to higher values, making it difficult to use the data for analysis. This case happens for multiple of the secondary beam transitions. For the second case a drop in the energy is visible, shifting the total energy to lower values. This case happens for some of the main beam transitions.

Another way of identifying clouds is to plot the average charge of each pixel for one laser transition. This can be done for all eyes. The laser covers a certain area of the field of view while it passes in front of the eye. Clouds become visible due to the larger signal in some of the pixels, causing stripes of higher charge within the pixel array. An example can be seen in figure 7.26.

Finally also the cloud cameras installed ad each of the FD-stations can be used. Those provide a mapping of the sky through thermal imaging, where clouds become visible as areas of higher temperature. These cloud camera images are not available for all eyes at all desired points in time. However, with the combination of the three different methods a separation between cloudy and clear nights can be made. The result of this separation for each Aeolus transition can be found in the appendix A. Unfortunately roughly half of all nights with Aeolus events appear to be cloudy. This makes especially the calculation of the laser energy during these nights untrustworthy and the results will therefore not be used in the following.

### 7.3.4.2. Measured Main and Secondary Beam Energy

For the reconstruction of the energy of main and secondary beam the likelihood fit method was used as described before. Therefore a scan over 200 energy values between 10 PeV and 1000 PeV for the main beam and between 1 PeV and 100 PeV in case of the secondary beam was done[10]. The energy with the maximum likelihood value was then selected for each event. On top of the selection by time, as used before, cuts were applied on the zenith and azimuth angle. Due to the fixed geometry in the reconstruction a narrow window of $\pm 0.1°$ around the target value could be chosen to reject events that did not fit the fixed

---

[10]The limits were obtained from samples done using the weighted mean approach of the energy reconstruction.

**(a)** Fr, 28th June 2019

**(b)** Sa, 20th June 2020
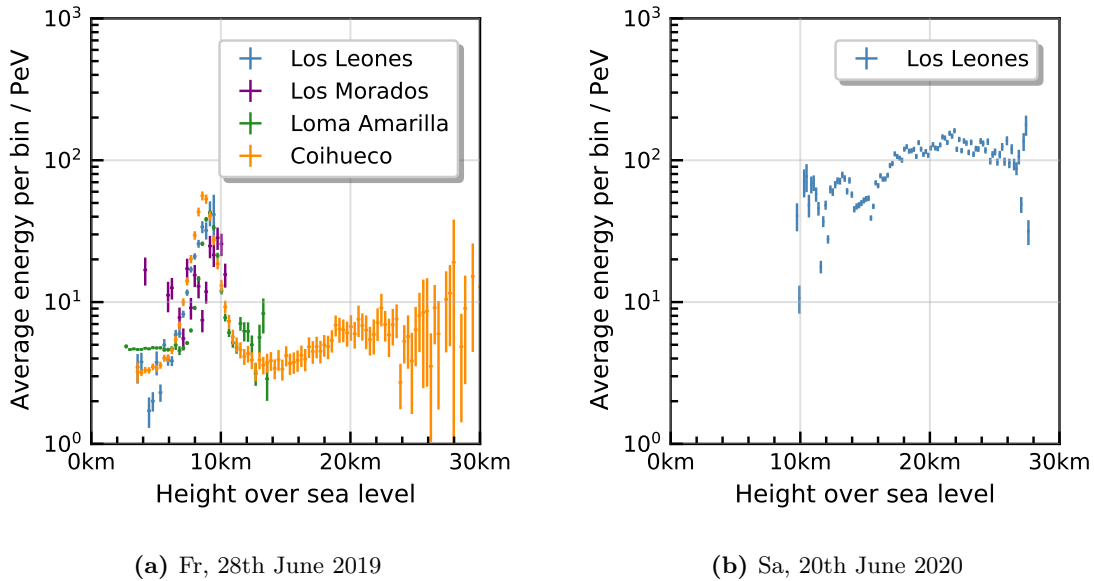
**Figure 7.25.:** Plot of the energy as a function of the height over sea level. Each point includes the average energy of the height bin over the laser transition. Plot (a) shows a peak in the secondary beam energy profile, caused by clouds in the laser beam path. Plot (b) shows a drop in the energy of the main beam laser profile.
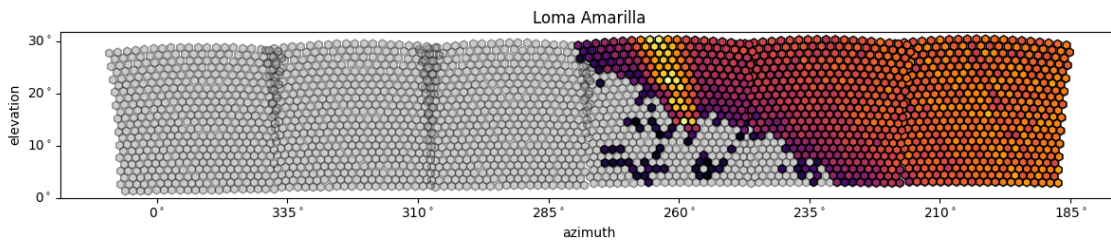


**Figure 7.26.:** Array of the pixels of all telescopes belonging to Loma Amarilla. The color indicates the average charge measured at each pixel during one transition (on 28th June 2019). The beam passes from the right of the image towards the center. A cloud becomes visible by a stripe of brighter pixels in the third mirror from the right.

geometry. Additionally, events were discarded where some pixels in the camera saturated, which happens for few events when the laser is close to the telescope. Moreover, we ignore events, that have their best-fit energy at the border of the fit range.

The result for one exemplary Saturday (3rd of August 2019, the same as used previously) is shown in figure 7.27. The mean value of all the main beam laser shots of this transition is approximately 218 PeV or 35 mJ. As stated earlier, the nominal Aeolus laser energy is around 65 mJ. However, this value is not completely fix but changes over the scale of weeks. Figure 8.6b shows the internally measured laser energy. For the investigated date the laser energy is roughly at 67 mJ, so even slightly larger. However, this value on the one hand has to be corrected by a scaling factor of 0.94 (for this day), on the other hand the laser beam loses intensity during its path between the laser system and telescope exit, which amounts to an additional transmission factor of 0.704 [54]. This leaves an expected energy of

$$E_{\text{exp}} = 67\,\text{mJ} \cdot 0.94 \cdot 0.704 \approx 44.3\,\text{mJ} , \tag{7.28}$$

which is $(21.2 \pm 0.7)\%$ larger than the measured value. Correcting the energy reconstruction bias (7.2.5) would lower the difference to $\approx 17\%$. It is however worthwhile noting, that at

this stage the energy is reconstructed assuming an aerosol profile, that is based on average values over many aerosol measurements. An analysis with a measured aerosol profile for this transition, will have an impact on the energy reconstruction. This issue is further discussed in the next chapter. In addition, the calibration uncertainty of Auger has to be considered, which is in the order of $\approx 11\,\%$ [65].

A histogram of the reconstructed energies of the secondary beam for the 9th August 2019 is shown in figure 7.28. The average energy here amounts to a value of approximately $6.77\,\text{PeV}$ or $1\,\text{mJ}$. For the secondary beam unfortunately no reference measurement exist to compare this value.
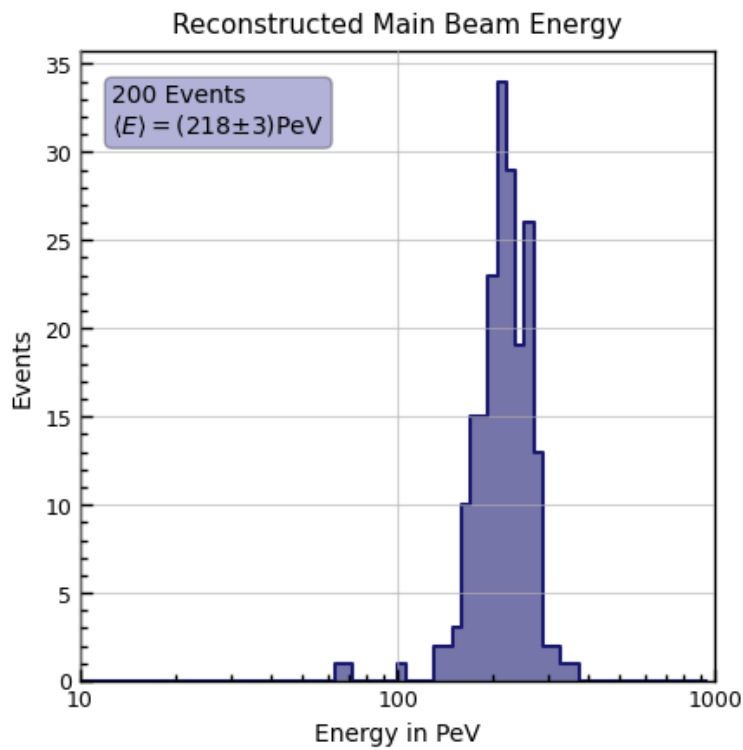
**Figure 7.27.:** Histogram of the main beam energy for the transition on the 3rd August 2019.
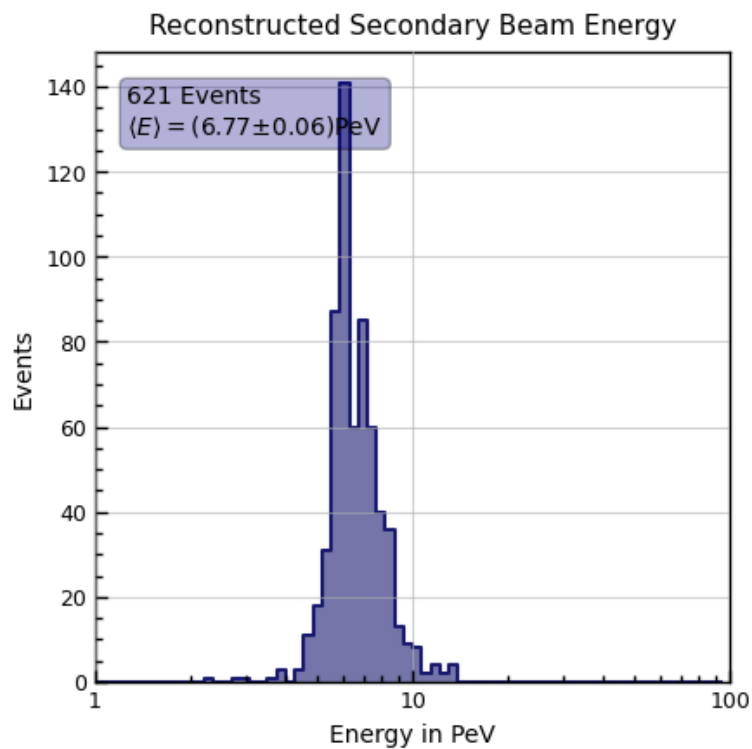


**Figure 7.28.:** Histogram of the secondary beam energy for the transition on the 9th August 2019.

# 8. Atmospheric Studies with Aeolus

The previous chapter showed, how the laser beam energy can be reconstructed using a likelihood scan. In these calculation the atmospheric conditions were already incorporated, in the form of an assumed aerosol profile. In the following the possibility will be discussed, to obtain both information about the energy and the aerosols, by including aerosol parameters into the likelihood scan.

## 8.1. Principle of Extracting Aerosol Parameters

The basis for the determination of aerosol information from Aeolus laser shots is the parametric aerosol model, as described in section 3.3.3. This model characterizes the aerosol profile through three parameters, the mixing layer height $H_{\mathrm{mix}}$, the attenuation length[1] at ground level $L$ and the scale height $H$.

When the energy of a laser event is reconstructed, as done in the previous chapter, an aerosol profile is assumed for the reconstruction, described by the three parameters. These values determine the calculated Mie attenuation of the light during the transmission through the atmosphere. Therefore also the calculated number of expected photons at the aperture, given a laser energy, is dependent on the chosen model parameters, meaning that the reconstructed energy is sensitive to the aerosol parameters. In the previous chapter the energies were reconstructed using a set of parameters, based on averaged values obtained by aerosol measurements done over a large time span[2]. The values used were an attenuation length of $52.6\,\mathrm{km}$, a scale height of $2.9\,\mathrm{km}$ and a mixing layer height of 0.

The likelihood scan, that was introduced in the previous chapter, compares the collected light flux at the telescope with the calculated amount of photons, based on a sampled energy. Since the chosen aerosol parameters change this number of photons as well, they can also be used as a fit variable. This means that instead of scanning only over the energy, as done in the previous chapter, here we will also vary the aerosol parameters during the likelihood scan. The combination of parameters and energy with the best likelihood value should then ideally yield the laser energy, as well as the set of parameters, that describes the atmosphere best. The leverage on the aerosols is thereby given by the range of different distances between laser and telescopes, within one laser transition. For example, an overestimation of the energy at a close distance could be compensated by an overestimation of the attenuation by aerosols. If this false combination of energy and aerosols is however tested with an event at a large distance, this will result in a low likelihood value, since the attenuation over the larger distance no longer agrees with the amount of light at the telescope.

---

[1] note that the attenuation length mentioned here and in the following corresponds to the parametric aerosol model, therefore only the aerosol attenuation is described. The attenuation caused by Rayleigh scattering is not part of this evaluation, as it can be considered a known quantity given the density profile of the atmosphere.

[2] Preliminary values for the measurement of the atmosphere conditions during the satellite transitions were only available few days before the deadline of this thesis. Therefore the average aerosol values had to be used during reconstruction.

Therefore, to obtain a set of aerosol parameters, each event of one transition has to be reconstructed many times, while testing the different combinations of energy and aerosol parameters. As described above, the evaluation of the light flux is done for many points along each measured laser beam, for each of which the likelihood value is calculated. For a transition with several hundred events, this leads to a number of calculated likelihood values that is in the order of magnitude of $10^5$, for every tested combination. All likelihood values belonging to one combination can be multiplied (and therefore the logarithm of the likelihood is added up)

$$\ln \mathcal{L}(E, L, H, H_{\mathrm{mix}}) = \sum_i^{\mathrm{events}} \sum_j^{\mathrm{bins}} \mathcal{L}_{ij}(E, L, H, H_{\mathrm{mix}}) \tag{8.1}$$

The best fit of energy and parameters is given by the highest likelihood value.

The multidimensionality unfortunately rapidly increases the number of required reconstructions. If one would perform a scan over all three aerosol parameters (plus the energy) of 10 values each, one would need to do 10000 likelihood calculations of every single laser event. With several hundred events per transition this results in a lot of calculation time. Therefore as a demonstration of the principle, in the following not all parameters were scanned over. The focus was mainly laid on the attenuation length in a two dimensional scan. The scale height was included in a three dimensional scan, as will be shown further below. For future applications, the implementation of a more efficient optimization algorithm than the scan used here will allow to perform a full four-dimensional fit of the three aerosol parameters plus the laser energy.

Instead of directly sampling the attenuation length, the sampling values were chosen to be equidistant values of the vertical optical aerosol depth $\tau_{\mathrm{a}}$ (or VAOD), as introduced in section 3.3.2. This allows for a more direct comparison to aerosol measurements, which usually use this quantity as a reference. According to equation (3.36), if only the attenuation length $L$ is fitted and the other aerosol parameters are kept constant, the VAOD and the attenuation length are linked by a factor $C(h, H, H_{\mathrm{mix}})$, which is dependent on the height $h$, scale height $H$ and mixing layer height $H_{\mathrm{mix}}$.

$$\tau_{\mathrm{a}} = \frac{C(h, H, H_{\mathrm{mix}})}{L} \ . \tag{8.2}$$

By choosing a reference height of e.g. 5 km, one can calculate the attenuation length from the VAOD or vice versa[3]. If both the attenuation length and the scale height are sampled, then the VAOD is dependent on both of these values, meaning that $\tau_{\mathrm{a}}$ can not be uniquely mapped onto one value of $L$.

## 8.2. Simulation

To test the principle of the multi parameter scan, simulated laser shots can be used. This allows for a comparison of the extracted energy and aerosol parameters with the values that were put into the simulation. Therefore one complete transition of the main beam and the secondary beam was simulated. Just like in the simulations of the previous chapter, this was done by using the laser properties that were reconstructed earlier. This includes the zenith and azimuth angle, as determined in section 7.3.2.1, as well as the positions of each laser shot, corresponding to a sample transition. For the main beam again the 3rd August 2019 was chosen as a sample, for the secondary beam the 9th August 2019. The main beam was simulated with an energy of 35 mJ ($\approx$ 218 PeV), the secondary beam with an energy of 6.52 PeV or approximately 1 mJ. The aerosol parameters that went into the simulation, to calculate the detector response, were the same averaged values as used before of $L = 52.6$ km, $H = 2.9$ km and $H_{\mathrm{mix}} = 0$.

---

[3]This height corresponds to the altitude above ground, see also the calculations in section 3.3.3
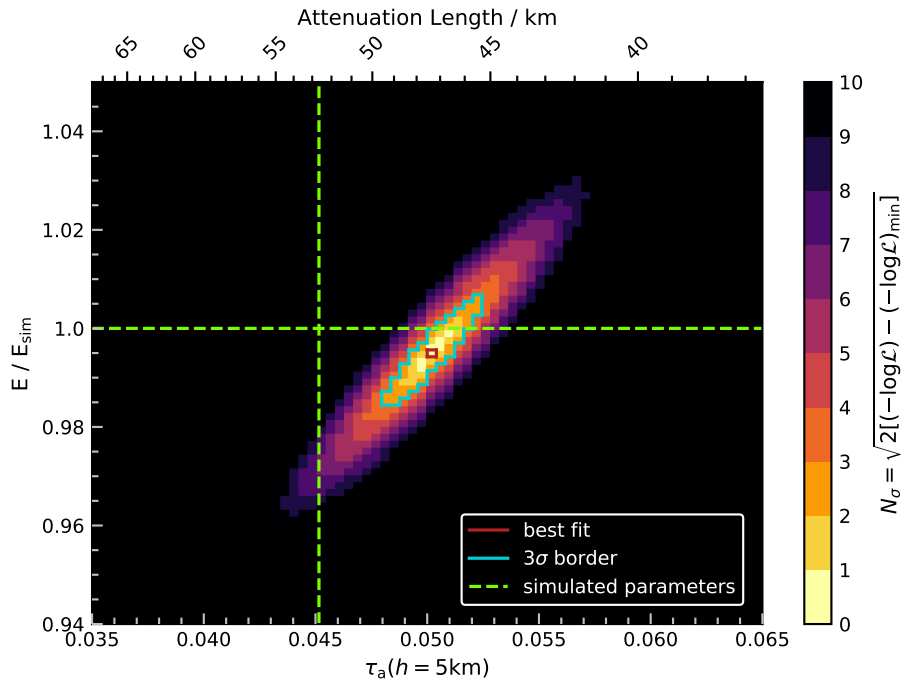
**Figure 8.1.:** A two dimensional scan over the energy and the VAOD $\tau_a$ for simulated laser shots of a main beam transition. The energy axis is normalized with the simulated energy. The coloring shows the number of $\sigma$ that separates each bin from the best fit value, in terms of statistical uncertainty. The best fit is marked by a red square. The simulated energy and VAOD are shown as green dashed lines and the $3\sigma$ statistical uncertainty is shown as a blue contour. The attenuation length $L$ corresponding to the VAOD at a reference height of $5\,\mathrm{km}$ is shown as an additional $x$-axis on top of the plot.

### 8.2.1. Two-Dimensional Likelihood Scan

During a two-dimensional scan, only the energy and the attenuation length are varied. The scale height and mixing layer height remained fixed at their simulated values of $2.9\,\mathrm{km}$ and $0$. As described above, instead of directly scanning the attenuation length, instead the VAOD $\tau_a$ is tested at equidistant values. Out of these values for $\tau_a$ then the attenuation length $L$ can be calculated, which is used as an input for the reconstruction. The calculation is done according to equation (3.36), with the fix values for $H$, $H_{\mathrm{mix}}$ and a reference height of $5\,\mathrm{km}$ above ground.

**Main beam**

For the reconstruction of the simulated main beam laser shots, the VAOD was scanned with 50 values between 0.04 and 0.06[4]. This corresponds to an attenuation length between approximately $39.6\,\mathrm{km}$ and $59.4\,\mathrm{km}$. The energy was sampled with 50 values between $210\,\mathrm{PeV}$ and $225\,\mathrm{PeV}$.

For each combination of $E$ and $L$ the combined likelihood value of all events was calculated. The best fit value is obtained by searching for the highest likelihood, or for the lowest value of the negative logarithm $-\log\mathcal{L}$. The result of this scan can be seen in figure 8.1. The color scale is given by the difference to the best likelihood value in the form

$$N_\sigma = \sqrt{2\left[(-\log\mathcal{L}) - (-\log\mathcal{L})_{\mathrm{min}}\right]}\,, \tag{8.3}$$

---

[4]This interval was determined through a previous reconstruction over a larger range. The reconstruction was then repeated over the smaller interval, for a better resolution in the region of interest.

which yields the statistical deviation from the best fit value in numbers of $\sigma$ (see e.g. [66]). The reconstructed energy is according to the best fit

$$E_{\text{fit}} = 217.3^{+1.1}_{-0.8}\,\text{PeV} \ . \tag{8.4}$$

The errors correspond to a $1\sigma$ interval around the best fit. Compared to the energy that was used for the simulation of $218.5\,\text{PeV}$, there is a bias of approximately

$$\delta E_{\text{syst.}} = 1.2^{+1.1}_{-0.8}\,\text{PeV} \tag{8.5}$$

or $\approx 0.5\,\%$ towards lower energies in the reconstruction. This bias is within the statistical precision of this scan and thus, for this test, the energy reconstruction can be considered to be unbiased. This is, however, not the case in general and if one looks at the reconstructed VAOD, the bias with respect to the simulation is larger. The best fit value for $\tau_{\text{a}}$ is

$$\tau_{\text{a,fit}} = 0.0502^{+0.0010}_{-0.0006} \ . \tag{8.6}$$

Compared to the simulated value of $\tau_{\text{a,sim}} = 0.0452$, the systematic bias is

$$\delta\tau_{\text{a,syst.}} = 0.005 \pm 0.001 \ , \tag{8.7}$$

which corresponds to approximately 10%. The systematic bias is significantly larger than the statistical uncertainty of the method. This is generally the case for this method, as confirmed by the subsequent scans. The reason for the small statistical uncertainty is the large number of measurement points ($\sim 10^5$), for which the likelihood values are combined. Therefore a very good statistic can be achieved, which is overshadowed by systematic effects. As can be seen in figure 8.1, the best fit value deviates by many $\sigma_{\text{stat.}}$ from the simulated value. To summarize, the reconstruction of the main beam simulation could reproduce the energy with uncertainties of

$$\frac{\delta_E}{E} \approx 0.5\,\%_{\text{stat.}} + 0.5\,\%_{\text{syst.}} \ , \tag{8.8}$$

and the VAOD with uncertainties of

$$\frac{\delta_{\tau_{\text{a}}}}{\tau_{\text{a}}} \approx 2\,\%_{\text{stat.}} + 10\,\%_{\text{syst.}} \ . \tag{8.9}$$

**Secondary beam**

The simulated laser shots of the secondary beam are reconstructed in the same way as explained in the previous section for the main beam. The only difference is the range of parameters, over which was scanned. The VAOD was tested in a range of 0.042 to 0.047 (corresponding to an attenuation length of $50.6\,\text{km}$ to $56.6\,\text{km}$), the energy in a range of $6.16\,\text{PeV}$ to $6.24\,\text{PeV}$.

The result can be seen in figure 8.2. Comparing to the main beam the situation is somewhat reversed. The fitted value of the VAOD is

$$\tau_{\text{a,fit}} = 0.0446^{+0.0003}_{-0.0002} \tag{8.10}$$

and therefore reasonably close to the simulated value of $\tau_{\text{a,sim}} = 0.0452$. The bias is

$$\delta\tau_{\text{a,syst.}} = 0.0006 \pm 0.0003 \tag{8.11}$$

and thus within a $3\sigma$ range of the fit value. However, the reconstructed energy is

$$E_{\text{fit}} = 6.206^{+0.004}_{-0.002}\,\text{PeV} \ . \tag{8.12}$$
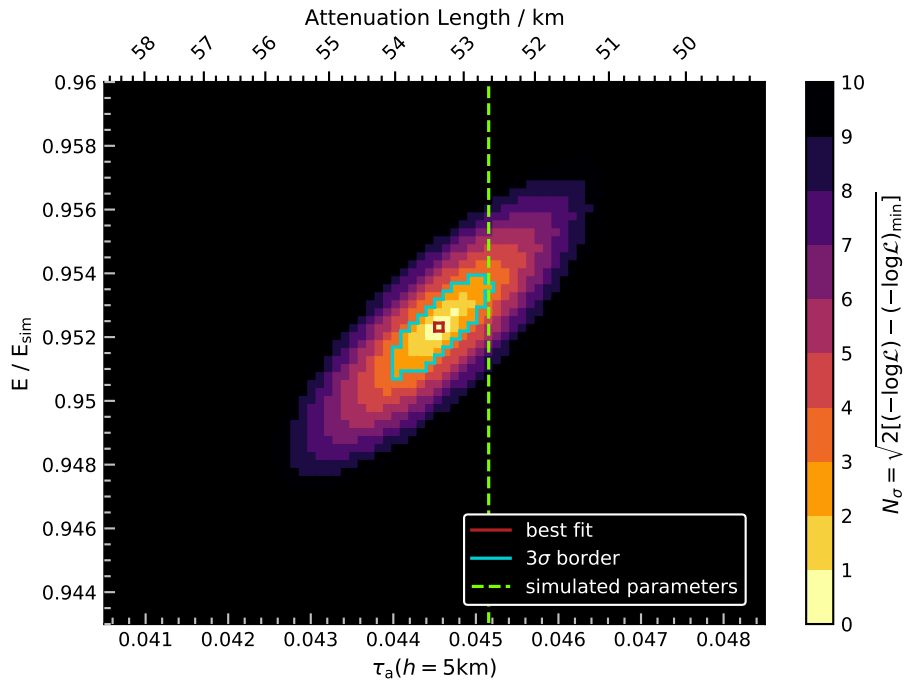
**Figure 8.2.:** A two dimensional scan over energy and VAOD, corresponding to a simulation of a secondary beam transition. The coloring shows the likelihood in numbers of $\sigma$ from the best fit value. Also plotted are the $3\sigma$ border and a dashed line, marking the simulated VAOD. The simulated value of the energy is outside of the depicted range.

This value is significantly lower than the simulated value of $6.52\,\mathrm{PeV}$, with a deviation of

$$\delta E = (0.311 \pm 0.004)\,\mathrm{PeV} \ . \tag{8.13}$$

This offset in the energy is similar to the $\approx 5\%$ energy bias, that was already observed in the simulations of the previous chapter. As in the case of the main beam, the results for the secondary beam indicate a good statistical uncertainty, but the overall precision is dominated by the systematic bias. Summarizing, the uncertainty is

$$\frac{\delta_E}{E} \approx 0.07\,\%_{\mathrm{stat.}} + 5.01\,\%_{\mathrm{syst.}} \tag{8.14}$$

and

$$\frac{\delta_{\tau_{\mathrm{a}}}}{\tau_{\mathrm{a}}} \approx 0.6\,\%_{\mathrm{stat.}} + 1.4\,\%_{\mathrm{syst.}} \tag{8.15}$$

for the reconstructed energy and VAOD respectively, using the secondary beam. It should be noted, that the $\chi^2$-value of this fit can be calculated as

$$\chi^2 = \sum_i \frac{(N_{\mathrm{exp}} - N_{\mathrm{obs},i})^2}{\sigma_{\mathrm{obs},i}^2} \ , \tag{8.16}$$

where $N_{\mathrm{obs}}$ and $N_{\mathrm{exp}}$ are the observed and (for the fit parameters) expected number of photons per time bin and $\sigma_{\mathrm{obs}}$ the uncertainty of the number of observed photons. One obtains a value of $\chi^2/N_{\mathrm{dof}} \approx 1$ for the number $N_{\mathrm{dof}} \sim 10^5$ of entries in the sum above (minus the number of fit parameter, which can be neglected).

These two parameter scans of the main and secondary beam show the current limitation of this method. The simulations indicate, that a very good statistical precision can be achieved, due to the large number of measuring points and consequently large amount of entries in

the sum over $\log \mathcal{L}$. However, the precision of the reconstructed parameters is dominated by a systematic bias. For the secondary beam the energy appears to be reconstructed at about 5 % below the simulation and this shift is accompanied by a bias of the VAOD. The effect is qualitatively different for main and secondary beam. What causes this bias has yet to be understood. A possible cause for the bias could be inconsistencies between the simulation and reconstruction of the same events, that are handled by different modules within $\overline{\text{Off}}\underline{\text{line}}$. A better understanding of this bias is important for the interpretation of results, obtained from actual measurements of the Aeolus laser.

Nevertheless, it is informative to compare the accuracy achieved with one Aeolus transition to the VAOD measurements taken with laser beams of the CLF. As was shown in section 4.3, the systematic uncertainty of the measurement of the VAOD with the CLF can be estimated as $\approx 25\,\%$. Based on the simulations done in this chapter, the systematic bias of the parameter scan method is still within the uncertainty of the CLF laser based VAOD determination. A similar remark can be made for the energy. The bias of $\approx 5\,\%$ is still low, compared to the calibration uncertainties of the eyes, which are of the order of $\approx 11\,\%$ [65]. Nevertheless, it would be desirable to find and eliminate the cause of the reconstruction bias.

## 8.2.2. Three-Dimensional Likelihood Scan

In a three dimensional scan the scale height $H$ is scanned as well as the energy and the attenuation length. In the two dimensional scan a direct conversion between the VAOD $\tau_\mathrm{a}$ and the attenuation length $L$ could be made, due to a constant value of $H$ (and a reference height $h$). This is now no longer possible, the VAOD is now a function of both $H$ and $L$, according to equation (3.36). To obtain the values for $H$ and $L$, that are used for a reconstruction, therefore an equidistant sampling is done over $H$ and $\tau_\mathrm{a}$. From every combination of $H$ and $\tau_\mathrm{a}$ then the attenuation length $L$ can be calculated.

As mentioned before, the higher dimensionality causes an increase in computing time. As a countermeasure, the number of sampled bins was decreased. Instead of 50 bins as used in the two dimensional scan, now only 10 bins were sampled in every dimension. The result for the simulated transition of the secondary beam can be seen in figure 8.3. Due to the difficulty of depicting the three dimensional dependency, now three plots are drawn, each showing the dependence on two parameters. The likelihood value (or more precisely the number of $\sigma$ calculated from it, as above) that is shown for each bin in two dimensions corresponds to the best (lowest) value found in the third dimension. Figure 8.3a shows the energy and VAOD as dependencies, figure 8.3b the energy and the scale height and figure 8.3c the scale height and the VAOD.

For this scan the sampling was done over a larger range, the VAOD was tested between 0.002 and 0.2, the energy between $4\,\mathrm{PeV}$ and $9\,\mathrm{PeV}$ and the scale height between $10\,\mathrm{m}$ and $4000\,\mathrm{m}$. This was done to see, if the simulated parameters are correctly found over a larger range of possible values. A consequence of this is, that the number of $\sigma$ reaches very high values, as indicated by the range of the plotted color bars. This is not unique for this scan, the same is also true for the previously done two dimensional scan. The plots shown there were focused around a relatively close region around the best fit, otherwise $N_\sigma$ would show a similar behavior. The high values of $N_\sigma$ show once again, that this method yields a very good statistical precision. In case of the three dimensional scan, the bin with the second to best fit is already more than $20\sigma$ away from the optimum. Therefore the achieved precision of this scan is by far determined by the bin size. To resolve the $1\sigma$ environment around the best fit, one would need to repeat the scan within a much narrower parameter range or with a finer sampling.
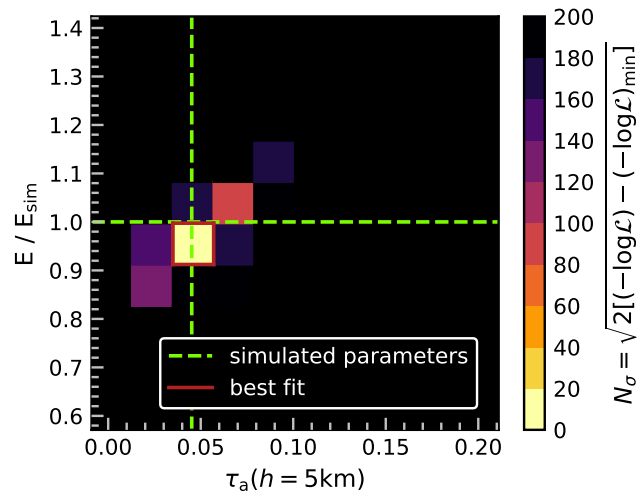
**(a)** Hidden: Scale height
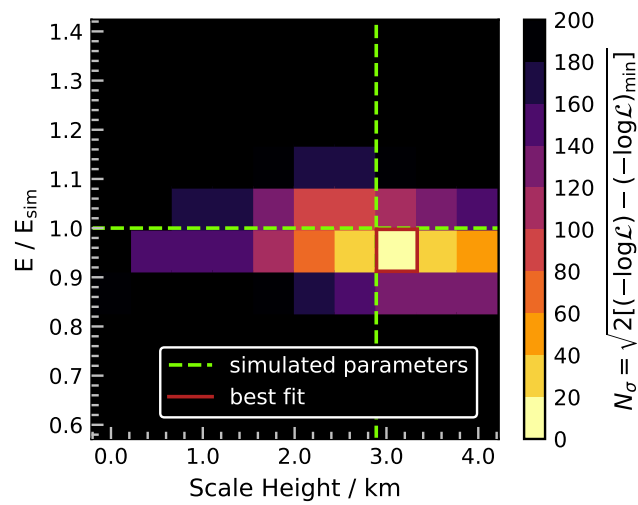


**(b)** Hidden: Attenuation length
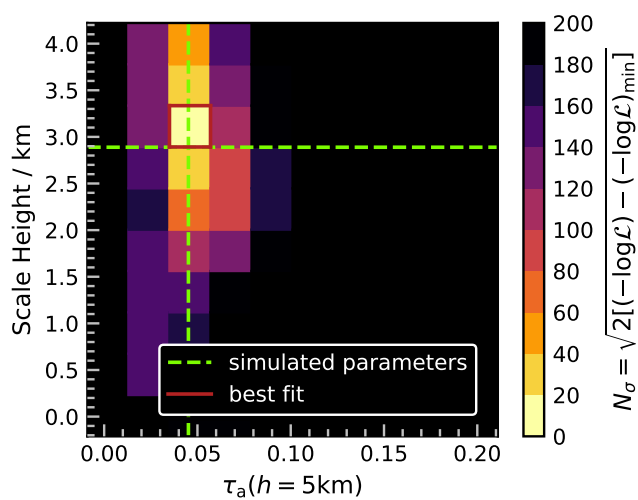


**(c)** Hidden: Energy

**Figure 8.3.:** The three plots corresponding to the parameter scan over energy, VAOD and scale height. Each plot shows the value of the highest likelihood, regarding the hidden dimension.

The differences between the fit results and the values, that were used in the simulation of the laser shots, are here

$$\delta\tau_{\mathrm{a}} = 0.001 \pm 0.011$$
$$\delta E = (0.3 \pm 0.3)\ \mathrm{PeV} \tag{8.17}$$
$$\delta H = (0.2 \pm 0.2)\ \mathrm{km}\ ,$$

where the uncertainties correspond to the step size of the scan. The differences are approximately within the uncertainty of the bin size. These results show, that the method is also working with a parameter scan in three dimensions. The simulated values were reproduced reasonably well. A bias, as the one seen in the previous scans, is likely also present here. It is however hidden by the worse resolution due to the bin size. To resolve the extend of the bias in three dimensions, a finer scan has to be done. However, the uncertainty of $\tau_{\mathrm{a}}$ reached in this configuration is with $0.011$ ($\approx 24\,\%$) still comparable to the aerosol measurements done with the CLF, as shown before. It needs to be kept in mind, however, that this uncertainty is the result of the specific scan with the chosen bin size, not the general limitation of this method. For future studies, it could therefore be worthwhile, to repeat this analysis with a finer scan. Notable is also, that the plot in figure 8.3c shows hardly any correlation between the scale height and the VAOD. This means, that a mismatch in the scale height could still result in a good reconstruction of the VAOD. This validates the two parameter scan, where the scale height was set to a fix value.

## 8.3. Data Analysis

The previous studies with simulations showed, that the aerosol parameters can in principle be obtained, using a parameter scan over the Aeolus laser shots. Even with a bias present that is not yet fully understood, the uncertainties are in an acceptable range. This makes it interesting to take a look at the measured Aeolus data.

As an example the transition of the secondary beam on the 9th August 2019 was examined in closer detail. The two parameter scan over all measured laser shots of this transition was done using the same method as for the simulated laser transition. The result of this scan can be sen in figure 8.4. A similar image is obtained as in the simulated cases. Notable is, that for the reconstruction of measured laser shots, fewer events are used in the likelihood scan, than for the reconstruction of the corresponding simulated laser shots ($\approx 700$ instead of $\approx 1500$). The reason is, that fewer events are recorded during real data taking, due to the dead time of the FD DAQ. For all of these measured events a simulation was done. In the simulation however, the detector dead time is not an issue, meaning that many simulated events are registered as stereo events, appearing in multiple eyes. Therefore the number of individual events in a simulation is higher than in the measurement that it is based on. This also results in a larger statistical uncertainty of the parameter values obtained from measured laser shots. The number of events is however still large enough to result in a very good statistical precision, the obtained parameter values with their $1\sigma$ statistical uncertainty are

$$\tau_{\mathrm{a}} = 0.0200^{+0.0004}_{-0.0006}$$
$$E = 5.140^{+0.005}_{-0.008}\ \mathrm{PeV}\ . \tag{8.18}$$

However, on top of that the systematic effects observed during the simulation have to be considered, since the origin of those is unknown and could also be present in the data analysis. Overall, the uncertainty of this measurement is thus at least

$$\frac{\delta_E}{E} \approx \pm 0.2\,\%_{\mathrm{stat.}} \pm 5.0\,\%_{\mathrm{syst.}}$$
$$\frac{\delta_{\tau_{\mathrm{a}}}}{\tau_{\mathrm{a}}} \approx \pm 3\,\%_{\mathrm{stat.}} \pm 1.4\,\%_{\mathrm{syst.}} \tag{8.19}$$
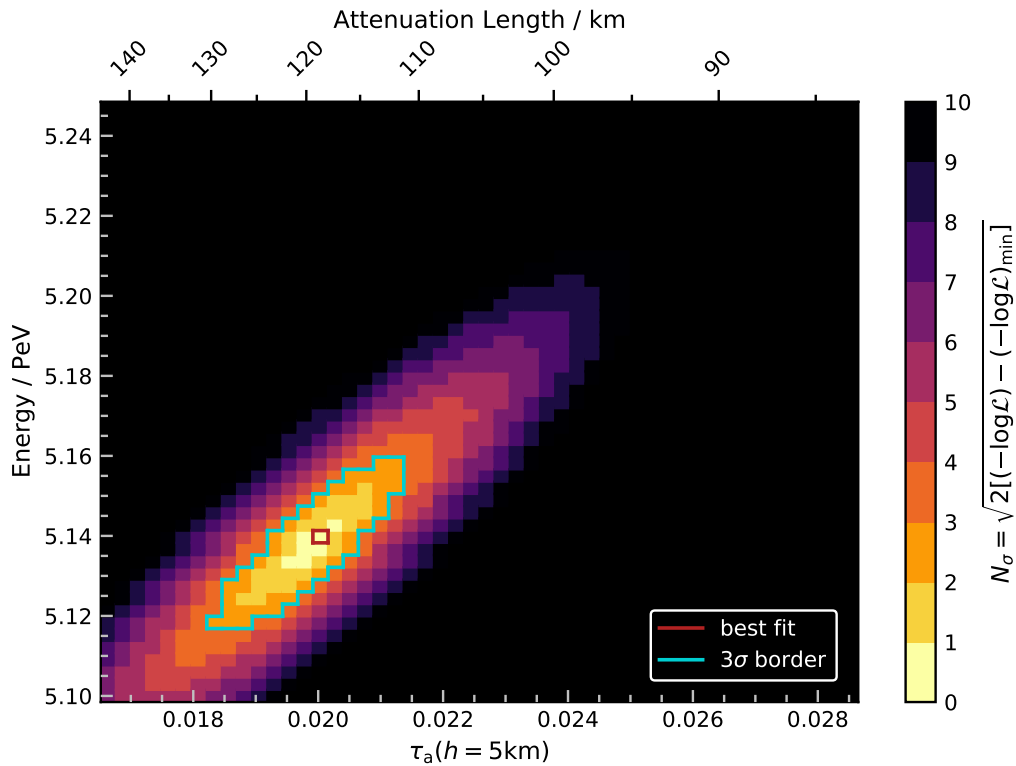
**Figure 8.4.:** Two dimensional scan over energy and VAOD, corresponding to the measurement of the Aeolus secondary beam on the 9th August 2019.

Additionally to the reconstruction bias, for the data the previously mentioned calibration uncertainty of 11 % has to be considered.

This evaluation can likewise be done for all main and secondary beam transitions. Unlike the example of the 9th August, that was just discussed, in the survey of all transitions a larger range of parameters was sampled[5]. Therefore their uncertainty is determined by the bin size, similarly to the three dimensional scan. Due to the chosen scanning intervals, one has an uncertainty on the VAOD of 0.005 and on the energy of 0.18 PeV or 4 PeV for the secondary beam or the main beam respectively.

In this manner, for each Aeolus laser transition, a value for the laser energy and for the VAOD is obtained. Figure 8.5 shows the extracted values for the VAOD over the time.

The obtained values seem to be in a sensible region. The typical range of VAOD measurements was shown in chapter 3 in figure 3.9a. These measurements are in a comparable range as the Aeolus measurement, especially considering the winter months with a clearer atmosphere[6].

A detailed comparison with the standard techniques used for the VAOD determination could not yet be made. Only recently, as of the last days of the writing of this thesis, preliminary values of the VAOD, measured with the CLF, became available [67]. A first look at these values show a good agreement to the reconstructions done here for some

---

[5]The zoomed in example transition was also initially scanned over a large range of parameters, to determine the region where a zoom would be sensible. This was not done for every Aeolus transition, since the broader scan suffices for the considerations done here.

[6]although one has to keep in mind, that the VAODs in figure 3.9a are at a reference height of 3.5 km, instead of 5 km. The according values at 5 km would be a bit higher, but still in accordance to the Aeolus measurement.
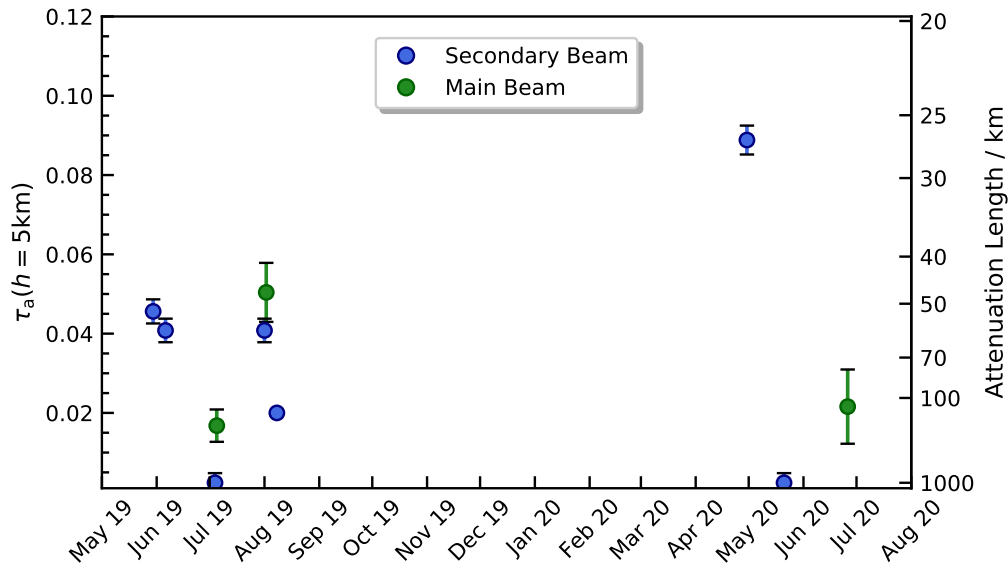
**Figure 8.5.:** The VAOD reconstructed from Aeolus laser shots as a function of time. Shown are the results for main and secondary beam. The errorbars correspond to the combined statistic and systematic uncertainty.

nights, but a significant deviation of $\sim \pm 0.05$ for other nights. This is far beyond the systematic bias, expected for either measurement (Aeolus or CLF). This calls for additional simulations, to account for other scenarios. In the cases that were simulated above, only one specific transition for main and secondary beam was considered. In reality, the tracks are not completely identical (see also the appendix A), for example on the 5th July 2019 only a short part of the track was observed, exclusively by Los Morados. Cases like this need to be simulated as well, to gain a better understanding of the obtained parameters and uncertainties.

Figure 8.6a shows the reconstructed energies for main and secondary beam over the time. As a comparison, figure 8.6b shows the laser energy as measured internally by Aeolus, until the end of 2019. The laser energy was continuously dropping after launch, because of which the backup laser was switched on, in end of June 2019. This caused the laser energy to jump up by $\approx 60\,\%$. This switch of the laser system happened between the secondary beam transitions on 7th June and 5th July 2019. The sudden jump in energy expected by the Aeolus measurements can however not be validated by the secondary beam reconstruction. The measured energy between these two dates increases only by about $4\,\%$, nowhere near the expected $+60\,\%$ jump[7]. A direct comparison with the reconstructed main beam is not possible, since the first detected main beam transition happened already after the backup laser was switched on. Another surprising observation is the differences in the reconstructed energies of the main beam. A notable increase is visible between the transitions on 6th July and 3rd August 2019. The expected main beam energy based on the Aeolus measurements is, as stated in section 7.3.4, approximately $44.3\,\mathrm{mJ}$. The reconstructed energies of

$$
\begin{aligned}
\text{6th July}: \quad & E = (23.2 \pm 2.8_{\mathrm{syst.}} \pm 0.3_{\mathrm{stat.}})\,\mathrm{mJ} \\
\text{3rd August}: \quad & E = (38.9 \pm 4.7_{\mathrm{syst.}} \pm 0.3_{\mathrm{stat.}})\,\mathrm{mJ}
\end{aligned}
\tag{8.20}
$$

deviate by $48\,\%$ or $12\,\%$ respectively. Thus, especially the former value is significantly below the expectation. The energy jump during the switch between laser systems is of a

---

[7]One should notice, that this argumentation assumes, that the secondary beam energy is proportional to the main beam. This was actually never confirmed.
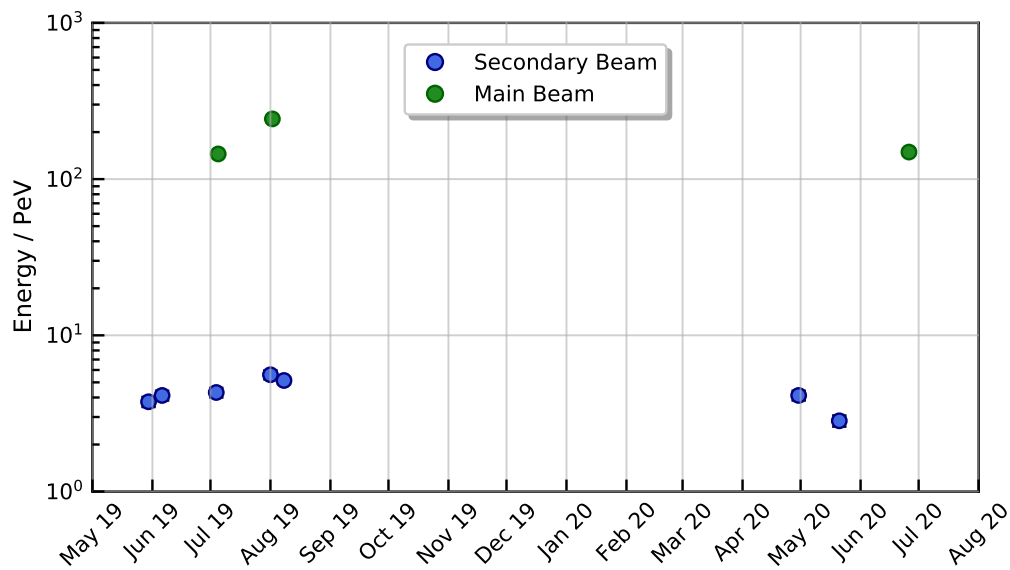
**(a)** Reconstructed energy over time
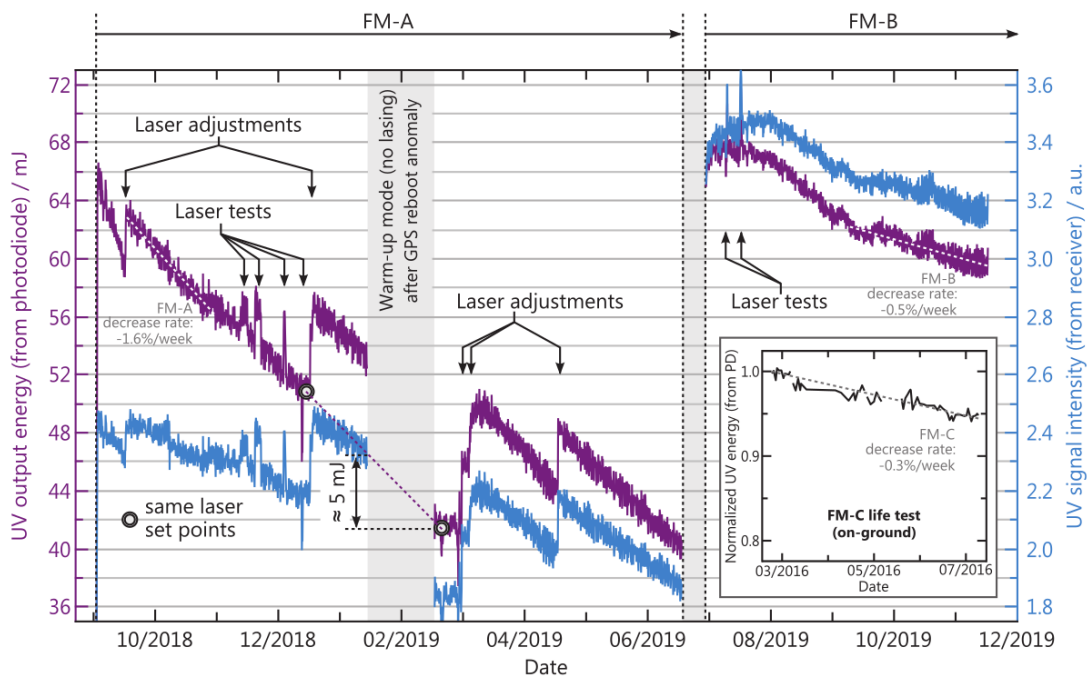


**(b)** Energy measured by Aeolus

**Figure 8.6.:** The reconstructed energy from two-parameter scans of all Aeolus laser transitions (top) and the internally measured laser energy of the Aeolus main beam throughout the first year after launch (bottom), taken from [53]. In the top plot, the dates affected by clouds were discarded. The error bars, including the statistical and systematic uncertainty, do not exceed the size of the markers. In the bottom plot, the measured laser energy is indicated by the violet lines. The energy decreased after launch, causing a switch to the secondary laser in end of June 2019. The laser energy shown here has to be corrected with a transmission factor of 0.704 [54], taking the attenuation within the satellite into account.

similar magnitude, the time of this switch does however not match the two dates listed above. According to the log files of Aeolus, there are also no other incidents corresponding to the 6th of July, that could explain a lower energy [54].

We conclude, that although simulations show, that good estimates of the VAOD and the energy is possible with Aeolus data, the first application to the data still leaves several open questions that need to be studied. As demonstrated by the narrow error ellipse in figure 8.4, the method has a very high statistical sensitivity, but the observed fluctuations in the reconstructed Aeolus energy suggest further systematical effects that need to be investigated. Dedicated simulations of each transition (including the exact number of triggered FD-stations) as well as a detailed comparison to the VAOD profiles from the CLF/XLF will help to improve the understanding of both the Aeolus laser and the aerosol properties above the Pierre Auger Observatory.

# 9. Conclusion

In this thesis, we examined the laser shots of the Aeolus satellite, a new type of artificial light beam, detected by the fluorescence telescopes of the Pierre Auger Observatory. For the first time, this data was systematically analyzed, the simulation and reconstruction framework of Auger was adapted to handle downward going laser shots, and the applicability of the laser shots for aerosol measurements was studied.

In a first step, the ground tracks of the laser beams were predicted, using publicly available information about the satellite position, in the form of so-called two line elements (TLEs). By projecting the laser beam from the satellite's position down onto the ground, the laser impact point can be calculated for different points in time. This allows also for a prediction of the time of day when the laser passes the observatory. By comparing the passage time with the time of sunrise, statements about the visibility throughout the year were made. As a second step, the properties of the laser beams were reconstructed. For this purpose, the existing method of the CLF laser reconstruction was adapted, to also account for a slanted laser beam coming from above. Using this method, the arrival direction of the laser beams is obtained. A new form of directional-constraint monocular reconstruction was used to vastly increase the quality of the reconstructed laser ground tracks. For the energy reconstruction, two approaches were tested in a simulation. The first one is based on a weighted mean, calculated from individual energy measurements. For the second one, a likelihood fit was implemented, containing a scan over the energy as a fit parameter. The likelihood method was then used for a reconstruction of the main and secondary beam energies. A technique was devised to determine the properties of aerosols in the air volume above the observatory with the help of a multidimensional likelihood scan over energy and parameters of an analytic model, which is describing the aerosol transmission as a function of height above ground level. The likelihood scan was tested with simulations in two and three dimensions. Finally, the two-dimensional likelihood scan was applied to the measured laser data.

These investigations led to a number of new results. The projection from TLEs can be used to roughly estimate the laser ground tracks. The periodicity of laser transitions, which is explained by the specific orbit of the satellite, can be understood using these calculations. More precisely, the calculated passage time, based on these TLE tracks, correctly predicts the time of day when the laser is seen by the telescopes. Also the visibility throughout the year, constrained by the time of sunrise, matches the observations. Thus, for the main beam, one can predict a visibility on Saturdays, at around 10:10 UTC, within the months June and July. The secondary beam can be measured on Fridays, at around 9:57 UTC, between mid-May and mid-August. If measurement phases extend into the astronomical twilight the visible time frame is enlarged.

The zenith angle of the main beam is measured to be $37.7° \pm 0.5°$. This is in good agreement with the expected value of $37.1°$, based on the nominal emission angle of Aeolus. The zenith angle of the secondary beam is $58.33° \pm 0.06°$, which also matches the rough estimation

of the secondary beam emission angle as given by ESA. The reconstructed laser beam positions form a straight line corresponding to the ground track. Here, however, the reconstructed ground tracks deviate several kilometers from the predictions provided by the Aeolus team. The reason for this discrepancy is not yet understood, but the difference is much larger than the uncertainty of the geometry reconstruction. As an additional result, the secondary beam radius is estimated to be approximately $550\,\mathrm{m}$.

The reconstruction of simulated laser beams shows that the weighted mean approach of the energy calculation results in a bias for larger beam distances. The alternative likelihood scan improves the energy reconstruction. However, a bias of $\approx 5\,\%$ is still present using this method, which could so far not be explained.

The simulation study of a two and three-dimensional parameter scan confirms that the likelihood scan is able to extract the energy and aerosol parameters. Due to the large number of events during one transition (usually several hundred events), the statistical uncertainty of the energy and VAOD estimates is very small. However, the reconstruction accuracy is dominated by a systematic bias. For the main beam, the simulation shows a systematic bias of $0.5\,\%$ for the energy and $10\,\%$ for the VAOD. The secondary beam has a systematic bias on the energy of about $5\,\%$ and on the VAOD of $1.4\,\%$. Since the origin of this bias is not yet identified, it needs to be accounted for as a systematic uncertainty. It is worthwhile noting that these systematic uncertainties are small with respect to the calibration uncertainty of the telescopes ($11\,\%$) and the precision of the VAOD determined by the method currently applied by the Pierre Auger Collaboration ($\approx 25\,\%$ at a comparable height).

The application of the two-dimensional scan with measured laser shots results in a fit of the laser energy and the VAOD for each Aeolus laser transition. In a detailed likelihood scan of one sample transition a statistical error of $0.2\,\%$ on the energy and $3\,\%$ on the VAOD is achieved. The small statistical uncertainties demonstrate the potential of the Aeolus data, to provide a precise cross-check of the VAOD derived with the monitoring devices employed at the Pierre Auger Observatory.

As a future prospect, a detailed comparison between the VAOD determined in a parameter scan and measurements taken with the CLF will show, how well the two techniques agree. More thorough simulations of different conditions might help to better understand the reconstruction bias and give an explanation for the energy mismatch. Whereas the reconstructed main beam event detected on the 3rd August 2019 was found to be within $1\sigma_{\mathrm{syst}}$ to the nominal value given by the Aeolus team, the other main beam event studied here (detected one month earlier) has a too low reconstructed energy, incompatible with the nominal energy. Further research is also required regarding the discrepancies between the reconstructed laser track and the Aeolus expectation.

Also, a more thorough investigation of additional effects on the reconstruction, only present for real data, is necessary. For example, calibration uncertainties between the individual telescopes could cause a bias of the reconstructed parameters. Such effects are not yet included in a simulation of the laser beams. Also, a possible polarization of the secondary beam might have an impact on the reconstruction. While the main beam is circularly polarized, this is not necessarily true for the secondary beam. Finally, also the observed bias between simulation and reconstruction has to be understood, to improve the parameter scan.

Another future field of study could be the test of horizontal uniformity with the help of the Aeolus laser. So far, the horizontal uniformity was implicitly assumed to gain information about the VAOD. In a different approach, one could, for example, divide one laser transition into multiple parts, to test how much the reconstructed VAOD changes during the transition.

If the Aeolus lasers could also be detected by Telescope Array, the interesting prospect of a direct comparison between the two experiments arises. This would allow, for the first time, a direct cross-calibration of the energy scales of the two observatories. It was shown, that the Aeolus laser tracks also cross the area of Telescope Array, albeit during the beginning of dawn. Therefore special precautions need to be taken, to extend measurements into the astronomical twilight. This is an encouraging prospect, since the Aeolus mission is planned to continue beyond its original lifetime, up until the end of 2022.

# Appendix

## A. Characterization of the Individual Nights with Measured Aeolus Shots

On the following pages, a characterization of the individual laser transitions is given, first for the secondary beam, then for the main beam. Included are plots showing the ground positions of the laser events (resulting from a monocular reconstruction with fixed angles), a histogram of the laser energies (based on likelihood scans for each individual event, with the aerosols set to average values), a plot that shows the energy as a function of time and a plot showing the energy as a function of the altitude over sea level. For each transition, also the average energy and number of events is listed for each eye individually. On a second page, the camera output is shown (where the coloring of each pixel indicates the average signal charge over the whole transition) above an image of the corresponding cloud camera, if available. An overview is given in the tables A.1 and A.2.

### A.1. Fridays

**Table A.1.:** Overview of the Fridays with measurements of the Aeolus secondary beam. Listed are the individual dates with an assessment of the data quality, based on the presence of clouds. Also listed is the average energy of the transition, calculated with an average aerosol concentration. The number of events corresponds to FD-events, meaning that individual eyes are counted separately.

| Date | Data Quality | $\langle E \rangle$/PeV | # Events |
|------------|--------------|---------|----------|
| 31.05.2019 | usable | 4.5 | 470 |
| 07.06.2019 | usable | 5.0 | 594 |
| 28.06.2019 | unusable | 10.6 | 306 |
| 05.07.2019 | usable | 6.1 | 113 |
| 02.08.2019 | usable | 7.2 | 652 |
| 09.08.2019 | usable | 6.8 | 621 |
| 01.05.2020 | usable | 4.7 | 542 |
| 22.05.2020 | ambiguous | 4.6 | 339 |
| 29.05.2020 | unusable | 5.2 | 414 |
| 26.06.2020 | unusable | 7.1 | 387 |
| 17.07.2020 | unusable | 5.6 | 98 |
| 24.07.2020 | unusable | 10.8 | 282 |

# 31.05.2019 - usable
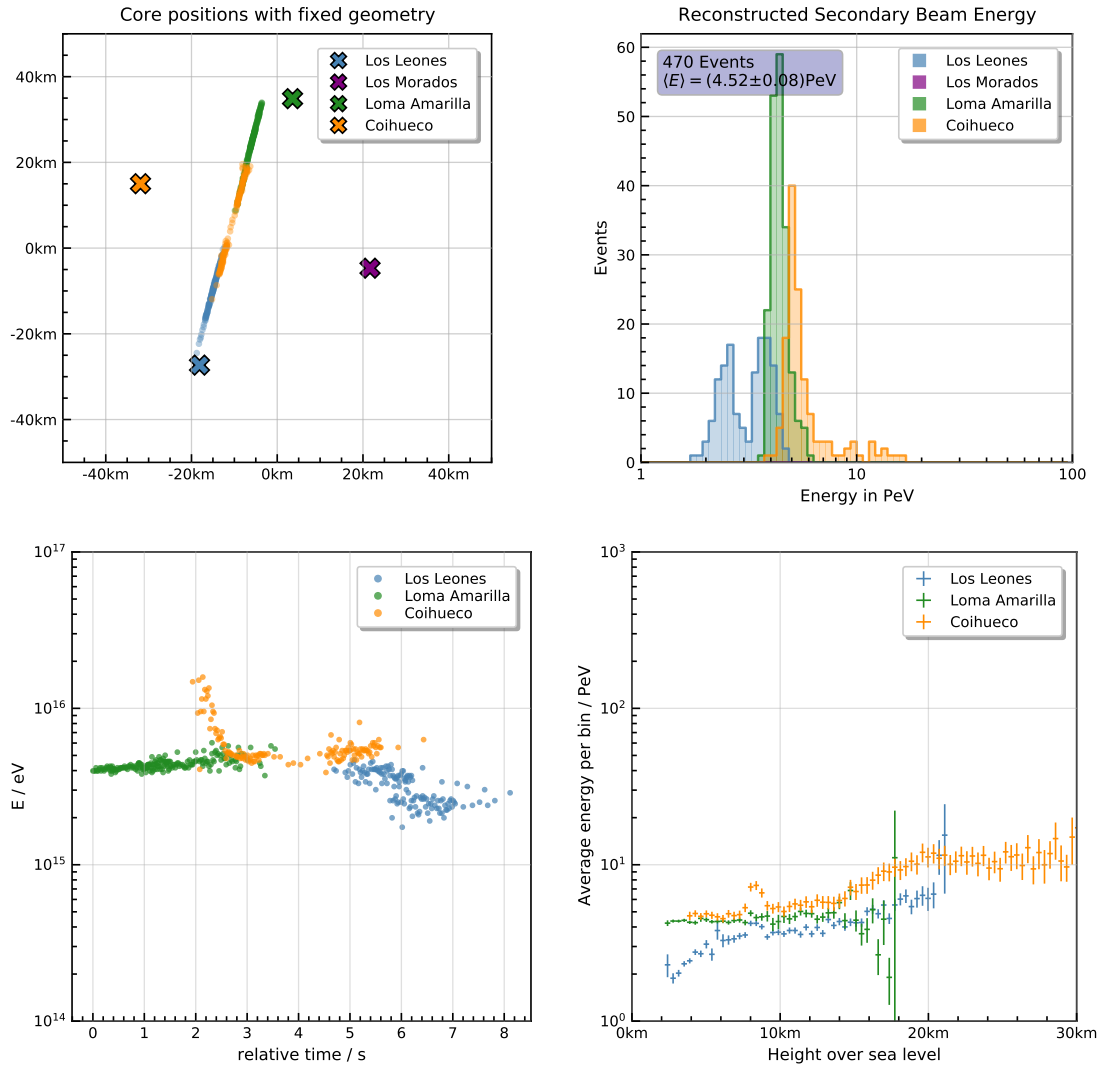


| FD Station | $\langle E\rangle$/PeV | # Events |
|---|---|---|
| Los Leones | 3.18 | 141 |
| Los Morados | - | 0 |
| Loma Amarilla | 4.41 | 194 |
| Coihueco | 6.06 | 135 |
| Total | 4.52 | 470 |

**Comments**

There is a possible hint for a cloud in Coihueco, however without a large impact on the energy reconstruction.
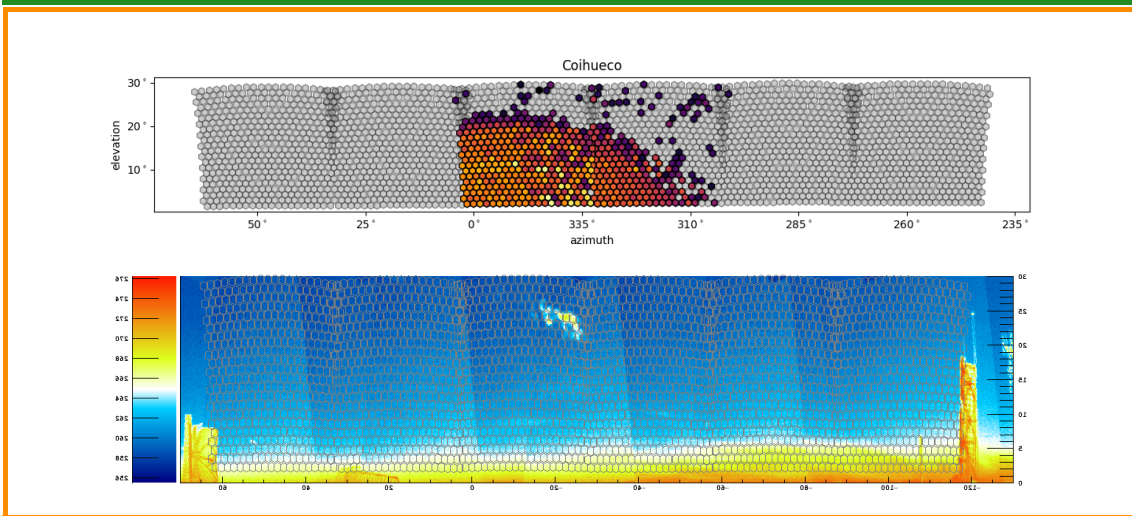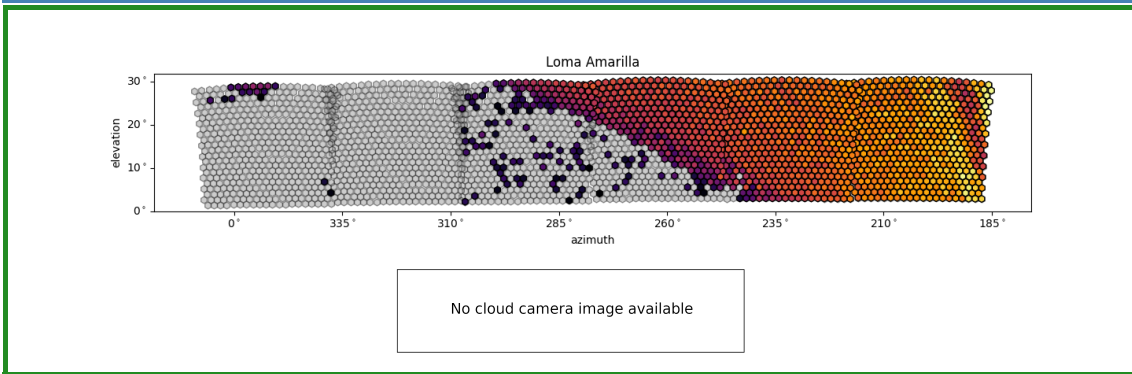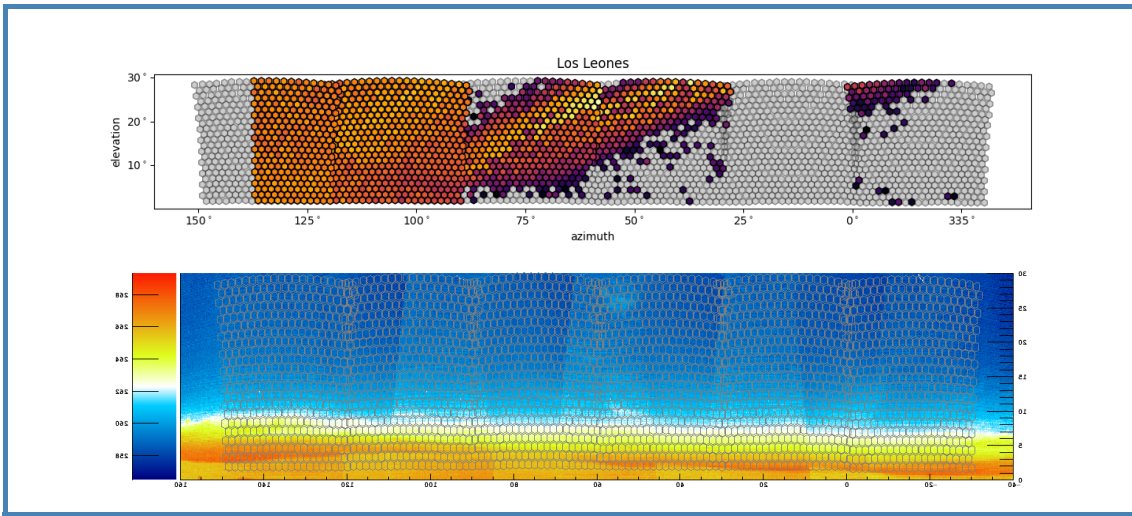
# 07.06.2019 - usable
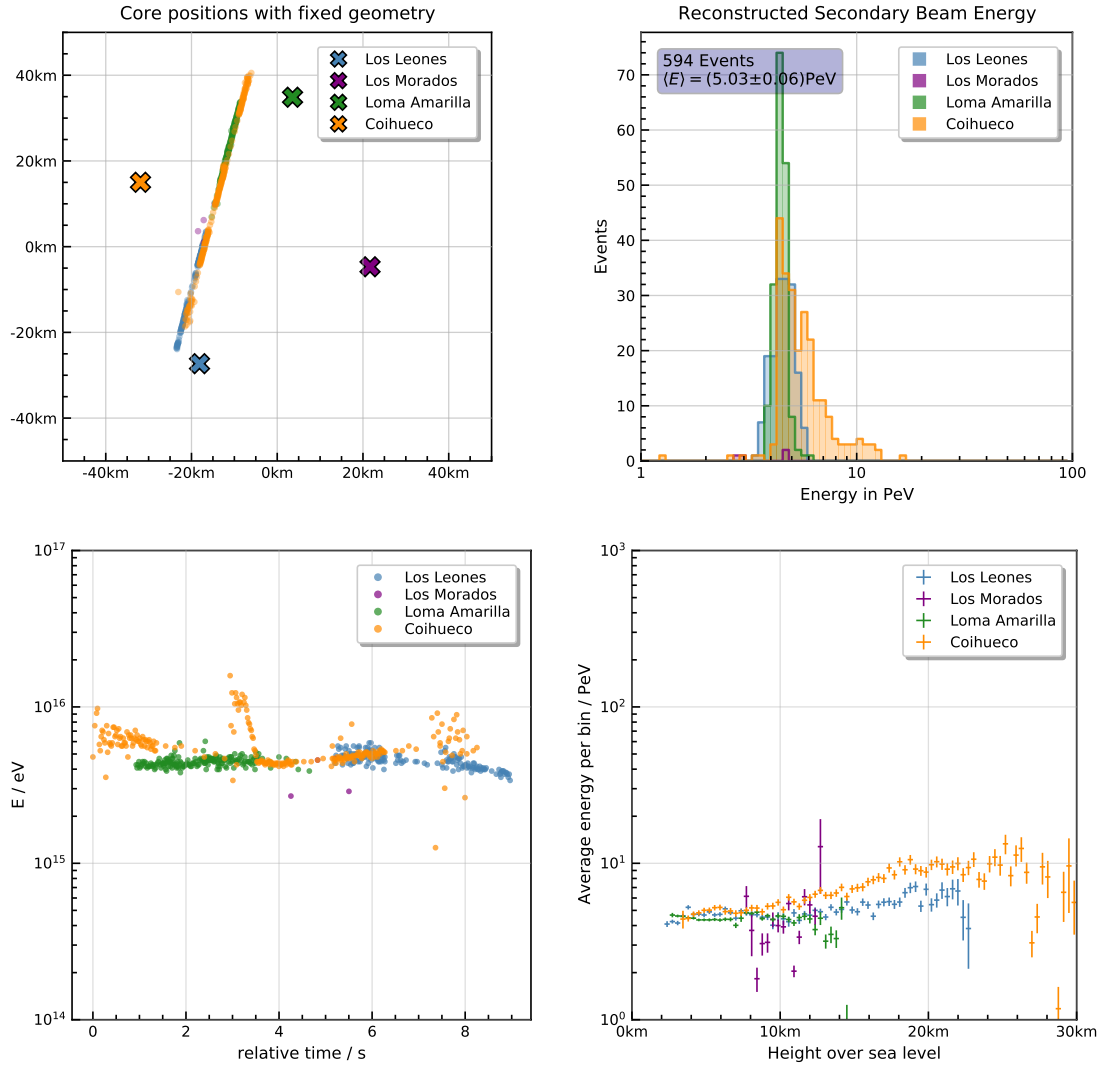


| FD Station | $\langle E \rangle$/PeV | # Events |
|---|---|---|
| Los Leones | 4.58 | 166 |
| Los Morados | 3.71 | 4 |
| Loma Amarilla | 4.45 | 182 |
| Coihueco | 5.79 | 242 |
| Total | 5.03 | 594 |

**Comments**
No indications for clouds.

Los Leones



Los Morados



Loma Amarilla

No cloud camera image available
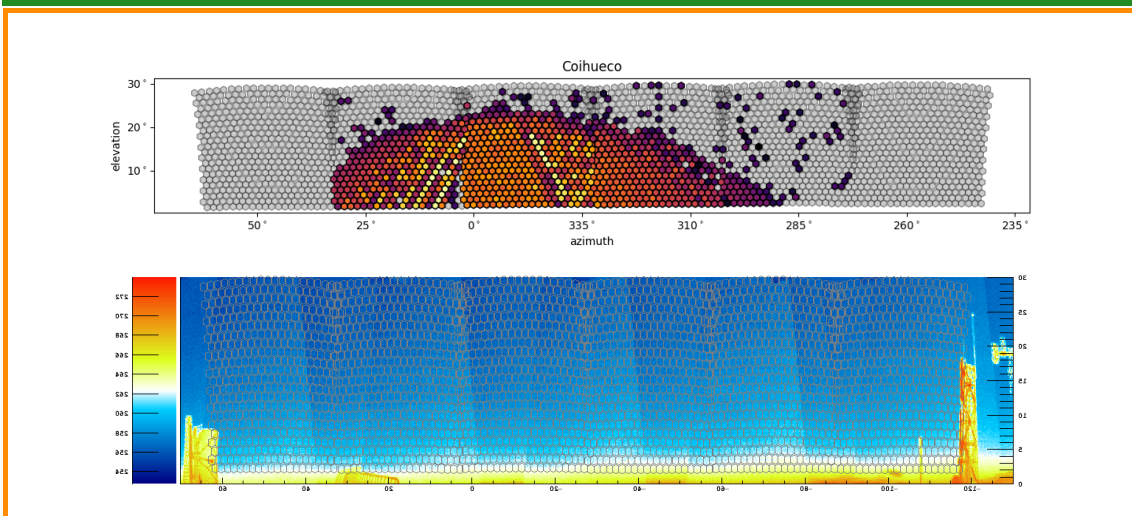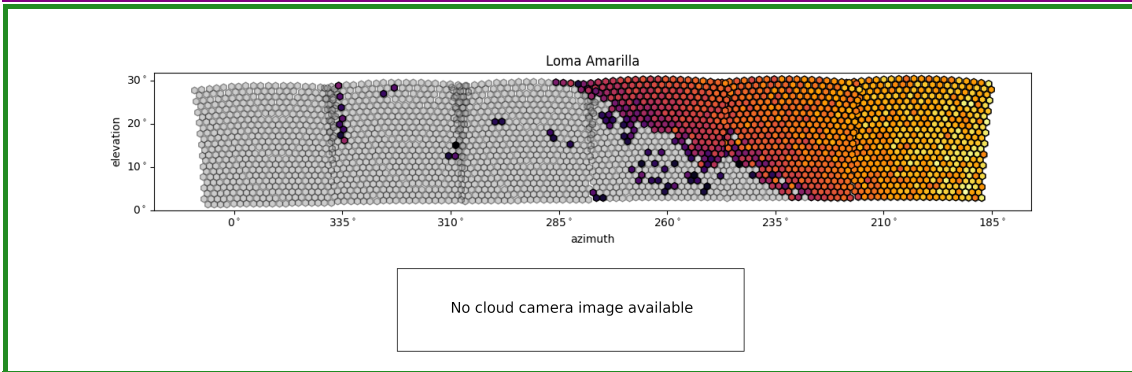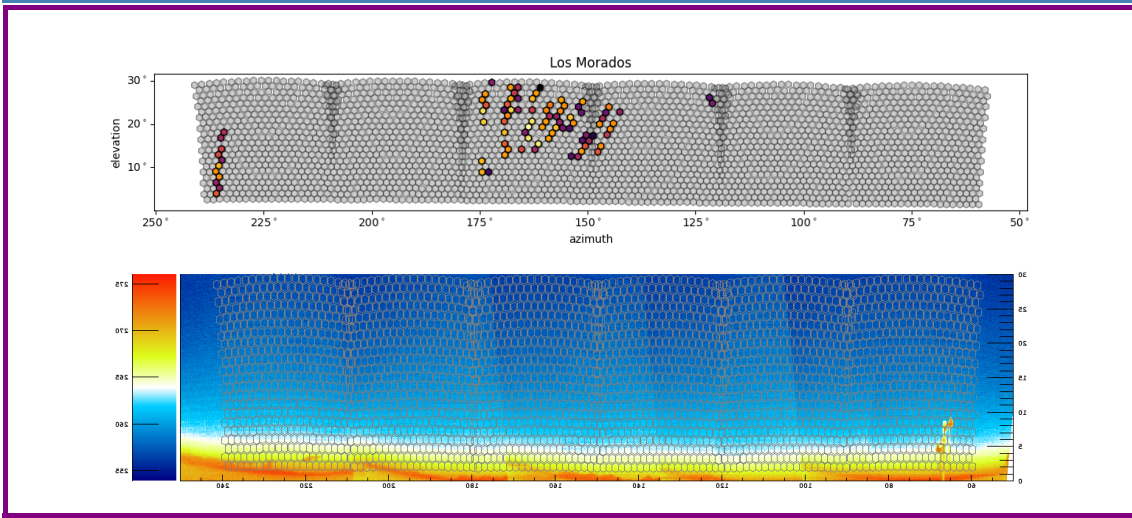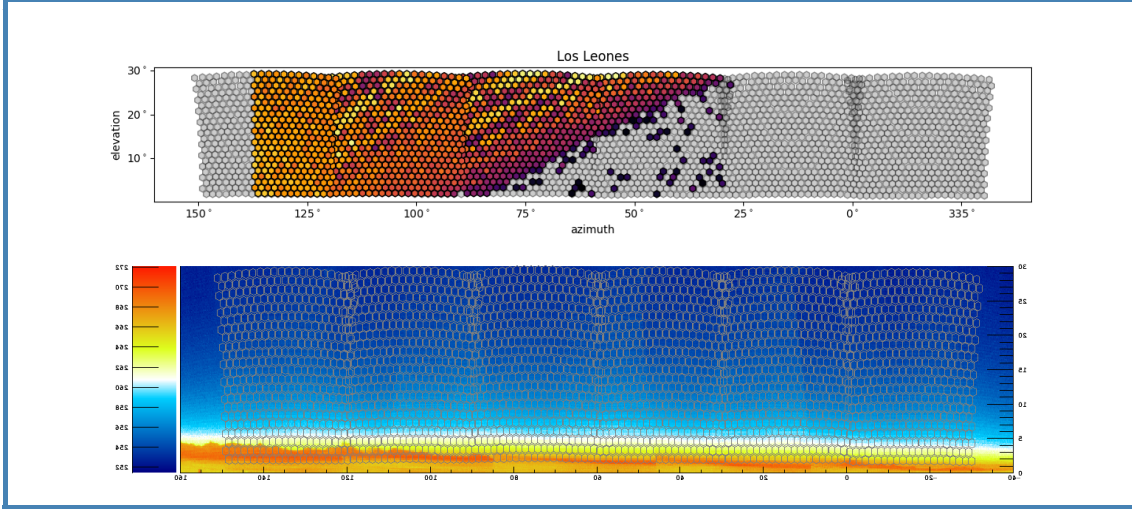
Coihueco

# 28.06.2019 - unusable
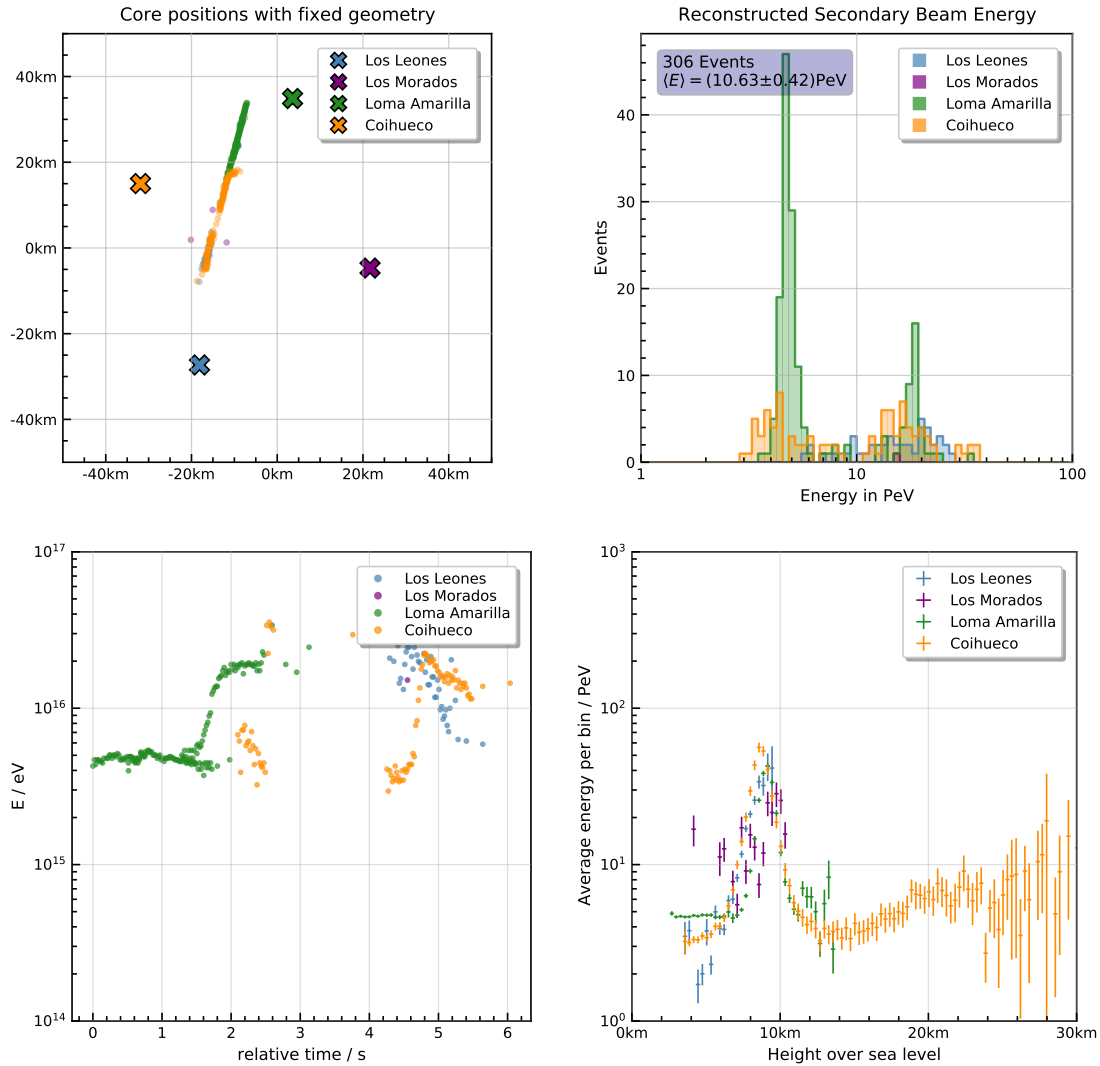


| FD Station | $\langle E \rangle$/PeV | # Events |
|---|---|---|
| Los Leones | 16.13 | 43 |
| Los Morados | 15.14 | 1 |
| Loma Amarilla | 8.37 | 167 |
| Coihueco | 12.06 | 95 |
| Total | 10.63 | 306 |

**Comments**

A clear indication for clouds can be seen both in the height plot and the camera images. The energy vs. time plot shows an increase in energy for Loma Amarilla, as soon as the cloud is hit by the laser.

Los Leones

No cloud camera image available



Los Morados



Loma Amarilla

No cloud camera image available
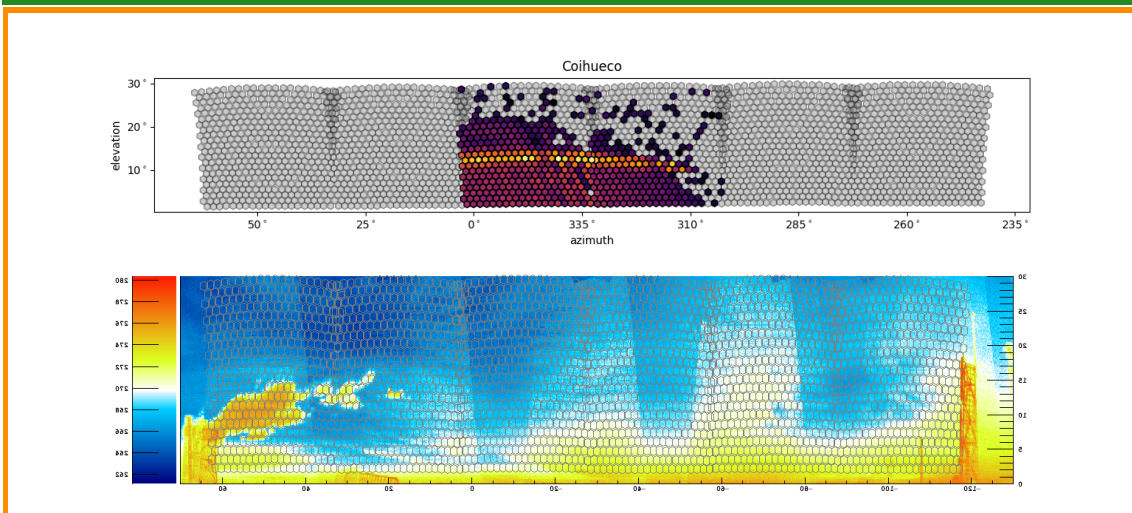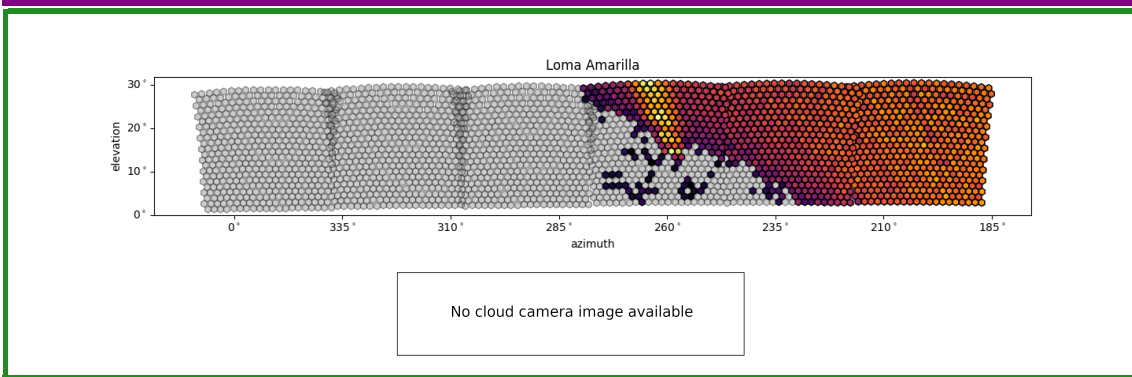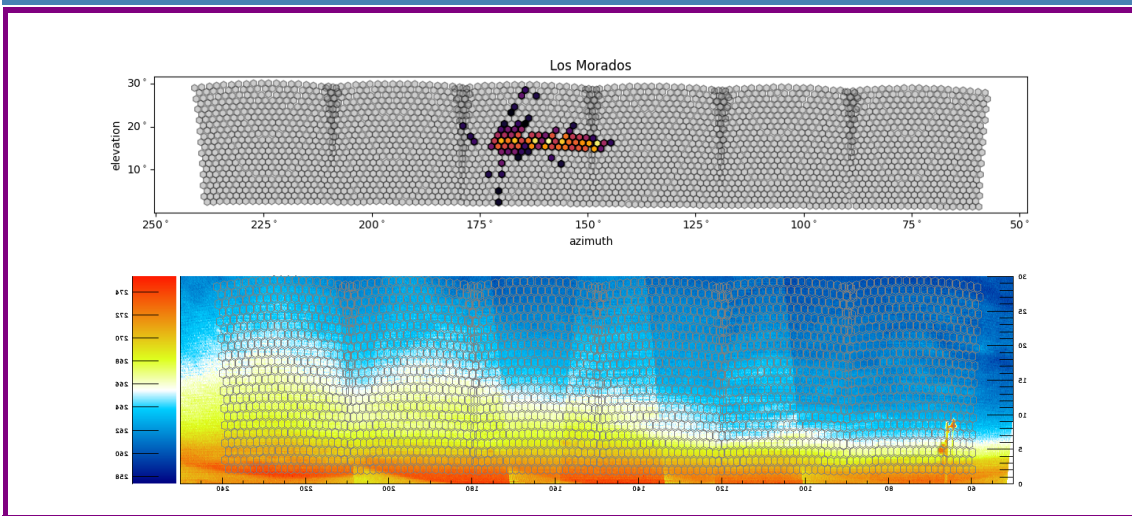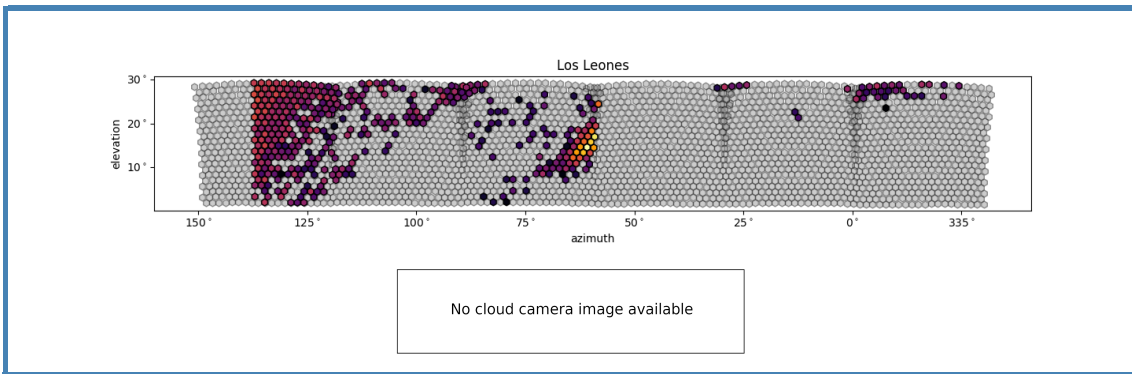


Coihueco

# 05.07.2019 - usable
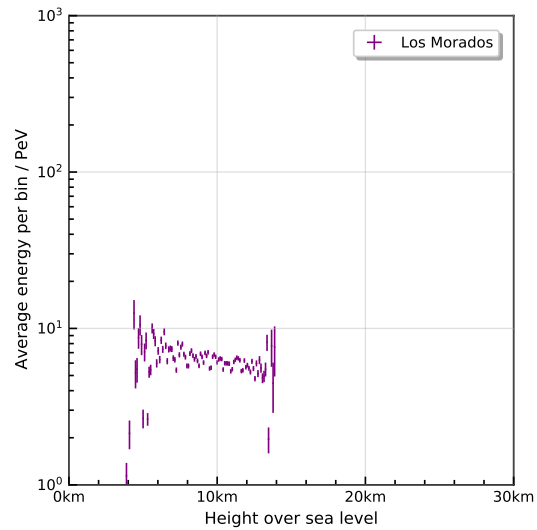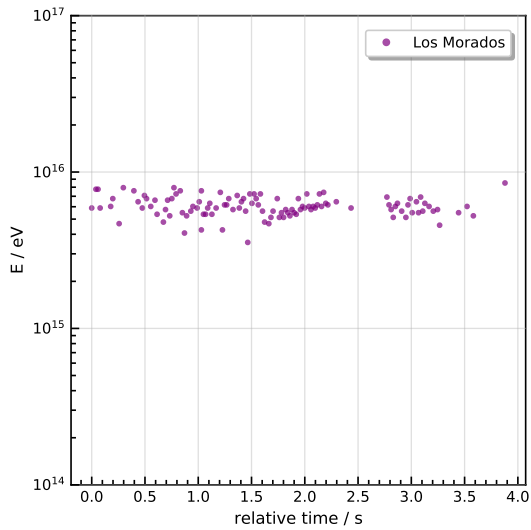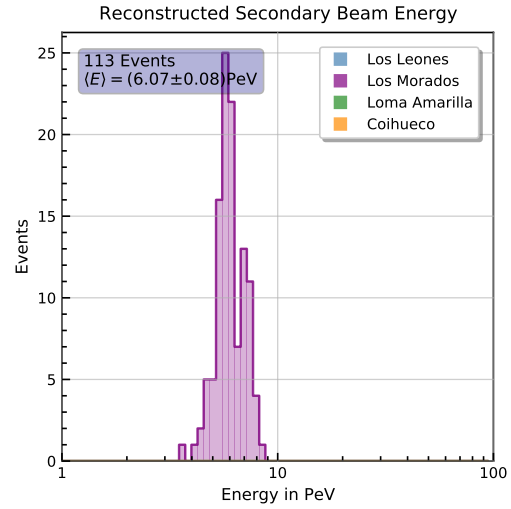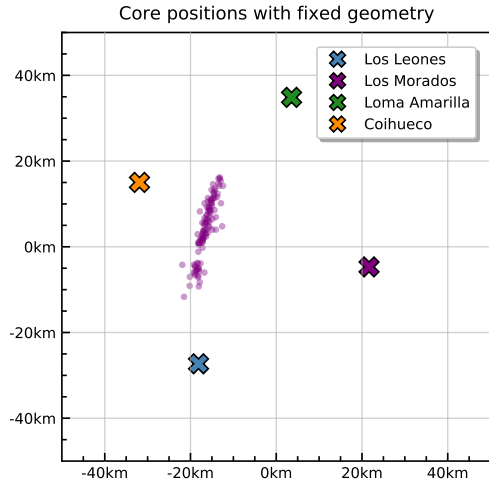


| FD Station | $\langle E \rangle$/PeV | # Events |
|---|---|---|
| Los Leones | - | 0 |
| Los Morados | 6.07 | 113 |
| Loma Amarilla | - | 0 |
| Coihueco | - | 0 |
| Total | 6.07 | 113 |

**Comments**
Los Morados is the only FD station that measured Aeolus events in this night. The other stations already terminated the measurement, due to the imminent dawn.
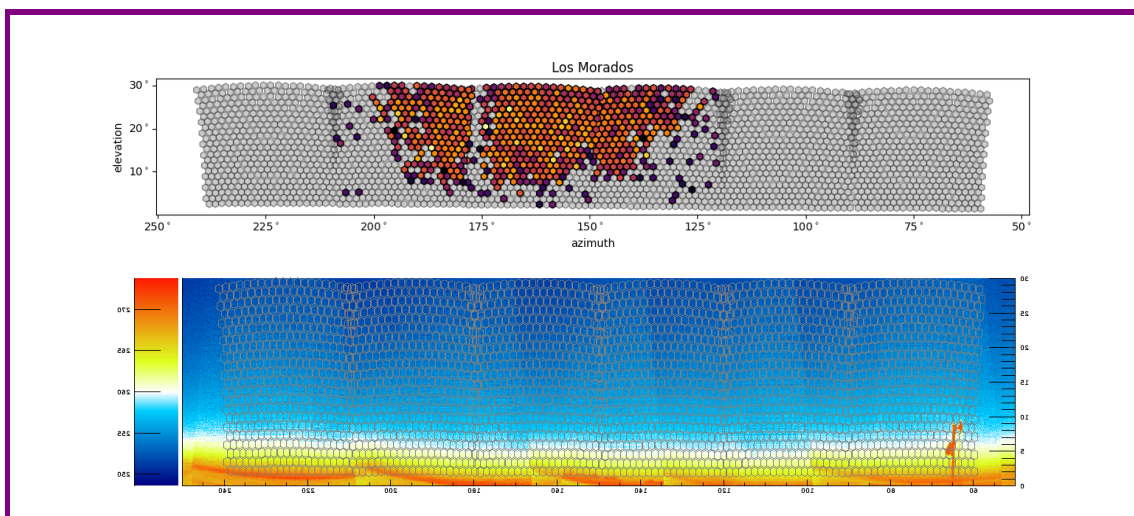
Los Morados
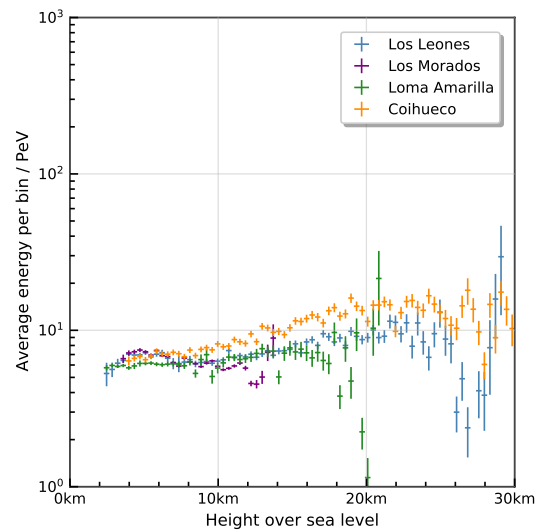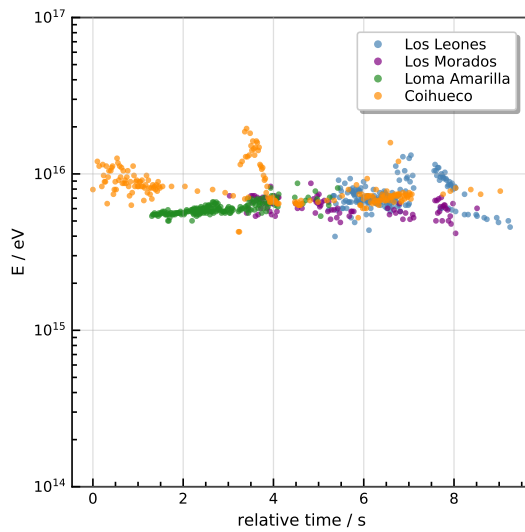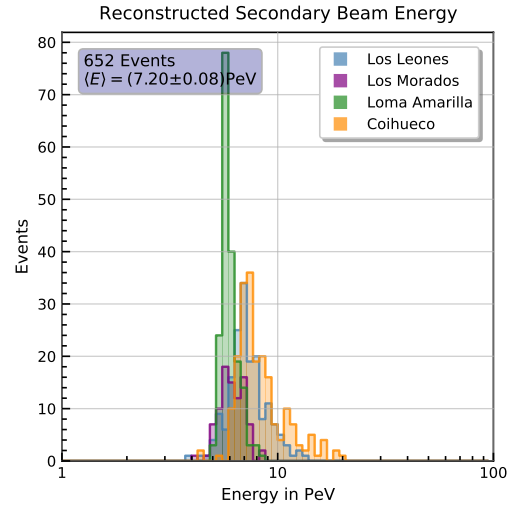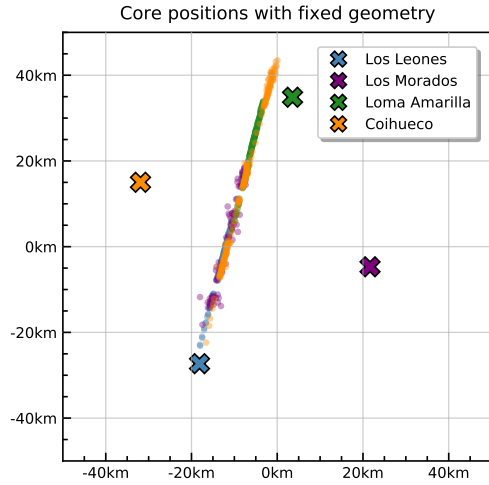
# 02.08.2019 - usable



| FD Station | $\langle E \rangle$/PeV | # Events |
|---|---|---|
| Los Leones | 7.38 | 174 |
| Los Morados | 6.18 | 89 |
| Loma Amarilla | 6.03 | 185 |
| Coihueco | 8.56 | 204 |
| Total | 7.20 | 652 |

**Comments**
No indications for clouds.

Los Leones



Los Morados

No cloud camera image available

Loma Amarilla

No cloud camera image available

Coihueco

No cloud camera image available
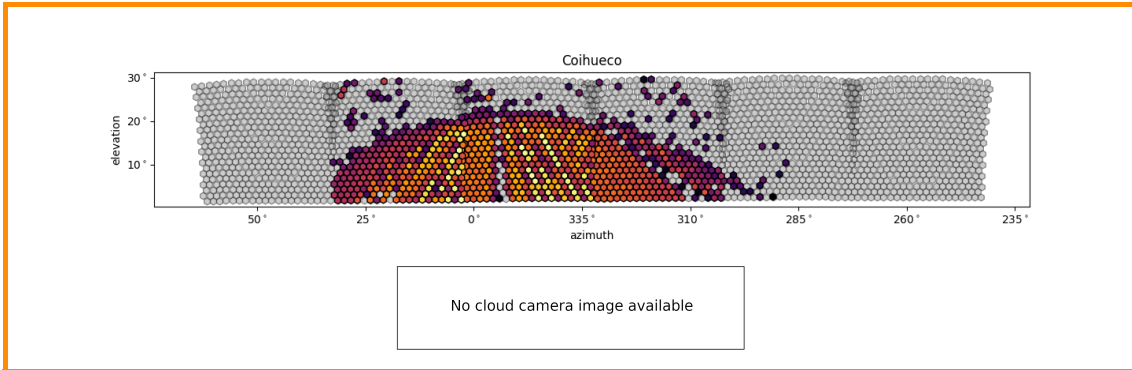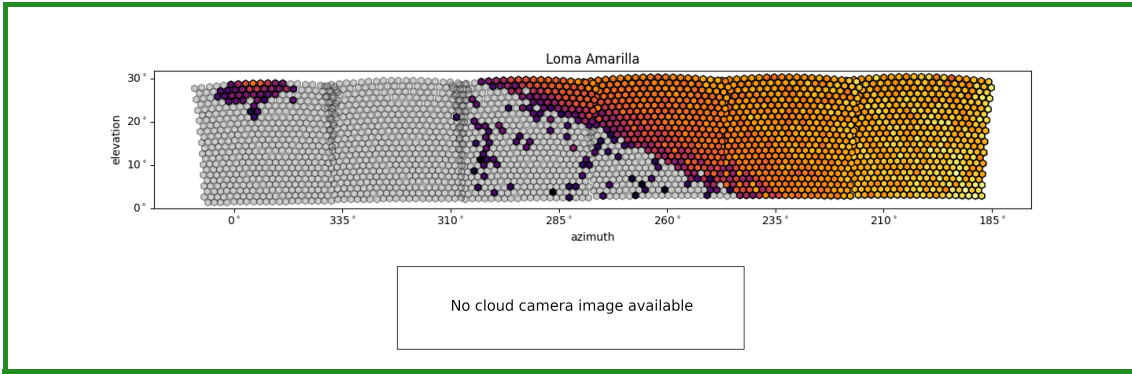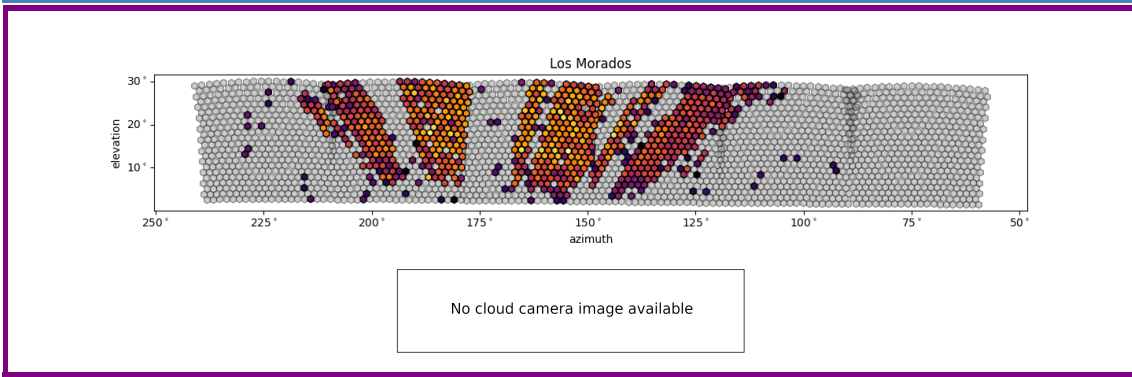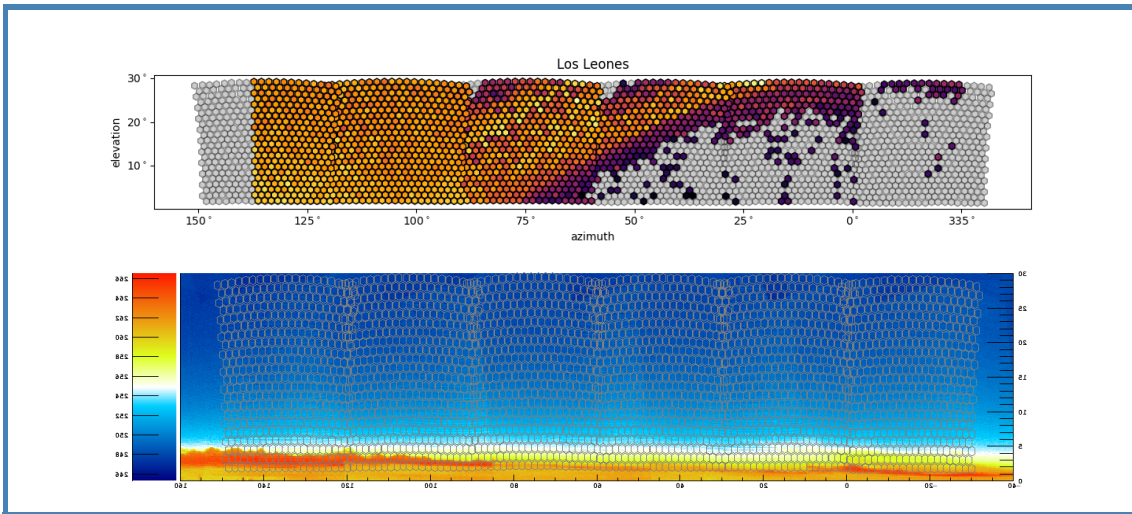
# 09.08.2019 - usable
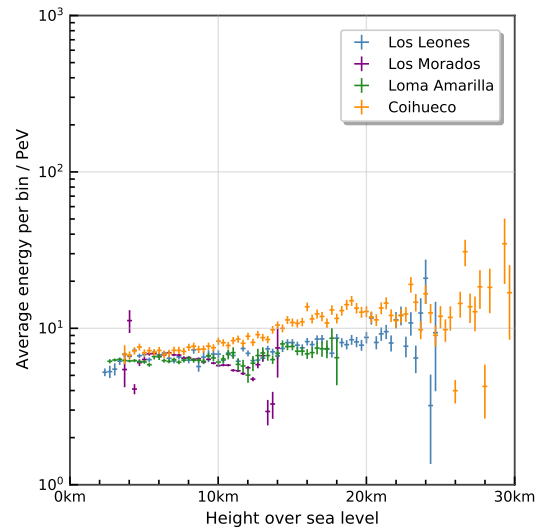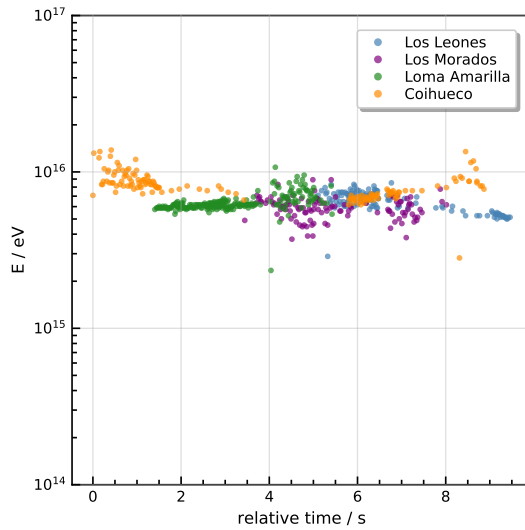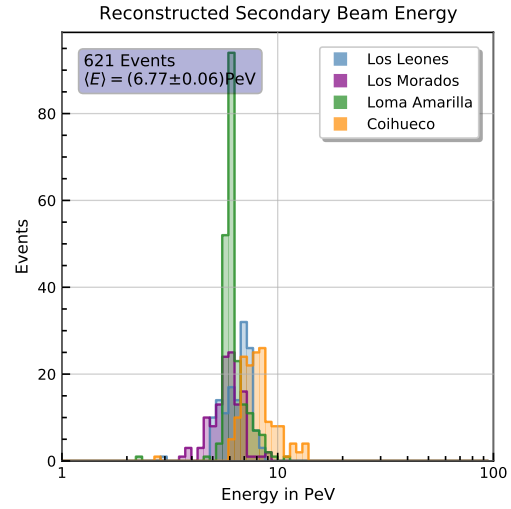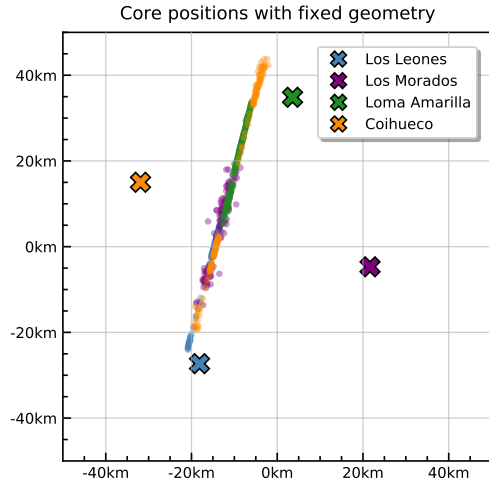


| FD Station | $\langle E \rangle$/PeV | # Events |
|---|---|---|
| Los Leones | 6.53 | 135 |
| Los Morados | 5.90 | 121 |
| Loma Amarilla | 6.38 | 216 |
| Coihueco | 8.26 | 149 |
| Total | 6.77 | 621 |

**Comments**
No indications for clouds.

Los Leones



Los Morados

No cloud camera image available



Loma Amarilla

No cloud camera image available



Coihueco

No cloud camera image available
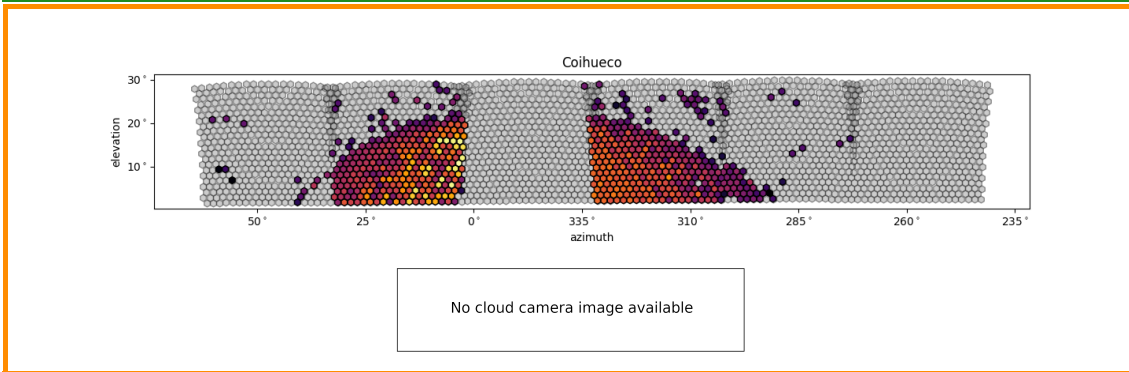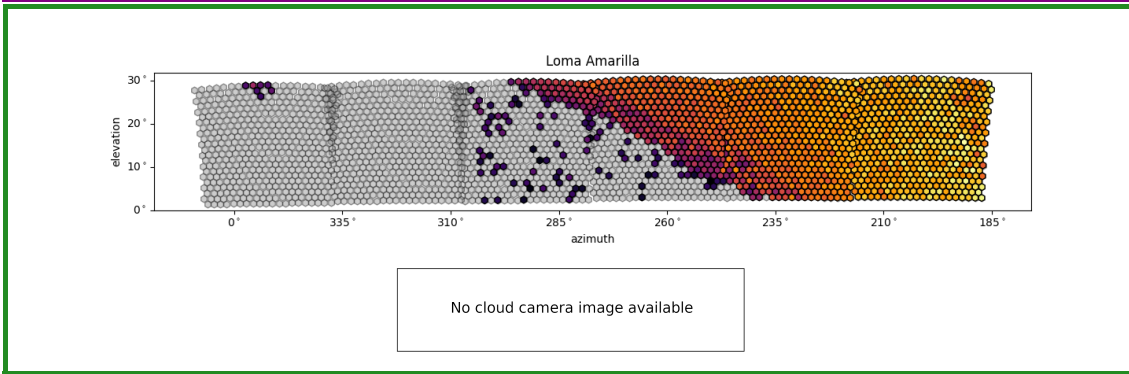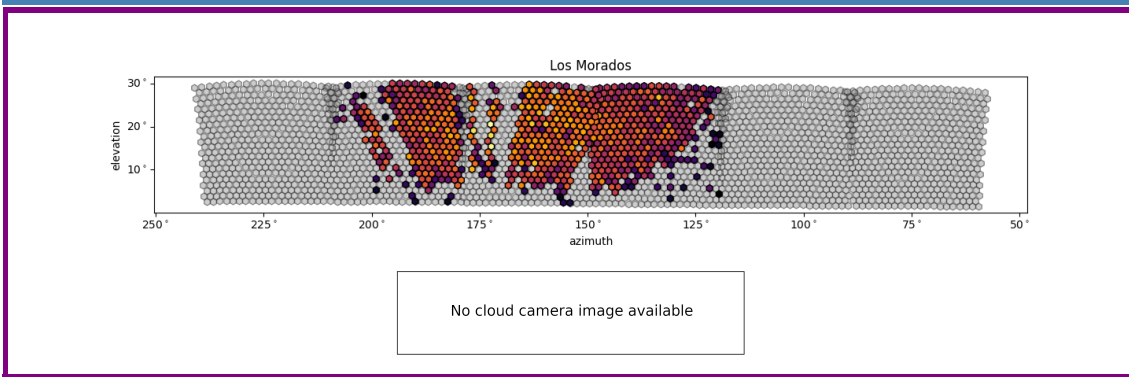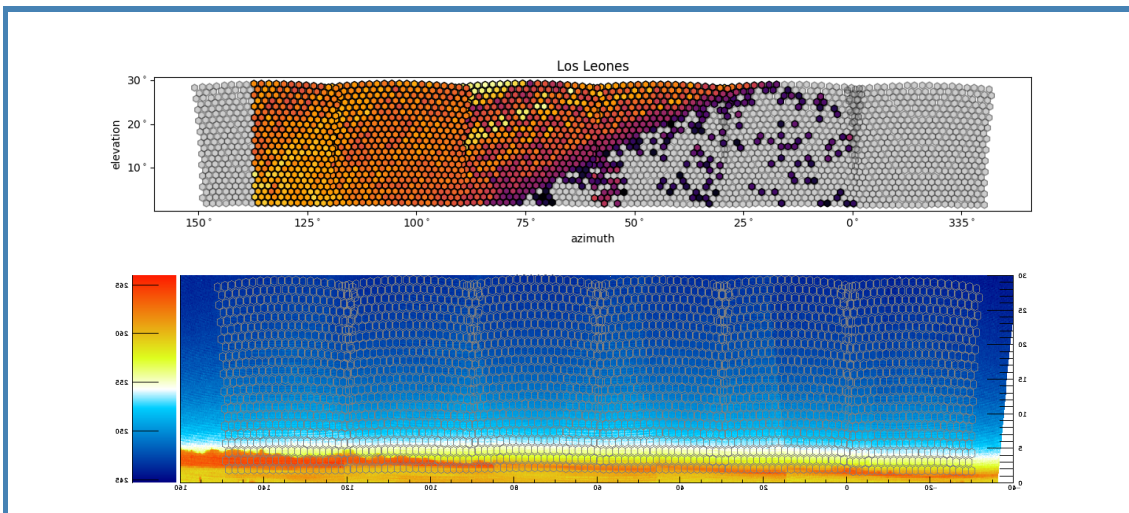
# 01.05.2020 - usable
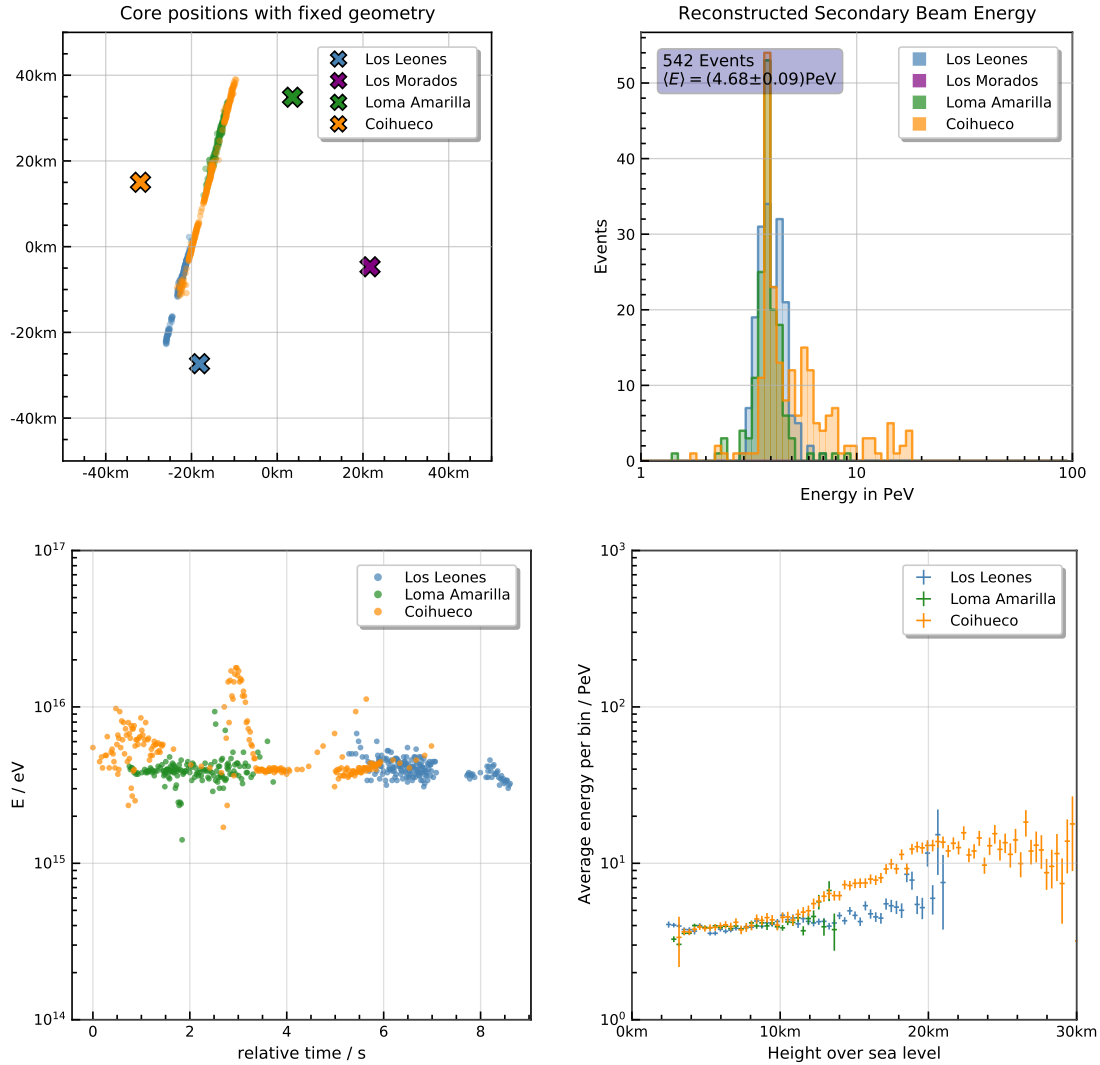


| FD Station | $\langle E \rangle$/PeV | # Events |
|---|---|---|
| Los Leones | 4.09 | 182 |
| Los Morados | - | 0 |
| Loma Amarilla | 3.96 | 152 |
| Coihueco | 5.73 | 208 |
| Total | 4.68 | 542 |

**Comments**
No indications for clouds.

Los Leones

Loma Amarilla

No cloud camera image available

Coihueco

No cloud camera image available
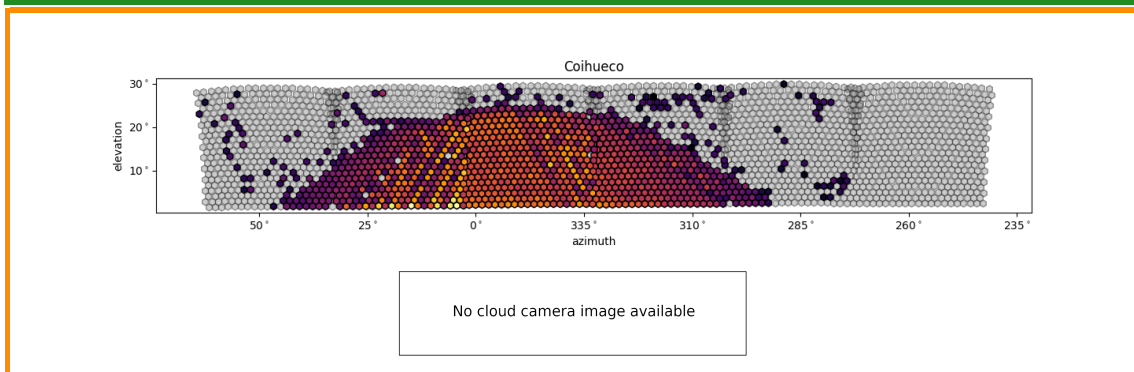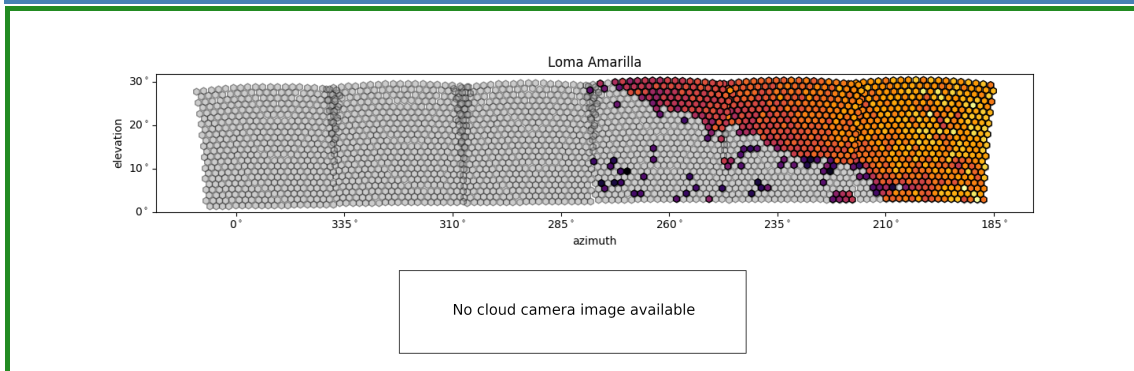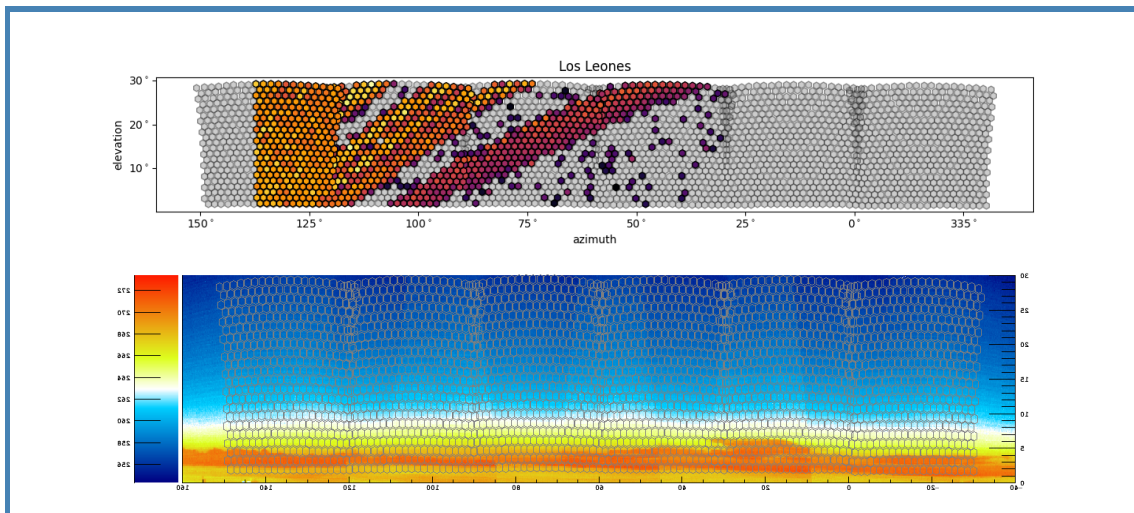
# 22.05.2020 - ambiguous
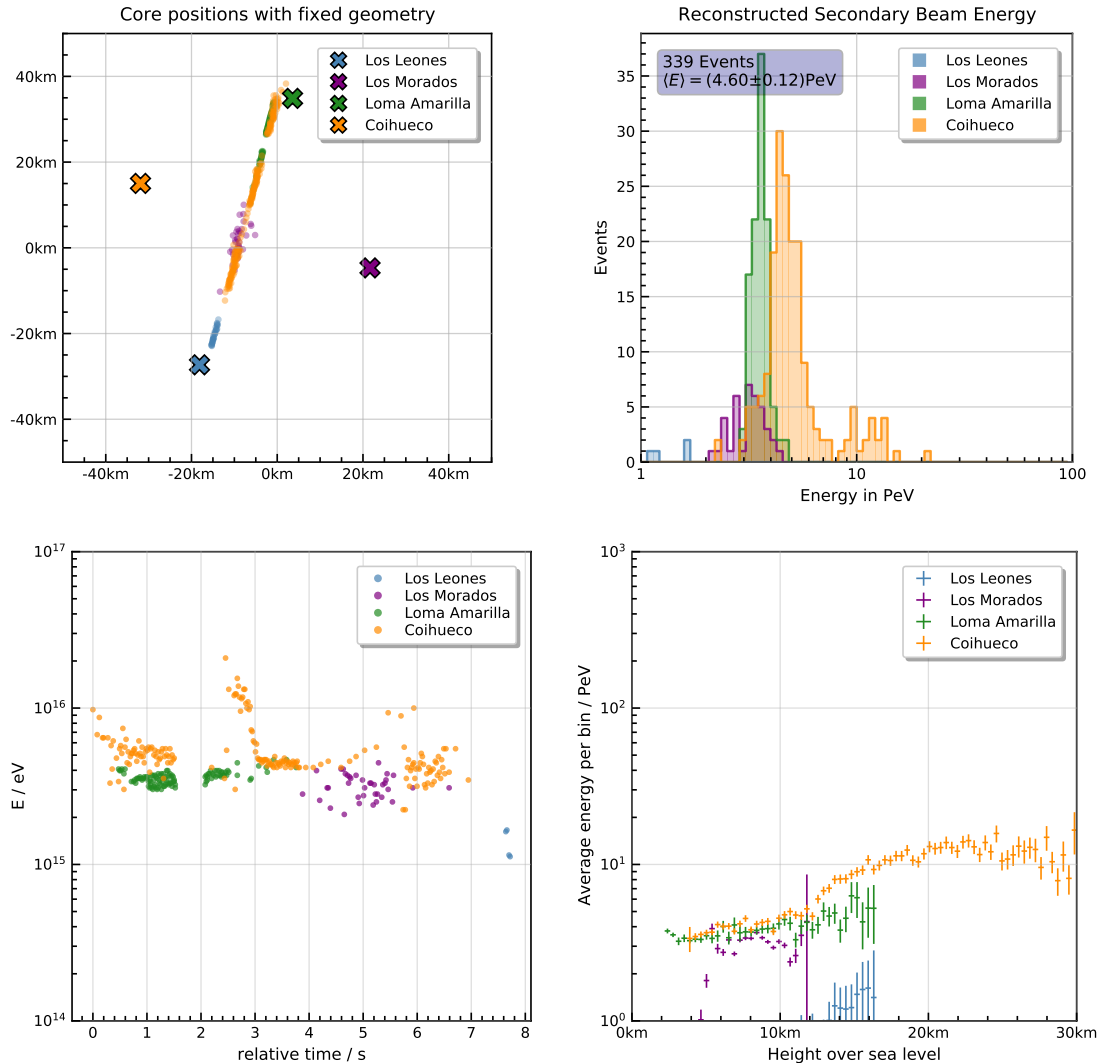


| FD Station | $\langle E\rangle$/PeV | # Events |
|---|---|---|
| Los Leones | 1.39 | 4 |
| Los Morados | 3.19 | 38 |
| Loma Amarilla | 3.61 | 110 |
| Coihueco | 5.53 | 187 |
| Total | 4.60 | 339 |

**Comments**
The cloud camera image of Los Morados shows the presence of clouds and the array of pixels for Los Leones shows a brighter spot. The indication for clouds is however not very distinct. The energy-height-plot for example does not show a characteristic peak.

Los Leones



No cloud camera image available

Los Morados



Loma Amarilla



No cloud camera image available

Coihueco



No cloud camera image available
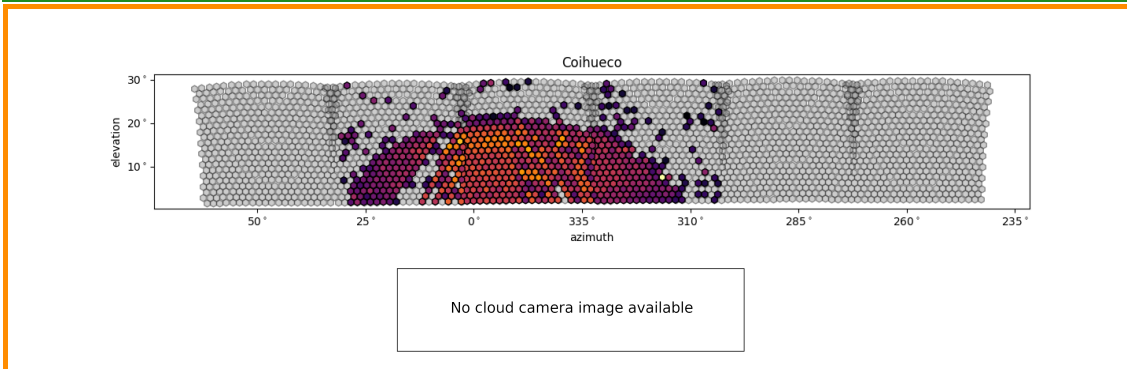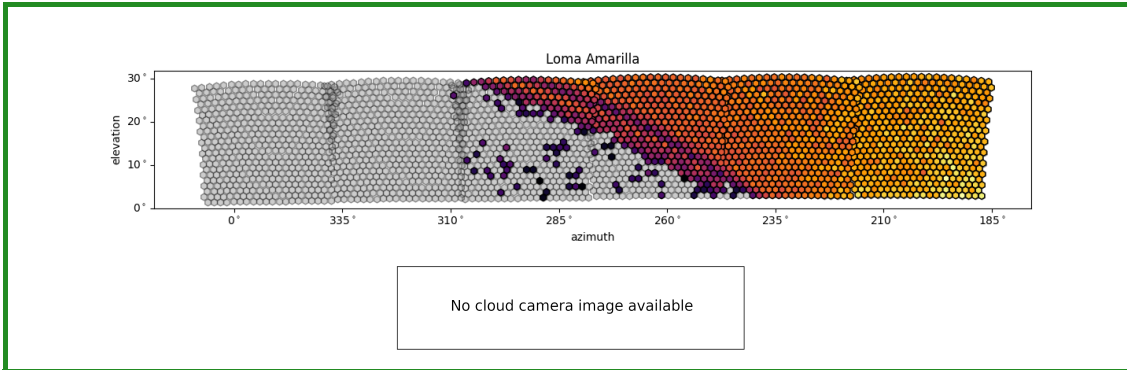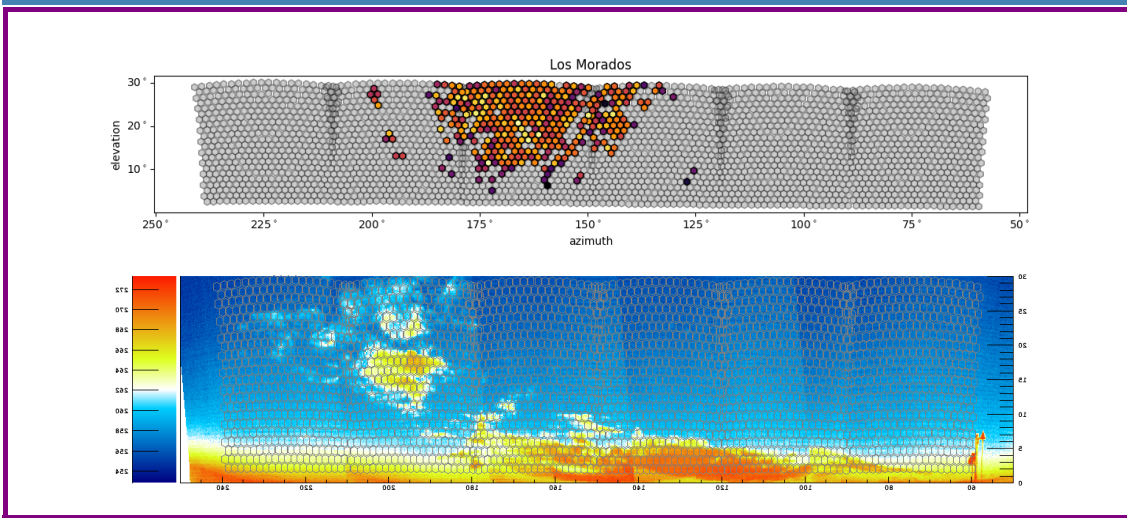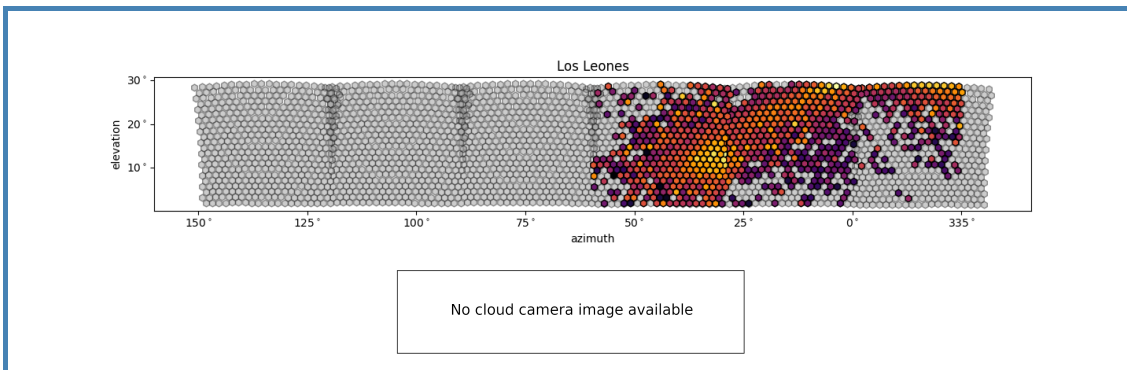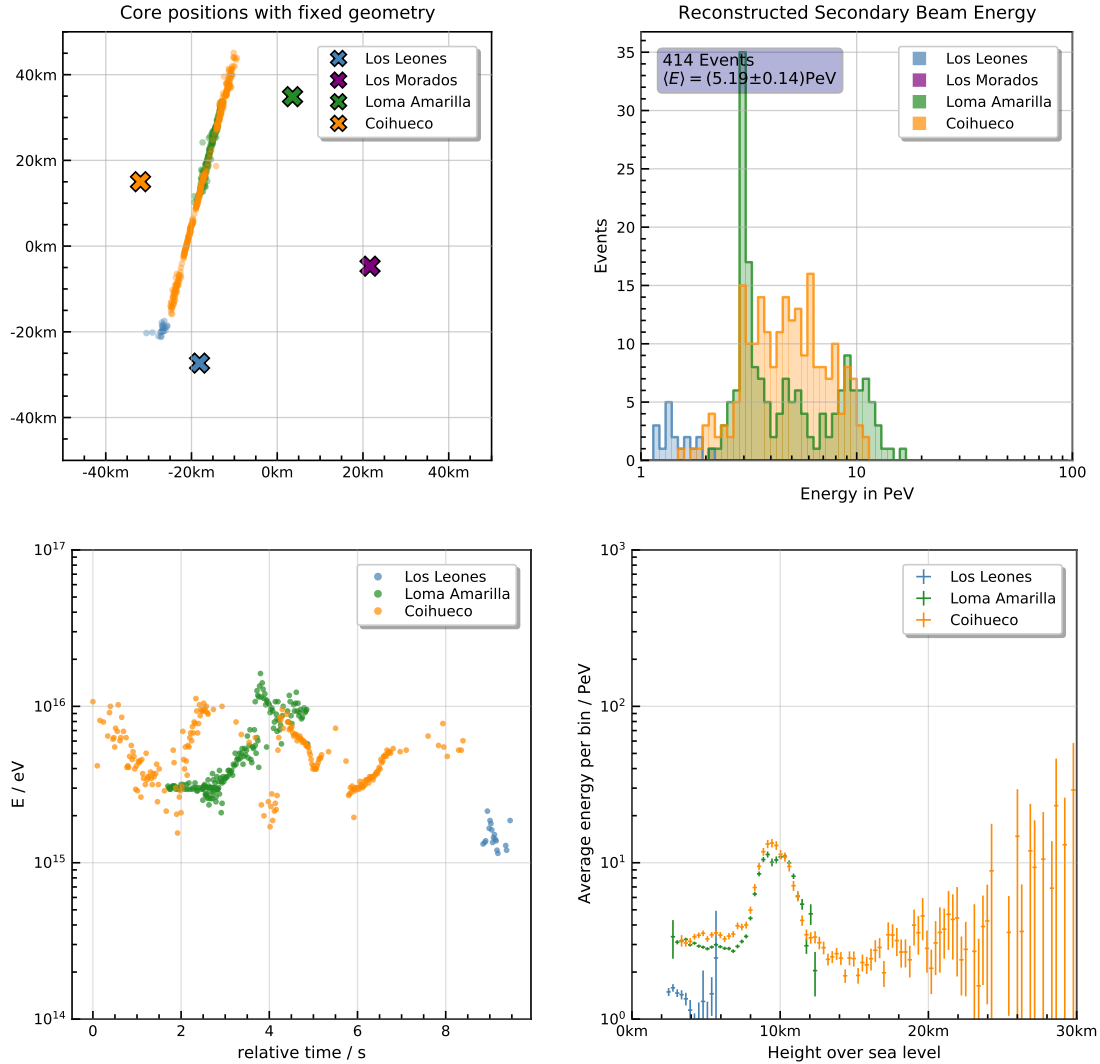
# 29.05.2020 - unusable



| FD Station | $\langle E \rangle$/PeV | # Events |
|---|---|---|
| Los Leones | 1.50 | 18 |
| Los Morados | - | 0 |
| Loma Amarilla | 5.59 | 174 |
| Coihueco | 5.17 | 222 |
| Total | 5.19 | 414 |

**Comments**
Indications for clouds can be seen in both the camera images, the pixel arrays and the energy-height-plot.
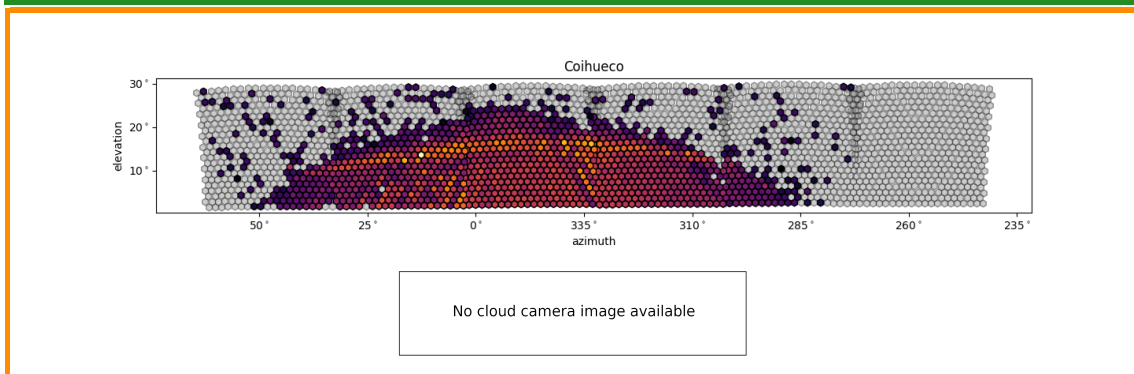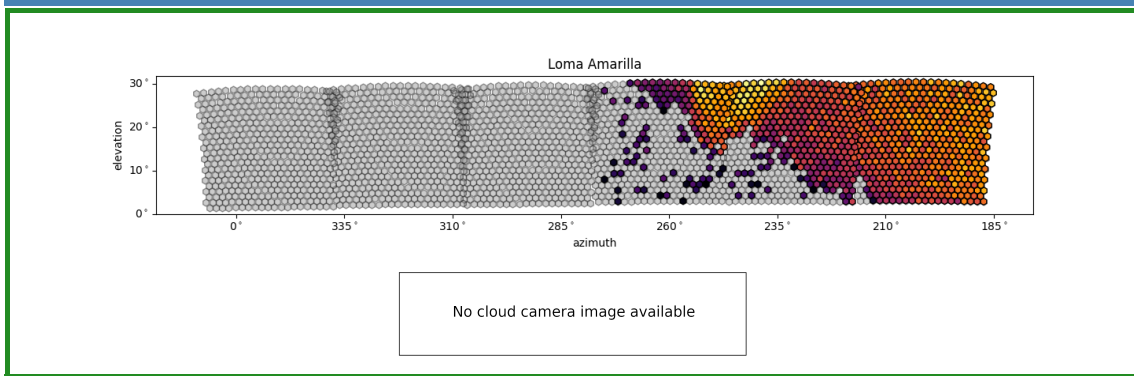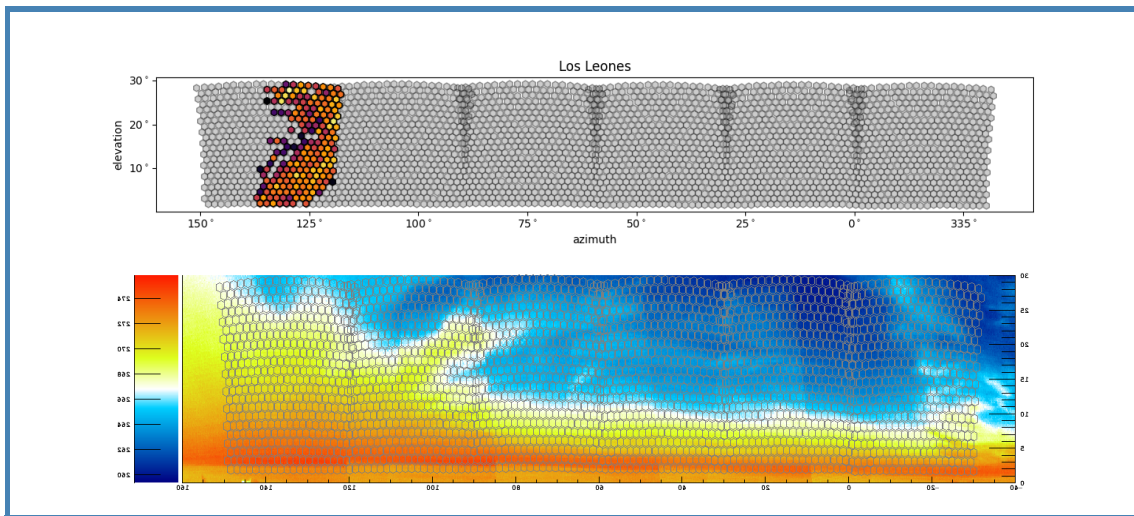
# 26.06.2020 - unusable
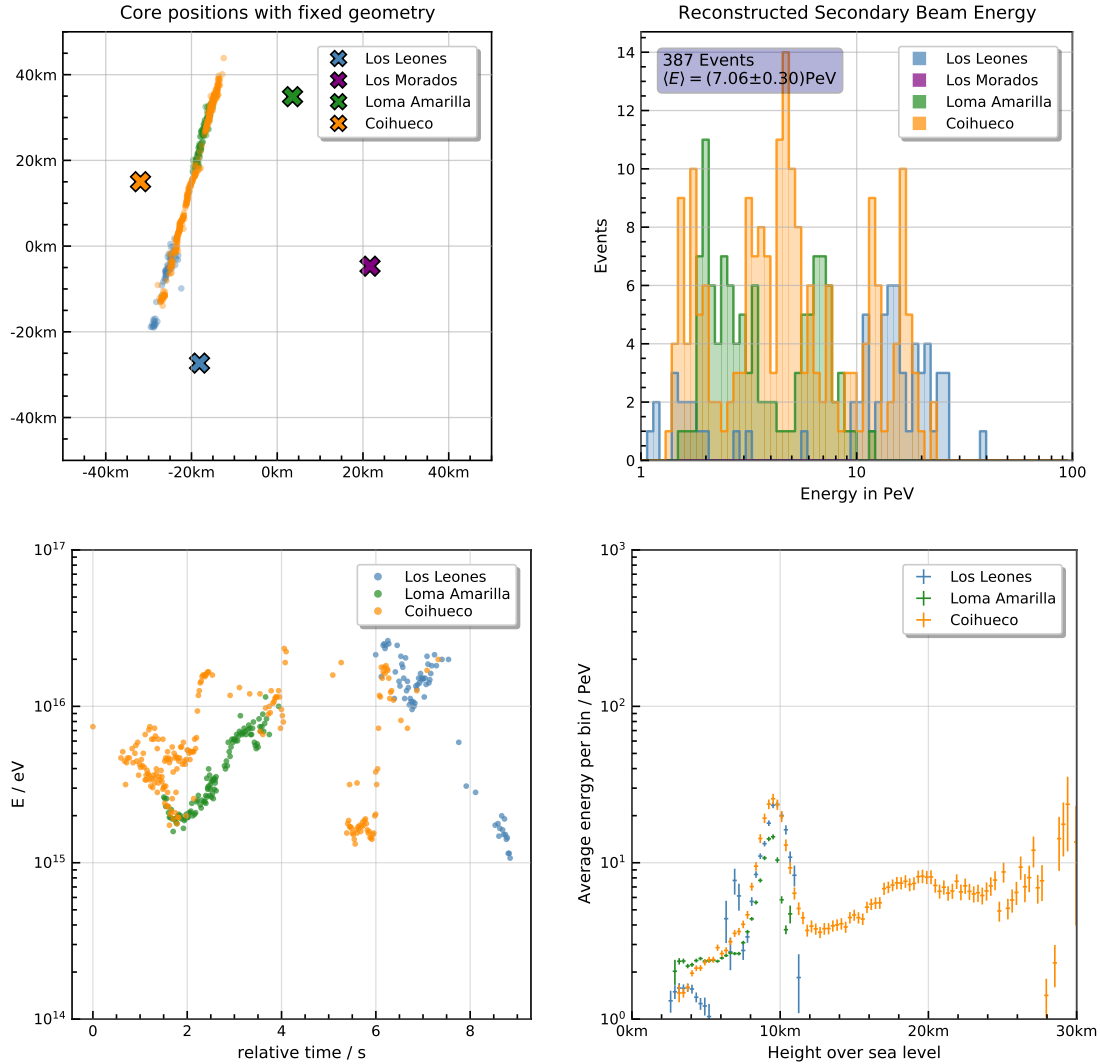


| FD Station | $\langle E \rangle$/PeV | # Events |
|------------|------------|----------|
| Los Leones | 13.16 | 69 |
| Los Morados | - | 0 |
| Loma Amarilla | 4.23 | 112 |
| Coihueco | 6.55 | 206 |
| Total | 7.06 | 387 |

**Comments**

Indications for clouds can be seen in both the camera images, the pixel arrays and the energy-height-plot.
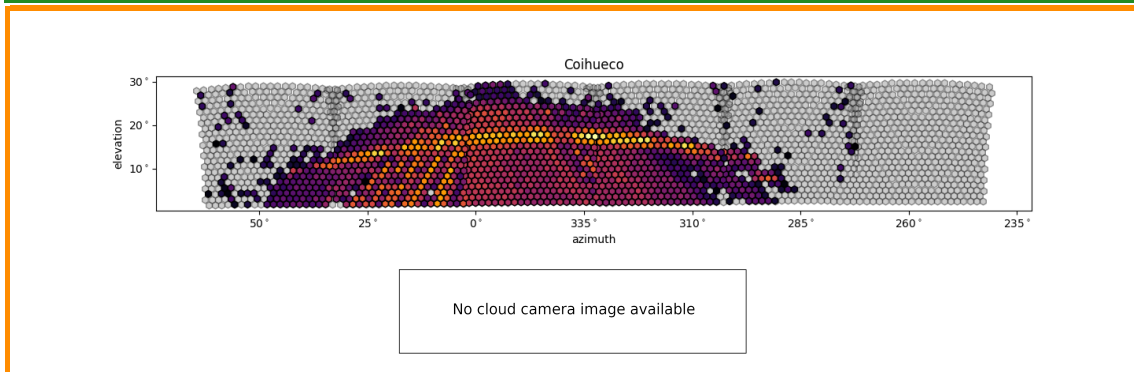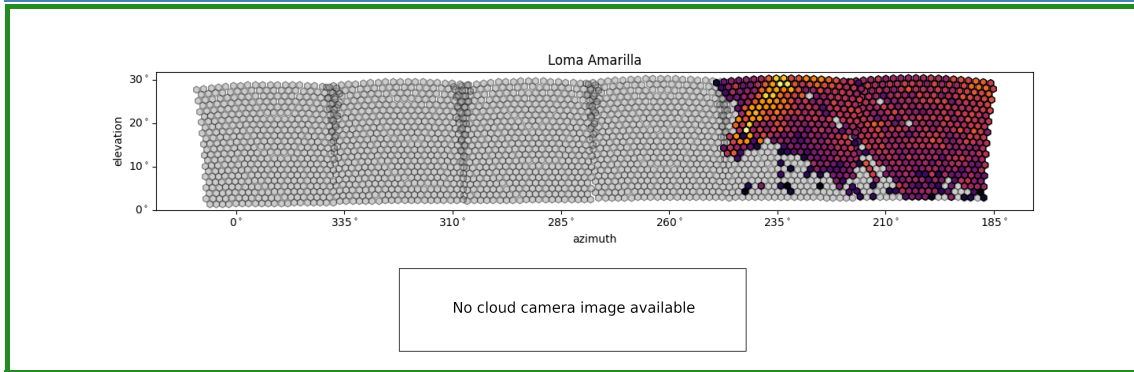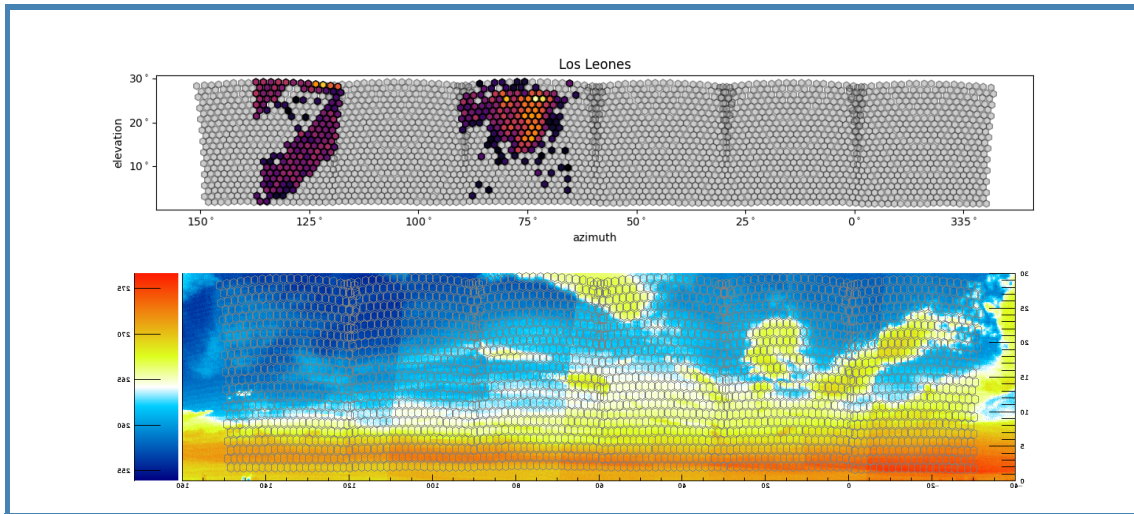
# 17.07.2020 - unusable
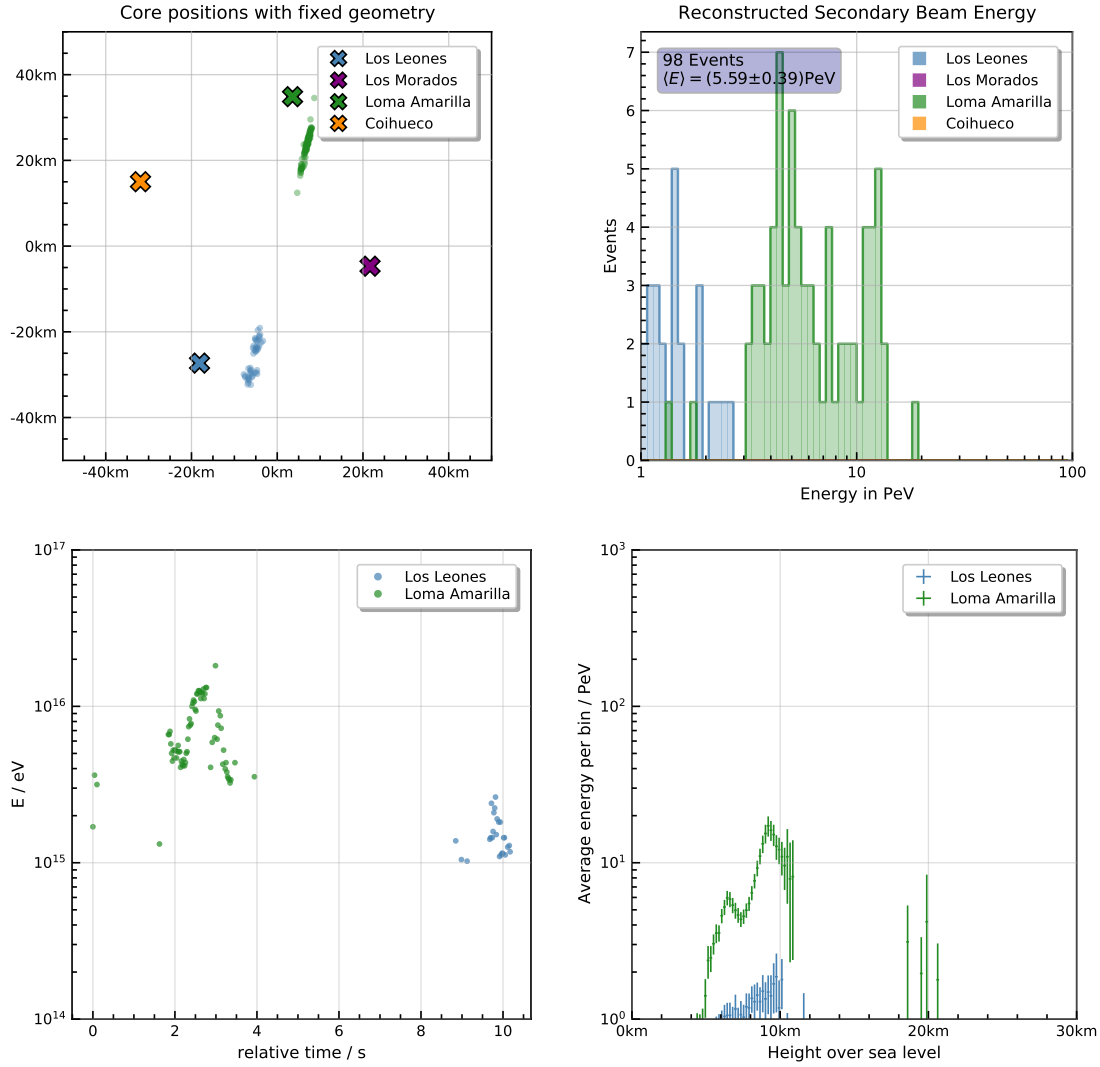


| FD Station | $\langle E \rangle$/PeV | # Events |
|---|---|---|
| Los Leones | 1.52 | 25 |
| Los Morados | - | 0 |
| Loma Amarilla | 6.98 | 73 |
| Coihueco | - | 0 |
| Total | 5.59 | 98 |

**Comments**
Indications for clouds can be seen in both the camera images, the pixel arrays and the energy-height-plot.

Los Leones



Loma Amarilla

No cloud camera image available
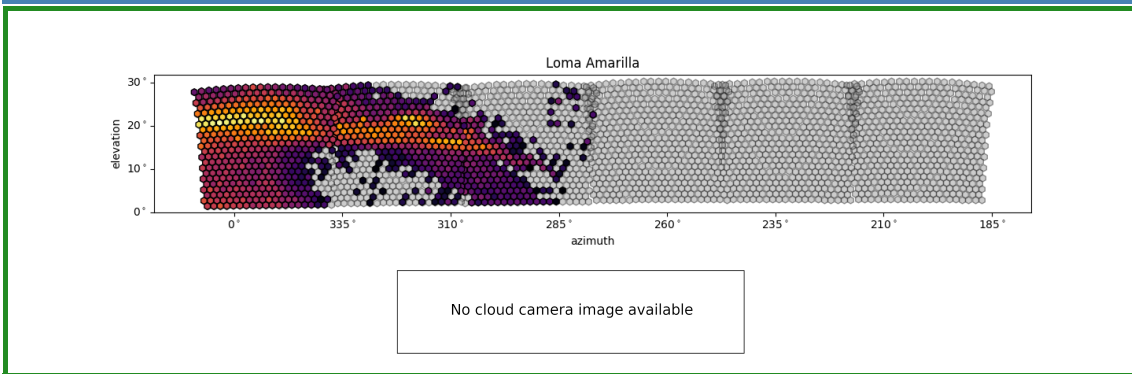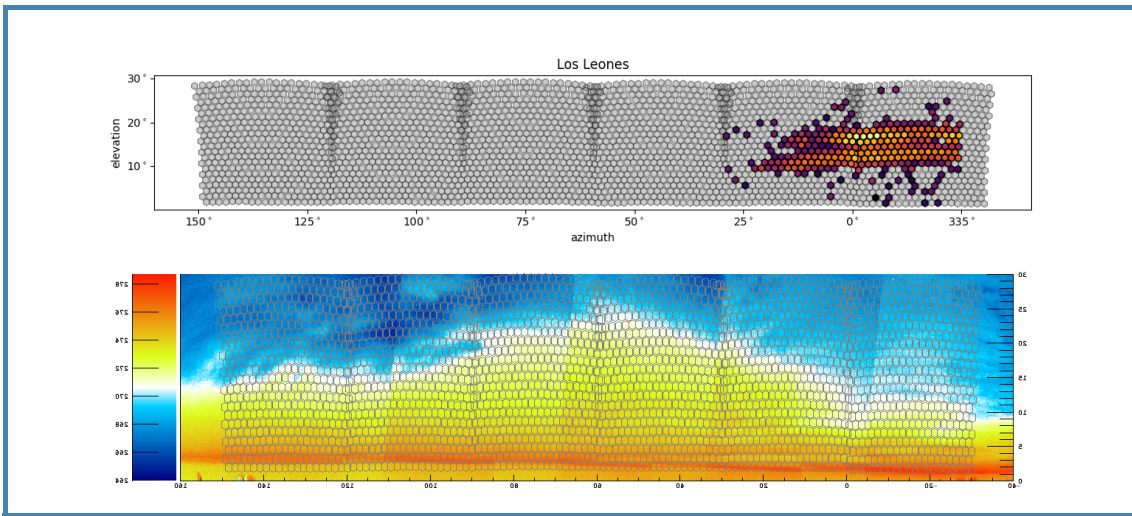
# 24.07.2020 - unusable
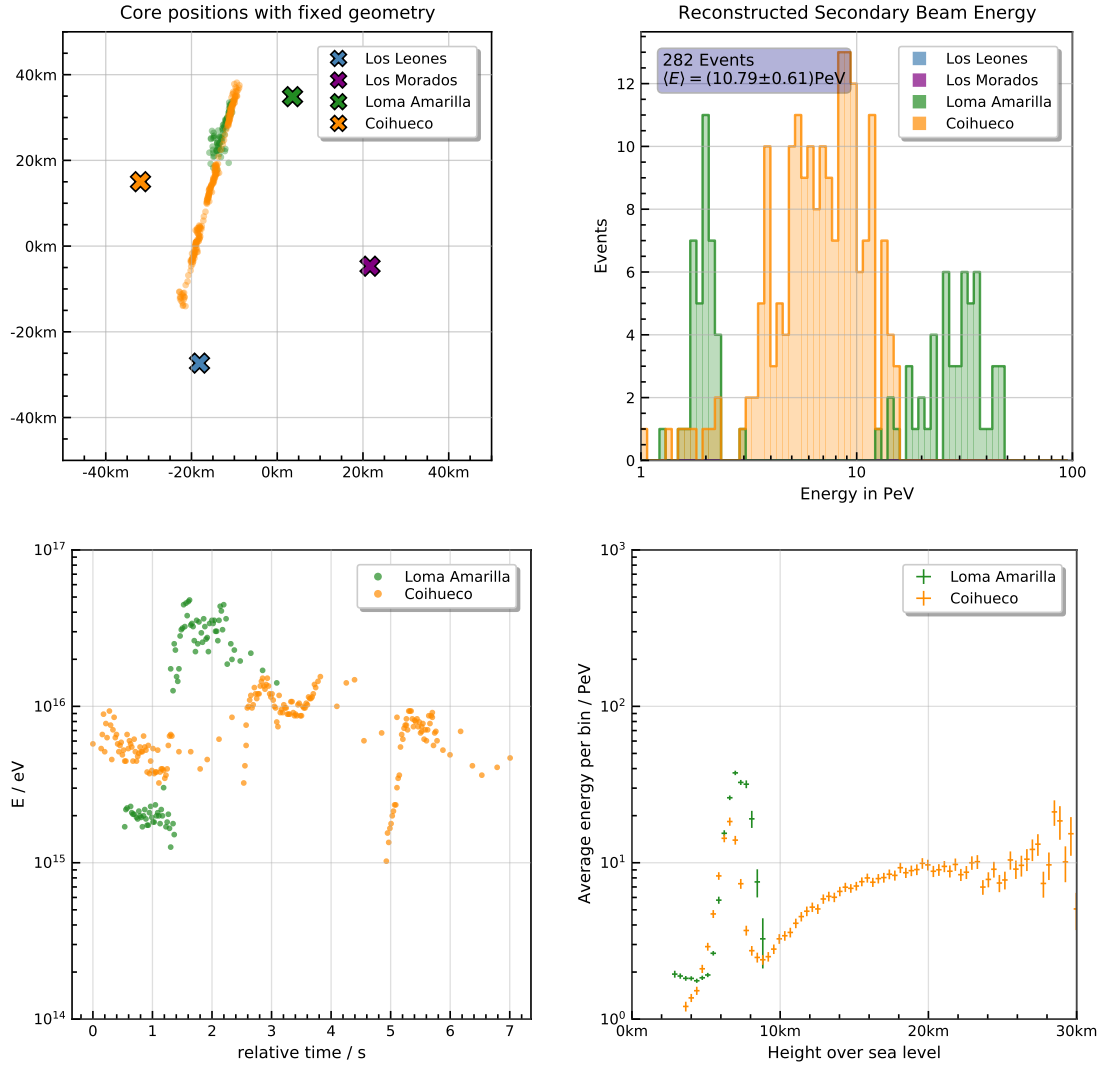


| FD Station | $\langle E \rangle$/PeV | # Events |
|---|---|---|
| Los Leones | - | 0 |
| Los Morados | - | 0 |
| Loma Amarilla | 17.85 | 90 |
| Coihueco | 7.49 | 192 |
| Total | 10.79 | 282 |

**Comments**
Indications for clouds can be seen in both the pixel arrays and the energy-height-plot.

Loma Amarilla

No cloud camera image available

Coihueco

No cloud camera image available
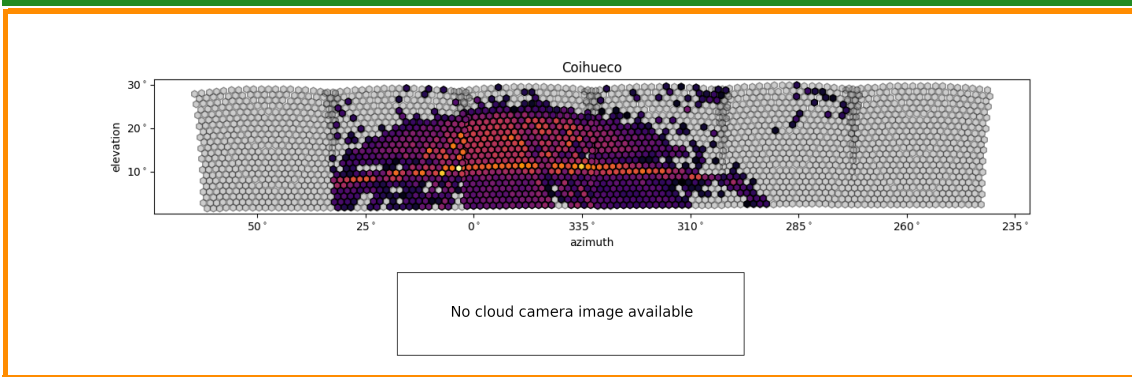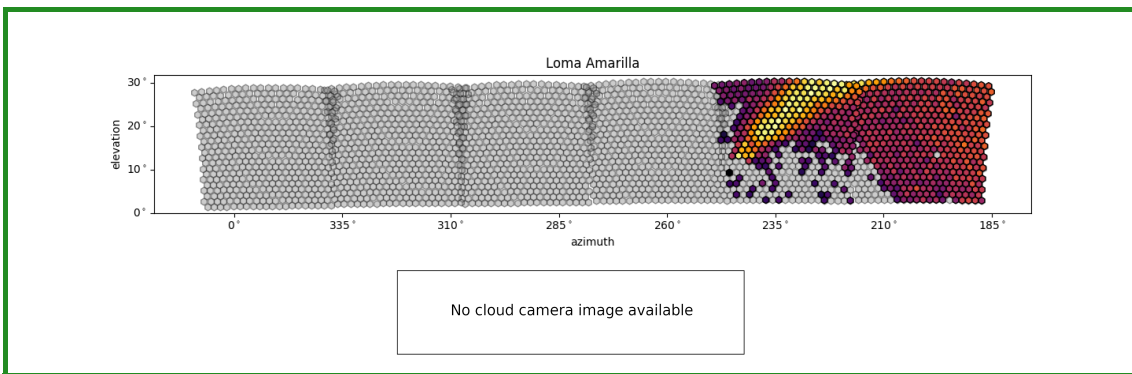
## A.2. Saturdays

**Table A.2.:** Overview of the Saturdays with measurements of the Aeolus main beam. Listed are the individual dates with an assessment of the data quality, based on the presence of clouds. Also listed is the average energy of the transition, calculated with an average aerosol concentration. The number of events corresponds to FD-events, meaning that individual eyes are counted separately.

| Date | Data Quality | $\langle E \rangle / \mathrm{PeV}$ | # Events |
|------|------|------|------|
| 29.06.2019 | unusable | 102.5 | 39 |
| 06.07.2019 | usable | 158.5 | 82 |
| 03.08.2019 | usable | 218.0 | 200 |
| 20.06.2020 | unusable | 100.8 | 90 |
| 27.06.2020 | usable | 152.8 | 60 |
| 18.07.2020 | unusable | 48.7 | 67 |

## 29.06.2019 - unusable
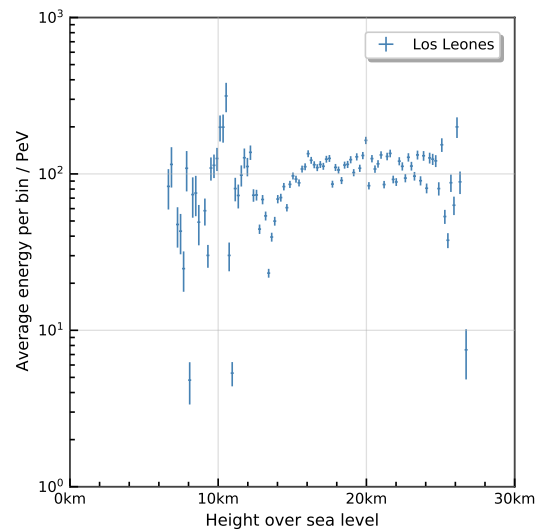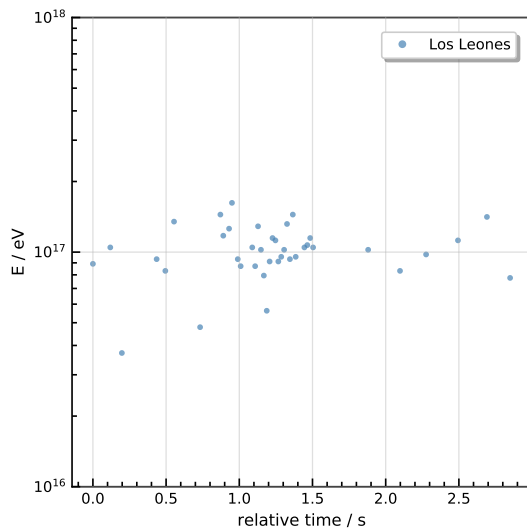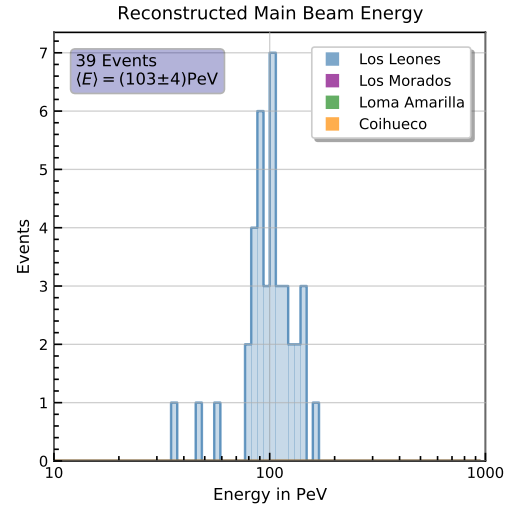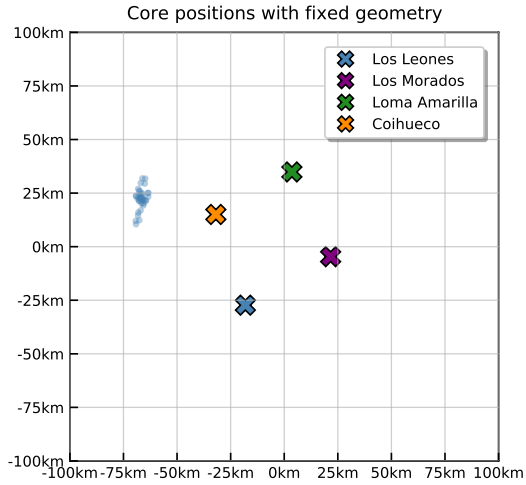


| FD Station | $\langle E \rangle$/PeV | # Events |
|---|---|---|
| Los Leones | 102.50 | 39 |
| Los Morados | - | 0 |
| Loma Amarilla | - | 0 |
| Coihueco | - | 0 |
| Total | 102.5 | 39 |

**Comments**
The cloud camera image shows a very clear indication for clouds.

# 06.07.2019 - usable

### Core positions with fixed geometry

### Reconstructed Main Beam Energy
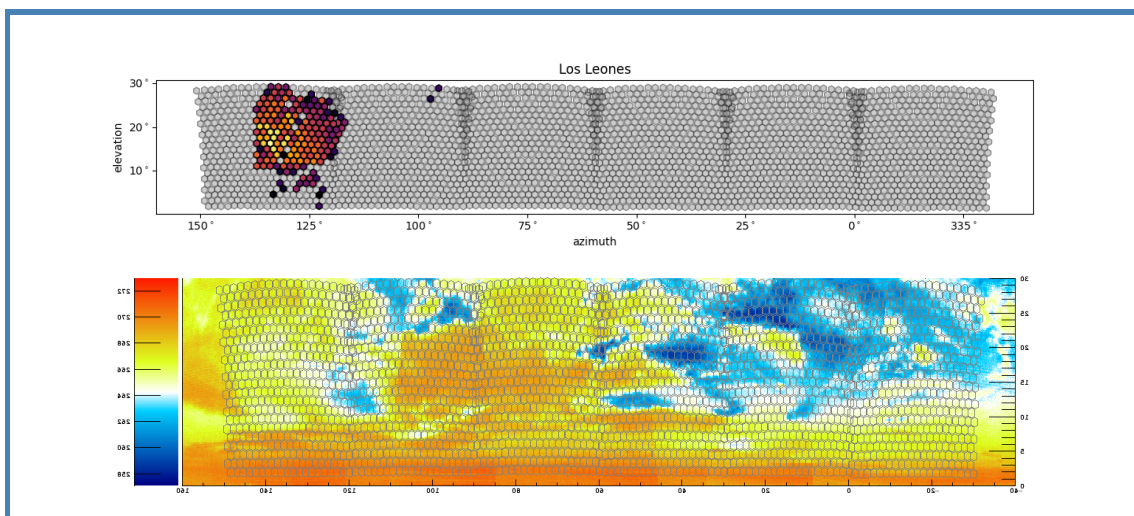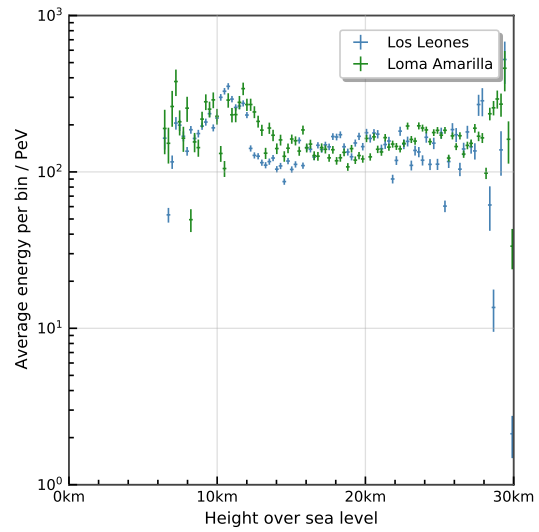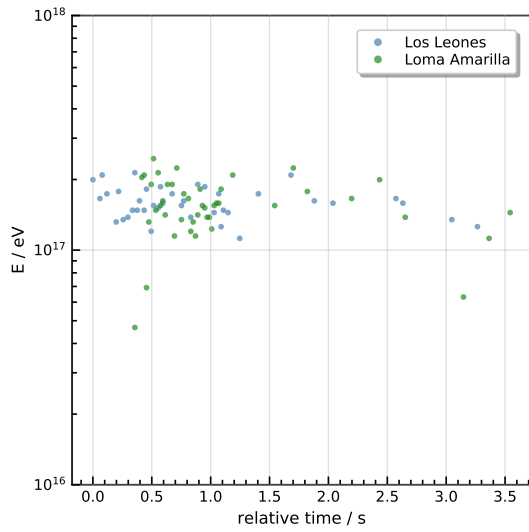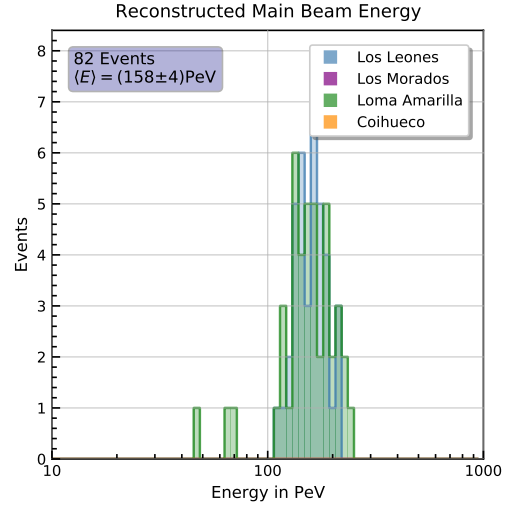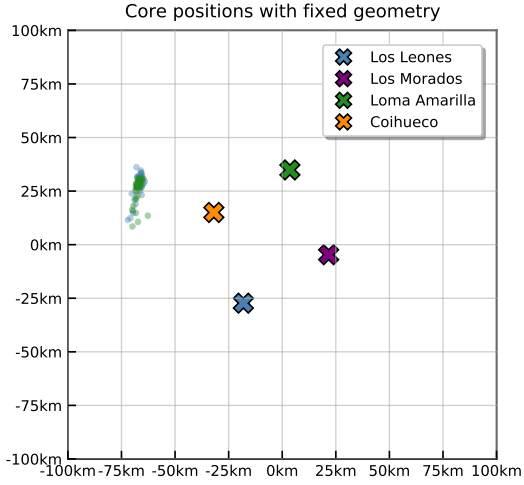
82 Events
$\langle E \rangle = (158 \pm 4)\,\text{PeV}$

| FD Station | $\langle E \rangle$/PeV | # Events |
|---|---|---|
| Los Leones | 160.17 | 39 |
| Los Morados | - | 0 |
| Loma Amarilla | 156.96 | 43 |
| Coihueco | - | 0 |
| Total | 158.5 | 82 |

**Comments**
No indications for clouds.

Los Leones



Loma Amarilla

No cloud camera image available
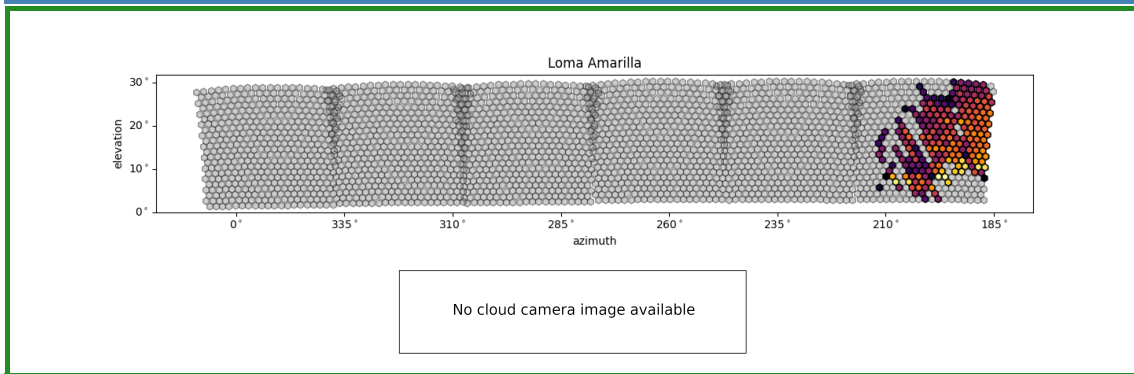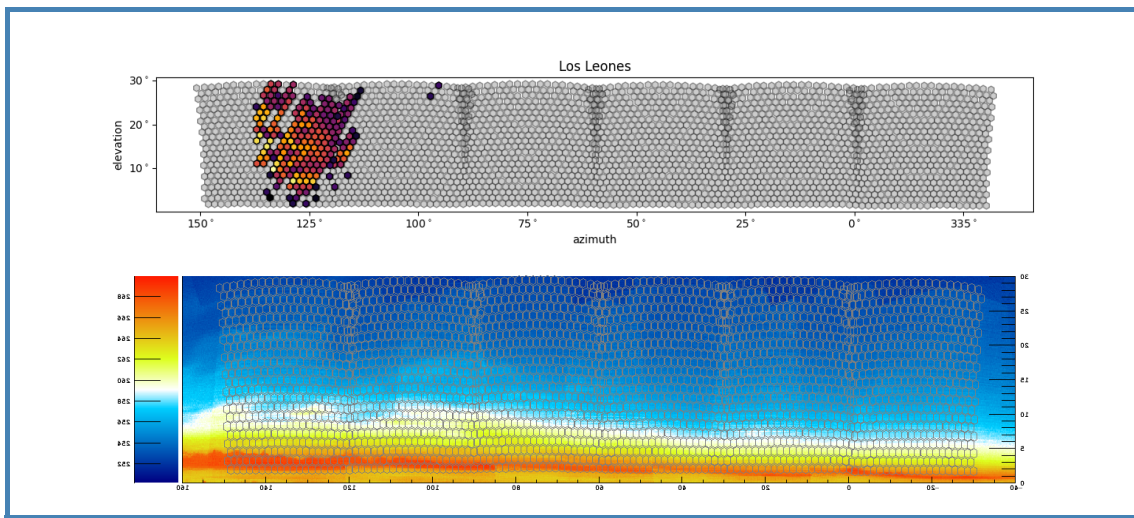
# 03.08.2019 - usable
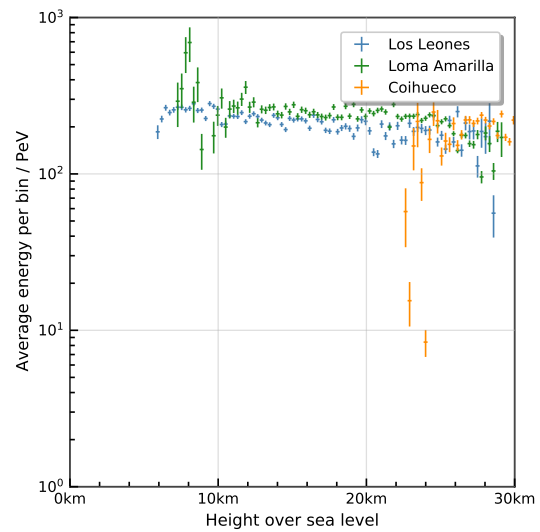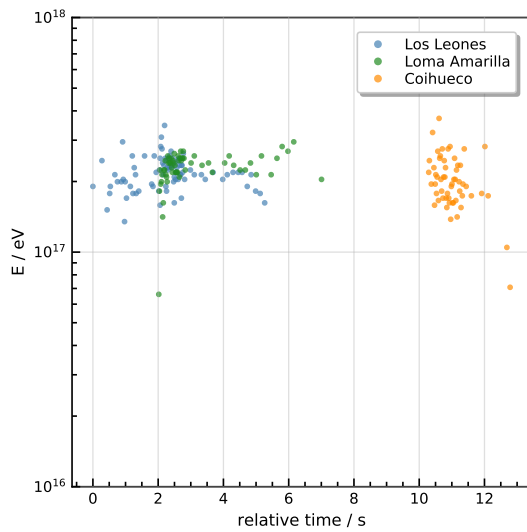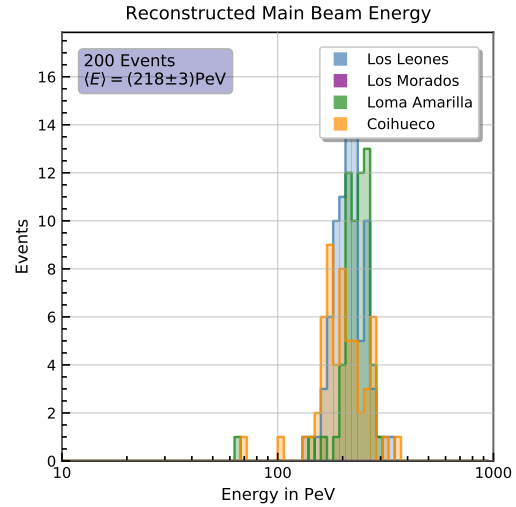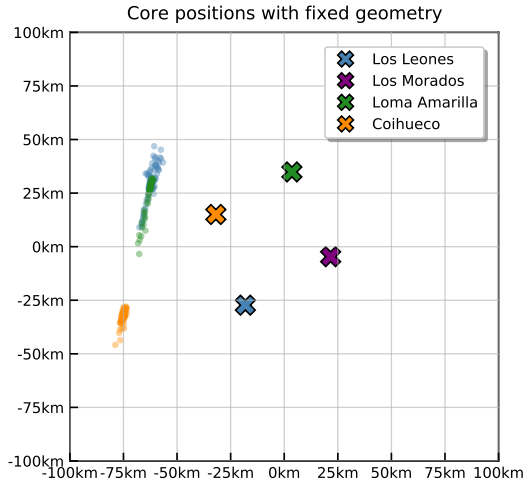


| FD Station | $\langle E\rangle$/PeV | # Events |
|---|---|---|
| Los Leones | 218.31 | 84 |
| Los Morados | - | 0 |
| Loma Amarilla | 230.05 | 60 |
| Coihueco | 204.60 | 56 |
| Total | 218.0 | 200 |

**Comments**
No indications for clouds.

Los Leones

Loma Amarilla

No cloud camera image available

Coihueco

No cloud camera image available
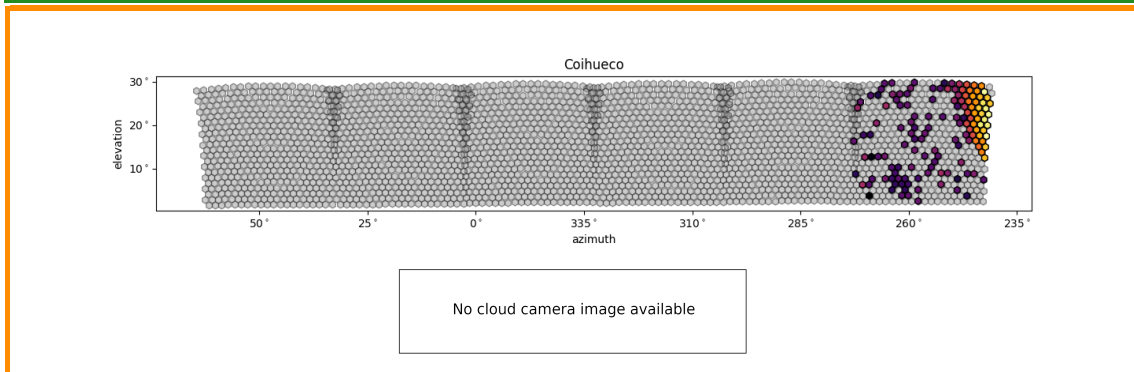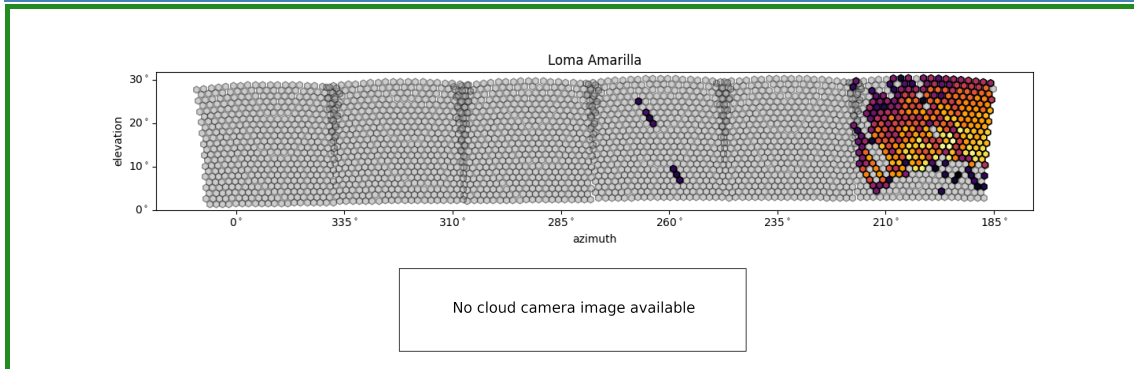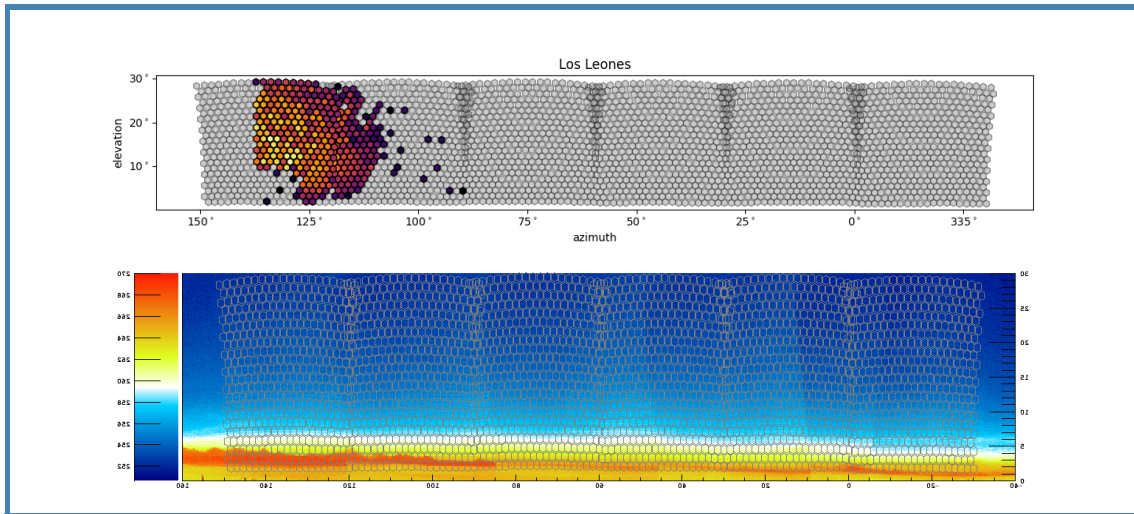
## 20.06.2020 - <span style="color:brown">unusable</span>
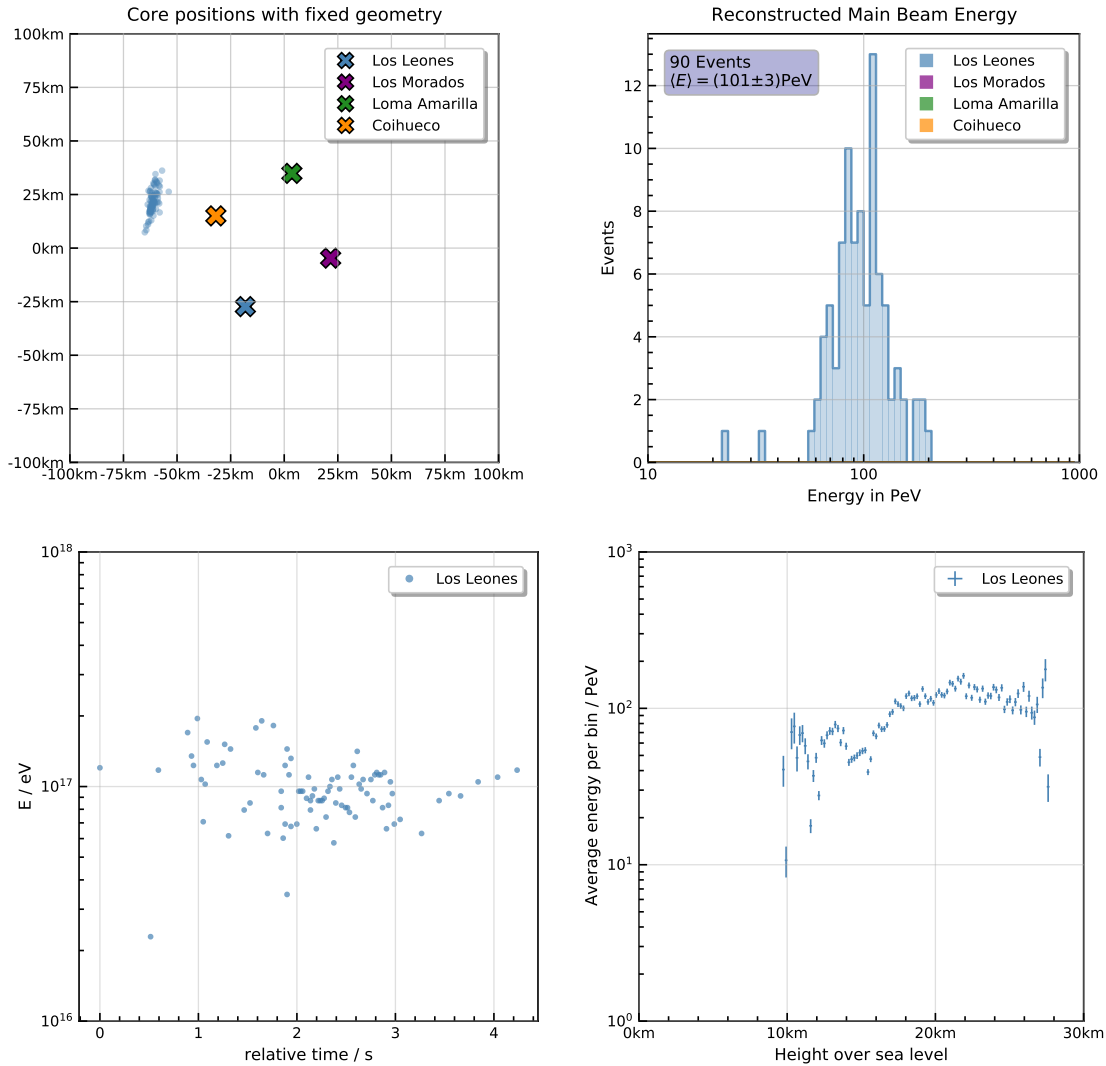


| FD Station | $\langle E \rangle$/PeV | # Events |
|---|---|---|
| Los Leones | 100.81 | 90 |
| Los Morados | - | 0 |
| Loma Amarilla | - | 0 |
| Coihueco | - | 0 |
| Total | 100.8 | 90 |

**Comments**

Indications for clouds can be seen in both the pixel arrays and the energy-height-plot.

Los Leones

No cloud camera image available
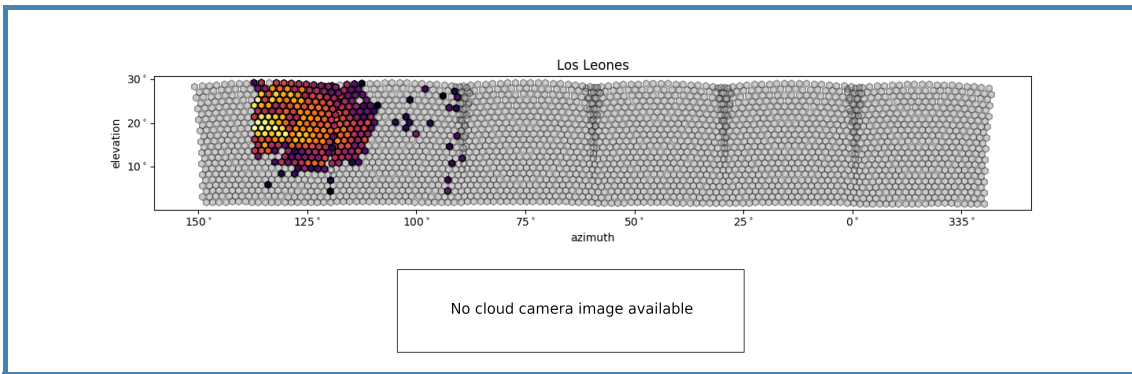
## 27.06.2020 - usable
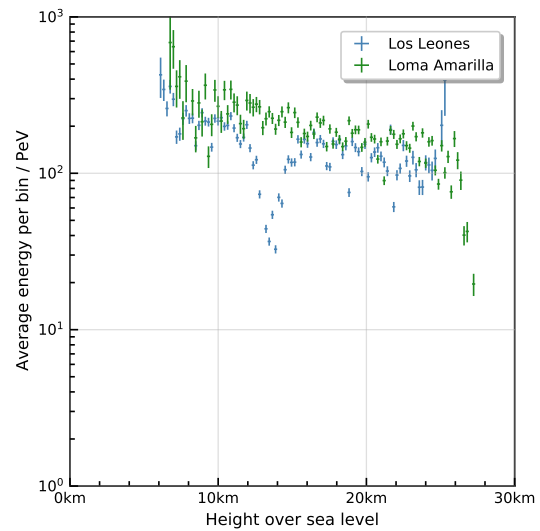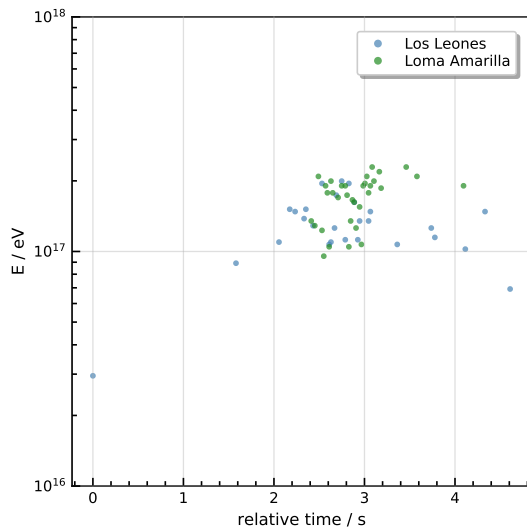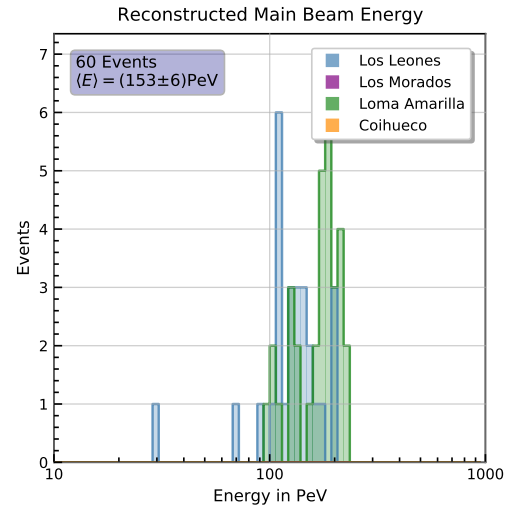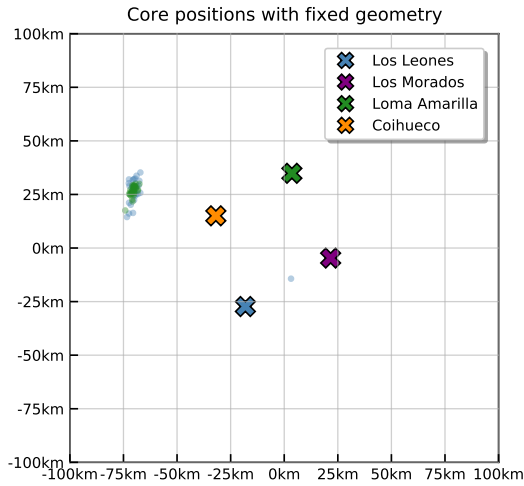


| FD Station | $\langle E \rangle$/PeV | # Events |
|---|---|---|
| Los Leones | 130.49 | 27 |
| Los Morados | - | 0 |
| Loma Amarilla | 171.12 | 33 |
| Coihueco | - | 0 |
| Total | 152.8 | 60 |

**Comments**

Los Leones shows a slight indication for a cloud in the energy-height-plot. The corresponding cloud camera image is mostly clear, however with a small cloud visible.
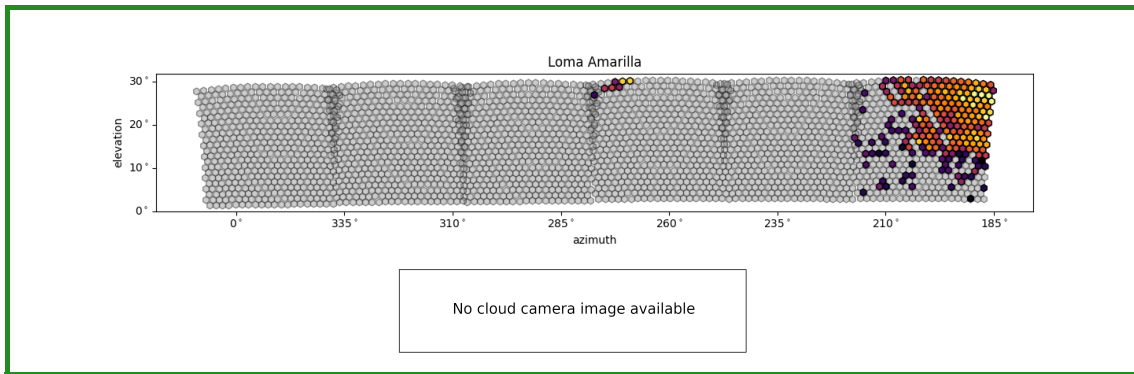
Los Leones



Loma Amarilla

No cloud camera image available
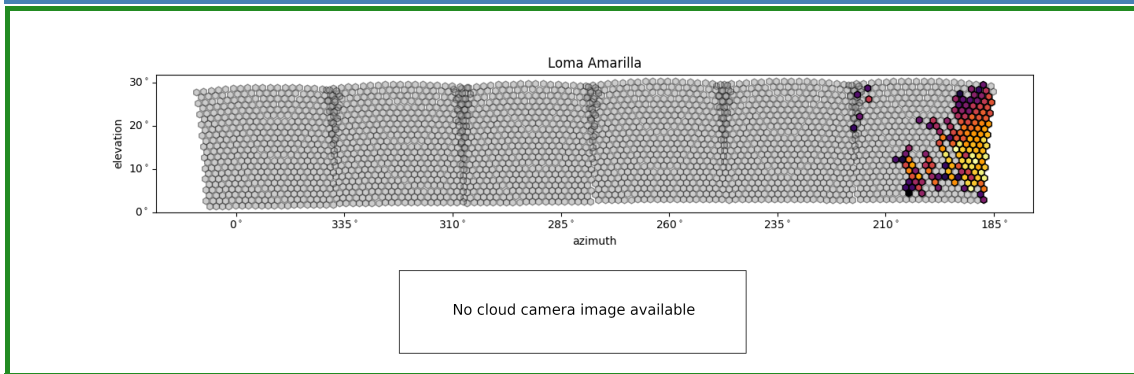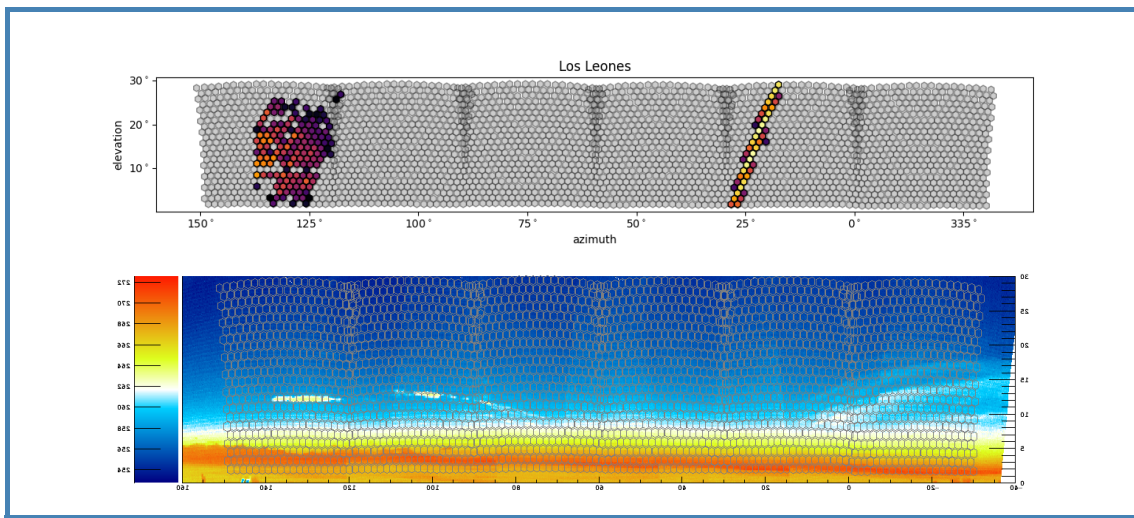
# 18.07.2020 - <span style="color:brown">unusable</span>
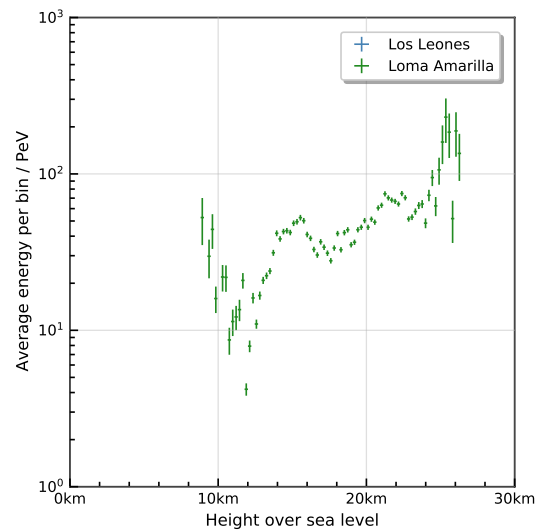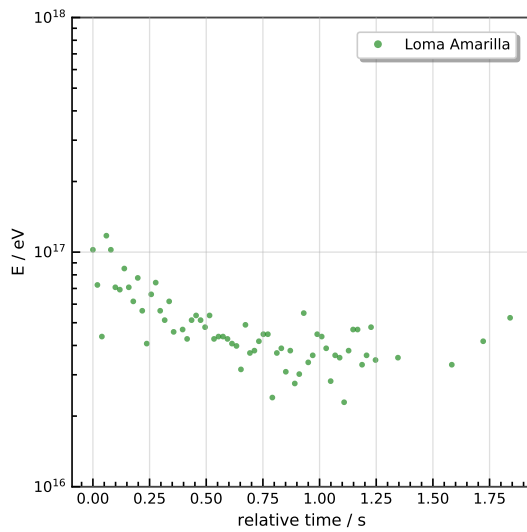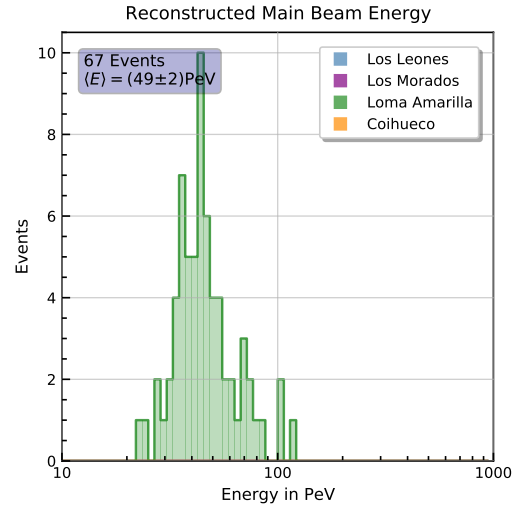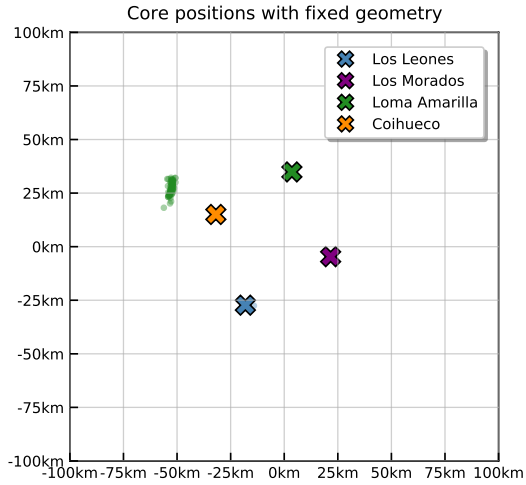


| FD Station | $\langle E \rangle$/PeV | # Events |
|---|---|---|
| Los Leones | - | 0 |
| Los Morados | - | 0 |
| Loma Amarilla | 48.67 | 67 |
| Coihueco | - | 0 |
| Total | 48.7 | 67 |

**Comments**
The energy-height-plot shows a clear indication of clouds.

Loma Amarilla

No cloud camera image available

# Bibliography

[1] V. F. Hess, "Über Beobachtungen der durchdringenden Strahlung bei sieben Freiballonfahrten," *Phys. Z.*, vol. 13, pp. 1084–1091, 1912.

[2] T. Wulf, "Ein neues Elektrometer für statische Ladungen," *Phys. Z.*, vol. 8, p. 246, 1907.

[3] W. Kolhörster, "Messungen der durchdringenden Strahlungen bis in Höhen von 9300 m," *Verh. deutsche phys. Gesellschaft*, vol. 16, pp. 719–721, 1914.

[4] A. H. Compton, "A Geographic Study of Cosmic Rays," *Physical Review*, vol. 43, pp. 387–403, 1933.

[5] P. Auger *et al.*, "Extensive Cosmic-Ray Showers," *Rev. Mod. Phys.*, vol. 11, pp. 288–291, 1939.

[6] J. Linsley, "Evidence for a Primary Cosmic-Ray Particle with Energy 1020 eV," *Physical Review Letters*, vol. 10, pp. 146–148, 1963.

[7] P. O. Lagage *et al.*, "The maximum energy of cosmic rays accelerated by supernova shocks.," *Astronomy and Astrophysics*, vol. 125, pp. 249–257, 1983.

[8] D. Perkins, *Particle Astrophysics.* Oxford University Press, 2003.

[9] J. A. Simpson, "Elemental and Isotopic Composition of the Galactic Cosmic Rays," *Annual Review of Nuclear and Particle Science*, vol. 33, no. 1, pp. 323–382, 1983.

[10] E. Fermi, "On the Origin of the Cosmic Radiation," *Phys. Rev.*, vol. 75, pp. 1169–1174, 1949.

[11] A. M. Hillas, "The Origin of Ultra-High-Energy Cosmic Rays," *Annual Review of Astronomy and Astrophysics*, vol. 22, no. 1, pp. 425–444, 1984.

[12] A. De Angelis *et al.*, *Messengers from the High-Energy Universe*, pp. 575–681. Cham: Springer International Publishing, 2018.

[13] J. Blümer *et al.*, "Cosmic rays from the knee to the highest energies," *Progress in Particle and Nuclear Physics*, vol. 63, no. 2, pp. 293–338, 2009.

[14] V. S. Berezinskii *et al.*, "A bump in the ultra-high energy cosmic ray spectrum," *Astronomy and Astrophysics*, vol. 199, no. 1-2, pp. 1–12, 1988.

[15] J. Beatty *et al.*, "The Highest-Energy Cosmic Rays," *Annual Review of Nuclear and Particle Science*, vol. 59, no. 1, pp. 319–345, 2009.

[16] J. Cronin, "Cosmic rays: the most energetic particles in the universe," *Rev. Mod. Phys.*, vol. 71, pp. S165–S172, 1999.

[17] M. Unger *et al.*, "Origin of the ankle in the ultrahigh energy cosmic ray spectrum, and of the extragalactic protons below it," *Phys. Rev. D*, vol. 92, no. 12, p. 123001, 2015.

[18] A. Batista *et al.*, "Open Questions in Cosmic-Ray Research at Ultrahigh Energies," *Frontiers in Astronomy and Space Sciences*, vol. 6, 2019.

[19] https://cds.cern.ch/images/CMS-PHO-GEN-2017-008-1/. accessed 11th Mai 2021.

[20] K.-H. Kampert *et al.*, "Extensive air showers and ultra high-energy cosmic rays: a historical review," *The European Physical Journal H*, vol. 37, no. 3, p. 359–412, 2012.

[21] T. K. Gaisser, *Cosmic rays and particle physics.* Cambridge University Press, 1990.

[22] W. Heitler, *The quantum theory of radiation*, vol. 5 of *International Series of Monographs on Physics.* Oxford: Oxford University Press, 1936.

[23] J. Matthews, "A Heitler model of extensive air showers," *Astroparticle Physics*, vol. 22, no. 5, pp. 387–397, 2005.

[24] E. Seo *et al.*, "Cosmic-ray energetics and mass (CREAM) balloon project," *Advances in Space Research*, vol. 33, no. 10, pp. 1777–1785, 2004. The Next Generation in Scientific Ballooning.

[25] M. Malacari, *Systematic Effects in the Measurement of Vertical Aerosol Profiles at the Pierre Auger Observatory.* PhD thesis, University of Adelaide, 2016. GAP-2016-074.

[26] A. Bucholtz, "Rayleigh-scattering calculations for the terrestrial atmosphere," *Appl. Opt.*, vol. 34, no. 15, pp. 2765–2773, 1995.

[27] S. Chandrasekhar, *Radiative transfer.* Dover Publications, 1960.

[28] J. Abraham *et al.*, "A study of the effect of molecular and aerosol conditions in the atmosphere on air fluorescence measurements at the Pierre Auger Observatory," *Astroparticle Physics*, vol. 33, no. 2, pp. 108–129, 2010.

[29] K. Louedec, *Atmospheric aerosols at the Pierre Auger Observatory: characterization and effect on the energy estimation for ultra-high energy cosmic rays.* PhD thesis, Université Paris-Sud 11, 2011. GAP-2012-075.

[30] P. Abreu *et al.*, "Description of atmospheric conditions at the Pierre Auger Observatory using the Global Data Assimilation System (GDAS)," *Astroparticle Physics*, vol. 35, no. 9, pp. 591–607, 2012.

[31] A. Aab *et al.*, "Origin of atmospheric aerosols at the Pierre Auger Observatory using studies of air mass trajectories in South America," *Atmospheric Research*, vol. 149, p. 120–135, 2014.

[32] P. Abreu *et al.*, "Techniques for measuring aerosol attenuation using the Central Laser Facility at the Pierre Auger Observatory," *Journal of Instrumentation*, vol. 8, no. 04, p. P04009–P04009, 2013.

[33] A. Aab *et al.*, "The Pierre Auger Cosmic Ray Observatory," *Nuclear Instruments and Methods in Physics Research Section A: Accelerators, Spectrometers, Detectors and Associated Equipment*, vol. 798, p. 172–213, 2015.

[34] The Pierre Auger Collaboration, "The Pierre Auger Observatory Design Report," 1997.

[35] M. Medina *et al.*, "Enhancing the Pierre Auger Observatory to the 1017–1018.5eV range: Capabilities of an Infill Surface Array," *Nuclear Instruments and Methods in Physics Research Section A: Accelerators, Spectrometers, Detectors and Associated Equipment*, vol. 566, no. 2, pp. 302–311, 2006.

[36] J. Abraham *et al.*, "The fluorescence detector of the Pierre Auger Observatory," *Nuclear Instruments and Methods in Physics Research Section A: Accelerators, Spectrometers, Detectors and Associated Equipment*, vol. 620, no. 2-3, p. 227–251, 2010.

[37] J. Abraham *et al.*, "A study of the effect of molecular and aerosol conditions in the atmosphere on air fluorescence measurements at the Pierre Auger Observatory," *Astroparticle Physics*, vol. 33, no. 2, pp. 108–129, 2010.

[38] J. Abraham *et al.*, "A study of the effect of molecular and aerosol conditions in the atmosphere on air fluorescence measurements at the Pierre Auger Observatory," *Astroparticle Physics*, vol. 33, no. 2, p. 108–129, 2010.

[39] S. BenZvi *et al.*, "The Lidar system of the Pierre Auger Observatory," *Nuclear Instruments and Methods in Physics Research Section A: Accelerators, Spectrometers, Detectors and Associated Equipment*, vol. 574, no. 1, pp. 171–184, 2007.

[40] V. Rizi *et al.*, "The Auger Raman Lidar: several years of continuous observations," in *European Physical Journal Web of Conferences*, vol. 197 of *European Physical Journal Web of Conferences*, p. 02003, 2019.

[41] J. Chirinos *et al.*, "Cloud Monitoring at the Pierre Auger Observatory," in *International Cosmic Ray Conference*, vol. 33 of *International Cosmic Ray Conference*, p. 2244, 2013.

[42] P. Ingmann *et al.*, *ADM-Aeolus Mission Requirements Document.* ESA Mission Science Division, 2016.

[43] P. Flamant *et al.*, "ADM-Aeolus retrieval algorithms for aerosol and cloud products," *Tellus A: Dynamic Meteorology and Oceanography*, vol. 60, no. 2, pp. 273–286, 2008.

[44] https://www.ecmwf.int/en/about/media-centre/news/2020/ecmwf-starts-assimilating-aeolus-wind-data. accessed 6th April 2021.

[45] https://www.esa.int/Enabling_Support/Space_Transportation/Types_of_orbits. accessed 3rd April 2021.

[46] O. Reitebuch *et al.*, "ADM-Aeolus ATBD Level1B Products," 2018.

[47] E. Andersson *et al.*, *ADM-Aeolus Science Report.* ESA Communication Production Office, 2008.

[48] http://www.esa.int/Applications/Observing_the_Earth/Aeolus/Aeolus_satellite. accessed 5th April 2021.

[49] https://www.ksat.no/no/news/news-archive/2020/ksat-ensures-aeolus-data-in-nrt/. accessed 17th Mai 2021.

[50] M. Schillinger *et al.*, "ALADIN: the lidar instrument for the AEOLUS mission," in *Sensors, Systems, and Next-Generation Satellites VI*, vol. 4881, pp. 40 – 51, International Society for Optics and Photonics, SPIE, 2003.

[51] O. Lux *et al.*, "Intercomparison of wind observations from the European Space Agency's Aeolus satellite mission and the ALADIN Airborne Demonstrator," *Atmospheric Measurement Techniques*, vol. 13, no. 4, pp. 2075–2097, 2020.

[52] O. Reitebuch *et al.*, "Initial Assessment of the Performance of the First Wind Lidar in Space on Aeolus," *EPJ Web Conf.*, vol. 237, p. 01010, 2020.

[53] O. Lux *et al.*, "High-power and frequency-stable ultraviolet laser performance in space for the wind lidar on Aeolus," *Optics Letters*, vol. 45, pp. 1443–1446, 2020.

[54] Oliver Reitebuch and Isabell Krisch (DLR), 2020. private communication.

[55] T. Moch, "Study of Ultrahigh-Energy Cosmic Rays Measured in Monocular Mode with the Fluorescence Telescopes of the Pierre Auger Observatory," Master's thesis, Karlsruher Institut für Technologie, Institut für Kernphysik, 2020.

[56] http://celestrak.com/columns/v04n03/. accessed 20th May 2021.

[57] D. Vallado *et al.*, "Revisiting Spacetrack Report #3,"

[58] B. Rhodes, "Skyfield: High precision research-grade positions for planets and Earth satellites generator," 2019. Software.

[59] T. Fujii, 2021. private communication.

[60] D. Kuempel *et al.*, "Geometry reconstruction of fluorescence detectors revisited," *Astroparticle Physics*, vol. 30, no. 4, p. 167–174, 2008.

[61] C. R. Wilkinson *et al.*, "Geometrical reconstruction with the High Resolution Fly's Eye prototype cosmic ray detector," *Astroparticle Physics*, vol. 12, no. 3, pp. 121–134, 1999.

[62] S. Falk *et al.*, "A First Look at HEAT Data," 2010. Auger internal note, GAP-2010-123.

[63] J. Debatin, "Investigation of Optical Properties of the Fluorescence Telescopes of the Pierre Auger Observatory," Master's thesis, Karlsruher Institut für Technologie, Institut für Experimentelle Kernphysik, 2015.

[64] B. Dawson *et al.*, "Shower Profile Reconstruction with Engineering Array FD Data," 2001. Auger internal note, GAP-2001-016.

[65] V. Verzi, "The Energy Scale of the Pierre Auger Observatory," in *33rd International Cosmic Ray Conference*, 2013.

[66] G. Cowan, *Statistical Data Analysis.* Oxford science publications, Clarendon Press, 1998.

[67] L. Valore, 2021. private communication.

# Acknowledgments